N 62 12172

CASE FILE COPY

Space Programs Summary No. 37-14, Volume I

for the period January 1, 1962 to March 1, 1962

jpl
JET PROPULSION LABORATORY
CALIFORNIA INSTITUTE OF TECHNOLOGY
PASADENA, CALIFORNIA

April 1, 1962

NATIONAL AERONAUTICS AND SPACE ADMINISTRATION
CONTRACT NO. NAS 7-100

Space Programs Summary No. 37-14, Volume I

for the period January 1, 1962 to March 1, 1962

JET PROPULSION LABORATORY
CALIFORNIA INSTITUTE OF TECHNOLOGY
PASADENA, CALIFORNIA

April 1, 1962

Preface

The *Space Programs Summary* is a two-volume bimonthly publication of the Jet Propulsion Laboratory. Research and development activities conducted by JPL having specific application to space programs under the sponsorship of the National Aeronautics and Space Administration are reported in this publication. Unclassified and classified activities will be documented in Volumes I and II, respectively.

The projects reported herein were undertaken in partial fulfillment of National Aeronautics and Space Administration Contract NAS 7-100.

W. H. Pickering, *Director*
Jet Propulsion Laboratory

Space Programs Summary No. 37-14
Volume I

Copyright© 1962
Jet Propulsion Laboratory
California Institute of Technology

Contents

PART ONE: RÉSUMÉ 1
I. Lunar Program 1
II. Planetary–Interplanetary Program 1
III. Deep Space Instrumentation Facility 1

PART TWO: LUNAR PROGRAM 3

I. *Ranger* Project 3
A. Systems 3
B. Space Sciences 7
C. Telecommunications 8
D. Secondary Power 8
E. Supporting Activities 11

PART THREE: PLANETARY–INTERPLANETARY PROGRAM . . . 13

I. Objectives 13

II. *Mariner* R Project 14
A. Space Sciences 14
B. Telecommunications 21
C. Secondary Power 22
D. Engineering Facilities 30

References 34

III. *Mariner* B Project 35
A. Space Sciences 35
B. Telecommunications 40
C. Secondary Power 41
D. Supporting Activities 44

References 46

PART FOUR: DEEP SPACE INSTRUMENTATION FACILITY 47

I. Tracking Operations 49
A. Participation in *Ranger III* 49

II. Facilities and Capabilities 53
A. New Equipment 53
B. Engineering Development 64
C. Engineering Studies 72

Reference 74

Contents (cont'd)

III. Research and Development 75
A. Transponder Ranging System 75
B. Low Noise Systems 99
C. X-Band Communications Components 109
D. Advanced Receiving Techniques 111
E. Mesa Antenna Range 116

References 117

IV. Advanced Antenna System 119
A. Synopsis 119
B. Supporting Studies 119

References 135

PART ONE
RÉSUMÉ

I. Lunar Program

At 15:30:11 EST on January 26, 1962, *Ranger III* was launched from Cape Canaveral into a heliocentric orbit. The spacecraft executed a mid-course maneuver on command, passed by the Moon at a distance of 22,800 mi, and was tracked to a distance of 560,000 mi by the DSIF. A failure in the spacecraft computer and sequencer during the lunar flyby prevented the recovery of TV pictures.

The *Ranger* RA-4 spacecraft and launch vehicle are at AFMTC being prepared for the next launch attempt.

II. Planetary–Interplanetary Program

Both flight spacecraft for *Mariner* R have been assembled and are in the process of electrical checkout. All major aspects of the project are proceeding on schedule.

Prerelease version of *Mariner* B Project Development Plan (PDP) has been completed and forwarded to both NASA Headquarters and Marshall Space Flight Center for coordination.

III. Deep Space Instrumentation Facility

All stations participated successfully in tracking and receiving telemetry from *Ranger III* until its signals were diminished following the terminal maneuver.

Recent improvements to the DSIF include the addition of parametric preamplifiers, stable oscillator control of transmitter frequency, and high power L-band antenna feeds. A helical tracking antenna, as an aid to acquisition, was utilized at the South Africa station with *Ranger III*.

Research and advanced development for the DSIF continued in the fields of ranging, low noise systems, X-band communication components, receiving techniques, antenna structures, and the Advanced Antenna System (AAS). A design for the AAS has been chosen specifying a diameter of 210-ft. Supporting studies for the large antenna were made with wind tunnel tests, servo and dynamic tests, servo simulator studies, and wind measurements at the site.

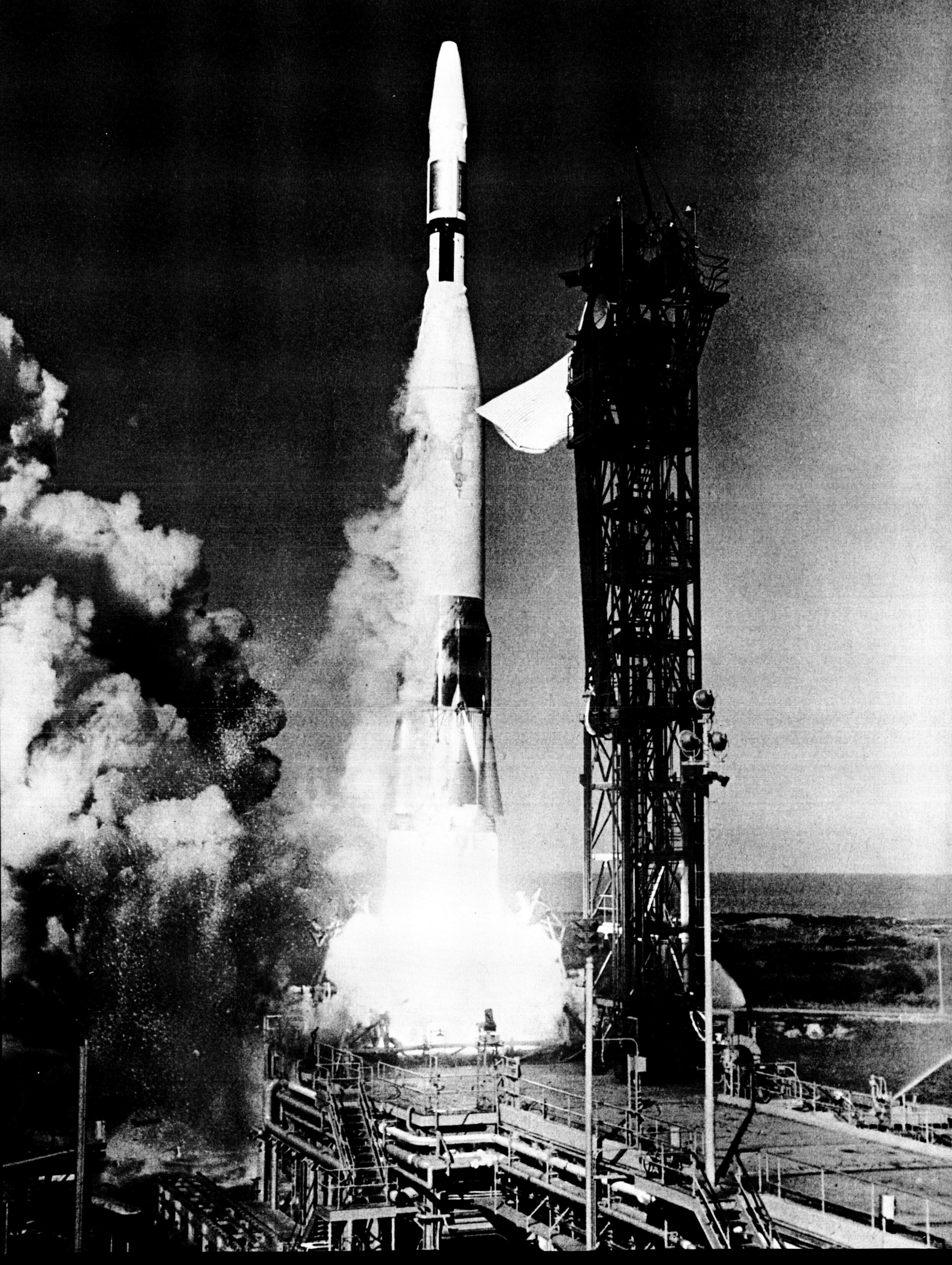

PART TWO
LUNAR PROGRAM

I. *Ranger* Project

The object of the *Ranger III* flight was to hit the Moon during a period of a few days around third-quarter phase in January 1962 when lunar lighting would have been good for photography and a near-vertical impact trajectory could have been achieved; the usable days were January 22 through 26. Range-safety and tracking azimuth constraints established a firing window of about 1 hr on each of the 5 days.

Preflight activities continued on schedule until January 19, when during *Atlas* fueling, the fuel tank insulation bulkhead failed. At first it appeared that the mission would have to be abandoned until the February lunar opportunity. But *Atlas* personnel, working around the clock, made an ingenious and unprecedented repair without removing the vehicle from the pad. The flight was rescheduled for January 26, and the spacecraft TV camera was adjusted so that January 27 could also be used if necessary, even though lunar lighting would be poor; the MA-6 *Mercury* flight was also scheduled for that day.

Ranger III was launched on January 26, 1962, at 15:30:11 EST (20:30:11 GMT). A failure in the *Atlas* ground guidance system resulted in a late booster cutoff with no control over the sustainer cutoff time to compensate for the excess velocity accumulated. Two programmed Agena burning periods followed and the spacecraft was injected into an orbit with too high an energy for it to intercept the Moon. The excess injection energy was considerably greater than that which the mid-course propulsion system was designed to correct, so that the possibility of a successful lunar impact mission was ruled out early in the flight.

The over-all flight performance of the *Ranger III* spacecraft was quite successful, but there were a few failures which have resulted in some modifications to the *Ranger* RA-4 spacecraft and supporting operations. The stations of the Deep Space Instrumentation Facility (DSIF) provided tracking and telemetry coverage continuously for 5 days except for periods when the RF signal was too weak to recover. The spacecraft signal was essentially lost at 18:54 GMT on January 31, shortly after the supply of gas used for attitude stabilization was exhausted.

A. Systems

1. Ranger III *Flight Performance*

The spacecraft performance can be divided into three distinct phases: (1) launch, (2) mid-course, and (3) terminal. The launch phase was initiated by starting the

launch counter in the spacecraft central computer and sequencer (CC&S) at 2 min before liftoff. The mid-course and terminal phases were initiated by real-time ground commands at times selected to optimize the ensuing maneuver sequences under abnormal trajectory conditions. Each phase consisted of a fixed sequence of events to be executed on command from the CC&S. The only variables within these sequences were the duration of the mid-course and terminal maneuver turns, the direction or polarity of each turn, and the velocity increment to be provided by the mid-course motor. These variables were read into the CC&S register from the ground as sets of three stored commands prior to initiating the mid-course and terminal maneuvers.

The spacecraft transmitter was switched back and forth by ground command to transmit over the low gain omnidirectional antenna or the high gain directional antenna. The spacecraft transmitter was on low gain antenna until first Goldstone acquisition and during the mid-course maneuver. It was twice commanded over during the vidicon period without improving the received signal.

Other ground commands were available to compensate for nonstandard performance. The first of these (hinge over-ride) was attempted when the signal was lost during the terminal maneuver. The spacecraft data encoder was switched by ground command out of scientific mode back to engineering cruise mode after 50 min of vidicon data. Other commands were also tested.

a. Launch phase. The countdown on January 26 was smooth, with only minor delays for pyrotechnics installation, and the vehicle lifted off at 20:30:11 GMT. As a result of various communications and equipment problems, the AMR tracking stations did not supply any real-time acquisition data to South Africa; however, the DSIF stations there acquired the spacecraft signal promptly using preflight predictions. It was soon evident that the trajectory energy was too high and the spacecraft would escape instead of following the desired lunar transfer ellipse. The travel time to the Moon would be only about 50 hr instead of 66 hr and the spacecraft would pass ahead of and below the Moon at a distance of many thousands of miles.

The objectives of the flight then became: (1) to test the spacecraft functions including the mid-course and terminal maneuvers, and (2) to obtain TV pictures of the Moon during the fly-by. (It would also have been desirable to fire the capsule retro-rocket as a test, but this could not be done because the system was intentionally designed in such a way that the capsule sequence could be initiated only via the radar altimeter, which would not trigger because of its distance from the Moon.)

Early telemetry data from the South Africa Station indicated that the spacecraft was functioning normally with the exception of the omnidirectional transmitting system. Both the telemetered transmitter output and the signal strength recorded at the ground station were low. The spacecraft stabilized and acquired the Sun and Earth at the desired time, and when transmitter power was switched to the high gain antenna, the output was normal and the signal was excellent. The difficulty with the omnidirectional system continued throughout the flight, and as the range increased, some data was lost when that antenna was used in an unfavorable orientation. In post-flight analysis it was found that the power to the omni-antenna dropped at the moment the squibs were fired to release the solar panels. The reason for this is still unknown.

The following functions were successfully performed during the launch phase:

(1) Capsule transmitter locked on and squib firing assembly armed by inertial switches during the boost phase.

(2) Transmitter power increased after separation.

(3) Solar panels extended (accompanied by sharp degradation in low gain antenna output).

(4) Sun acquisition (pitch and yaw stabilization, switch to solar panel power).

(5) Earth acquisition (locks high gain antenna on Earth).

(6) Gamma ray spectrometer turned on (followed by an abnormal increase in temperature of the instrument).

b. Mid-course phase. About 12 hr after injection, during the first Goldstone pass, the mid-course maneuver commands went to the spacecraft. The spacecraft turned through the desired angles in roll and pitch, the mid-course rocket fired at the proper time, and the attitude control system reacquired the Sun and the Earth. However, post-maneuver tracking showed that the desired trajectory had not been achieved. It was soon evident that the commands had been reversed in sign. The sign error was later confirmed as due to a long-standing difference in sign convention between the maneuver code used in the IBM 7090 computer, and the maneuver code in the spacecraft. Preflight tests had failed to reveal the sign reversal because the maneuver digits went through

the entire system correctly; only their meaning was changed in the process.

Because of the initial large trajectory errors, the reversal of the mid-course maneuver had negligible effects on the remainder of the mission. The maneuver changed the flight path in such a way that the lunar intercept would come near the end of the second Goldstone pass, instead of earlier in the pass as had been desired, but the entire lunar fly-by would still be above the Goldstone horizon.

Recovery of spacecraft telemetry during the latter part of the mid-course maneuver pitch turn, the motor firing, and start of Sun reacquisition was seriously hindered because the spacecraft was commanded to an orientation that violated the omni-antenna constraint. This was a calculated risk decided upon during the operation and was complicated by the following factors:

(1) The spacecraft turned in the opposite direction from that predicted.

(2) The transmitted signal from the low gain antenna was abnormally low.

(3) The receiver at the Goldstone Echo Station apparently had a malfunction during this period.

Sufficient telemetry was recovered to indicate that the CC&S successfully commanded the following functions:

(1) Telemetry to mid-course mode.

(2) Start and stop commanded roll turn, switching in mid-course guidance system, extend high gain antenna.

(3) Start and stop commanded pitch turn.

(4) Ignite mid-course motor and shutoff on commanded accelerometer signal (possibly accompanied by a temperature bridge malfunction).

(5) Switch out mid-course guidance system; telemetry to cruise mode, and Sun reacquisition.

(6) Earth reacquisition.

(7) Gamma ray boom extension.

c. Terminal phase. As the spacecraft neared the Moon, the terminal maneuver commands were sent and stored in the CC&S memory. The turn commands were calculated (with sign reversed, to correct for the situation discovered at mid-course) to place the spacecraft in such an orientation that the TV camera would scan across a strip of the Moon during the fly-by.

At 17:21:39 GMT on January 28, the *execute* command was sent from Goldstone. The spacecraft performed its first turn (pitch) properly. An extraneous pitch turn command occurred a few seconds after the first commanded turn ended and continued until the commanded yaw turn ended. The high gain antenna tracked the Earth as the spacecraft continued pitching until the Earth sensor shield blocked off the Earth. When the Earth sensor, mounted along the antenna axis, lost the Earth's light, a roll search was started, and the RF signal from the high gain antenna was lost. During the commanded yaw turn while the spacecraft was still pitching and rolling, the antenna apparently locked on the Moon. The precise spacecraft orientation during and after this period is still being investigated.

The TV camera began sending pictures on schedule, but the video signal was obscured by noise because of the loss of antenna gain. Several real-time commands were sent during the next ½ hr in attempts to improve the signal or reacquire the Earth, without success. The spacecraft then passed below the Goldstone horizon.

The Woomera Station and the South African Station continued to track, and during the next Goldstone pass further commands were sent as an experiment. As the spacecraft, now under gyro control only, drifted away from a Sun-oriented attitude, its performance deteriorated due to temperature changes and low solar-panel output; by January 31, the response to commands was erratic. Shortly thereafter, the attitude control gas ran out and the spacecraft began to tumble. Intermittent signals continued to be received until February 2, when the spacecraft was at a range of more than 500,000 miles.

The CC&S successfully commanded the following functions during the terminal maneuver sequence:

(1) Break solar lock, start vidicon warmup, and start and stop first commanded pitch turn.

(2) Start and stop commanded yaw turn.

(3) Start and stop commanded second pitch turn, telemetry to scientific mode, and start vidicon pulse train.

(4) Uncover vidicon lens, and deploy altimeter. (No verification of its extension was obtained.)

(5) Deploy low gain antenna.

(6) Turn on altimeter, and commutate scientific data.

2. Spacecraft Integration

a. **Ranger III.** During J-FACT testing at AMR, the spacecraft bus L-band receiver was found to have a

threshold of only −90 dbm instead of the normal −138 dbm. Subsequent investigation both at AMR and at Pasadena showed that the bus transmitter was exciting the capsule transmitter and generating spurious frequencies that were loading the receiver such that the AGC would not allow a threshold of less than −90 dbm.

Flight Capsule 10 was tried for compatibility with the spacecraft and (although found to be not as interfering as the transmitter in the electronic mockup) was not considered satisfactory for flight. Flight Capsule 12 was tested and found satisfactory for flight. Subsequent flight experience does not indicate any further capsule–bus RF interference problem. Aeronutronics has been requested to desensitize the capsule transmitter to avoid excitation from the bus transmitter.

No other design discrepancies were noted on *Ranger III* before flight, and the spacecraft was launched during the first window attempt. Flight telemetry records have revealed several design deficiencies which will be corrected on subsequent spacecraft:

(1) During mid-course motor burn, all temperature measurements were upset and read out of band. All came back to normal about 30 min later. This problem was traced to a special high temperature lead used for the 2000°F motor chamber transducer. At high temperature, the insulation material (magnesium oxide) develops a very low leakage resistance, unbalancing both temperature bridges. The lead will be modified for *Ranger* RA-5, but for *Ranger* RA-4 it will have to be disconnected to assure the proper operation of the bridges to obtain other pertinent measurements.

(2) The attitude control nitrogen gas pressure transducer stayed pegged on full pressure longer than necessary. It then reduced about 50%, apparently reading correctly until the gas supply was depleted. Subsequent investigation has shown that a potting material can bubble out during sterilization and that this material can be dragged onto the windings when the transducer is overpressurized. The transducer for *Ranger* RA-4 has been checked for this problem with no inadvertent operation noted. A new type will be introduced on later spacecraft; however, this new type cannot be ready in time for *Ranger* RA-4.

After completion of the terminal maneuver, the spacecraft cruised by the Moon and was continually tracked by all the stations of the DSIF. The capsule transmitter was tracked frequently, with good receiver lock characteristics. At approximately 3 hr after initiation of terminal maneuver, the spacecraft battery depleted since the *Ranger III* and *Ranger* RA-4, -5 design did not allow for reacquisition of the Sun in the event of a lunar flyby. This has since been changed so that the reacquire command from CC&S will be given at 1 hr 40 min after initiation of terminal maneuver on *Ranger* RA-5 and subsequent spacecraft.

b.* Rangers *RA-5 through -9. Some innovations have been introduced into the design of *Rangers* RA-5 through -9 as a result of the experience gained from *Ranger III*. These new designs are not vital to the impacting mission, but do enhance the capability of the spacecraft in some of the possible failure modes.

The antenna-switchover backup command is used in the event that a normal ground-commanded antenna switchover (omnidirectional to high gain) cannot be used. In the original design, this backup command is timed for 2½ hr after initiation of mid-course maneuver. If all command capability was lost, the command to switch antennas would never occur and the spacecraft would remain on omni-antenna, limiting the tracking range. A design change has been initiated, whereby this command has been placed on the launch counter to occur 16 hr and 6 min after launch. This command will be ineffective if an antenna switchover command is given previously from the ground. The TV subsystem engineering telemetry has also been tied to this command.

Beginning with RA-5, some of the launch azimuth–time-of-month combinations can be such that injection occurs as late as 45 min after launch. The present design calls for opening the solar panels at 30 min after launch and activation of the attitude control system 33 min after launch. This could result in the panels being opened before *Agena* separation, or worse, before the end of second burn. As a result, panel opening time has been extended to 48 min after launch and the attitude control system is to be activated at 51 min after launch. This may cause additional battery use until the panels acquire the Sun, but sufficient contingency exists without detrimentally affecting the mission. The spacecraft will be given a maximum time of 30 min to acquire the Sun; *Ranger III* accomplished this in 4 min.

Two types of tests are to be performed on *Rangers* RA-5 through -9 in the space simulator. The first test will be a thermal balance test to verify that proper heat transfer is accomplished to keep the spacecraft at the proper operating temperature. During the test a minimum number of cables will be connected to the spacecraft to keep the shadowing and heat conduction effect to a

minimum. After the thermal balance has been verified, all the direct access connectors will be connected to the spacecraft, and a functional test will be run while the temperature of the spacecraft is maintained at a desired point by controlling the environment.

During the testing, a space flight operation test is to be conducted. The purpose of this test is to check in real time all ground command loops between spacecraft, system test complex, space flight operations, deep space instrumentation facility, and control computing facility.

During the functional test of the spacecraft in the space simulator, tests are to be performed on the attitude control subsystems. These tests will cause the expulsion of gas from the attitude control subsystem. Preliminary calculations indicate that the space simulator will be able to maintain the desired vacuum when gas is expelled from the attitude control subsystem. At the present time, plans are being made to experimentally verify the calculations before the spacecraft is tested.

To ensure that the spacecraft will not be damaged by the GSE, a spacecraft simulator will be used to verify the GSE and cabling before the flight spacecraft is connected at the different complexes, particularly the launch complex. Present plans call for the modification of one of the spacecraft simulators used for *Ranger III* and RA-4.

A standard cable concept was considered for the *Ranger* RA-5 through -9 GSE. Using standard cables would require less time for design and fabrication of the cables required to test each spacecraft. They would also reduce cost, through reuse on other programs. Since many of the cables from previous *Ranger* missions are usable for the RA-5 through -9 series, and the use of standardized cables would require some modification to existing GSE, a standard cable concept was not adapted at this time.

A tape recorder is to be used to record the telemetry modulation signals during system test. If discrepancies are noted during system test, the recording can be analyzed to determine their cause. The tape recorder will be a valuable troubleshooting aid, and will also keep operating time on the spacecraft to a minimum by reducing the number of system tests necessary to isolate a malfunction.

Test philosophy specifies that isolation will be provided in each monitor line from the spacecraft. During testing of RA-4, several instances were noted where the test cabling had an effect on the test results. Procedures are to be developed for testing RA-5 through -9 whereby the effects of the test cabling can be determined early during the test operation, and compensation techniques worked out.

The requirement for one system test complex (STC) to be reserved for use with the *Ranger* proof test model during the launching and flight of RA-4 leaves only one system test complex available for modification to support RA-5 until then. The one STC is to have the capability of testing RA-5 for either the lunar capsule or TV mission.

Equipment layout diagrams have been generated for the areas where a system test complex is to be used. These areas are located in the spacecraft assembly facility, the environmental test facility, and the space simulator at JPL as well as the spacecraft assembly facility at AMR. Attention is given to the equipment layouts to ensure compatibility between the various test positions for signal flow, cable routing and length, accessibility of equipment for troubleshooting, and ease of operation.

A block diagram defining interconnecting cables has been completed. A PERT diagram showing the flow of the system test complex equipment from the start of fabrication to the start of spacecraft testing has been prepared.

B. Space Sciences

1. Ranger III *Vidicon Experiment*

The bypass of the Moon by *Ranger III* in a nonstandard trajectory made it impossible to televise photographs of the lunar surface as planned. However, telemetered vidicon data received from Goldstone and Woomera tracking stations demonstrated that, following the terminal maneuver, the camera shutter and vidicon scan system did operate until contact was lost. The optical telescope imaged some exterior light source on the vidicon photoconductor and the reference crosses on the face plate were definitely recorded by the scan. The intensity of the illumination was too low and the noise background too severe to identify the light source.

Efforts to reduce the noise background and improve the signal by multiple photographic printing of successive images and by computer analysis techniques were successful in increasing the contrast of the reference crosses

on the vidicon face plate, but did not succeed in demonstrating a recognizable lunar image. In fact, due to misalinement of the spacecraft during terminal maneuver, it is not certain that the telescope was pointed at the Moon. Efforts are continuing to identify the exterior light source which illuminated and imaged the vidicon reference crosses.

C. Telecommunications

1. Antenna and RF Components

a. **Ranger III,** ***and RA-4 and -5.*** A change in the retrorocket thermal shield structure from the proposed clamshell arrangement outlined in *SPS 37-12* to a multiple layer aluminized mylar shower curtain type shield, necessitated the taking of a new set of omnidirectional antenna patterns for the *Ranger III* vehicle configuration. The vehicular mockup with thermal shield in place, mounted on the pattern range rotator, is shown in Figure 1.

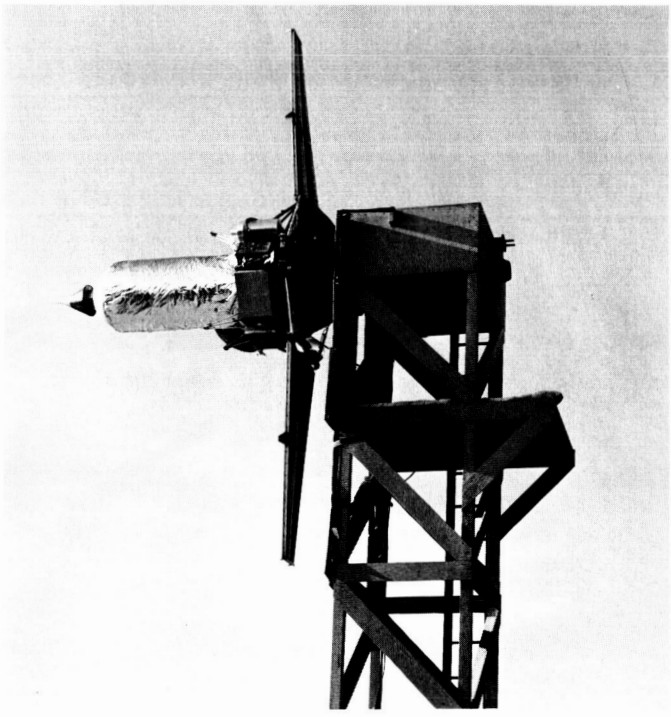

Figure 1. *Ranger III* mockup with shower curtain thermal shield

The omnidirectional antenna radiation patterns were taken, in the manner outlined in *SPS 37-12*. Indications were that omni-antenna performance was not appreciably degraded by the presence of the thermal shield.

b. **Rangers** ***RA-6 through -9.*** Preliminary analysis of the radiation pattern of a *Ranger I*-type omni-antenna mounted on a prototype TV subsystem package, as outlined in *SPS 37-13*, indicated that program requirements for antenna pattern coverage would be met with the antenna mounted in this manner.

Since that time, further information has become available as to the final TV subsystem configuration. At this time, a more detailed measurement of the omni-antenna radiation pattern is being made, in the manner outlined in *SPS 37-13*. The detailed measurements will provide data for communication link analysis for various modes utilizing the omni-antenna.

D. Secondary Power

1. Ranger III Power System

A review of telemetry information received from the *Ranger III* flight indicates that the power system operated normally. The converter and inverter monitors indicated normal operation throughout most of the flight. There were some abnormal indications during mid-course maneuver on the attitude control, data encoder, and scientific monitors. However, further investigation of the analog composite records indicated that the data obtained during this portion of the flight were not reliable and system performance appeared normal.

The preliminary analysis of the *Ranger III* flight has been completed. Portions of the flight were analyzed and Figures 2, 3, and 4 depict the power system performance during the peak power demand periods such as initial Sun acquisition, mid-course and terminal maneuvers. Sufficient data is plotted prior to and after the maneuvers to establish the cruise mode conditions.

a. Initial Sun acquisition. Figure 2 is a plot of the initial Sun acquisition phase of the flight. The system voltage

clearly indicates the Sun acquisition, the system voltage rising from 19 v (launch and backup battery) to 28.2 v (solar panels). A scan of data recorded before and after Sun acquisition resulted in the stabilized conditions indicated in the figure.

After Sun acquisition the power system operates with the solar panels at approximately 30.7 v, and 2.5 amp per panel; the system voltage and current are 28.2 v and 4.1 amp, respectively. The solar panel shunt regulators appear to be in a conducting region and remain so until the mid-course maneuver.

b. Mid-course maneuver. The graph in Figure 3 depicts the performance during mid-course maneuver. The effect of the spacecraft performing the maneuver can be followed until approximately 10:15 GMT on January 27 when the data becomes obscured with noise. At this time the system voltage has dropped from 28 v (solar panels) to approximately 18.6 v. The low system voltage reading accuracy is questionable since the measurement VCO is indicating an extreme (zero v) condition.

Since the reacquisition of the Sun was accomplished without incident, there is no doubt that the spacecraft power system performed properly. The cruise conditions after mid-course maneuver appear to be similar to the cruise conditions prior to mid-course. The system voltage returned to 28.2 v and the system current to approximately 4 amp.

c. Terminal maneuver. The graphs in Figure 3 are plots of the terminal maneuver portion of the flight. The power system can be observed as it transfers from solar panels to battery. The system voltage remains at the level established by the battery (approximately 18.6 v) until the data can no longer be read. The varying load conditions of the spacecraft are reflected in the voltage and current measurements; good correlation during load sharing and eventual battery takeover can be derived from the graphs. Status of the spacecraft power system after the terminal maneuver has not yet been analyzed. An analysis of this portion of the flight along with a more detailed review of the flight will be accomplished.

d. Cruise mode. Typical cruise mode values for the solar panels are given in Table 1.

This data indicates that normal cruise mode power supplied by the solar panels was approximately 140 w. Typical cruise mode booster–regulator input power was 118 w, and power drop across the power switch and logic was expected to be approximately 7 w, for a total load requirement of 125 w. The difference between power supplied (140 w) and power demanded (125 w) was dissipated in the zener regulator diodes. This is the

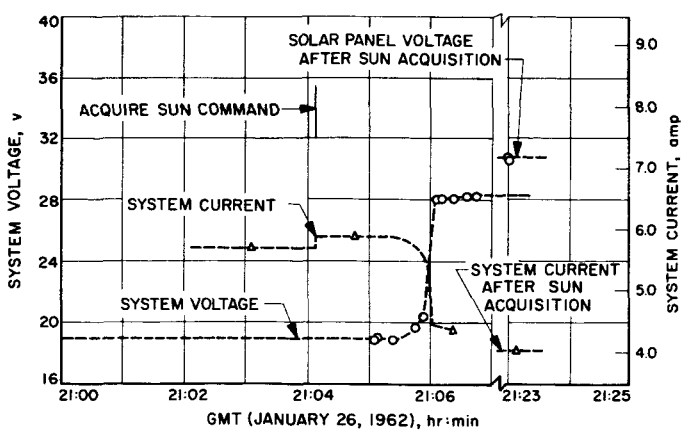

Figure 2. Power system performance during Sun acquisition

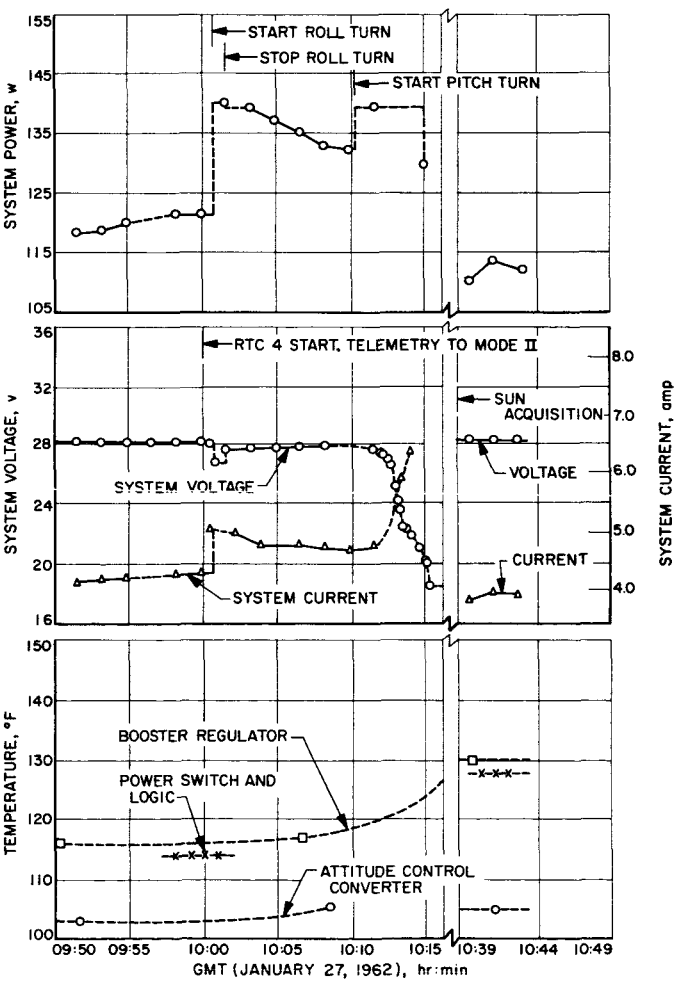

Figure 3. Power system performance during mid-course maneuver

expected value of zener power at the observed panel voltage and temperature.

Performance of the *Ranger III* flight battery appears to have been normal. Due to the sharing of the load with the solar panels, it is not possible to determine the exact capacity drained from the battery. However, it is known that the battery supplied 4.2 amp-hr in the period 5 min before launch to 36 min after launch. The battery again supplied the power during mid-course maneuver for approximately 30 min at a load of 7 amp or 3.5 amp-hr. The battery supplied power a third time from a period just after initiation of the terminal maneuver to its final depletion.

Table 1. Typical cruise mode values

Panel No.	Voltage	Current, amp	Front temperature, °F	Back temperature, °F
9	29.2	2.5	145	120
10	29.4	2.4	140	120

In addition to the verification of system performance, some design data is being derived from the telemetry analysis. Calculations are in progress to determine the expected space spectral correction factor for the solar panels. The nominal value of this factor used in initial solar panel design was 0.85. This indicates that the panel can be expected to be 85% as efficient above the Earth's atmosphere as it is on the Table Mountain testing site. Figure 5 indicates a Table Mountain solar panel current–voltage curve extrapolated up to the observed temperature and expected solar intensity conditions. It can be seen that the cruise mode data points fall on the curve

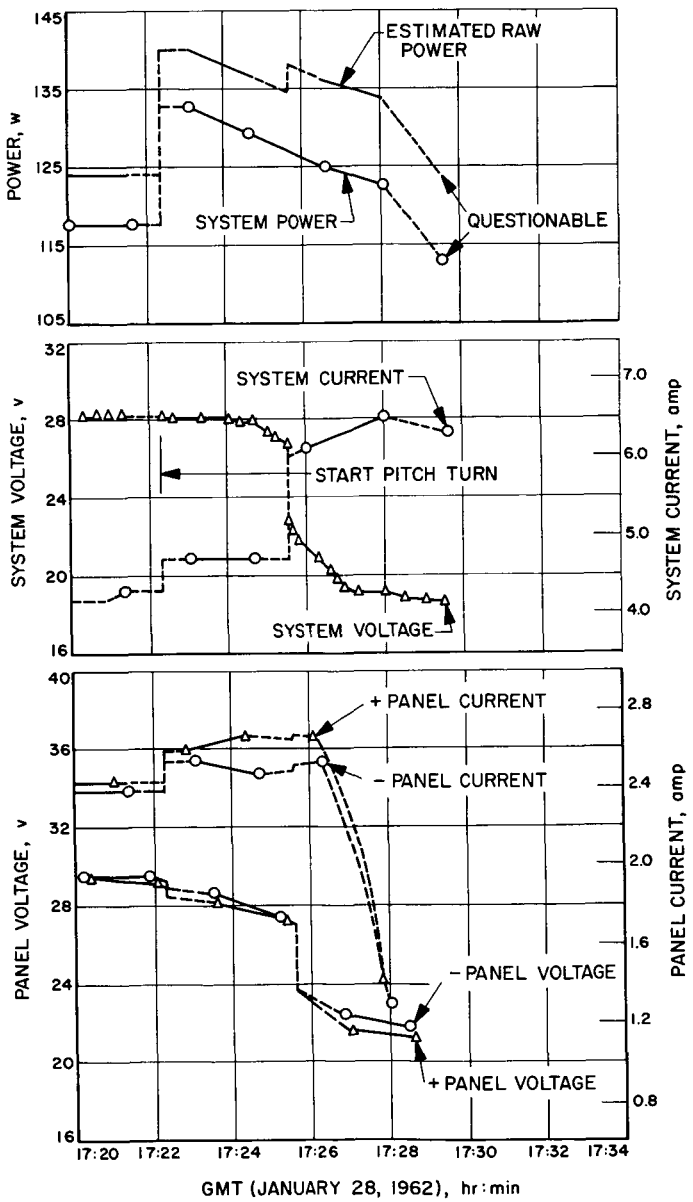

Figure 4. Power system performance during terminal maneuver

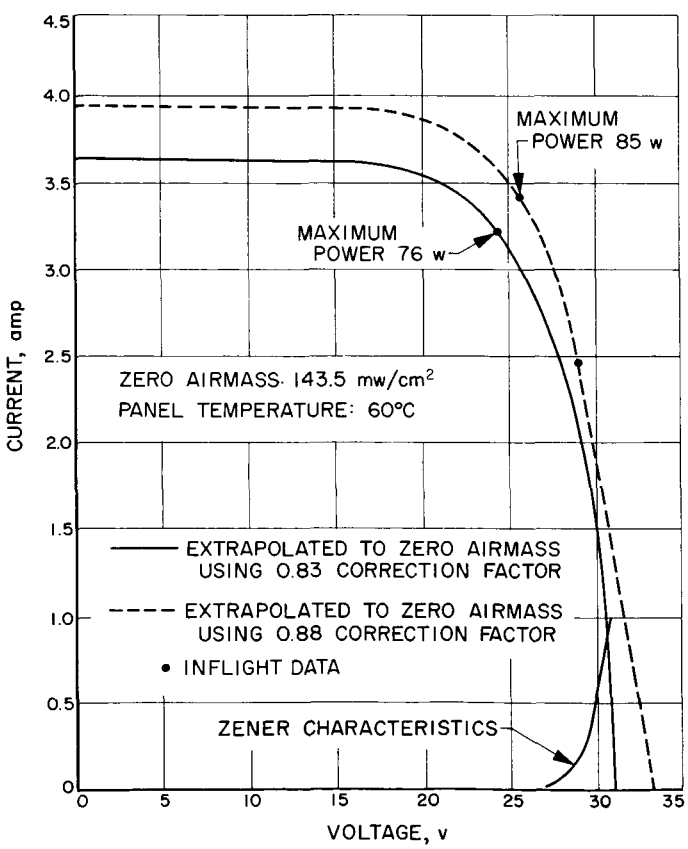

Figure 5. *Ranger* solar panel current–voltage characteristics

drawn with a 0.88 spectral correction factor; however, inaccuracies in the telemetry system, in solar intensity, and in the extrapolation method may account for the observed difference. Additional data reduction is planned before this number is finalized.

Data obtained from the engineering evaluation module containing open circuit voltage and short circuit current measurements of blue cells are being evaluated. Preliminary measurements indicate that a short circuit current extrapolation factor of 0.86 was obtained.

2. Rangers *RA-4 and -5*

Ranger RA-4 has completed systems testing. The flight units and the spares have been defined and prepared for shipment to AMR. No problem areas have been encountered in the RA-4 power system during the spacecraft systems tests. An engineering change order was introduced to increase the telemetry measurement range of power system voltage. This was initiated by the insufficient telemetry data range encountered in the flight performance of *Ranger III*.

a. Solar panels. *Ranger* RA-4 Panels 11 and 12 were shipped to AMR for *Ranger III* spares and RA-4 flight. *Ranger* RA-5 Panel 13 was accepted after rework of partially damaged P-contact connections and cold solder joints. A total of 16 modules were replaced by the vendor. This panel was tested at Table Mountain and had an electrical output of 52.9 w/langley/min at 39°C (minimum acceptable is 50 w/langley/min). Panel 13 has been mounted in its flight frame and is ready for flight acceptance tests.

Panel 14 has been delivered to JPL. Tests run at Table Mountain gave an electrical output of 43.2 w/langley/min at 39°C. The panel was inspected at JPL and was rejected due to damaged P-contacts and cold solder joints. The panel was redelivered and is now being assembled into its flight frame for flight acceptance testing.

b. Battery. The *Ranger III* spacecraft, with an approved deviation, was flown with a flight battery whose potting compound was not conclusively proven to be sporicidal. Tests are presently in progress to obtain evidence on the sporicidal nature of those potting compounds which exhibit proper battery manufacturing characteristics outlined in *SPS 37-12*. Due to the time required for these evaluation tests, it appears that the RA-4 flight battery will also be flown with the same potting compound used in the *Ranger III* flight battery (Shell Chemical Epon 815 with TETA).

E. Supporting Activities

1. Vacuum–Temperature Testing

Several temperature control shrouds used for testing *Ranger* components and assemblies in vacuum chambers have been built. The shrouds are made by soft soldering ½-in. copper tubing to copper sheet metal cylinders which are closed at one end.

The desired shroud temperature is obtained by controlling the flow of liquid or gaseous nitrogen through the copper tubing. A typical use of a temperature control shroud may be seen in Figure 6, which shows a vacuum–temperature test setup for the vidicon telescope used on *Ranger III* and *Ranger* RA-4.

2. Ranger *Environmental Test Program*

During January and February, 153 experimental, type approval, and flight acceptance tests associated with the *Ranger* Program were handled by the JPL environmental test laboratory. This was a decrease in *Ranger* test work compared with the previous period and reflects the completion of much of *Ranger* RA-4 testing.

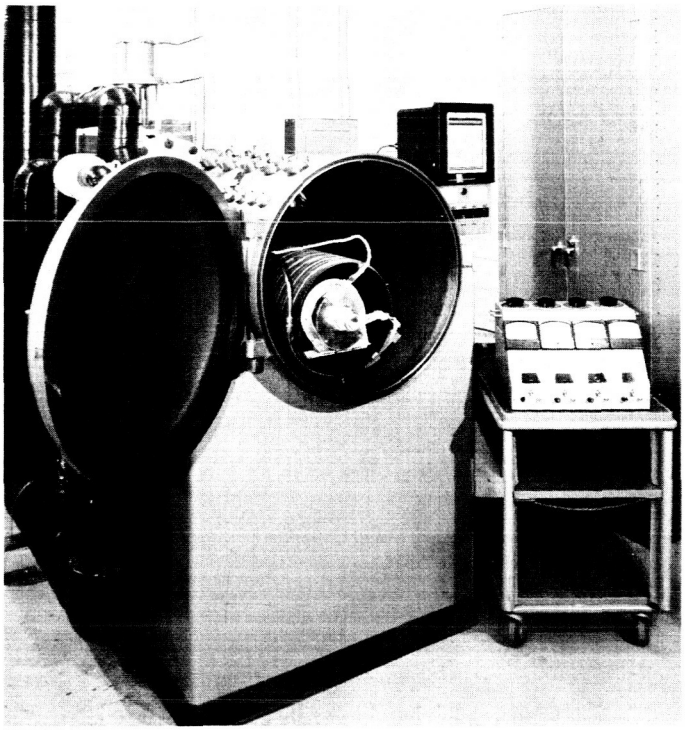

Figure 6. Vacuum–temperature test setup showing temperature control shroud

Page intentionally left blank

PART THREE
PLANETARY–INTERPLANETARY PROGRAM

I. Objectives

The primary long range objective of the NASA Planetary–Interplanetary Program is the development of automatic, unmanned, interplanetary spacecraft technology and the use of this technology in the form of space probes to gather fundamental scientific knowledge concerning the planetary and interplanetary environments, the planets themselves, and solar phenomena, both out of and within the plane of the ecliptic.

The secondary long-range objective of the program is the development of technology and the collection of scientific data which will contribute to the successful manned exploration of the planets and interplanetary space.

The primary objective of the program by 1970 is to have rather completely demonstrated and, to some reasonable extent, exploited (in terms of acquired scientific data) spacecraft capable of (1) being put into orbit around and (2) landing on the surface of Mars and Venus.

A secondary objective during this period will be the initial effort toward extending the above capability toward the planets Mercury and Jupiter and space shots out of the plane of the ecliptic and in toward the Sun. The immediate objective of the program is the initial probing of Mars and Venus.

The Planetary–Interplanetary Program at present consists of three projects: *Mariner* R using the *Atlas–Agena* B vehicle, *Mariner* B using the *Atlas–Centaur* vehicle, and the *Voyager*, using the *Saturn* vehicle. The missions planned for these projects are obviously subject to change because of such influences as new scientific discoveries or unexpected developments in vehicle availabilities.

II. Mariner R Project

The intent of the *Mariner* R project is to perform flyby missions to Venus in 1962. These missions are a replacement for the *Mariner* A project which was cancelled during September 1961 due to unavailability of *Centaur* launch vehicle.

The primary objective of the *Mariner* R project is to develop and launch two spacecraft to the near vicinity of the planet Venus, to receive communications from the spacecraft while in the vicinity of Venus, and to perform a radiometric temperature measurement of the planet. A secondary objective is to make interplanetary field and/or particle measurements on the way to Venus and in the vicinity of Venus.

Two spacecraft, *Mariner* MR-1, *Mariner* MR-2, were assembled and electrical subsystem testing performed during January and February 1962. This phase of the work has progressed on or slightly ahead of schedule even though some subsystems are experiencing delays in delivery of fully flight ready equipment to the spacecraft. Full system tests, space simulator tests, and other environmental tests on fully assembled flight spacecraft are scheduled for March and April.

Coordination meetings at the project level were held with the vehicle system people and the AMR operations people to discuss and review current status of each system, and to bring to light any remaining problem areas.

The Project Development Plan, reviewed and agreed upon by Marshall Space Flight Center and JPL, has been submitted to NASA Headquarters for final approval.

A. Space Sciences

1. Solar Plasma Analyzer

a. Spacecraft integration. Since January 1, 1962, two flight units have been assembled, environmentally tested, and delivered to the spacecraft assembly facility. The units were installed in the appropriate hex box and preliminary data conditioning system (DCS) and GSE interface checks were made. Figure 1 displays the instrumentation in its spacecraft configuration.

The GSE interface checks on the first unit (*Mariner* MR-1) disclosed that the squarewave power on the spacecraft had a faster rise time and higher voltage than the supply used in the laboratory. This manifested itself when the dc voltages generated in the unit were measured. The spacecraft supply was set for 50 v rms while the lab supplies were set to give 50 v peak which is almost, but not quite, the same as 50 v rms for this particular square wave. These larger spacecraft voltages had no effect on the operation of the electrometer (Table 1) but did cause the negative output voltage of the sweep amplifier to be 3 v lower than the positive output. MR-1 was returned to the lab to investigate the difference in

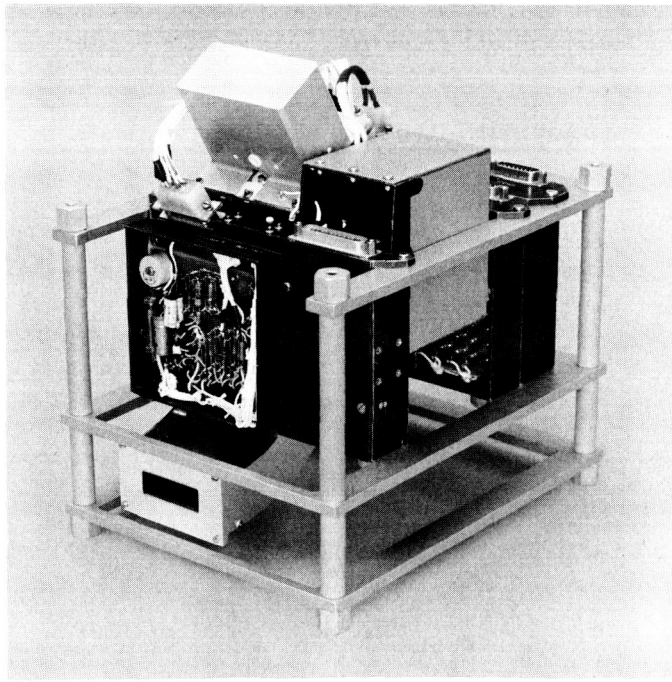

Figure 1. Solar plasma analyzer

Table 1. MR-1 electrometer calibrations

Input current, amp	Bench calibration, v	Spacecraft GSE calibration, v
10^{-6}	3.077	3.072
10^{-7}	3.348	3.349
10^{-8}	3.589	5.584
10^{-9}	3.803	3.805
10^{-10}	4.024	4.020
10^{-11}	4.237	4.230
10^{-12}	4.450	4.4
10^{-13}	4.643	4.730
zero	4.730	—

sweep amplifier output voltages. It was found that the higher voltage and faster rise time of the power supply caused one of the zener diodes used for overload protection in the sweep amplifier output offset supply to fire prematurely due to a poor knee in the zener region. When this diode was replaced, both output voltages were the same. No problems were encountered during the DCS interface checks. The electrometer output readings that were obtained by the DCS compared closely with those obtained in the lab and by the GSE. The interface checks on *Mariner* MR-2 are still in progress at this writing.

b. Circuits. Problems experienced in the electrometer during assembly were:

(1) Quadrature in the carrier signal as evidenced by a large demodulator waveform.

(2) Low gain in the ac amplifier section.

(3) Low frequency ripple on the electrometer output.

Since MR-1 was the first unit built, it constituted an engineering model insofar as component layout and wire routing were concerned. Subsequent rerouting of the critical wires in the electrometer compartment either eliminated the quadrature or brought it well within acceptable limits.

The low gain between the modulator and demodulator was investigated thoroughly, although persistent efforts could not restore the gain to the levels obtained with identical circuits on *Ranger*. Drifts occurring in the dc filter–amplifier appear at the electrometer input reduced by the dc gain, G_1, preceding the filter–amplifier (Fig 2). To preclude input drifts attributable to demodulator and filter–amplifier drifts, a minimum portion of the electrometer loop gain, which may be expressed

$$K_{loop} = G_1 G_2$$

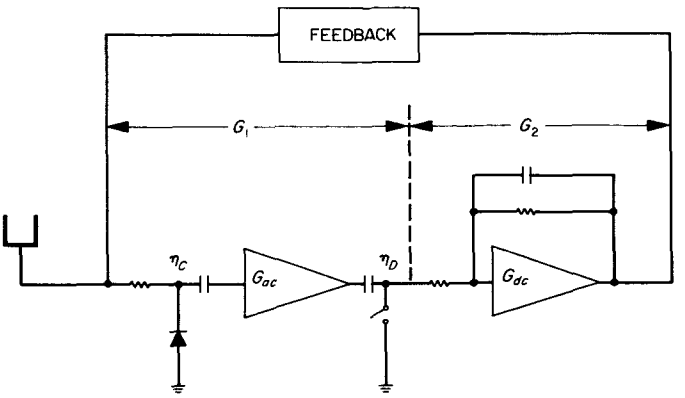

Figure 2. Electrometer amplifier circuit

must be incorporated into the carrier section (G_1). The dc carrier gain may be written

$$G_1 = \eta_C G_{ac} \eta_D$$

where

η_C = modulation conversion efficiency

G_{ac} = ac amplifier gain

η_D = demodulation efficiency

The carrier gain and electrometer loop gain were then measured over the instrument's specified temperature range (Table 2). Since the dc filter–amplifier is highly degenerated and as a result produces a gain, G_2, that is quite stable, any variations in loop gain, therefore, reflect changes in the carrier gain G_1. The test results, as shown in Table 2, reveal an acceptably stable, though somewhat low, loop gain. While working on MR-2, a minor layout change in the carrier amplifier raised the ac amplifier gain to the desired level. This change was subsequently incorporated into all the units with similar increases in ac gain as a result.

The major problem experienced on MR-1 was a low frequency ripple on the electrometer output, the magnitude of which was high enough to give poor output resolution for input currents below 10^{-11} amp. In the worst case, the peak-to-peak magnitude of this signal was large enough to register in any of three adjacent quantization levels of the analog-to-digital converter in the DCS. This ripple was found to be the difference, or

Table 2. MR-1 electrometer gains

Temperature, °C	Loop gain, G_1G_2	Carrier gain, G_1
−10	470	14.0
25	600	17.7
70	605	17.8

beat frequency, produced when the power frequency and the carrier frequency were nearly equal. The 3-db bandwidth of the dc amplifier is 0.5 cps and any beat-frequency signal of a few cps will be amplified and appear at the output. One solution to this problem was to have the carrier frequency lowered so that the difference frequency would be well out of the pass band of the dc amplifier. Since the carrier frequency is fixed for any modulator by its mechanical resonance, the power frequency was varied and it was found that, when the difference between carrier and power frequency was in excess of 30 cps, no beat frequency ripple was observed at the electrometer output. Modulators with mechanical resonant frequencies of 200 cps lower than that of the power frequency will be used to replace those presently on the instruments.

MR-2 also had the problems of quadrature and low ac gain, but the beat frequency ripple did not exist because the carrier frequency was 30 cps lower than the power frequency. Quadrature was eliminated as in MR-1 by the rerouting of wires in the electrometer compartment. The ac gain was raised to the desired level as mentioned before by a layout change in the ac amplifier.

Delivery of flight and spare units to SAF will be completed by the end of March 1962.

2. *Particle Flux Detector*

The ionization chamber, which has already been developed for a radiation monitor (Ref 1, and *SPS 37-2*, p 12), measures the total ionization rate per unit volume of gas produced by radiation able to reach the sensitive part of the instrument. This ionization is proportional to the rate of energy dissipation per unit volume of gas but does not depend upon the flux of ionizing radiation in a unique way. It is, therefore, useful to measure this flux with an instrument so matched to the ionization chamber that the two instruments respond to particles of the same energies.

The simplest device which can measure the required flux is a Geiger–Müller (GM) tube with a wall the same as the ionization chamber's. The GM tube puts out a pulse of charge each time an ionizing particle produces one or more ion pairs within its sensitive volume of gas. The pulse rate is therefore proportional, within limits, to the omnidirectional flux of ionizing particles which traverses the sensitive volume. This flux comprises: primary (natural) particles which penetrate the wall of the counter, penetrating secondary particles produced in the spacecraft and surrounding materials, and secondary particles produced in the wall and filling gas of the counter.

In adapting a GM tube to making an actual measurement, two principal problems must be solved. It is first necessary to connect it to a high voltage supply and to an output amplifier which isolates the tube from all following counting equipment. The amplifier should allow the pulse rate to be linear with particle flux up to as high a rate as possible. The associated circuit as a whole must provide a pulse rate which is as independent of temperature and time as possible. Second, the counting rate of the system must be calculated and measured for all possible types of incident radiation.

a. Instrumentation. A GM tube particle flux detector has been developed for use with the ionization chamber on *Mariner* R. Figure 3 shows the complete package, which contains three GM tubes. The thermal shield has been removed. Tubes I and III are mounted in the two large cylindrical shields, while the smaller shield contains GM Tube II. The package also contains the output amplifiers for the three tubes, a pulse shaper for the ionization chamber, and a power supply which converts spacecraft 2400-cps power to the high and low voltages required by both the ionization chamber and the GM tubes.

The Geiger counter detectors use commercial Geiger counters mounted in specially designed shields and coupled to amplifiers designed at JPL to operate at very high counting rates. Tubes I and III are Radiation Counter Laboratories (RCL) No. 10311 Geiger counters that operate at 750 v, and are glass with 0.030-gm/cm^2 thick walls. The sensitive volume is cylindrical (6.6 cm

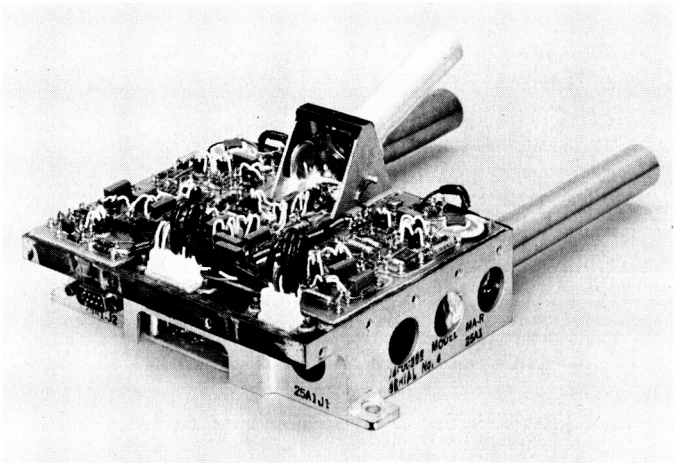

Figure 3. Geiger–Müller-tube particle flux detector

in length and 1.5 cm in diameter) so that the omnidirectional geometric factor is about 8.8 cm². Tube I is shielded by 0.160 gm/cm² of stainless steel to match (together with the glass of the tube) the 0.2 gm/cm² wall of the ion chamber. Tube III is shielded by 0.113 gm/cm² of beryllium so that both it and Tube I detect protons with $E > 10$ Mev as does the ion chamber. The tubes will also detect alphas with $E > 40$ Mev, and electrons with $E > 0.5$ Mev by direct penetration. Electrons will also be detected through the bremstrahlung process with the efficiency depending upon their energy; however, the two tubes will respond differently because of the different atomic number of their shields.

The ratio of the counting rates of Tubes I and III will depend upon the number and energy of electrons present. The ratio of the rate of ionization (measured by the ion chamber) and the counting rate of GM Tube I will be proportional to the average specific ionization of the detected particles.

Tubes I and III will count approximately 15/sec due to galactic cosmic rays. Their maximum apparent rate with the present amplifiers is about 45,000 counts/sec. Due to the finite dead time of the counters, the corresponding true rate is considerably higher.

Tube II is an Anton 213 end window Geiger counter which measures the flux of particles unable to penetrate the other detectors. The window is covered by approximately 1.2 mgm/cm² of mica, and admits electrons with $E > 40$ Kev and protons with $E > 0.5$ Mev. A small shield defines the solid angle through which particles can enter the window. The solid angle has the shape of a cone with an opening angle of 90 deg.

The unidirectional geometric factor for the window is 0.1 cm² sterad. The remainder of the tube is shielded by approximately 0.55 gm/cm² of matter, which permits the passage of electrons with $E > 1$ Mev and protons with $E > 20$ Mev. The tube has an omnidirectional geometric factor of 0.2 cm². Galactic cosmic rays will produce about 0.2 counts/sec in this tube. The maximum apparent counting rate is 20,000 counts/sec, which corresponds to a maximum resolvable rate of about 10^7 true counts/sec. (Tube II in its shield is being supplied to JPL by Dr. J. A. Van Allen of the State University of Iowa, SUI, Physics Department; the tubes are calibrated at Iowa.)

Table 3 summarizes the characteristics of the GM tubes and of the accompanying ion chamber.

Each GM tube is associated with a separate pulse amplifier. The amplifiers contain three stages and are similar in design. The first two stages contain minor loop feedback, while the output stage stability is enhanced by a large ratio of base bias to minimum holding current. Stability and fast time resolution are especially important in the electronics for Tubes I and III, since at high counting rates average deadtimes and charge amplitudes decrease in excess of an order of magnitude.

The first stage of each amplifier consists of a two-transistor charge sensitive preamplifier. The current integration time constant is set to 2.2 μsec for Tubes I and III and 130 nsec for Tube II. The integration capacitor in each case is 10 pf. The preamplifier is long time constant coupled to a one-transistor inverting stage with emitter current feedback. The output stage is a three-transistor, one-shot multivibrator with a complementary output to provide both a low and symmetric drive impedance. The multivibrator has a current sensitivity of 200 μamp; is coupled with a short time constant to the inverting amplifier; and has a minimum output pulse width of 3 μsec.

At counting rates the order of 100 per second the rate remains stable within ±1% at room temperature. The

Table 3. Characteristics of *Mariner* R radiation detectors

Detector	Shielding, gm/cm²	Corresponding energy for penetration, $E >$ Mev	Geometric factors	Dynamic range and counting rates[a]
Integrating ion chamber	0.2 gm/cm² stainless steel	Protons: 10 Electrons: 0.5	1 liter argon at 4 atm, 10^{-10} coulombs per count	10^{-3} to 10^3 per sec, 300 to 3×10^7 ion pairs per cm²-sec-atm-of-air
GM Tube I (RCL 10311)	0.030 glass plus 0.160 stainless steel	Protons: 10 Electrons: 0.5	8.8 cm², omnidirectional	15 to 45,000 per sec
GM Tube II (Anton 213)	0.0012 mica window	Protons: 0.5 Electrons: 0.040	0.1 cm² sterad, unidirectional	0.1 to 30,000 per sec
	0.55 stainless steel and magnesium	Protons: 20 Electrons: 1	0.2 cm², omnidirectional	
GM Tube III (RCL 10311)	0.030 glass plus 0.113 beryllium	Protons: 10 Electrons: 0.5	8.8 cm², omnidirectional	15 to 45,000 per sec

[a] Minimum rates are those to be expected from galactic cosmic rays, detectors can count slower by a factor 10^{-2}, and maximum rates are determined by the instrument responses.

tubes and amplifiers will be more sensitive to temperature at higher counting rates. However, at a nominal rate of 12,000 per second the rate does not vary more than ±8% over the temperature range −30 to +75°C.

b. Location on spacecraft. The detectors respond to particles moving in all directions. Therefore, to minimize the number of secondaries from the spacecraft which can be detected, the particle flux package must be placed as far as possible from the main mass of the spacecraft. It is also necessary to place the ionization chamber close to the particle flux detectors in order that both shall see the same flux of radiation. The window of GM Tube II must be shielded from the Sun.

c. Calibration. The effective volumes of Tubes I and III are measured by JPL using a collimated beam of beta rays and by calipering the bare tubes. Their efficiency for detecting penetrating charged particles will be measured with a coincidence technique using sea level cosmic rays as the source of radiation. The response to gamma rays is measured using radioisotopes, while the effect of the shields upon protons and heavier particles can be calculated using range-energy tables.

The response to electron bremstrahlung must be measured using electrons incident upon shields having the same atomic number as the tube shields. This calibration will be accomplished at SUI over the range 0 to 140 Kev electron energy. In order to extend this measurement to higher energy, it is planned to place GM tubes having both beryllium and stainless steel shields in the beam from an electron accelerator capable of producing energies from 0.150 to 1 or 2 Mev.

The relationship between apparent counting rate and true counting rate (i.e., that which would be observed by a GM counter with zero dead time) must be measured with tubes and amplifiers connected in the final flight configuration using a source of very high radiation flux. Each unit must be calibrated individually. This is being accomplished at SUI by using an X-ray machine which has been previously calibrated with a Victoreen R meter. Tube II and the ion chamber are being calibrated at the same time.

d. Future work. It is anticipated that a similar set of detectors will be used with the ionization chamber as a monitor of radiation on future spacecraft. In some cases the Anton 213 tube may not be carried. The coincidence rate between the RCL 10311 tubes will be measured as well as individual counting rates to provide better discrimination between electrons and heavier particles.

3. Scientific Instruments GSE

a. General description. The scientific instruments ground support equipment (GSE) consists of five consoles. A Flexowriter is used in conjunction with these consoles for data readout (Fig 4).Three of these consoles are for testing the following scientific instruments: magnetometer, ion chamber, particle flux, cosmic dust, solar plasma, radiometer, and IR radiometer. The remaining two consoles and the Flexowriter are used for testing the data conditioning system (DCS). The Flexowriter produces a permanent copy of the scientific information which can then be manually reduced. In addition, a punch data tape is produced for reduction by the JPL computer.

One of the scientific instruments, the radiometer, requires an electro-optical alinement which is accomplished by means of a special test bench.

The GSE uses a patchboard arrangement for connecting the various voltmeters, printers, and signals to the scientific flight instruments. A separate board is used for testing each individual scientific instrument and for testing all the instruments simultaneously during a systems test.

b. Stimulus and response.

Magnetometer. The magnetometer panel is used for adjusting the bias coils for the three axes of the flight instrument to null out all external magnetic disturbances. Once a quiescent state is established, a calibrated bias signal is injected into a specific axis and the value of the analog output for this particular coil is observed on a meter. This calibration input represents a change of the magnetic field that would normally take place during the

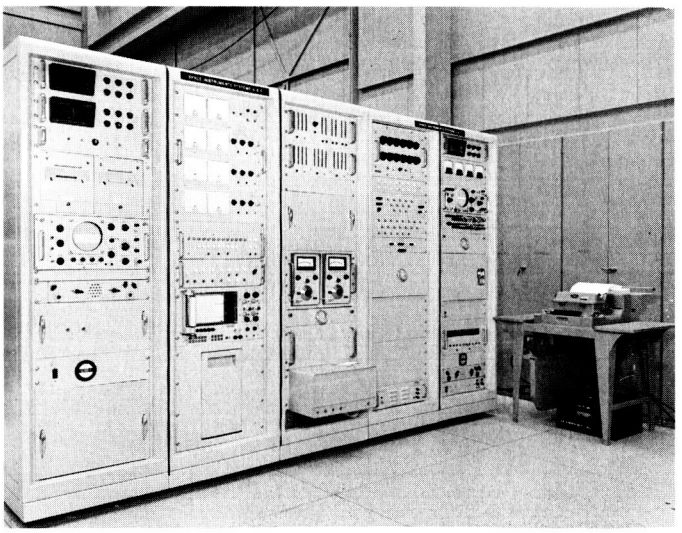

Figure 4. Scientific instruments GSE

flight. There are two calibration inputs for each axis. One input is to test the magnetometer's low scale while the second input is used for switching the mode and testing the magnetometer's high scale operation.

Ion chamber and particle flux detector. The ion chamber and particle flux devices are stimulated by a radioactive Cesium 137 source placed in the vicinity of the spacecraft. The pulse rates from these instruments, one from the ion chamber and one from each of the three tubes of the particle flux detector, are displayed on counters in the GSE system and read out automatically once per minute. The readout and the time of readout are registered on a printer.

Cosmic dust. A signal from the GSE, representing a micrometeorite impact, is sent to the cosmic dust detector and triggers the binary stages in this instrument. The condition of these binary stages can be observed by indicators on the GSE and also by digital voltmeters (DVM) which read the analog output of each binary stage. The DVM signal can be manually printed out at any time.

Solar plasma detectors. GSE indicators are used to display the high voltage sweep position. By knowing the sweep position, the voltage on the analyzer plates can be compared with previous calibrations. This voltage is always measured with an electrometer because of the loading problem.

A current injection device has been mounted on the science case to inject eight current levels into the sensor of the solar plasma unit. These levels, ranging from 10^{-6} to 10^{-13} amp, represent plasma levels which the instrument is expected to encounter in flight.

Radiometer. A Sanborn recording instrument is used to observe the two analog outputs of the radiometer instrument. These outputs represent the temperature of the planet in the microwave region and are used to verify whether the planet has an atmosphere. The recording periodically shows the application of a calibrate command from the flight DCS system.

During the alinement of the radiometer by the radiometer test bench, the Sanborn recorder is used to measure the variation of the radiometer output as a function of antenna distance from the optical axis between test bench and radiometer. The signal should always decrease when the radiometer is moved from this axis.

Infrared radiometer. A change of temperature at the two infrared radiometer sensors produces a change of the analog output of the instrument. This analog output is normally displayed on the scientific instrument GSE DVM and can be manually printed out at any time. To date, although both dry ice and liquid nitrogen have been considered as temperature inputs to the sensors, no decision has been made as to the exact mechanization of this test.

c. Integration. The design of the GSE system for *Mariner* R and the manner in which the GSE system was integrated has been based on most of the experience gained on *Rangers I* and *II* for similar instruments. The ion chamber and particle flux readout equipment has been directly obtained from the *Ranger I* and *II* GSE. Although there was a plasma current injection device used on *Rangers I* and *II*, the one designed for *Mariner* R has been greatly improved with respect to ruggedness and compactness. Special attention has been given to noncontamination of components used in this current injection device. There has also been very close coordination between the DCS and science GSE which has produced a compatible system for analyzing the scientific instrument flight operation.

In an attempt to eliminate as many problems as possible prior to delivery to the spacecraft assembly facility, all of the scientific instruments were scheduled for precheckout with the GSE in the labs. Unfortunately, only about 50% of the flight instruments were available for these tests. Problems were discovered with the instruments that were tested and these problems were eliminated prior to the GSE delivery to the systems area.

d. Subsystem testing. For the first time, an isolation box was used as part of the ground checkout system. This isolation box is located at the spacecraft and contains line amplifiers for driving signals over the long cables between the GSE and the spacecraft instruments. By doing this, the integrity of the signals has been maintained. Isolation amplifiers are also used to decouple some of the GSE and flight instrument signals.

The GSE has been designed to produce all of the power and signals normally supplied by other subsystems. This has allowed complete testing of each instrument of the scientific subsystem without involving any other portion of the spacecraft. During the scientific subsystem test, very little noise was observed in the scientific system. However, when spacecraft power is used in place of GSE power, the noise increases considerably. This noise has detrimentally affected the operation of the solar plasma instrument.

It was at first thought that the magnetometer would be unstable in its low scale, 0 to 60 γ. However, this has not been the case. The instrument can be easily tested in this low scale with stable results.

Aside from the testing described under *b. Stimulus and Response*, the various signals can be observed on an oscilloscope or DVM. They can then be automatically or manually read out onto a printer. The patchboard system has made this flexibility possible.

e. Data analysis. The scientific system has been mechanized through the DCS system so that a Flexowriter prints out a permanent record of the data from all of the science flight instruments. This information can be sampled and manually reduced during both the subsystem and systems test. In addition to the manual reduction of this information, the Flexowriter produces a punch tape which is supplied to a teletype reader and sent to the central computer facilities. Teletype readers are located for this purpose at the spacecraft assembly facility, the space simulator, the environmental test lab, and AMR.

f. Calibration. The current injection device used in conjunction with the solar plasma experiment has been calibrated in the lab prior to delivery to SAF. This unit has maintained its calibration exceedingly well during all subsystem tests and appears to be suitable for calibrating the solar plasma instrument on the spacecraft.

The radiometer test bench has been designed to aline, both optically and electrically, the axis of the radiometer antennas (Fig 5). This alinement has been attempted and the 13.5-mm radiometer antenna has been successfully calibrated. A problem presently exists due to leakage of the 19-mm klystron. Excessive radiation of the klystron has prevented any calibration of the 19-mm antenna. This radiometer test bench has been designed so that the radiometer may be calibrated on the spacecraft. These calibrations will be conducted during the JPL subsystem tests, just prior to the shipment of the spacecraft to AMR and just prior to the final AMR systems test.

g. Maintenance. One major problem appears to be the operation of the GSE DVM units. Several of these instruments have had to be replaced. The problem is presently under investigation. All GSE spares are in the process of being assembled for delivery to the spacecraft system. In most cases, the spares are not complete items but replacements for plug-in assemblies which are used throughout the GSE system.

h. Documentation. A complete file of all flight instrument and GSE drawings is being assembled. The file will be maintained to effect the repair of any portion of the science area. Log books are also available and contain a history of all tests and modifications to both flight instruments and GSE systems. A technical report is being prepared describing all the scientific instruments, the ground support equipment, subsystem and system testing of the scientific effort. Further documentation in the form of a motion picture of the scientific operation is also being prepared.

i. Analysis of GSE and subsystem tests. The patchboard system for setting up the various tests provides extreme flexibility and saves considerable time. All investigations seem to indicate that there is no interaction between the different scientific instruments or between the scientific instruments and other subsystems. The one exception to this is the effect of spacecraft power on the solar plasma experiment. Isolation amplifiers and line drivers have proven to be mandatory for the testing of the science flight instruments with the GSE. All procedures have been written and the computer facilities have been given information on the reduction of the scientific data.

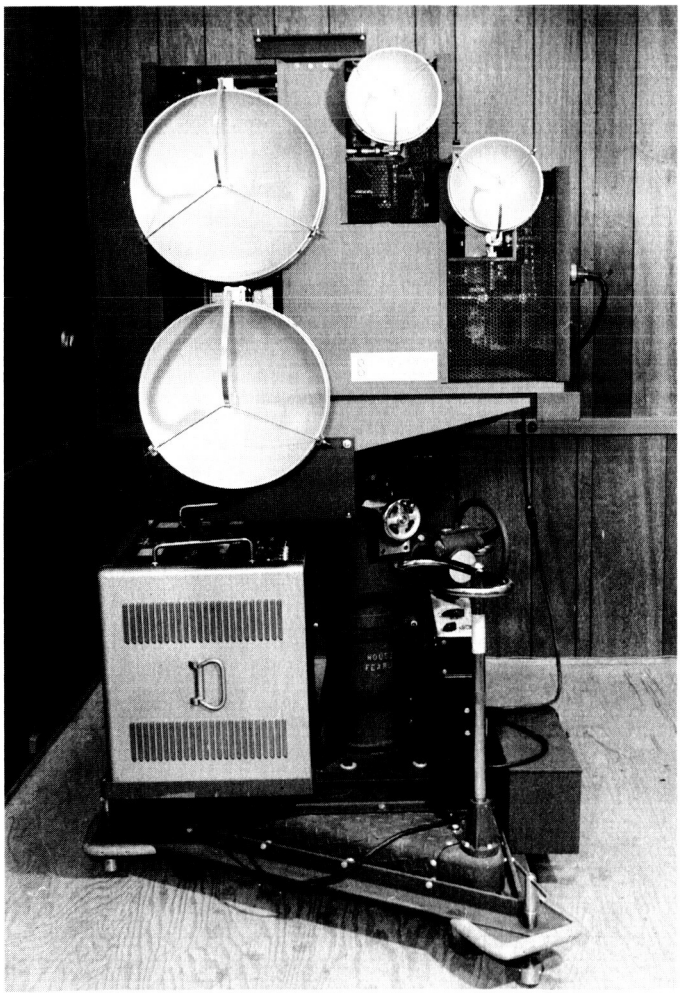

Figure 5. Radiometer test bench

B. Telecommunications

1. RF Couplers

The basic differences between the *Mariner* R and the *Ranger I* and *II* spacecraft *Agena* B RF coupler interfaces are:

(1) The *Mariner* R high gain antenna is circularly polarized instead of linear.

(2) The *Mariner* R uses separate command antennas mounted on one of the solar panels instead of diplexing both 890 and 960 mc through the omni-antenna as in *Rangers I* and *II*.

It was found during a recent RF coupler test that these differences necessitated two essential, yet minor, changes to the *Agena* coupler system.

Due to the fact that the *Mariner* R high gain antenna feed is a turnstile, its four elements are oriented at 45 deg on either side of the dipole feed location on the *Ranger* RA-5 high gain antenna. Thus, the *Agena–Ranger* coupler probe, which was lined up with the dipole elements, is at 45 deg to the *Mariner* R high gain antenna feed elements. In this location the probe is in a highly unstable and rapidly changing part of the field. The coupling loss in this position was 17 db. By moving the probe from its *Ranger I* to RA-5 position in the center of the screen in the *Agena* forward equipment rack antenna well to the corner of the well (Fig 6), the probe can be brought parallel to one pair of turnstile elements and the coupling performance improved.

This change was requested of Lockheed and during RF coupler tests conducted at JPL, January 1962, a prototype model of this probe was installed in the *Agena* forward equipment rack and measured in this new location. (The test setup is shown in Figures 7 and 8.) The coupling loss from the output of the communications pan, Point D, through two flight type coax cables, the type approval model of the rotary joint, the high gain antenna, and to the output of the coupling probe (Point E), was 6.6 $\pm$0.5 db. This loss figure is satisfactory.

During the tests of the *Agena* shroud coupler, it became apparent that the absorber material, which comprises the lower half of the coupler cover, has a critical effect on the coupling between the command antennas and the coupler. The coupling loss varied between 25 and 40 db depending on the position of the absorber panels. As a solution to this problem, the lower 3 in. of the absorber were trimmed off. Under these conditions the command antenna–coupler loss (Fig 2, Point C to Point A), became quite stable and the omni-antenna–coupler loss increased only a fraction of a db.

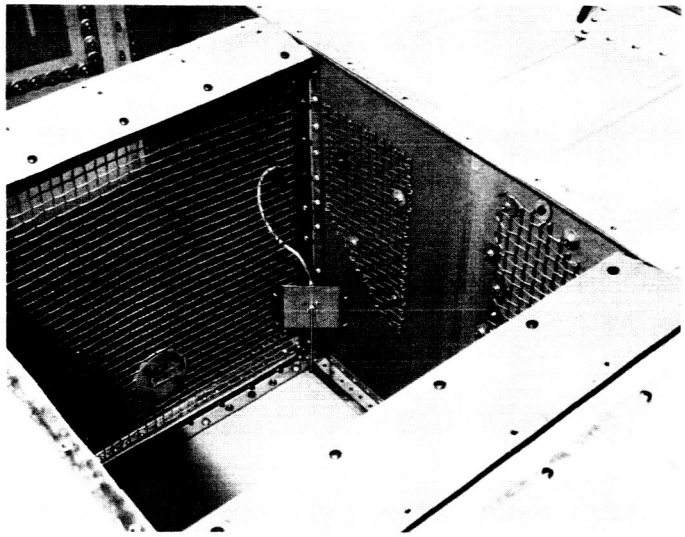

Figure 6. High gain antenna coupler probe

Table 4 summarizes the results obtained with the modified shroud coupler. The omni-antenna-to-coupler spacing was varied in three steps in order to improve the data points taken, and in order to simulate the differential shroud–spacecraft growth during the launch phase due to aerodynamic heating. The 0.86-in. spacing was the maximum available extension of the coupler.

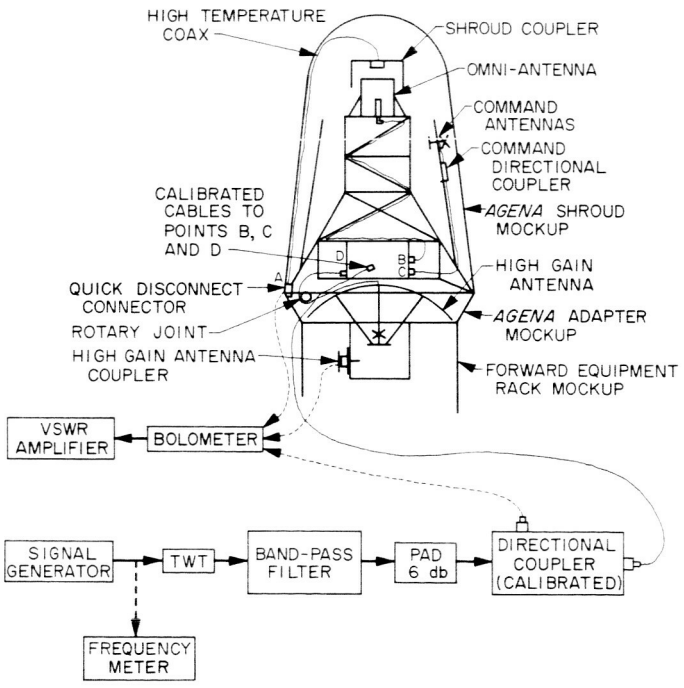

Figure 7. *Mariner* R RF coupler test setup details

Table 4. Results obtained with modified shroud coupler

Omni-antenna–shroud-coupler spacing, in.	Loss, db	
	Omni-antenna B to A	Command C to A
0.40	9.0	27.5
0.50	9.5	27.6
0.86	10.7	27.8

See Figure 6.

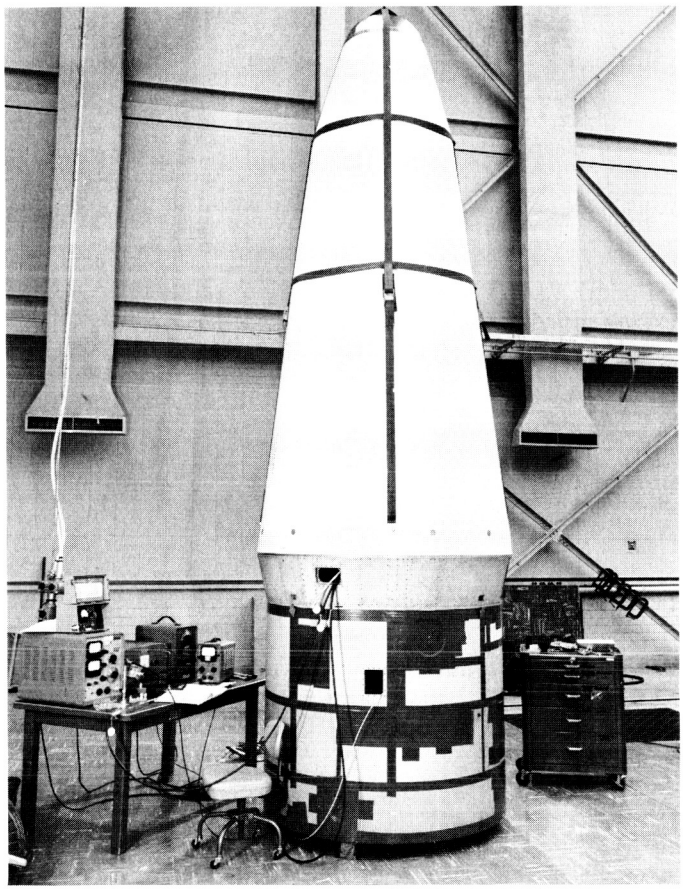

Figure 8. *Mariner* R RF coupler test setup

C. Secondary Power

1. Power System Analysis

The power system analysis is designed to be a general purpose tool for simulating power system component operation and interaction. Although the analysis was built around the *Mariner* R spacecraft, a sufficient number of the system parameters may be varied so that the simulation would represent any of the family of solar-cell-powered spacecraft. With minor modifications, any power source (such as fuel cells or thermionic diodes) could be put in place of the solar cells.

The method of analysis utilizes the IBM 1620 digital computer as well as an analog computer. The digital computer simulation yields power profile totals, discrete dissipation figures, and battery and solar panel sizing information. The analog simulation is used to determine battery charger characteristics and the effect of time-varying parameters. By freezing time in the analog simulation, cross plots of parameter interaction may be obtained. The basic units of the simulation are watts, hours, and volts.

a. Functional description of power system. In the design of a power system, the user's needs are the initial input. The sizing of the energy storage and converting devices are predicated on the peak power demands. Each type of power need is presented in a power profile, which represents the power level as a function of flight time. All of the individual power needs are supplied as either 400 cps, three-phase or single-phase sine wave, 2400-cps square wave or battery direct current. The 2400- and 400-cps inverter–amplifiers are fed at a constant voltage from a boost–regulator whose power input is the solar panels. The efficiency of the inverter–amplifiers is a function of their output power. The efficiency of the booster–regulator is a function of both its input voltage and its output power. Because the voltage of the solar panels varies widely with the distance from the Sun, the booster–regulator must be designed to regulate over a large range of input voltages, resulting in a loss in efficiency.

There are times when the spacecraft is not Sun-oriented, necessitating an alternative energy source. In the *Mariner* R spacecraft, this energy is provided by a battery. The battery is connected so that it may be used in parallel with the solar panels. This mode of operation is called load sharing. Momentary peak loads cause the panels to current saturate, and the battery can supply the difference, allowing an optimization in panel sizing. The power system is represented in Figure 9.

b. Component description.

Solar panels. The solar panels are composite groups of photo-voltaic cells wired in series and parallel to provide

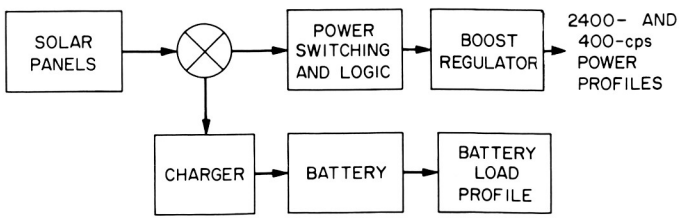

Figure 9. Power system

the required current and voltage properties. The regulation characteristic of the solar panel is nonlinear and double-valued in power output. For a given power demand below the peak power point, there are two panel output voltages which may occur. The important difference between these two points is that the slope of the characteristics has opposite signs. Figure 10 is a plot of a typical panel characteristic in the power-voltage plane. It may be seen that the region to the right of the peak power point always exhibits a negative slope and to the left, always positive.

For a given power demand P_1, there are two possible operating voltages E_1 and E_2. If the load were passive, either of these operating points would be permissible. The characteristic of the booster–regulator load is not passive, however, and causes an interesting phenomenon which is discussed in a following section.

Power switching and logic. Figure 11 is a functional diagram of the power switching and logic.

When the current drain on the panels causes the voltage to drop to the no-load battery terminal voltage, the diode in the battery circuit is unblocked, and the balance of current demand is supplied by the battery. This is the load sharing mode of operation. The solar panel voltage is held at the battery terminal voltage until current is no longer drawn from the battery, whereupon the panels rise to the voltage dictated by the power demand.

Booster–regulator. The booster–regulator is a device which accepts input power at varying current and voltage

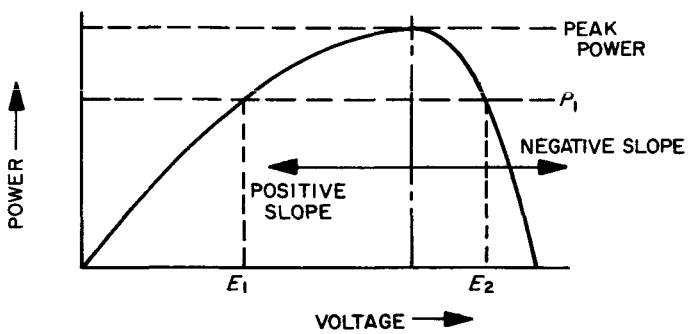

Figure 10. Source regulation characteristic

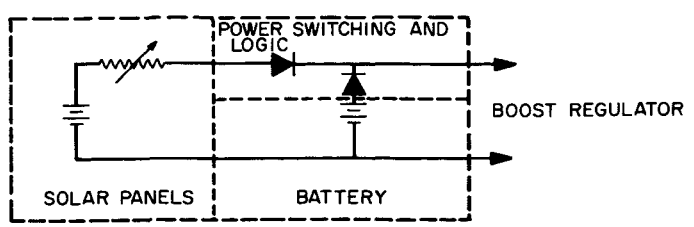

Figure 11. Power switching and logic

values and converts it to output power at a fixed voltage level. An increase in load at a fixed voltage requires an increase in output current. The characteristics of the regulator are such that, to supply the demand, the regulator requires more input current, and consequently an increase in input power. If the system is to be stable, the source must deliver an increase in power to the input of the regulator when more current is required.

The region of the power–voltage characteristic for the source that allows stable booster–regulator operation is defined in the following:

Stated mathematically, the requirement for stability is

$$\frac{dP}{dI} \geqq 0$$

where P = power delivered by the source, and I = the current from the source.

The solar panel characteristic is plotted in the power–voltage plane, and therefore an equivalent expression for dP/dE is required.

By the definition of power,

$$P = E_S I$$

where E_S = the source voltage, thus

$$\frac{dP}{dI} = E_S + I\frac{dE_S}{dI}$$

Then, for stability it is required that

$$E_S + I\frac{dE_S}{dI} \geqq 0$$

Therefore,

$$\frac{dE_S}{dI} \geqq -\frac{E_S}{I}$$

inverting

$$\frac{dI}{dE} \leqq -\frac{I}{E_S}$$

where E_S and I are always positive, also

$$\frac{dP}{dE_S} = \left(\frac{dP}{dI}\right)\left(\frac{dI}{dE_S}\right)$$

The product of the derivatives is always negative because, for stability, $dP/dI \geqq 0$ and $dI/dE_S \leqq$ a negative constant. Therefore,

$$\frac{dP}{dE_S} \leqq 0$$

Hence, for booster–regulator stability, the source power–voltage curve must have a negative slope. This criterion is satisfied by the region in Figure 10 to the right of the peak power point. This holds for any source.

If there were some load on the panels in parallel with the booster–regulator which changes the solar panel characteristic, the booster–regulator stability region would change:

(1) *Solar Panel Characteristic Combined with a Charger Load*

First it is assumed that the charger load is a linear function of the source voltage above the battery voltage, E_b.

$$P_{ci} = K_c (E_S - E_b)$$

where P_{ci} is charger power input and K_c is a constant. Then, use is made of the fact that the total power out of the solar panels in the same as the booster–regulator load and the charger load.

$$P'_S (E_S) = P_{ci} (E_S) + P_E (E_S)$$

where P'_S = panel output power and P_E = booster–regulator input power.

P'_S is a function of E_S as given by a plot of the solar panel characteristic as shown in Figure 10.

P_E may be solved as a function of E_S by:

$$P_E (E_S) = P'_S (E_S) - P_{ci} (E_S)$$

Because of the form of $P'_S (E_S)$, it is easier to obtain a graphical solution of the equation (Fig 12).

The stability of the power system is determined by the slope of the combined source characteristic $P_E (E_S)$. Any load taken directly from the panels will yield an altered characteristic at the input of the booster–regulator which will change the stability region. Hence, for stability of the booster–regulator, the condition is now

$$\frac{dP_E}{dE_S} \leqq 0$$

The area to the right of the stability boundary line in Figure 10 is the stable portion of the operating characteristic. The effect of the charger load P_{ci} is to move the peak of the P_E curve to the left of the peak of the P'_S curve, and thus the system is stable to a lower voltage. This new stability boundary is determined by the characteristics of the parallel load placed on the solar panel.

In order to be unconditionally stable down to the battery voltage, it is necessary that

$$\frac{dP_E (E_b)}{dE} \leqq 0$$

Substituting $P'_S (E_b) - P_{ci} (E_b)$ for $P_E (E_b)$ and rearranging terms

$$\frac{dP'_S}{dE} (E_b) \leqq \frac{dP_{ci} (E_b)}{dE}$$

This is equivalent to saying that the slope of the charger power-voltage curve must be greater than or equal to the slope of the solar panel characteristic at the battery voltage for unconditional stability.

(2) *Solar Panel Characteristic Combined with Zener Load*

The load of a zener diode is essentially similar to a charger which picks up load at an extremely high rate above the zener voltage E_z (Fig 13). The solar panel characteristic may be altered considerably by the addition of this type of load.

A near optimum power source combination would have the zener voltage, battery voltage, and maximum power voltage occur as closely as possible. A typical graph of an optimal system is shown in Figure 14. This system exhibits the desirable characteristic of a comparatively small output voltage range which makes it possible to design a more efficient voltage regulator. The battery voltage should be placed enough below the zener voltage

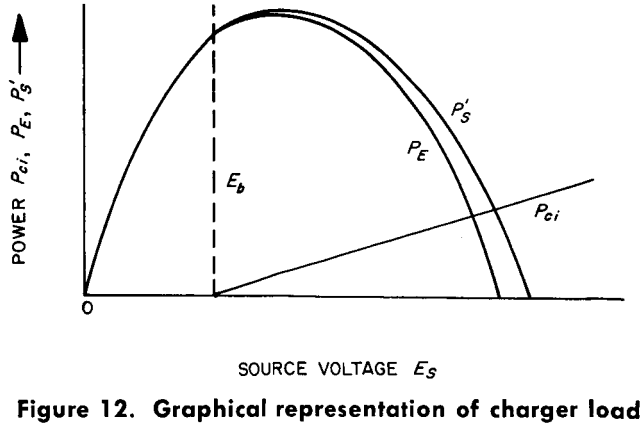

Figure 12. Graphical representation of charger load

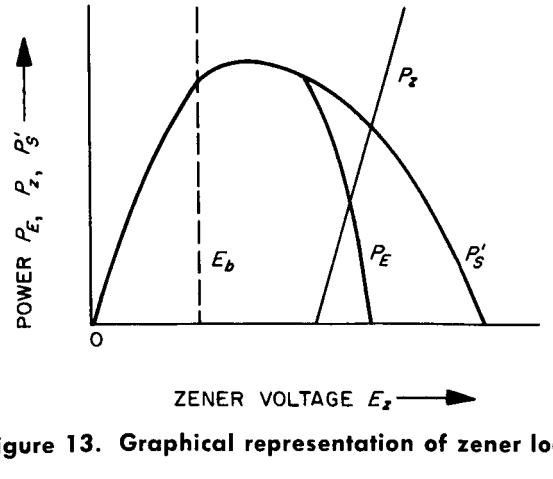

Figure 13. Graphical representation of zener load

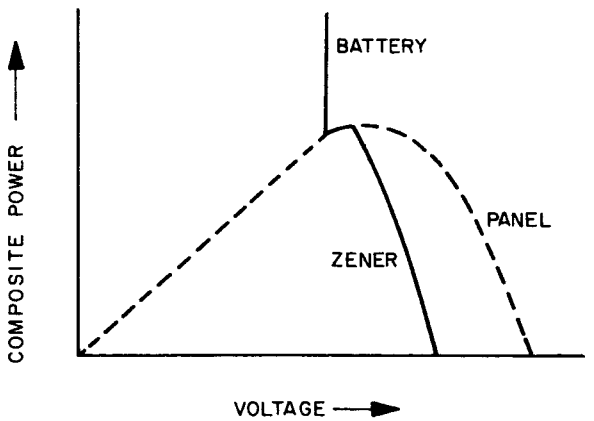

Figure 14. Compensated panel characteristic

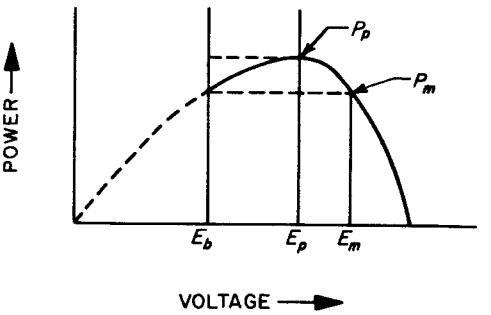

Figure 15. *Mariner* R power characteristic

to permit charging. The system exhibits virtually no regions of instability and is currently receiving further study.

An interesting phenomenon occurs in the *Mariner* R power system because of the values chosen for the battery voltage and the peak power point. Referring to the previous discussion on the power switching and logic, it was seen that the panel voltage was supported by the battery when in load sharing. Postulating that the battery has no internal resistance, the regulation characteristic on the power-voltage plane would be a vertical line at the battery voltage. The intersection of the panel characteristic and the battery characteristic defines the amount of power available from the panels at the battery voltage. Figure 15 shows the approximate *Mariner* R relationship.

As the power demand increases over that available from the solar panels, the voltage jumps down from E_p to E_b. The power level remains essentially constant (except for variations in the booster–regulator efficiency). The power must now drop to P_m before the battery is cut off. At this point, the voltage jumps from E_b to E_m. The power drawn from the panels remains constant, but as the voltage rises, the current drops.

c. Simulation results. In addition to the effects discussed in the previous paragraphs, information as to the sizing of the battery and solar panels was obtained. In all cases, the *Mariner* R power system is adequately sized to handle the anticipated power demand.

2. Flight Equipment

The *Mariner* R power system less solar panels is presently installed in the spacecraft which is being subjected to system tests at the spacecraft assembly facility.

a. Electrical conversion. Four complete flight sets of electrical conversion equipment have been received. These units have been subjected to complete functional and flight acceptance testing prior to delivery. One of these sets has nearly completed the type approval testing at the Laboratory. The other three sets have been delivered to the spacecraft assembly facility for *Mariner* MR-1 and -2 spacecraft and one spare. A fifth set of flight equipment is presently undergoing flight acceptance testing and will be delivered to the SAF as a second spare unit.

System, flight acceptance, and type approval testing have presented some problems requiring rework or modification of flight hardware. During flight acceptance testing of the first four sets of equipment, two failures occurred. A 2N1015C transistor in the oscillator circuit of the booster–regulator shorted. The unit showed no excessive heat indication and no abnormal electrical characteristics prior to failure. This failure was not attributed to design problems because the component was operated well within its electrical characteristics. The transistor has been turned over to the component parts group for investigation.

The second failure occurred in a three-phase, 400-cps power amplifier. During vibration, a relay (which switches in a capacitor for power factor correction when the unit operates as a single phase supply), developed shorted contacts. The relay was removed and sent to the laboratory for investigation. Upon examination the relay showed that some arcing had occurred between contacts. The relay is being turned over to the manufacturer for further investigation. An apparent recurrence of this failure was observed on a different set of equipment on the MR-1 spacecraft. Again arcing of the relay contacts was observed. This problem is under active study and a design change will be made.

A third problem involved damaged insulators around the guide leads of the 2N1015C power transistor in the three-phase, 400-cycle supply. This created a collector-to-

chassis short. This problem appeared during the 12-day high temperature high vacuum portion of the type approval (TA) test. It is being corrected by bending the transistor guide leads away from the chassis after mounting. The manufacturer's representatives have been informed of the problem, and investigation is underway of new insulating materials which can withstand the heat without damage. Although this problem has not appeared in any other modules where these power transistors are used, it is expected that all insulators will be replaced by the new recommended insulating material.

b. Batteries. Battery design testing has progressed to the simulated space flight portion of the test program. Three batteries similar to the *Mariner R* design are undergoing test throughout the full range of environments required. Prior to the space flight portion of the test program, these three batteries had been subjected to the following environments in the sequence listed:

(1) Transportation vibration.

(2) Handling shock.

(3) Temperature and humidity (10 days).
TA 1, 50°F and 95% humidity.
TA 2, 120°F and 95% humidity.
TA 3, 85°F and 95% humidity.

(4) Static acceleration.

(5) Low frequency vibration.

(6) High frequency vibration.

(7) Shock.

(8) Vacuum and temperature. During a period of approximately 5 months the battery is exposed to vacuum and is charged and discharged at the appropriate current rates in accordance with the expected actual flight requirements. Each battery is maintained at a different temperature within ±2°F limits throughout the test. The temperatures are 50°F (TA 1), 100°F (TA 2), and 80°F (TA 3).

The present condition of these life cycle tests is as follows: TA 1 has successfully completed the launch and mid-course maneuver power phases and is now in the tenth week of simulated flight (cruise mode). TA 2 is in the fifth week of simulated flight, and TA 3 has started the third week of simulated flight. The electrical conditions for the cruise mode for all three batteries are a constant drain of 0.2 w and simulaneous low rate charging by a flight model battery charger. TA 1 and 2 have reached the fully charged condition, and the charger has automatically adjusted the output current accordingly. Thus, the total charger current for either TA 1 or 2 is approximately 16 ma, with a current distribution of approximately 60% to the battery and 40% to the constant load. TA 3 has not been on charge as long and, therefore, the charger current is larger (approximately 40 ma).

c. Solar panels. The *Mariner* R sample panel which is partially covered with 1000 flat mounted cells was subjected to the TA flight vibration test and then tested at Table Mountain. Extrapolation of electrical performance to the full complement of 4896 cells indicates that the specification requirement of 63 w/langley/min at 34°C and 34 w/langley/min at 127°C were met. This panel is to be subjected to the remainder of the TA tests.

All cells have been laid down on the TA panel and the panel is scheduled for completion by March 5. Flight panel No. 1 is ready for cell lay down and the electrical insulating layer is being applied to the second flight panel.

Spectrolab has submitted the final engineering evaluation report which included absorbtivity and thermal emissivity tests and ultraviolet radiation tests on different possible solar panel materials and solar cell and filter evaluation.

During this past period an intensive investigation of the five reference solar cells was made. These cells are used as part of a switching device which removes at least 5% of the load from the 2400-cps bus in order to avoid continuous sharing with the battery after mid-course maneuver. A 1000-ohm resistance was calculated to be sufficient for measuring open circuit voltage of the five cells. The criterion for selecting the cells was that at no time should the switching occur at less than the battery voltage or greater than the voltage at 90% of solar panel maximum power point. The selection of cells for this application is critical and care must be taken in their selection.

3. Secondary Power GSE

a. System test set. The system-test power GSE for *Mariner* R provides the necessary elements of power monitoring and control to support the spacecraft power system through test operations consisting of: initial power application, power subsystem evaluation, spacecraft system tests, environmental testing, and final integrated system test conducted just prior to transport to the launch pad. In addition, it is capable of automatic self test before or *during* any operation in conjunction with the spacecraft. The maximum duration of this automatic sequence is 90 sec, and on successful completion, assures that the monitor, recording, and power control functions

of the GSE are operating within the required tolerances. Because all simulation is self contained, no external equipment is necessary to complete the self test.

Figure 16 shows one set of power GSE as installed at the JPL spacecraft assembly facility. The set consists of two consoles of equipment with assemblies mounted from both the front and rear of the consoles to conserve space. All assemblies weighing less than 100 lb are slide mounted to facilitate acceptance testing and interchangeability as required.

Figure 17 is a block diagram of the system test GSE. The following is a brief description of each major assembly within the test set:

Power monitor and control panel assembly. The control panel assembly presents all primary controls and monitors normally encountered in system test operations. The operator may conduct a GSE self test, a test in conjunction with the spacecraft power system, or both. Interlocks are provided to prevent the operator from inadvertently damaging the spacecraft or the GSE.

Transfer and tolerance detector assembly. This assembly, on command, selects either the self test assembly or the spacecraft functions. It is interlocked so that it cannot apply power to the spacecraft during a self test. Also, should a self test be performed on the GSE during an operation with the spacecraft, power will not be removed from the spacecraft. All external functions pass through the transfer assembly so that a logical selection between self test or operate can be made.

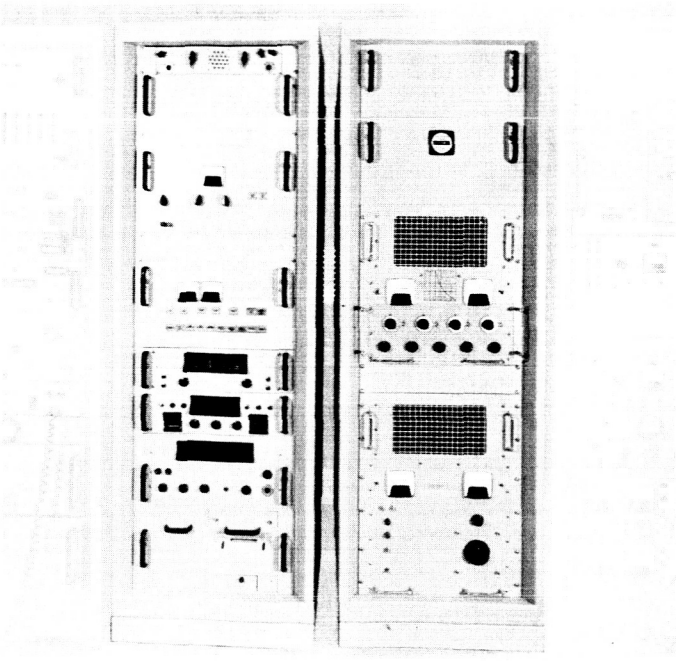

Figure 16. System test power GSE

Tolerance detector. Circuit cards make up a system of primary continuous monitors to detect malfunctions in the spacecraft power subsystem. The output of these detectors is a fail indication on the operator control panel. During automatic self test the detectors are required to respond to signals that are out of tolerance high, out low, and in tolerance. If all test conditions are satisfied for all detectors, a single self test complete indication is given.

Self test assembly. This assembly provides simulation for all spacecraft power functions monitored or controlled by the GSE. Its test routine is commanded automatically from the control panel assembly upon transfer to GSE test.

Automatic digital monitoring and recording subsystem. Four assemblies make up this portion of the GSE. It is capable of fully automatic, semiautomatic, or manual operation at the discretion of the operator. The monitors are visually presented and permanently recorded on printed tape; channels are available for forty inputs which may include ac, dc, and resistance measurements. It is controlled in self test by the control panel, automatically, to provide a printed record of the GSE during this mode. A clock assembly is included to provide timed automatic scans at prescribed intervals without an operator, for overnight use, or during extended life tests.

As indicated in Figure 17, it is designed to operate in conjunction with an optional digital comparator assembly for tolerance detection. Modification to existing equipment is not necessary to include this additional assembly.

Test monitor assembly. A special test assembly is included in the GSE to provide direct access to all functions (whether simulated or spacecraft) for purposes of fault finding, analog recording, or manual testing.

Power supplies. The second console contains all power equipment and associate control circuits to supply external spacecraft power, simulated solar panel power, battery charging, GSE auxiliary power, and precision monitoring excitation. All external functions leaving the GSE are short-circuit protected so that a failure in the spacecraft or associated equipment will not destroy the cabling.

Special remote controls. The power GSE is mechanized to be remotely controlled from other elements of GSE that include: system test, central computer and sequencer (CC&S) GSE; environmental test area, CC&S GSE, chamber vacuum sensor; and launch area, CC&S GSE. The

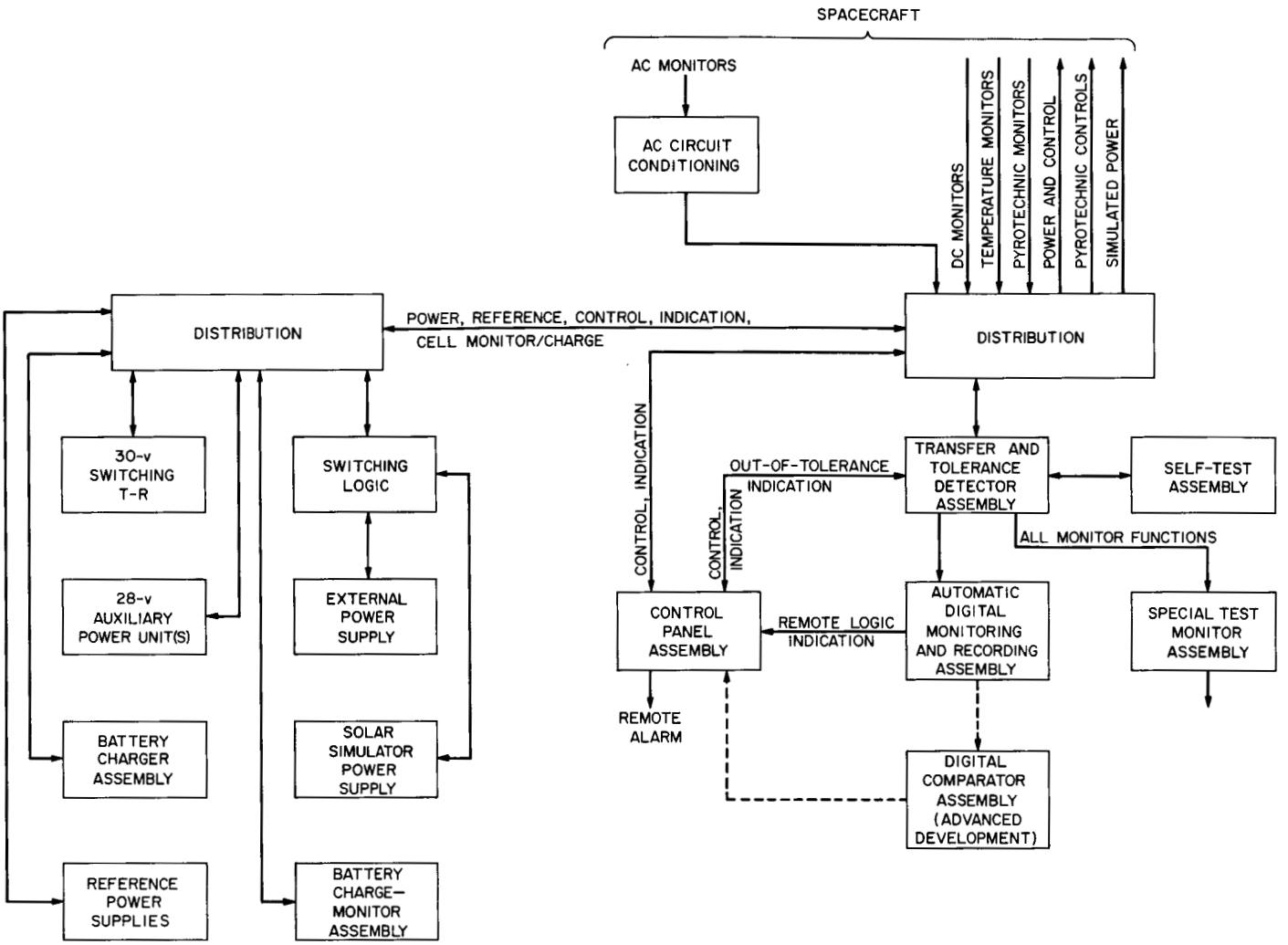

Figure 17. Power GSE functional block diagram

CC&S GSE has the capability in system test and environmental test lab (ETL) test to prevent spacecraft power from being applied unless hold current and relay position interlocks are satisfied. Once spacecraft power is applied, these two interlocks may be removed to allow the issuance of CC&S commands without losing spacecraft power. If CC&S GSE power is lost, however, spacecraft power will be turned off by the power GSE.

The same power GSE interlocks are used to turn spacecraft power off in the event of a vacuum chamber failure. Most of the ETL tests are conducted on internal power and, because spacecraft power may not be turned off unless the power system is in the external mode, the vacuum fail indication initiates a sequence that transfers the spacecraft from internal to external power and removes external power. Once this action has taken place, the power GSE is latched in the *off* position, the remote power control indicator is *on* and will remain in this condition until the operator manually resets the controls after the fail indication is removed.

b. Lab test set, power. The power lab test set (Fig 18) provides the means of performing detailed analysis of the following elements of the secondary power system, either individually or as a complete system: power switch and logic, booster–regulator, synchronizer, 2.4-kc and 400-cps inverters, and the flight battery charger. Subassemblies under test are installed on aluminum channels through openings in the panels. Each module, when seated, protrudes sufficiently to permit installation and removal of its connector(s), yet is maintained at a reasonable temperature by virtue of the large radiating surface of its channel.

Subassembly panels. In addition to the capability for testing the *Mariner* R power subsystem, the test set will

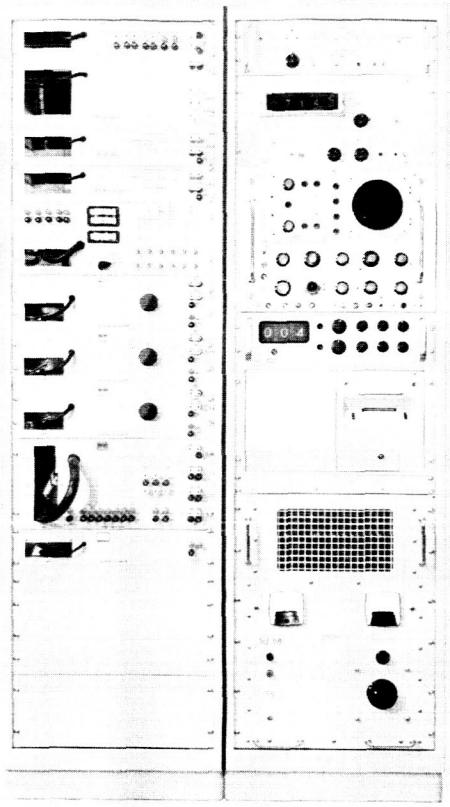

Figure 18. Power lab test set

test the *Mariner* B power subsystem; therefore, ten subassembly panels are provided. The *Mariner* R power subsystem, however, consists of only six subassemblies: (1) synchronizer, (2) 400-cps inverter, (3) 2.4-kc inverter, (4) booster–regulator, (5) power switch and logic, and (6) flight battery charger.

Synchronizer panel. Test points are provided for observing synchronizer output wave shapes and frequencies. The 38.4-kc synchronizer input may be switched off for tests of free-running operation.

400-cps inverter panel. The three-phase, 26-v output may be switched to a delta-connected resistive load bank, variable in three discrete steps. The resistive loads were selected to simulate all possible modes of normal spacecraft operation; i.e., the number of steps and the wattage value at each step were selected to correspond to each significant step specified on the load profile. The resistive load may be switched off and external loads connected to front panel binding posts.

2.4-kc inverter panel. The 50-v, 2.4-kc square wave output may be switched to:

(1) A resistive load, variable in three discrete steps corresponding to each significant step specified on the load profile.

(2) The T–R position, which permits selection of any combination of up to seven flight-type transformer–rectifier (T–R) units, which in turn are connected to typical fixed resistive loads.

Booster–regulator panel. The input to the booster–regulator is from the power switch and logic unit. A transfer switch permits the booster–regulator to be switched in or out of the system. In the booster–regulator position, the output is fed to the 400-cps, and 2.4-kc inverters as in the spacecraft. This permits analysis of the booster–regulator working into actual inverter loads and conversely permits testing of the inverters with booster–regulator excitation. In the rack power position of the switch, the inverters are fed directly from the Dressen–Barnes dc supply, and the booster–regulator output is connected to a continuously variable resistive load labeled *Load Adjust*. Input current monitoring test points are provided on the booster and inverter panels.

Power switch and logic panel. Proper operation of this unit is indicated by load transferral as the voltage is manually varied from the following sources:

(1) Rack power supply.

(2) Battery simulator (connections provided on front panel).

(3) Solar panel simulator (connections provided on front panel).

Kinetic switch control and indication is from a separate dc supply. Indication of science cruise mode relay position appears on the panel. A number of test points are brought out for monitoring the telemetry outputs, booster–regulator oscillator drive, and dc levels.

Battery charger panel. Testing of the flight charger consists of plotting the output transfer function as an externally-connected load is varied.

Measuring equipment. In addition to the test capabilities described above, a rack-mounted oscilloscope is provided for waveshape analysis, and a digital voltmeter and printer are provided. The digital voltage measuring system consists of a voltage-to-frequency converter operating into a counter. Frequency-measuring capability is provided by simple bypassing the voltage-to-frequency converter.

Voltage and frequency analysis is performed automatically and sequentially by a scanner with a maximum

capability of 100 channels. The scanner may be operated in conjunction with the digital printer to provide a printed record of the functions monitored and can be automatically or manually controlled.

As the scanner steps from one channel to the next, it is necessary that the voltage-to-frequency converter be programmed to the proper range, to ac or dc mode, or bypassed if a frequency measurement is desired. A printed-circuit board was therefore designed which would accommodate 10 channels and permit rapid changing of logic diodes whenever a change of range or other modification is required. Ten of the printed-circuit boards are located on the logic chassis, allowing diode programming of up to 100 channels.

Power supplies. A dc power supply provides power for:

(1) Energizing the booster–regulator through the power switch and logic.

(2) Energizing the 2.4-kc and 400-cps inverters directly. A 38.4-kc crystal-controlled oscillator of the type used in the CC&S generates the sync signal for the synchronizer.

D. Engineering Facilities

1. Space Simulator

As reported in *SPS 37-12*, the basic stainless steel vacuum shell was completed, along with several preliminary pumpdowns, in October 1961. The time subsequent to the above date was utilized by the contractor, Consolidated Vacuum Corporation, for the following functions:

(1) Completion of the building which houses the simulator.

(2) Installation of water, air, and cryogenic lines necessary to serve the various auxiliary systems.

(3) Installation of external optics, starters, and power supplies required for the operation of the 131 2½-kw mercury-xenon lamps.

(4) Installation of the Tenney Engineering Company cryogenic shroud which lines the internal walls and floor of the vacuum chamber.

(5) Assembly and erection of the 25-ft segmented cooled parabolic mirror in the dome of the chamber.

(6) In addition to these major tasks, parallel work has been essentially completed on the many gages, heaters, motors, control lines, and related instrumentation readouts required for the operation of the simulator.

Due to requirements peculiar to the *Mariner* R test scheduled for February 1962, JPL undertook the construction of a special support and shroud (described as the *Mariner* R mount) to ensure the on-time performance of the essential tests scheduled. This mount (Fig 19) was installed in the chamber in February 1962. All auxiliaries peculiar to the *Mariner* R mount have been satisfactorily checked from 250 to −320°F with the system being completely leak tight to a helium mass spectrometer.

The initial testing with solar simulation has verified the conceptual design of the system, but on the basis of

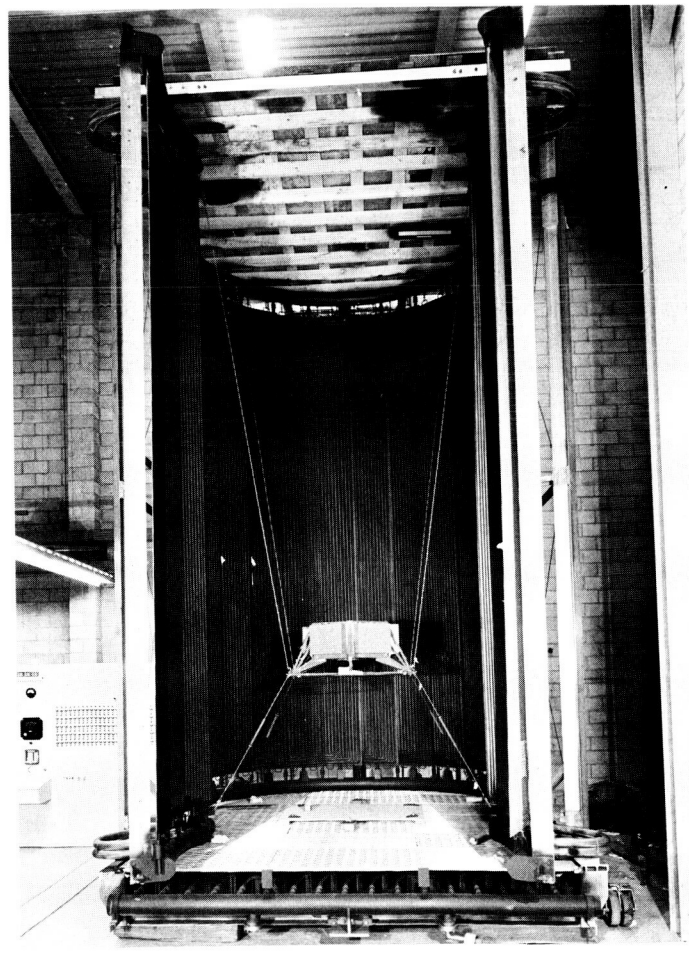

Figure 19. Dummy *Mariner* R hex suspended in JPL special support shroud

initial tests, there is a deficiency in the energy reaching the test value. Preliminary operations indicate that, after additional adjustment and improved alinement, the solar simulation will be ready for spacecraft testing.

Optical development and solar simulator. As a necessary step to calibrating radiation readouts, there has been devised a relatively uniform area of light approximately 6 in. in diameter of 1 solar constant intensity. This was achieved by mounting a 2½-kw mercury-xenon light in a 24-in. searchlight with the arc located slightly ahead of the mirror focus. A trial and error distribution of holes in attenuation screens has produced the above described uniform area. The lamp output is monitored according to the short circuit current provided by silicon solar cells, one looking directly at the arc and the other at the light reflected from the parabolic mirror. Over a period of 3 months, with intermittent use, the output of these detectors has remained stable within 1%. Consequently, it has been possible to calibrate two basic different types of thermopiles and correlate with a pyroheliometer within 1%. Additional correlations have been made using the same Eppley thermopiles in vacuum (with and without cold walls surrounding the thermopile) to demonstrate the effect of environment on output (Figs 20 and 21). In general, it has been found that the variation in calibration is less than 10% due to the cold shroud, but that an effective pressure of 10^{-5} mm Hg produces a change in output in the order of 300% for units calibrated at atmospheric pressures.

In addition to the intensity measurements, it is necessary to evaluate spectral content of the solar simulation. An intensity-ratio spectrophotometer is being utilized to provide a rapid method of determining the spectral distribution as compared with a tungsten strip lamp. A special quartz window has been installed in an observation port of the 25-ft space simulator to enable spectral measurements to be performed during testing. At this time measurements of the spectral distribution of 200-w xenon and mercury-xenon lamps are being used to develop the necessary techniques and explore the problems which occur because of the extreme line content of these particular sources.

Contracts have been entered into with Englehard Industries, Hanovia Division, Inc. and P.E.K. Labs Inc. for compact arc lights containing neon, argon, and krypton, in addition to the standard xenon (as well as introducing cadmium, zinc, and barium) in an attempt to eventually develop a high power light that will provide an improved spectral match to sunlight. This is a long-term development which should lead to major spectral improvements. As an example, the spectrum of a 70-w barium-mercury-amalgram xenon lamp has undergone

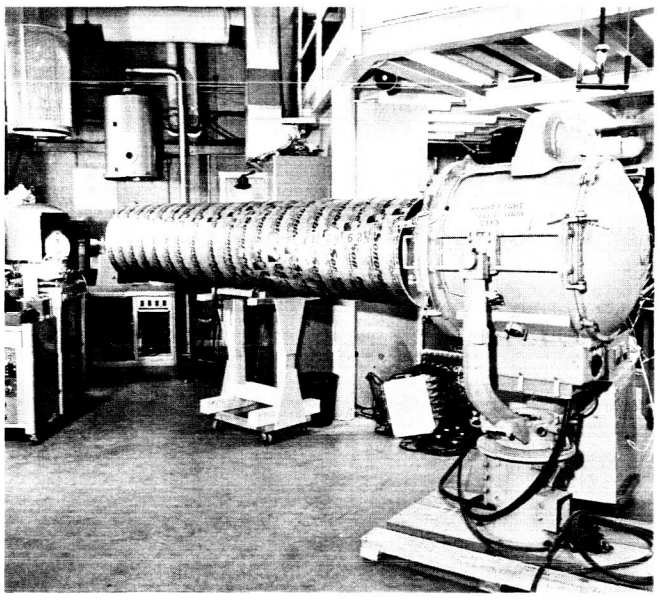

Figure 20. Thermopile being illuminated with 1 solar constant of radiant energy from 2½-kw Hg–Xe lamp

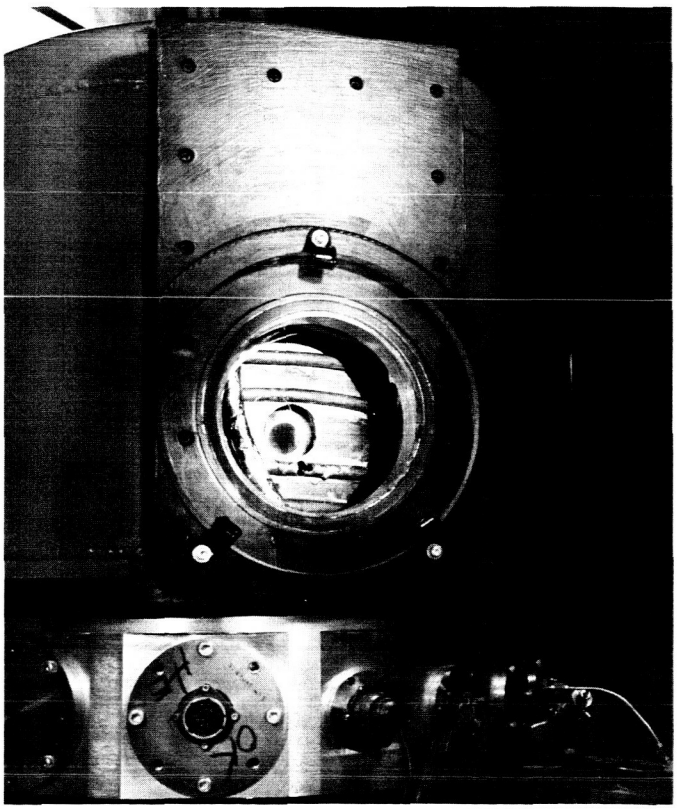

Figure 21. Eppley thermopile in vacuum chamber surrounded by LN_2 cooled shroud

preliminary evaluations with the results shown in Figure 22. The energy increase in the 2-μ range is due to the radiation from the tungsten electrodes entering the system. In a larger lamp this characteristic would not be observed.

2. Environmental Testing

a. Vibration testing. Several *Mariner* R composite structures have been run during January and February to simulate the effects of vibration that accompany the *Atlas* and *Agena* motor burning during the launch phase. These tests were to verify the structural design of the spacecraft as a unit during launch conditions.

The first of these tests was run with the spacecraft mounted to the Lockheed–*Agena* B adapter and enclosed by the shroud to verify clearances between spacecraft and shroud under vibration conditions. Figure 23 shows the spacecraft–adapter–shroud configuration prior to the test. The second test was run without the shroud to evaluate the Earth sensor mount and to check clearances of the mount during spacecraft resonances.

b. Explosive atmosphere testing. An explosive atmosphere chamber has been purchased and calibrated. The chamber, shown in Figure 24, is 35 in. in diameter and 63 in. deep. To ensure a homogeneous fuel mixture at all times, the walls are electrically heated to prevent fuel condensation. A test chamber is provided for test firing a sample of the air–fuel mixture prior to electrically actuating the specimen under test. This procedure ensures that a combustible mixture is present in the testing area of the chamber. The chamber is capable of simulating altitudes up to 115,000 ft and, at present, it has been calibrated for various air–fuel ratios up to 40,000 ft.

c. Space simulation. Preparations were completed to test the temperature control model (TCM) (*Mariner* R), in the 25-ft space simulator. Purposes of the test are to:

(1) Verify the passive temperature control design.

(2) Verify freedom from large thermal gradients.

(3) Estimate thermal time constants.

(4) Verify that the vacuum–temperature tests performed during assembly-level environmental tests included an adequate margin of safety.

The TCM will be operated at various power modes while being subjected to various degrees of simulated solar radiation with the chamber pressure below 10^{-4} mm Hg and with the walls of the *Mariner* R mount cooled by liquid nitrogen. Figure 25 shows the open vacuum chamber with the special mount designed for testing the *Mariner* R. The equipment installed in the bottom of the chamber is being used to calibrate the solar simulation system. This test has been scheduled for the last 2 weeks of February and the first week of March.

During January 1962, the *Mariner* R hex temperature control model was operated in a vacuum (10^{-4} mm Hg) temperature environment in the 6-ft space simulator.

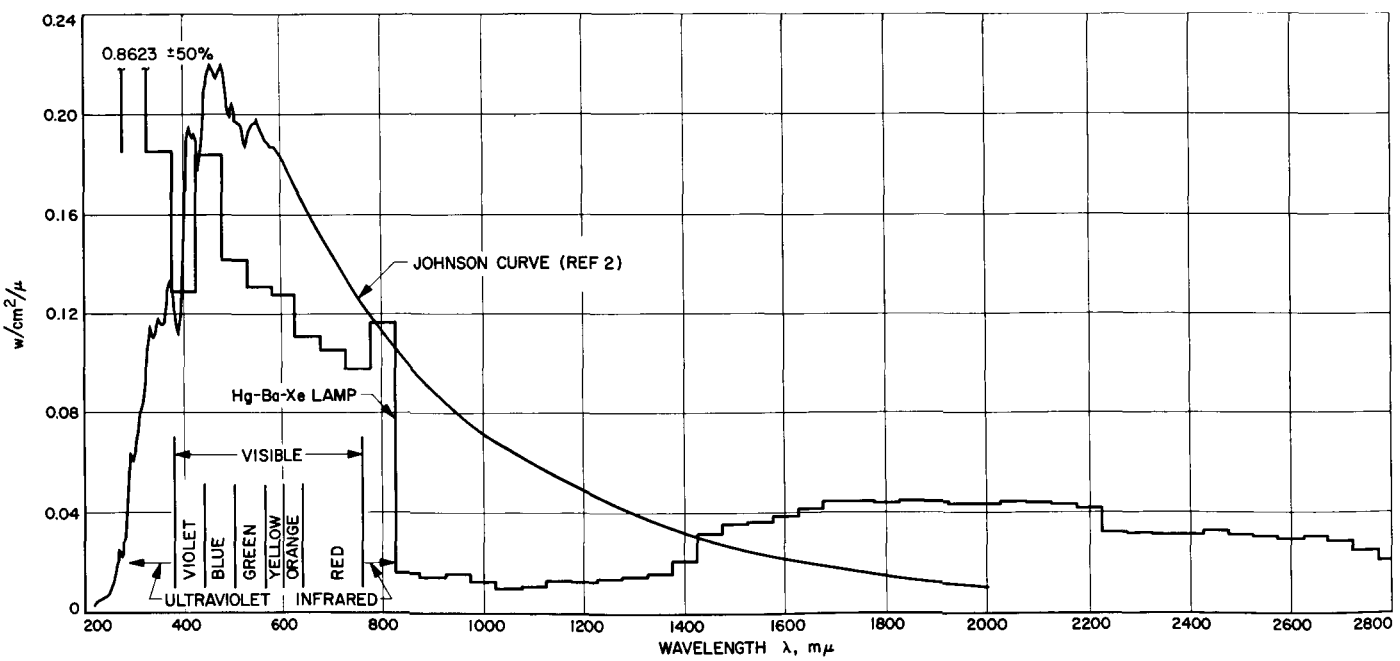

Figure 22. Preliminary spectral comparison between Johnson solar radiation curve and Hg–Ba–Xe lamp

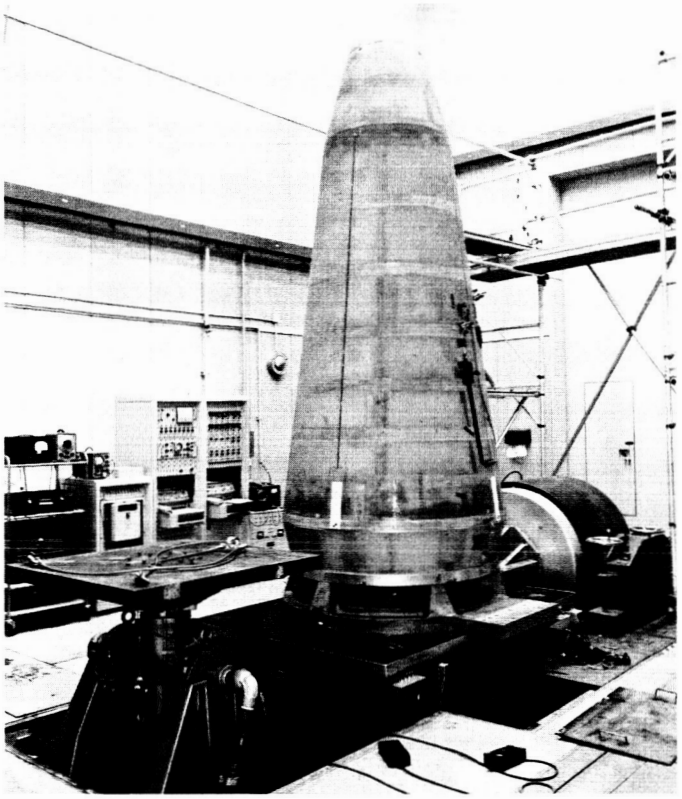

Figure 23. *Mariner* R spacecraft–adapter–shroud configuration prepared for vibration test

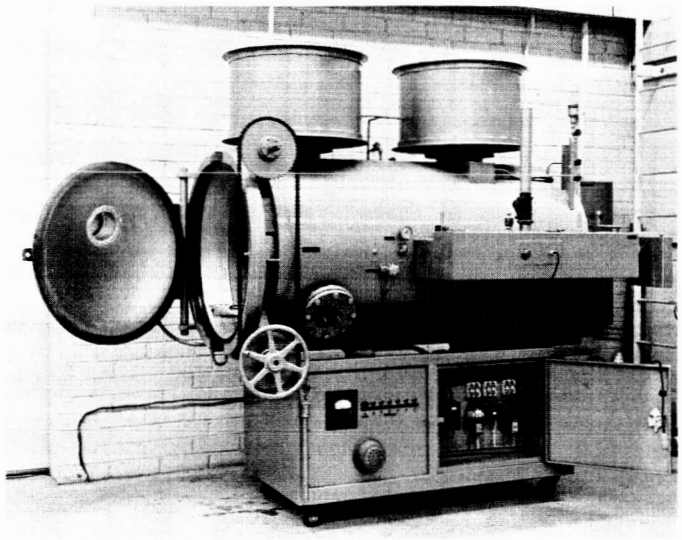

Figure 24. Explosive atmosphere test chamber

New hangars were fabricated and used to mount the model 6 in. higher than normal and off of center. This position permitted clearance for the long range Earth sensor and other extended equipment during the test. Resistance heaters mounted on the model were used for solar simulation. Objectives of the test were to:

(1) Determine temperature distribution throughout hex portion of spacecraft with internal power.

(2) Verify temperature distribution particularly in the long range Earth sensor area.

(3) Determine if bolting arrangement of the boxes is critical.

(4) Determine effectiveness of the temperature control paint patterns.

The facility was occupied for a total period of 10 days, and test time amounted to 173 hr. The test verified that temperatures are within their proper range.

d.* Mariner *R environmental test program. During January and February, 309 experimental, type approval, and flight acceptance environmental tests associated with the *Mariner* R were handled by the JPL environmental test laboratory.

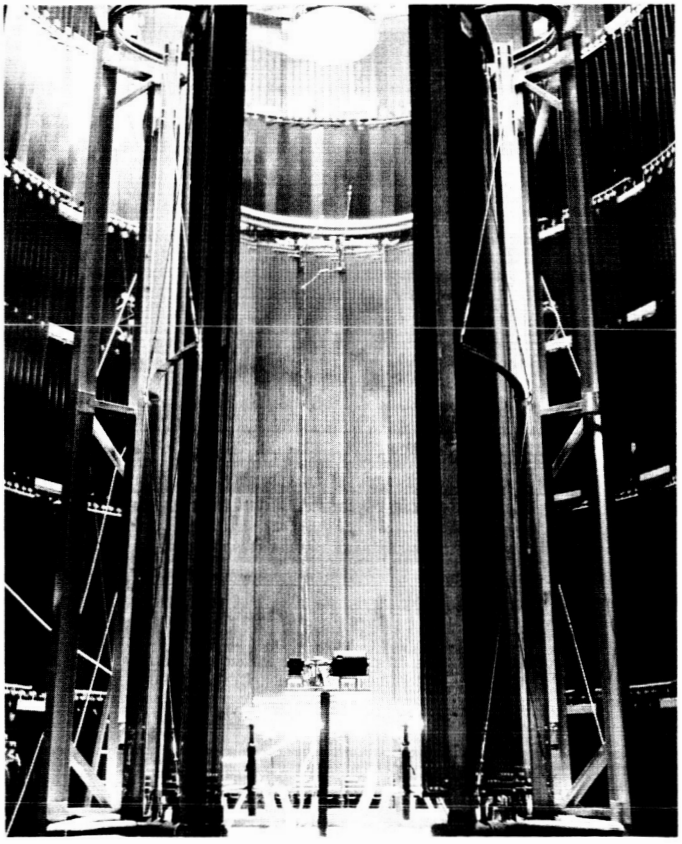

Figure 25. *Mariner* R mount installed in 25-ft space environment simulator

References

1. Jet Propulsion Laboratory, *Scientific Experiments for Ranger 1 and 2, Technical Report No. 32-55,* Jet Propulsion Laboratory, Pasadena, January 3, 1961.

2. Johnson, F. S., "The Solar Constant," *Journal of Meteorology,* Vol II, No. 6, pp 431–439, December 1954.

III. Mariner B Project

The primary purpose of the *Mariner B* project is to permit scientific investigations of the planets Venus and Mars during their periods of availability in 1964 through 1967. Secondary purposes in order of priority are: (1) to make interplanetary scientific investigations in the regions between Earth and Mars, (2) to develop experience in the design of a spacecraft that has considerable flexibility with regard to the specific missions for which it is basically capable of covering, (3) to provide experience and knowledge which will permit a quality and efficient design of the later *Voyager* spacecraft. To these ends, the spacecraft will be designed for a precision flyby mission and will incorporate the capability of either carrying or not carrying a small landing capsule.

The *Mariner B* spacecraft will be injected by the *Centaur* launch vehicle. Two identical probes are expected to be launched at each of the planet launching opportunities. Deep space probes, scheduled between periods of Mars and Venus availability, are also included in the *Mariner B* project.

Mission objectives and design criteria were generated and have been used for the preliminary design effort. This effort was initiated in October 1961, is proceeding on schedule, and will be completed on April 1, 1962. Design characteristics and restraints have been completed and will be used to generate the functional specifications scheduled for completion on April 1. A prerelease Project Development Plan (DPD) has been completed. Copies of this plan were transmitted to NASA Headquarters and Marshall Space Flight Center for coordination during the week of February 26. A final coordinated issue of this PDP is scheduled for release on April 1.

A. Space Sciences

1. Television Subsystem

A photo-geomorphological survey of the Mars surface is to be made by two TV cameras mounted on the planetary horizontal platform (PHP) of *Mariner* B. High-resolution pictures will be taken with a long focal-length objective having a red filter, while overlapping larger areas will be covered by a short focal-length camera. Sequentially operated filters on the second camera will permit heterochromatic analysis for an improved understanding of Martian morphology.

Two views of Mars as observed from *Mariner* B for a 1964 planned trajectory approaching to 13,000 km are shown in Figure 1. These present views of most interest for geomorphological picture studies. Depicted are a sub-solar view at −3.34 hr and a Mars terminator view at 0.66 hr from closest approach. Superimposed are the corresponding scanned fields of view for the two TV cameras with objective fields of 0.62 deg (Camera A) and 3.15 deg (Camera B). The more valuable information will be secured in the region of the Mars terminator when the major portion of the 100 pictures to be transmitted to Earth will be taken.

The relative intensity of Mars luminosity, as observed from Earth (Ref 1), is shown in Figure 2. The data is for a phase angle of 39 deg, corresponding to the *Mariner* B picture of Figure 1. Relative intensity was determined by photometric microdensitometry of a photographic negative of the planet taken with a red filter. The maximum variation of intensity over the sub-solar portion of the planet is of the order of 15%. Small areas of the surface that would be covered by the narrow-angle camera have greatly reduced light gradations, approaching 1% of the maximum high-light illumination. Pictures that will be imaged onto the photosensitive surface of the TV camera tubes may thus be categorized into two classes: bright low-contrast pictures and dark pictures of medium-to-high-contrast with an over-all dynamic range of illumination of the order of 100:1.

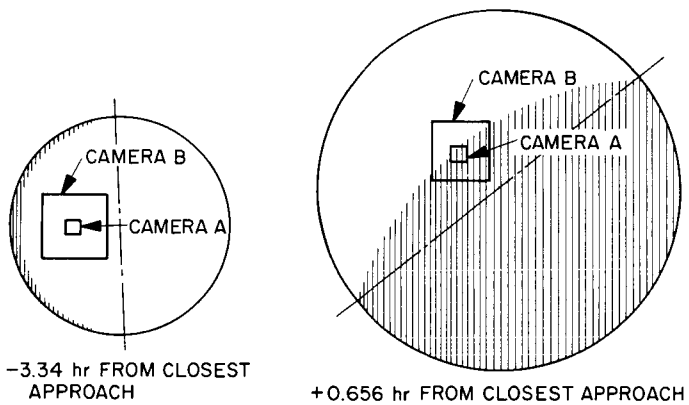

Figure 1. View of Mars as observed from *Mariner* B spacecraft

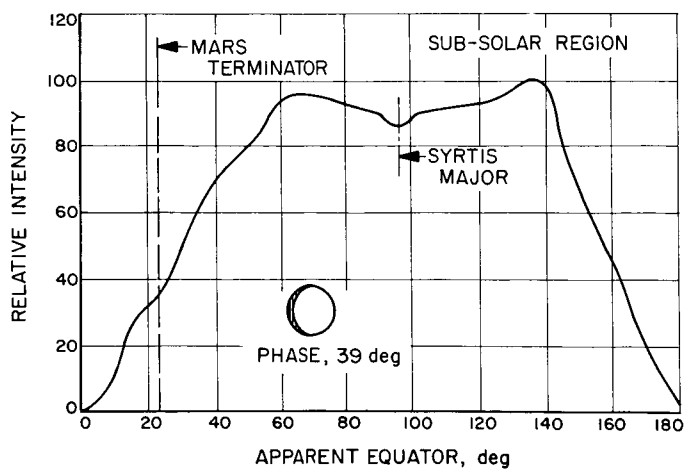

Figure 2. Relative intensity of Mars 1939 luminosity as observed from Earth

a. Block diagram. A block diagram of the TV subsystem is shown in Figure 3. Scanning and control functions for the two cameras will be logically controlled from a master 1-mc clock signal. To simplify control operations, both cameras will take pictures continuously and alternately, following planetary acquisition. The stored picture readout time is 14.8 sec, and an equal period is taken to reprocess the photosensitive target. Thus, with interleaved operation, the maximum picture taking rate is 4 pictures/min. Command signals at stated intervals will select pictures for data encoding and subsequent transmission to Earth.

b. Camera tube. The provisionally selected camera tube for the Mars mission is a 1-in. vidicon using electrostatic deflection and focusing and an ASOS (antimony sulfide oxy-sulfide) photoconductive target. There are presently no tubes available that completely meet *Mariner* B requirements. Although the ASOS electrostatic vidicon is somewhat lacking in sensitivity, it is compact, ruggedized, lightweight, economical of power, has adequate storage time for slow picture readout, and can withstand decontamination temperatures of over 100°C. An electrostatic tube, unlike tubes relying on magnetic fields for beam control, will not cause interference with the magnetometer experiment.

Resolution is expected to exceed the requirements for the 400 line TV scan that will be used for both cameras with an active scanned area of 0.44 × 0.44 in.

c. Vidicon transfer characteristics. A typical transfer characteristic for an ASOS vidicon (estimated from Fig II E-8 of Ref 2) is shown in Figure 4. Related are the photo-target illumination in ft-candle/sec, and the target high-light current in microamperes. The gamma over the linear range is 0.72. A provisional exposure of 40 msec for the high-resolution camera produces a photo-target illumination of approximately 0.3 ft-candle/sec over the sub-solar region. Thus, with the expected dynamic range of Mars illumination of 100:1 the vidicon sensitivity (i.e. the ability to produce a high resolution picture clear

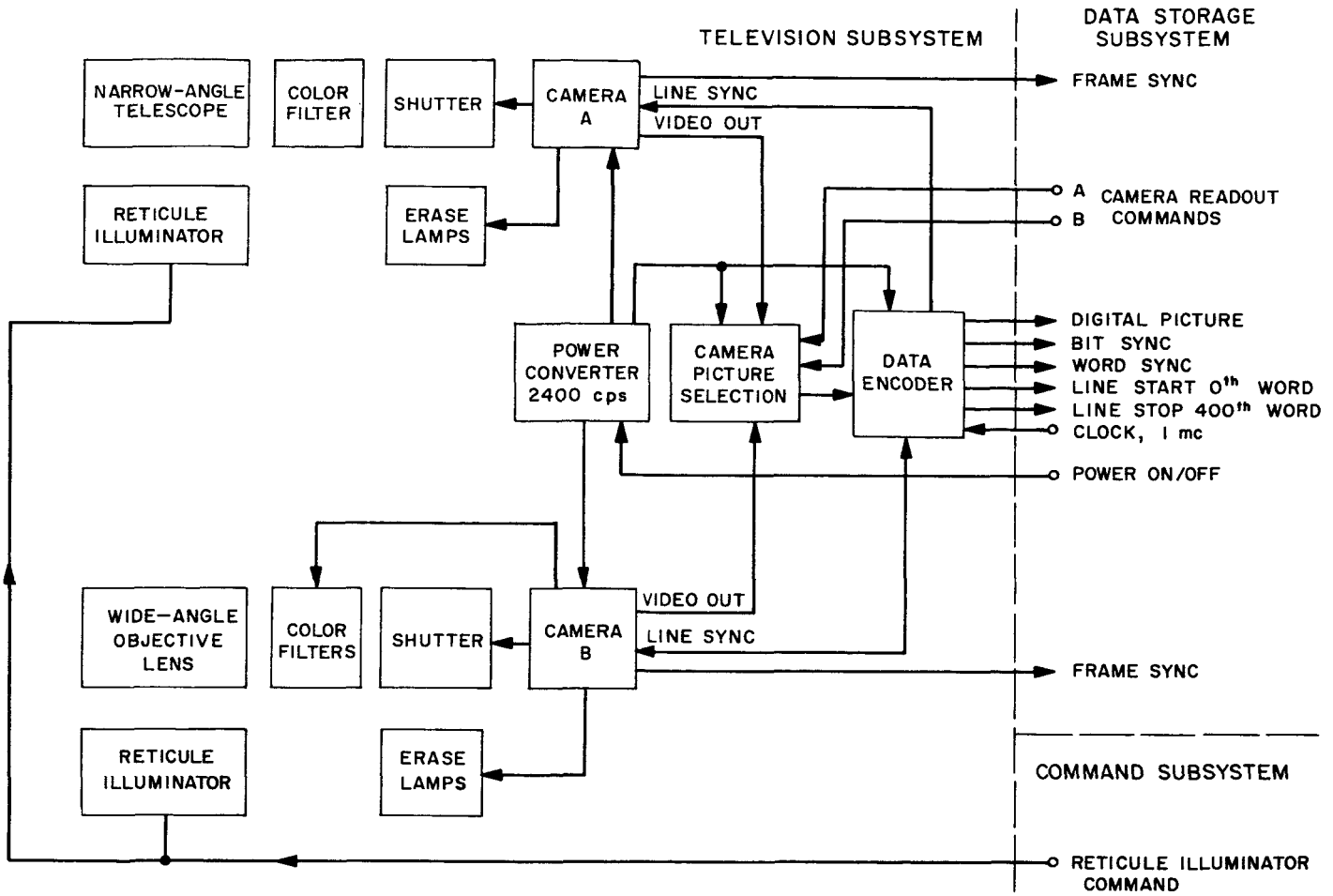

Figure 3. *Mariner* B television subsystem

of noise) should exceed 0.003 ft-candle/sec. The minimum vidicon signal for clear pictures is seen to be in the region of 0.006 ft-candle/sec.

The output signal from the vidicon after suitable amplification will be quantitized into 64 levels for digital encoding. To ensure a maximum number of quantitized shades of gray in any one picture, some form of exposure control is desirable. However, the problem of platform stability during exposure has defined a shutter time that has been chosen as a compromise between picture smearing and vidicon sensitivity. An alternative to light exposure control is to change the electronic operating parameters of the vidicon tube to match the target illumination for a particular scene.

d. Hardware. A vidicon camera-tube assembly is now being fabricated that will incorporate a modified *Ranger* shutter and the necessary electronic circuitry for logical control. Flight approved components are being used throughout, and the modules are being constructed in a manner that will simplify integration into the final flight packaging. Only essential electronic units such as the video preamplifier, and the vidicon supply distribution box will be contained on the PHP with the cameras. One of the units to be mounted on the PHP is shown in Figure 5.

The major portion of the electronics, including all vidicon control functions, will be contained in a separate package on the main bus, with a second unit that will include the 2400-cps power converter. Figure 6 shows the partially completed module arrangement for the camera circuitry that will be carried on the main bus. Insofar as applicable, proven *Ranger* camera circuitry will be utilized with necessary changes to conform to the *Mariner* B control functions.

e. Present plans. The immediate objective is to have a complete experimental electronic assembly that will enable vidicon camera-tubes to be evaluated in terms of the Mars mission. This same assembly will permit circuit functions to be checked for correct operation. It is

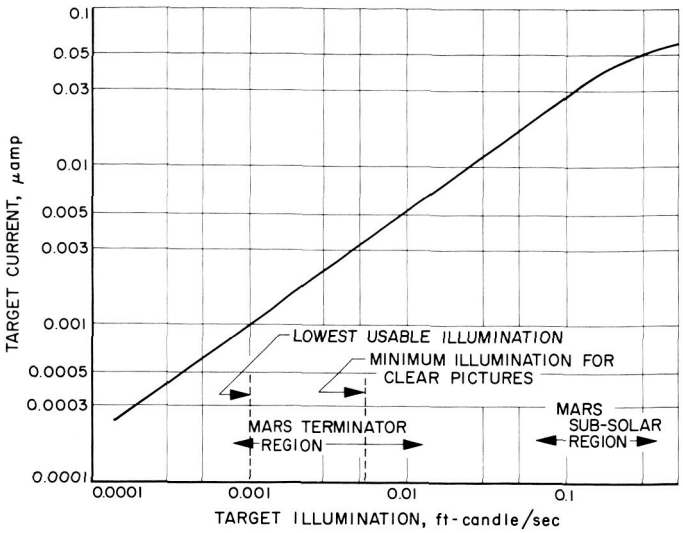

Figure 4. ASOS vidicon transducer characteristics

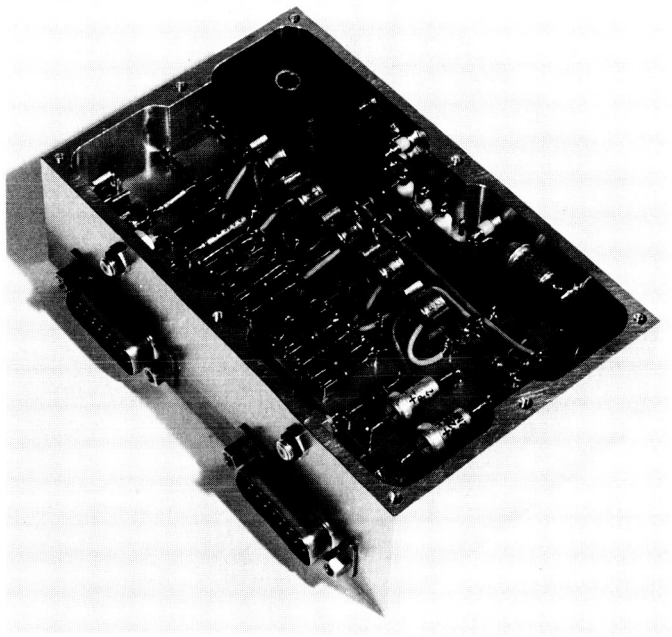

Figure 5. Vidicon distribution and 125-kc oscillator unit for *Mariner* B TV camera

hoped to obtain an improvement in vidicon sensitivity by optimization and refinement of the target control circuitry; more particularly by improving the electromechanical layout surrounding the vidicon target. A solution to the exposure problem is being sought that will permit a simple, reliable, intelligence system to be inserted that will evaluate conditions existing at picture taking time in terms of (1) past picture history and (2) light-intensity interpretations made by a strategically placed photo-cell. This system will then perform simple electronic control

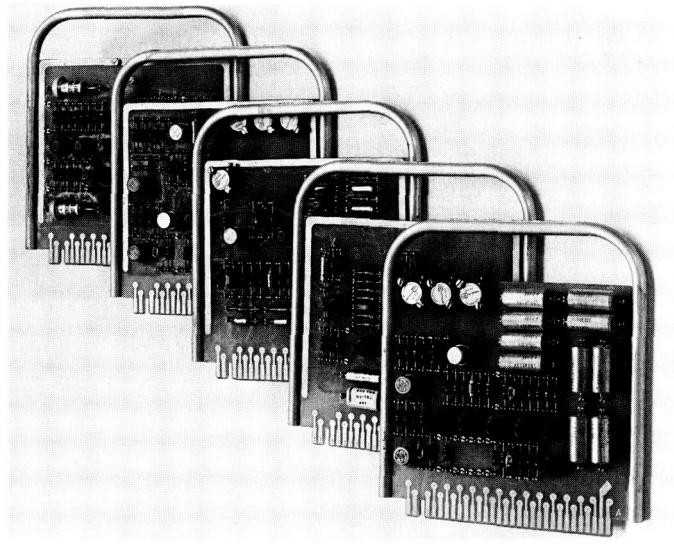

Figure 6. Module arrangement for electronic control of *Mariner* B TV camera

functions as required to adjust camera performance for optimum picture resolution.

2. Plasma Probe

A development program has been initiated to perfect an advanced design plasma probe (Fig 7) for use in the *Mariner* B. Although the eventual goals of the experiment are much the same as those intended for the *Ranger I* and *II* instruments (*SPS 37-11*), utilization of techniques achieved in the development of the *Surveyor* plasma probe will afford higher resolution measurements of a broader particle energy spectrum than obtainable with the *Ranger* instrument.

The instrument will contain seven sets of electrostatic analyzers with Faraday charge collector cups whose look angles are arranged to cover small segments of a solid angle of about 2π sterad centered on the Sun. Because of the increased sensitivity and improved response time of the electrometer amplifier, the deflection plates will be substantially smaller than those used in the *Ranger* and *Mariner* R probes. This will result in a more narrow angle of acceptance and the spread in particle energy for a given electric field between the plates will also be reduced; both the directional sensitivity and the differential particle energy selectivity will be increased. At present, the absolute values of the particle energy spectrum to be examined have not been determined, but there will be provisions for monitoring 32 electron and 32 positive ion energy levels. According to the proposed deflection plate geometry, the energy levels will lie between 20 ev and 20 kev.

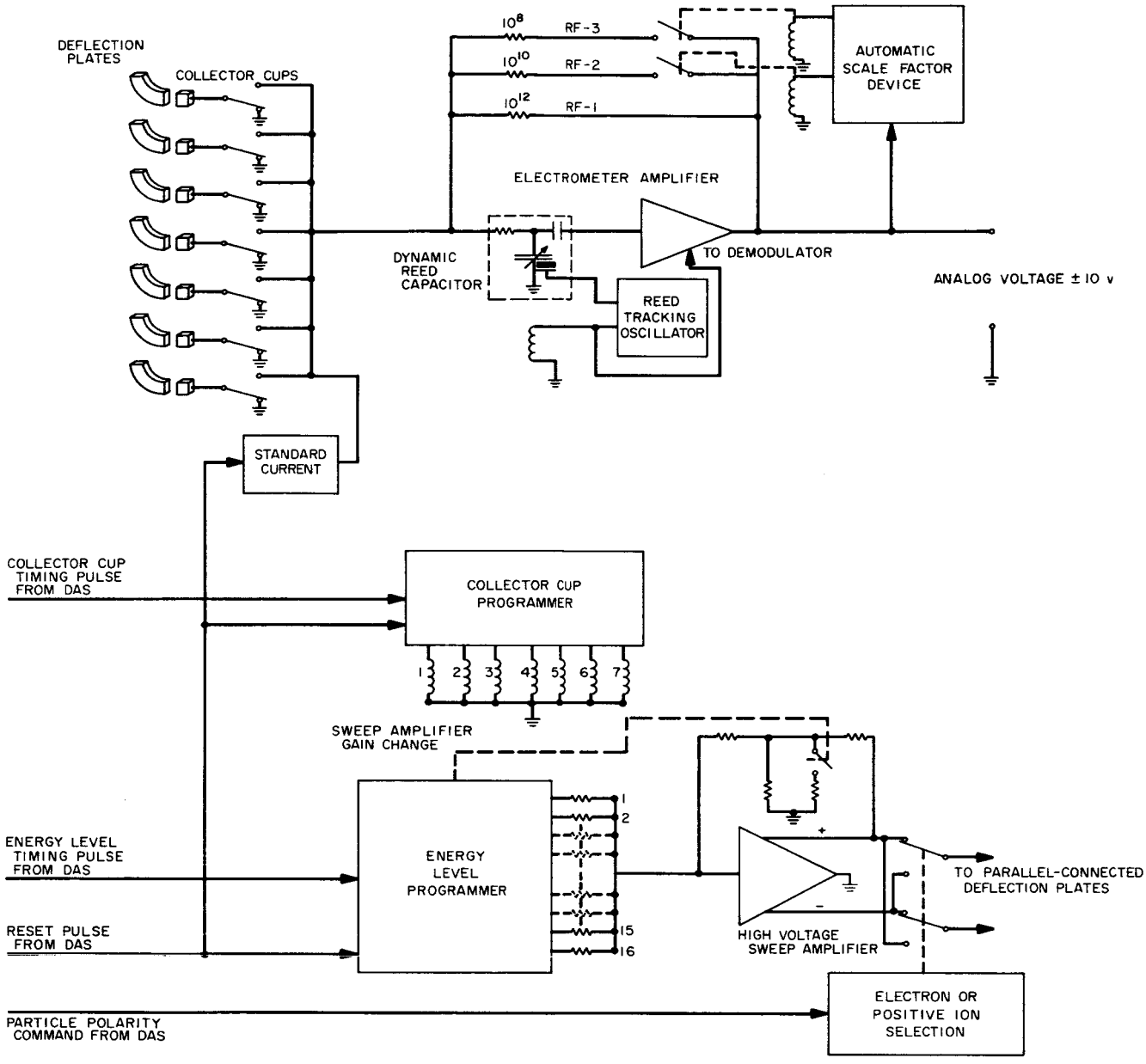

Figure 7. Logical diagram of *Mariner* B plasma probe

As in previous versions of JPL plasma probes, the *Mariner* B instrument will consist of the deflection plate-collector cup assemblies with an electrometer amplifier and a deflection voltage and cup selection programmer system.

a. Electrometer amplifier. The *Mariner* B probe will use the electrometer with the linear range compression that was developed for the *Surveyor* plasma probe. This electrometer and the automatic scale factor device which provides the linear range compression has been described in *SPS 37-13*, Volume II. As in the *Surveyor* device, the collector cups will be consecutively gated into the electrometer by means of ultra-high impedance switches. The collector cups are gated by a 3 × 7 diode matrix driven by a three-stage binary counter which receives a timing pulse from the data automation system (DAS). The idle collector cups are grounded when not in use to prevent a high voltage buildup across the collector cup capacitance due to continuously incident charged particles.

b. Deflection voltage system. The deflection voltages for the electrostatic deflection plates are generated by a carrier-type high voltage operational amplifier driven by a digital programmer. The digital programmer con-

sists of a 4 × 16 diode matrix driven by a four-stage circulating binary counter. While the counter circulates through one cycle, it injects 16 different signal currents into the sweep amplifier; upon completion of one cycle it changes the feedback resistance of the sweep amplifier and circulates once more. Thus, by changing the gain of the sweep amplifier in this manner and cycling through the matrix a second time, 32 discrete output voltages are obtained for 16 discrete inputs. The rate at which the deflection voltages are changed is governed by a timing pulse from the DAS. A programmable polarity pulse from the DAS changes the connection of the high voltage sweep amplifier to the deflection plates, and, thereby, permits measurement of 32 energy levels of electron current.

A programmable reset pulse from the DAS resets both the cup selection and energy level programmers to the zero state. It also drives a standard current device which injects a known current into the electrometer amplifier. The current device cycles through three different current levels (one for each reset pulse) so that all ranges of the automatic scale factor device, controlling the feedback loop of the electrometer, are checked.

c. Development status. Breadboards of the various subsections of the instrument are in design or evaluation. It is anticipated that thermal evaluation of the entire breadboard instrument will be completed during May 1962 and that fabrication of a prototype instrument will begin in June.

B. Telecommunications

1. Antennas, RF Components, and Couplers

Two basic types of antenna systems are required for the *Mariner* B program. An omnidirectional antenna system is used for short range communication with the spacecraft, during mid-course maneuvers, the period of time when the spacecraft is not attitude stabilized, and during various emergency modes. A high gain antenna is used at ranges beyond which the omni-antenna system is not adequate.

a. High gain antenna. The high gain antenna will consist of a 4-ft parabolic reflector with $f/D = 0.35$. The feed will be similar to that used for the *Mariner* R program with the exception that the present antenna will be used at 2113$\frac{5}{16}$ and 2295 mc. The antenna will be optimized at 2295 mc, which is the spacecraft telemetry frequency. The design gain at this frequency is 27 db. Since the antenna will not be optimized at 2113$\frac{5}{16}$ mc, which is the spacecraft command frequency, a gain of 24 db or better will be provided at this frequency. Since the antenna will have 2 deg of freedom relative to the spacecraft, two rotary joints will be required in the antenna gimbals.

There are a number of problem areas that are now being evaluated. With the gimbaling system and the location that has been proposed for the antenna, the high gain antenna comes very close to looking at various parts of the spacecraft. An investigation is to be performed to determine how much the antenna pattern will be squinted by the spacecraft when the antenna is pointed near the spacecraft structure. A second area being studied is the effect of various feed support structures on the antenna's electrical performance. Also being studied is the effect of reflector mesh size on antenna performance to determine the largest allowable mesh size usable for the parabolic reflector surface.

b. Omni-antenna. The omni-antenna system is to be operable at both 2113$\frac{5}{16}$ and 2295 mc. Preliminary trajectory information indicates that for Venus missions the required pattern coverage is within a hemisphere centered on the spacecraft axis and pointed toward the top of the spacecraft. For a Mars mission the hemispherical coverage would be in the opposite direction (aft of the spacecraft). To meet this type of coverage it is planned to mount a turnstile antenna at either end of the spacecraft looking in opposite directions. Then for normal trajectories, only one of the antennas would be in use, depending on the mission. If for some reason the spacecraft enters a nonstandard flight situation and the spacecraft orientation is such that the antenna in use no longer can radiate toward the Earth, the spacecraft can be commanded to switch to the second antenna which would now be looking toward the Earth.

Recently a second family of trajectories has been designed for Venus missions where the coverage required is off the side of the spacecraft. The type of antennas that would be required is somewhat more complicated and different in configuration than those described above. To accommodate this requirement it may be necessary to have different type antennas available for the different family of trajectories. The various approaches to this problem are now under investigation.

c. Coaxial rotary joint. As on previous vehicles, some method of coupling RF energy between the communi-

cations boxes on the bus and the movable high gain antenna is necessary. Since the high gain antenna will have 2 deg of freedom, two identical coaxial rotary joints will be utilized for this purpose.

Preliminary design work has been completed on this rotary coaxial joint and it is estimated that it will have the following parameters:

(1) Envelope, 1.31 in. diameter by 3.37 in. long.

(2) Weight, approximately ½ lb.

(3) Operating frequencies, 2113$^{5}/_{16}$ and 2295 mc.

(4) Insertion loss per joint, 0.15 db at the operating frequencies.

(5) VSWR, less than 1.2 at the operating frequencies.

Parts have been ordered for the prototype rotary joints, and delivery is expected in April 1962.

C. Secondary Power

The *Mariner* B power system is now in the preliminary design phase. The estimated power requirements have been obtained from the various power users, and tentative power systems are under study.

From the mission objectives and design requirements, a system similar to *Mariner* R will be adopted for the larger portion of the power conversion. This system provides regulated ac output voltage to the users which will be converted to the required voltages by the users' transformer–rectifier (T–R) and filter networks. In addition to the ac distribution system, a dc-to-dc regulated converter will be used to provide power to the communication transponder (the largest power user). The separation of the communication power supply from the rest of the system was decided upon because of the unique requirements of the communication system and to improve the system efficiency.

The *Mariner* B power sources are composed of a minimum of four solar panels for supplying continuous power and a rechargeable silver-zinc battery which provides power to the spacecraft prior to Sun acquisition, during short-term power demands in excess of the capability of the solar panels, and during periods in which the solar panels are not illuminated. The battery charging is expected to take place during the cruise modes of the flight.

The electronic portion of the power system includes the equipment associated with the functions of power sources selection, regulation, inversion, conversion, and recharging. A block diagram of the complete power system is indicated in Figure 8.

1. Electrical Conversion Systems

The tentative design for the *Mariner* B power switch and logic (PS&L) will use diode input circuits from the solar panels and the battery. The voltage ranges will be similar to those of *Mariner* R, 25.8-v minimum battery voltage to 50-v maximum panel output. Consideration is being given to the addition of shunt zener diodes on the panels to limit the voltage to 45 v.

The use of a silicon controlled rectifier (SCR) for the battery series diode would reduce the possibility of battery sharing when the panel output is low in voltage but is still capable of furnishing the required power. The battery output would be available immediately when the panel output dropped, as during a maneuver. The SCR would be reset to its high impedance state when the panel output exceeded the battery voltage after the maneuver period.

The unregulated output from the PS&L furnishes the dc inputs for the transponder converter and the booster regulators. The PS&L would also contain the logic and controls for the battery charger and the power monitor. This latter item will control the predetermined procedure of the load dumping or cycling during periods of power limiting or overload.

The booster–regulators will furnish a regulated dc output to operate the 400-cps inverter, the 2400-cps inverters, the power synchronizer, and the telemetry circuits. Since this regulated dc output must furnish over 300 w during peak conditions, the load will be shared by two booster modules. The use of two medium power units instead of one high power booster will offer a limited amount of redundancy, permit more optimum package location, and avoid the concentration of over 100 w of dissipated power in one package.

The presently proposed three-phase, 400-cps inverter will have a stepped square wave output in which the third harmonic has been eliminated. Recent tests have indicated that the gyro motor loads can operate from such a waveform without difficulty. The advantages of using such an output are the reduction in the size and weight of the inverter and a big improvement in the operating power efficiency of the unit.

Table 1. *Mariner* B estimated average power requirements, in watts

Flight sequence	Transponder[a]	Data encoder[b]	Command[c]	Ranging	Attitude control	CC&S	Science	Data automation system	Capsule related items	Subsystem power required[d]	Power conversion efficiency[e]	Charger telemetry sync	Total power required	
													Battery	Solar panels
Launch to start acquisition	75.40	26.20	5.40	8.40	43.00	30.00	—	—	—	188.40	57.5	7.00	327.10	—
Start acquisition	75.40	26.20	5.40	8.40	79.56	30.00	—	—	—	224.96	57.5	7.00	391.40	—
Cruise	75.40	26.20	5.40	8.40	33.46	30.00	15.00	17.00	—	210.86	52.0	47.00	—	405.70
First mid-course maneuver	75.40	26.20	5.40	8.40	105.00	30.00	—	—	—	250.40	57.5	7.00	435.80	—
Cruise	75.40	26.20	5.40	8.40	33.46	30.00	15.00	17.00	—	210.86	52.0	47.00	—	405.70
Second mid-course maneuver	75.40	26.20	5.40	8.40	105.00	30.00	—	—	—	250.40	57.5	7.00	435.80	—
Cruise and guidance	75.40	26.20	5.40	8.40	43.46	30.00	15.00	17.00	—	220.86	52.3	47.00	—	423.30
First approach maneuver	75.40	26.20	5.40	8.40	105.00	30.00	—	—	—	250.40	57.5	7.00	435.80	—
Cruise and guidance	75.40	26.20	5.40	8.40	43.46	30.00	15.00	17.00	—	220.86	52.3	47.00	—	423.30
Second approach maneuver	75.40	26.20	5.40	8.40	105.00	30.00	—	—	—	250.40	57.5	7.00	435.80	—
Cruise and guidance	75.40	26.20	5.40	8.40	43.46	30.00	15.00	17.00	—	220.86	52.3	47.00	—	423.30
Capsule release	75.40	26.20	5.40	8.40	33.46	30.00	15.00	17.00	24.00	234.86	52.4	47.00	—	447.70
Miss maneuver	75.40	26.20	5.40	8.40	105.00	30.00	—	—	24.00	274.40	58.0	7.00	477.80	—
Pre-encounter	75.40	26.20	5.40	8.40	45.30	30.00	30.00	17.00	24.00	261.70	52.5	47.00	—	496.60
Encounter	75.40	26.20	5.40	8.40	45.30	30.00	30.00	17.00	24.00	261.70	52.5	47.00	—	496.60
Post-encounter	75.40	26.20	5.40	8.40	33.46	30.00	15.00	17.00	—	210.86	51.5	47.00	—	410.00

[a]Transponder power requirements assumes: two receivers, one with ranging; two RF drivers; and two Amplitron power amplifiers—only one operating at a time.

[b]Data encoder power requirements include power to tape storage.

[c]Power to command system assumes one system without backup.

[d]All subsystem power requirements shown are to the subsystem transformer–rectifiers where applicable.

[e]Power conversion efficiency is power delivered to the loads excluding charger, telemetry, and power sync divided by power at input to power switch and logic $\times 100$.

Notes: (1) Transient battery power and peak loads required by attitude control not shown.
(2) Planet tracker subassembly activated prior to first approach maneuver; deactivated after second approach maneuver.
(3) Horizon scanner activated at pre-encounter; deactivated at start of post-encounter.

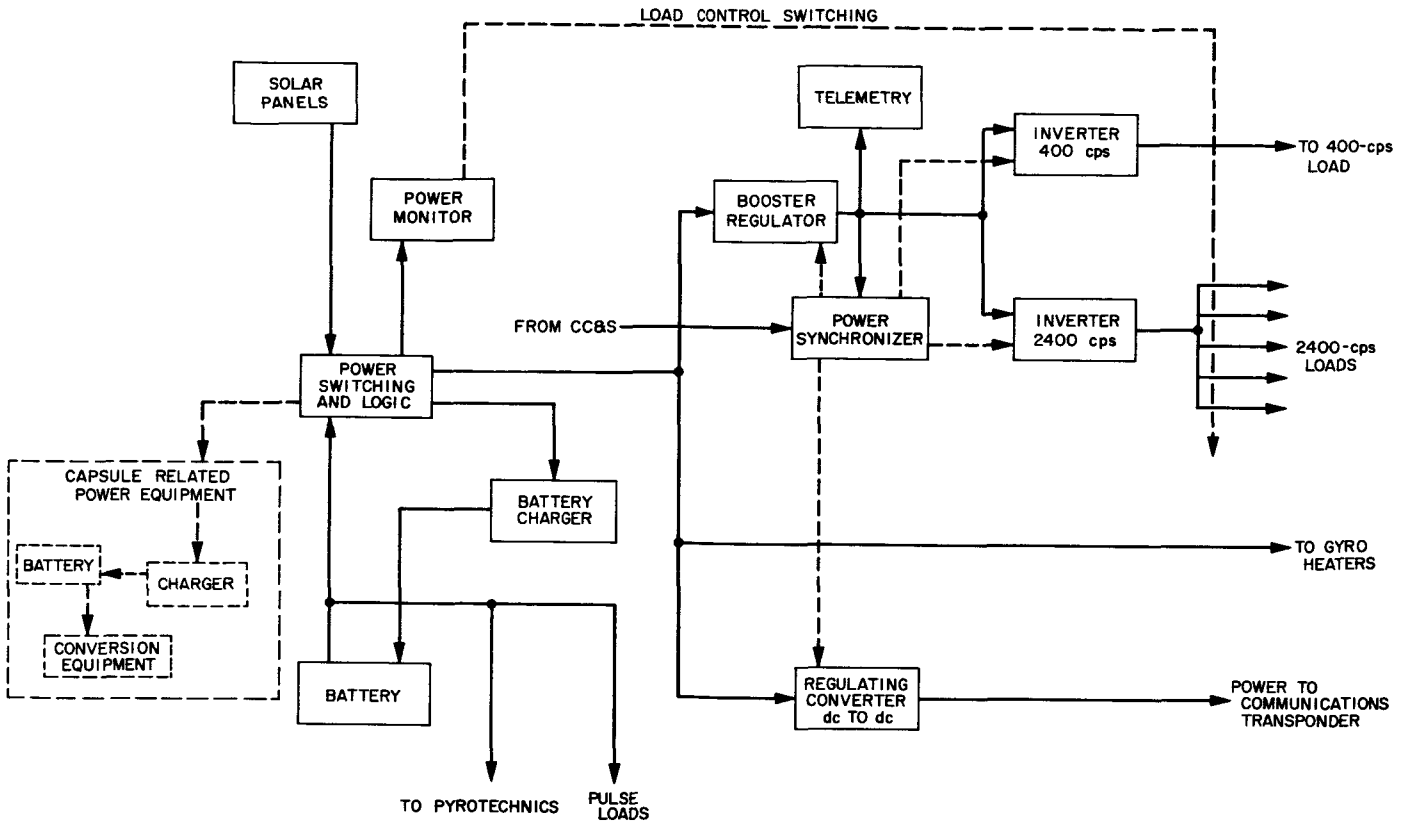

Figure 8. Tentative *Mariner* B power system

The proposed design for the 2400-cps inverters and the power synchronizer will be very similar to the *Mariner* A–*Mariner* R equipment. The majority of the power will be distributed on the 2400-cps, ac bus to the user's T–R units. Users requiring better than 5% regulation will add additional regulating circuits after the T–R units, but this must be kept to a minimum in order to have the required over-all system efficiency.

The transponder converter will be the only special dc-to-dc converter in the *Mariner* B power system. This approach was chosen for the transponder because of the special nature of the large amount of power needed by this user. The proposed communications equipment will require 40 w at 1800 v dc and 2 w at 1200 v dc. These must be regulated to better than 2% and contain less than 0.5-v ripple. In addition, there will be a special filament output of 5 w at 6 v and a low level output of 20 w at ±15 v dc. Special switching must be provided between the supply and alternate transponder equipment.

The estimated power requirements for the *Mariner* B system are given in Table 1. The table shows several cruise and maneuver flight sequences.

2. Solar Panels

Performance evaluation of solar cells for *Mariner* B application is being carried out. Temperature–intensity data on a test panel of 40 blue-sensitive silicon solar cells indicated a pronounced dependency of panel efficiency on solar intensity. To determine whether this effect was an inherent characteristic of silicon solar cells, the output of a number of single cells was measured at Table Mountain, California, for various intensities. Both P on N and N on P cells were tested. Figure 9a shows the typical efficiency–intensity characteristic of a blue-sensitive P on N silicon solar cell. The cell does exhibit a decrease in efficiency at lower intensities. The N on P solar cells exhibited the same type of characteristic, though not as pronounced. This dropoff in efficiency at lower intensities was primarily attributable to a decreasing maximum power point voltage as shown in Figure 9b. Also, shown in Figure 9b is the open circuit voltage as a function of intensity. The maximum power point voltage essentially followed the open circuit voltage characteristic except at higher intensities where series resistance effects cause divergence. The maximum power point current is shown in Figure 9c. The current is essentially a linear function

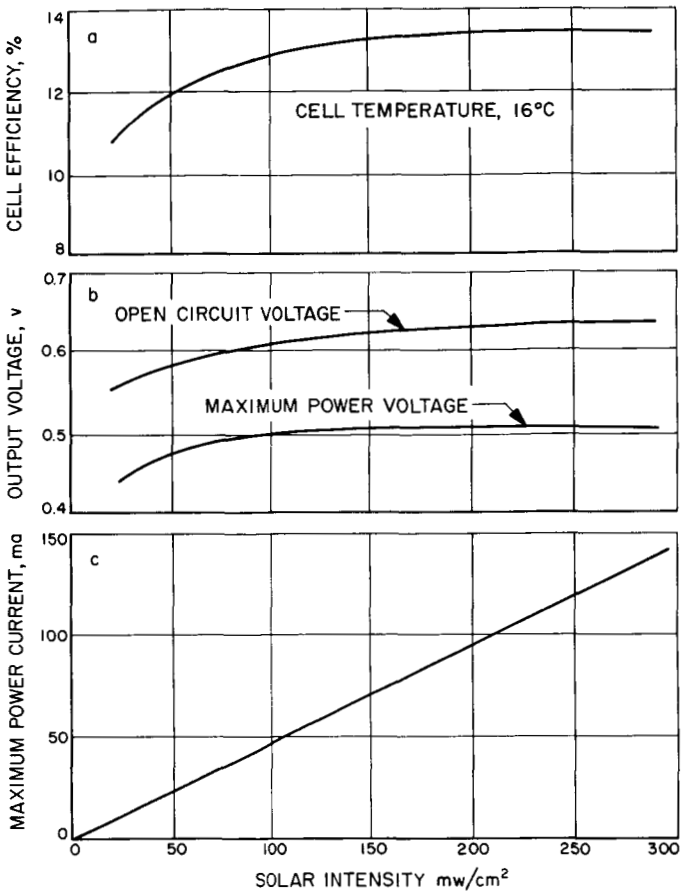

Figure 9. Blue-sensitive silicon solar cell characteristics as a function of solar intensity

of intensity. Additional experiments are to be performed to determine grid configuration, diffusion depth, cell type, and other parameters to optimize the Mars solar panels.

D. Supporting Activities

1. Electronic Component Reliability

a. Reliability program. The demand for ever-increasing reliability in spacecraft operation is developing a sensitivity to numbers and types of piece-parts used in the space programs. Of the many kinds of parts employed, electronic components or piece-parts are of particular concern due to their vast numbers and wide variety of types. For example, a recent survey conducted at JPL on *Mariner*-type spacecraft indicated the use of more than 9800 electronic components. The count was made up of the following basic classes of components: capacitors, connectors, diodes, relays, resistors, variable resistors, and transformers. This large population of electronic components was comprised of more than 240 types of devices.

The assembly of a large component part population, together with the required complex interconnecting wires and cables results in a severe reliability problem. Employment of the highest grade component obviously will help in the solution of such a problem. However, the use of a large number of part types almost always precludes the employment of only superior parts. The question of piece-part reliability in spacecraft programs depends, therefore, to a considerable extent upon the selection of the electronic components.

It has long been recognized that the commercial grade component is not satisfactory in its reliability characteristics. Further, it is well understood that a large number of the component manufacturers produce components of a better grade than the ordinary commercial variety. The *Preferred Parts List* (PPL) has been in use at this Laboratory for several years, serving as a guide to distinguish between the inferior or commercial grade component and the superior devices. The PPL is not a standards catalog detailing all aspects and characteristics of the given parts, but rather lists in brief form the recommended components. More detailed information on the components listed in the PPL must be supplied by the engineers utilizing the PPL. This information can be obtained from the component specialist engineers in the components group. Catalogs and other manufacturer information are also relied upon for these details.

The term *preferred* in its present concept or meaning indicates that the preferred component part has been qualified in at least four areas of environmental stress. These are vibration and shock, life, moisture, and temperature. It is felt that one or more of these environmental stresses will prove to be a critical environment for all types of electronic components of general interest. Space environments and their effects on component parameters will be included as a part of the *preferred* environments in the very near future. Because the PPL has evolved through several programs, all listed components have not yet been fully qualified to the listed environments. However, this situation is rapidly being remedied, with the result that a high percentage of all listed components will be qualified in the near future. In the interim period a component may be tentatively approved pending further tests.

There are two deficiencies in the preferred parts program. First, the preferred parts status is based on a sampling technique; therefore, only a statistical guarantee

can be given to the parts actually in use. Second, the preferred parts category does not require that components be serialized or identified. This negates any detailed followup of failure or other operational information.

Realizing that these deficiencies exist in the preferred parts endeavor, a Hi-Rel effort was initiated in the spring of 1961. Due to the magnitude of the Hi-Rel program, a limit was placed upon the number of parts that would be initially considered Hi-Rel components. Six categories of components were selected including capacitors, connectors, diodes, resistors, transformers, and transistors. In each of the categories, five individual types were selected, based upon the Laboratory use factor. These 30 types have been documented in a series of procurement specifications. The specifications were prepared as joint actions between the engineer or user at JPL, the component parts engineer at JPL, and the component vendor or representative. The documents detailed a 100% burn-in or screening technique in the quality assurance provision. This is to be done at the vendor's facility prior to component shipment. The documents also require that the components be serialized and that each component be accompanied by the appropriate IBM card bearing the burn-in or screening information.

The burn-in tests are repeated at JPL on a sampling basis. The size of the sample will vary, as deemed appropriate with the information gained through the sampling techniques. The information that is gained through the test efforts at JPL, significant to failure modes, is immediately sent to the vendor.

These tests include a short-time life cycle of from 168 to 240 hr. The data obtained from the JPL burn-in test must agree within close limits with the information delivered to this Laboratory on the IBM cards. This information is used for three main purposes. It provides a method: (1) for JPL and the appropriate vendor to become intimately correlated in measurement techniques, (2) of obtaining a much better understanding of the component operation and quality, and (3) of determining the quality of those items involved in the sample check at JPL.

The JPL component Hi-Rel program has been established to promote and increase component reliability through product improvement. Therefore, the Hi-Rel philosophy is designed and operated to the end that product improvement will take place through the combined efforts of this Laboratory and the vendor.

In conjunction with the Hi-Rel–preferred parts program, a drawing review effort is conducted. Drawings originating at JPL are reviewed with the PPL as criteria. The review is conducted early in the design phase of the equipment with the appropriate engineer being notified where component changes should be incorporated in the design. The drawing review is also used to determine use factor information on component parts. Components having unusually low use factors are given attention through special evaluation tests.

Every effort is being made to increase the scope of the Hi-Rel program so that all parts in any given project, where reliability is a prime consideration, are included. The term *preferred* will be expanded to mean not only that components have been evaluated, but that the component qualifies as a Hi-Rel device because of superior quality characteristics. This means that proper documentation, appropriate 100% tests at vendor's facilities, serialization of components, and adequate followup measures at JPL have been established on the devices. It was previously mentioned that at the present time only 30 types of components are included in the Hi-Rel program. This is a first phase effort and is soon to be expanded to include a second group of 30 components.

b. Supporting evaluation. A connector committee has been in operation for the past 2 months for the purpose of studying reliability of various interconnection techniques and connector problems. The committee is concerned primarily with spacecraft connectors; however, ground support equipment connectors are also covered where such would affect the reliability of the system.

The aims of the committee are to establish Laboratory standard methods, techniques, and connector types. Represented on the committee are specialists in packaging, cabling, quality assurance, reliability, and procurement, as well as representatives from the various divisions.

The scope of interest of the committee includes the following: (1) microminiature connectors, (2) miniature connectors, (3) removable contacts, (4) contact crimping (as opposed to soldering), (5) acceptable wire types and sizes, (6) connector potting and materials, (7) connectors for welded interconnects, (8) coaxial connectors, (9) termination techniques, and (10) specifications.

To date, the committee has initiated the following actions:

(1) Evaluation of Cannon's (Micro-D) microminiature connector. This connector is a smaller version (size reduction about 50%) of Series D.

(2) Evaluation of Microdot, Series 43 connector. This connector is a round multipin type and somewhat smaller than the Pygmy series. It is a hybrid type

in that it permits intermixing pins of different size and sex, and may include coaxial and standard contacts in the same connector. The contacts are removable and may be either soldered or crimped.

(3) Correction of discrepancies found in the Deutsch connectors which are being used in system cabling where space does not permit the use of a Pygmy type.

(4) Formation of a connector philosophy for *Mariner* B. Preliminary discussions indicate that, in general, existing practice will prevail. An innovation may be attempted in certain areas. This may consist of the use of the Cole ball-and-socket-type contact, where the reliability of the basic spacecraft is not jeopardized.

(5) Recommendation that potting of Series D connectors for future assemblies be eliminated. Potting has caused difficulties in the past due to the compound flowing into mating area and fouling the detent spring as well as reducing the floating action of the contact.

In addition to the connector activity, component evaluation has continued in several other areas, and complete documentation of the test results were disseminated to JPL.

References

1. Martz, E. P., Jr., *Astronomical Journal*, Vol 58, No. 1212, No. 8, p 221, February–December 1953.

2. R.C.A., *Ranger TV Mission Second Bi-Monthly Progress Report*, Radio Corporation of America, New York, N.Y., December 15, 1961.

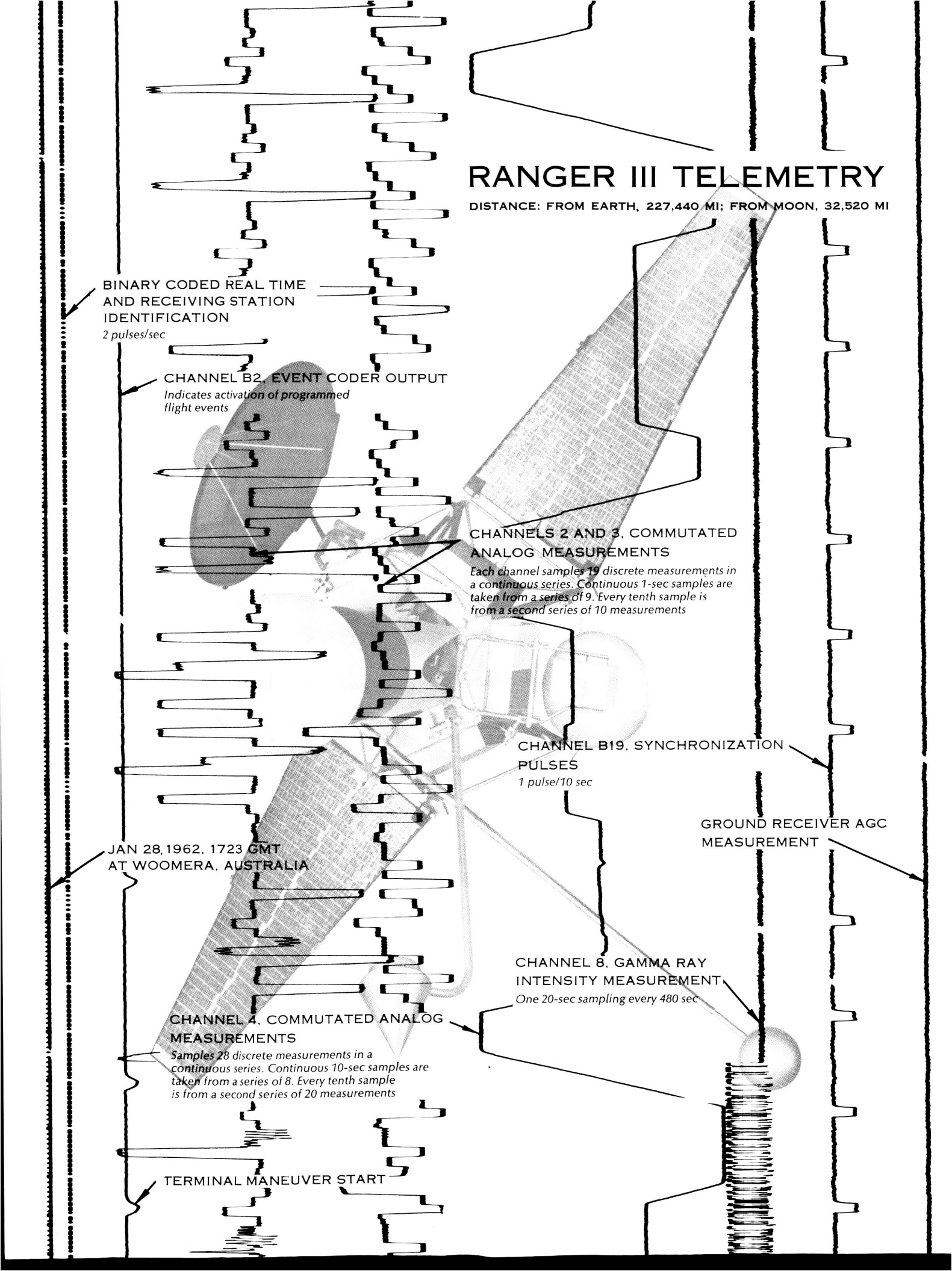
RANGER III TELEMETRY
DISTANCE: FROM EARTH, 227,440 MI; FROM MOON, 32,520 MI
BINARY CODED REAL TIME AND RECEIVING STATION IDENTIFICATION
2 pulses/sec
CHANNEL B2, EVENT CODER OUTPUT
Indicates activation of programmed flight events
CHANNELS 2 AND 3, COMMUTATED ANALOG MEASUREMENTS
Each channel samples 19 discrete measurements in a continuous series. Continuous 1-sec samples are taken from a series of 9. Every tenth sample is from a second series of 10 measurements
CHANNEL B19, SYNCHRONIZATION PULSES
1 pulse/10 sec
GROUND RECEIVER AGC MEASUREMENT
JAN 28, 1962, 1723 GMT AT WOOMERA, AUSTRALIA
CHANNEL 8, GAMMA RAY INTENSITY MEASUREMENT
One 20-sec sampling every 480 sec
CHANNEL 4, COMMUTATED ANALOG MEASUREMENTS
Samples 28 discrete measurements in a continuous series. Continuous 10-sec samples are taken from a series of 8. Every tenth sample is from a second series of 20 measurements
TERMINAL MANEUVER START

PART FOUR
DEEP SPACE INSTRUMENTATION FACILITY

All stations participated successfully in the launch of *Ranger III* on January 26, 1962. Excellent telemetry was received and the spacecraft responded correctly to commands up to the initiation of the terminal maneuver. Following this command, sent by the Goldstone Echo Station at 17:21 GMT on January 28, a spacecraft failure caused the strength of the transmitted signals to drop rapidly and become erratic. Unsuccessful efforts were made to correct this condition by sending various commands to the spacecraft. Loss of signals was complete by February 1.

Improvements in the DSIF facilities and capabilities are continuing. Recent equipment additions include parametric amplifiers, stable voltage controlled oscillators for generating the transmitter excitation frequency, and high power L-band antenna feeds. Also the Goldstone Echo Station site Az-El antenna is being replaced with a DSIF standard operational 85-ft HA-Dec antenna. The Az-El antenna is being moved to the high power transmitter site.

In preparation for the installation of new equipment, engineering development is proceeding on the design of: a wide beam tracking antenna which can be used as an aid in acquisition; ranging equipment for use with S-band receiving and transmitting equipment; a telemetry to teletype data encoder for the *Mariner* R project; high power L- and S-band diplexers to enable a single antenna to receive and transmit simultaneously; and prototype S-band RF subsystems.

An investigation into a periodic angular encoder error on the antenna at the Goldstone Echo Station site determined that the major portion of the error was caused by deformation in the flexible couplers between the angle resolver and the antenna shaft.

A design study is now underway to determine what structural modifications can be made to the 85-ft antennas to further improve their communication and tracking capability.

The recent results of DSIF supporting research and development are primarily in the following areas:

Ranging system. Equipment has been designed and constructed to demonstrate that extremely accurate range measurements can be made at interplanetary distances by transmitting and receiving a range code which can be synchronized rapidly and reliably. At planetary distances the code and carrier will be regenerated in the spacecraft transponder, while at lunar distances a simple turn-around transponder will be satisfactory.

Low noise systems. A very low noise system at 960 mc, which consists of a Cassegrain antenna feed system and a cavity-type maser preamplifier, has been developed and demonstrated.

A series of radiometric measurements have been made to measure the minimum absolute antenna temperature, the effect of elevation angle on antenna temperature, the temperature and position of several celestial radio sources which are potentially useful for antenna gain calibrations, and the temperature of extra atmospheric background noise.

Faraday polarization rotation measurements were made on *Ranger III*. A closed-cycle He refrigerator has been installed at Goldstone for evaluation purposes.

X-band communication components. Plans for antenna feeds at 8450 mc on 85-ft antennas indicate that antenna gains of 61.9 and 63.4 db for transmission and reception, respectively, can be obtained. A maser preamplifier has been ordered and a system of temperature instrumentation has been planned.

Advanced receiving techniques. A new high speed, high capacity autocorrelator has been designed and built which will measure the autocorrelation function in real time with an input signal.

A six-fold improvement in communication system capability is expected when a new large aperture, low noise antenna (which is now being designed) is available. As the result of extensive structural and environmental analyses, a specific design has been chosen which specifies a diameter of 210 ft and a f/D of 0.42. Servo and dynamic tests on the 85-ft antenna, servo simulator studies, site wind measurements and wind tunnel studies of different antenna models have been made in support of the detailed design.

I. Tracking Operations

A. Participation in *Ranger III*

DSIF participation for the *Ranger III* operation had begun by January 10, 1962. At this time checkout and preparation of the various station subsystems was in progress. A trailer containing equipment for recording video signals was located at the Goldstone Space Communications Station. Operational readiness tests involving the whole DSIF were conducted on January 16, 19, and 23. On January 24 the DSIF was ready for the *Ranger III* launch.

The DSIF was intended to provide several spacecraft communication capabilities during the *Ranger III* mission:

(1) All stations (Table 1) would have the capability of recording on magnetic tape telemetered information from the spacecraft; DSIF-3 and -5 also had equipment for encoding selected telemetry measurements into a teletype format for transmission to JPL for near real time analysis.

(2) All stations would provide tracking data consisting of time labeled pointing angles and doppler frequency.

(3) Transmitters at DSIF-1 and -3 would allow more accurate tracking data to be obtained by these stations being able to interrogate the spacecraft transponder; the transmitter at DSIF-3 would also allow desired spacecraft operations to be commanded from the ground.

(4) The receiver at DSIF-2 was equipped with a maser amplifier and a Cassegrain antenna feed system, and would provide this station with the most sensitive listening system in the DSIF for use during the capsule retro-maneuver.

Launch of the spacecraft occurred at 20:30 GMT on January 26; the DSIF experienced no difficulty in acquir-

Table 1. Identification of DSIF stations

Name	DSIF station
Mobile Tracking Station, Johannesburg	1
Goldstone Pioneer Station	2
Goldstone Echo Station	3
Woomera Tracking Station	4
Johannesburg Tracking Station	5

ing and tracking (Table 2) the vehicle. The spacecraft was initially acquired by DSIF-1 at 20:55 GMT and by DSIF-5 at 20:56 GMT. At this time the spacecraft was using the omni-antenna and the received signal strengths at DSIF-1 and -5 were approximately −114 and −104 dbm, respectively. At 21:50 GMT the signal strength at at DSIF-1 and -5 were approximately −114 and −104 DSIF-1 had decreased to −143 dbm so that the telemetry data could no longer be recovered. Shortly before, at approximately 21:27GMT,DSIF-4 acquired and continued tracking until 01:42:30 GMT on January 27 when the spacecraft passed below the station horizon. During this period the spacecraft signal levels were −146, −126 and −131 dbm at DSIF-1, -4 and -5, respectively.

After the initial acquisition DSIF-1 and -5 continued tracking until approximately 10:00 GMT on January 27 or about 1½ hr after acquisition at DSIF-2 and -3. DSIF-1 and -5, during their tracking periods, obtained tracking data and telemetry data. This data was used in determining the spacecraft orbit and evaluating the spacecraft performance.

Table 2. DSIF view periods

DSIF station	Acquisition, GMT	Lost, GMT
1	Jan 26/20:55:23	Jan 27/09:58:00
5	26/20:56:39	27/09:56:24
4	26/21:27:00	27/01:42:30
3	27/08:39:03	27/18:36:55
4	27/14:53:20	28/02:50:30
5	27/22:16:42	28/10:22:47
1	28/04:23:49	28/10:40:12
3	28/08:39:03	28/17:54:00
4	28/15:01:00	29/02:58:00
5	28/22:30:44	29/10:14:00
3	29/08:39:10	29/19:03:55
4	29/15:03:00	30/02:58:00
5	29/22:38:36	30/10:16:50
3	30/08:33:00	30/19:07:00
4	30/15:00:00	31/02:57:00
5	30/22:31:48	31/10:13:00
2	31/10:35:40	31/18:53:24
3	31/15:57:00	31/18:53:24
4	31/14:57:00	31/23:05:00[a]
5	31/23:45:22	Feb 1/09:32:00[a]
4	Feb 1/14:56:00[b]	1/23:00:00[b]
5	1/22:30:00[b]	2/10:00:00[b]
2	2/11:10:00[b]	2/12:00:00[b]

[a]Searching for spacecraft signal, very little data obtained.
[b]Acquisition attempts generally unsuccessful.

Approximately ½ hr after the spacecraft rose above the Goldstone horizon, while DSIF-1 and -5 were still tracking, a command was transmitted to the spacecraft to switch the transponder signal from the omni-antenna to the high gain antenna. This switchover caused an immediate increase in the received signal strength of about 18 db. This increase in signal strength was sufficient to allow DSIF-1 to again record telemetry information.

By the time the spacecraft was acquired at DSIF-2 and -3, it was apparent that: the orbit was nonstandard, the spacecraft would not hit the Moon and that the spacecraft would not pass close to the Moon during a Goldstone visibility period. This latter occurrence would preclude the possibility of obtaining TV pictures of the lunar surface.

It was determined that the corrective maneuver required to obtain a lunar impact was beyond the capability of the spacecraft. Therefore, a fly-by maneuver was decided upon and the necessary commands generated by the Space Flight Operations Center. These commands would insure that the spacecraft passed in the vicinity of the Moon during a Goldstone Station visibility period.

After the spacecraft signal was switched to the high gain antenna, preparation of the spacecraft for the mid-course maneuver began. The three stored commands defining the mid-course maneuver were transmitted at 1-min intervals. The first command was transmitted at 09:23 GMT and the last command was transmitted at 09:25 GMT. Successful reception of these commands was indicated by spacecraft telemetry. Prior to the transmission of the mid-course maneuver initiate command, one final preparatory command transmission was done. The antenna switchover command was transmitted at 09:55 GMT and caused the output of the transponder to be switched from the high gain (directional) antenna to the omni-antenna. This switchover dropped the received signal strength from −110 to −145 dbm, but it enabled communication to be maintained with the spacecraft during the attitude changes required for the mid-course maneuver.

The mid-course maneuver initiate command was transmitted from DSIF-3 at 10:00 GMT on January 27. Response of the spacecraft was detected immediately by a change in the type of telemetry being transmitted. DSIF-2 and -3 continued tracking the spacecraft during the maneuver until 10:15 GMT when DSIF-3 lost the signal; DSIF-2 lost lock 2½ min later. Both stations had reacquired the signal by 10:20 GMT, but the signal strengths were so low (−153 dbm at the DSIF-3 and

−160 dbm at the DSIF-2) that no telemetry data could be recovered. At 10:30 GMT the signal strength began increasing and by 10:40 GMT, all telemetry data was again being recorded. However, by this time, as scheduled in the maneuver sequence, the telemetry transmission mode had cycled to the cruise mode.

After reacquisition, DSIF-2 and -3 continued tracking with the received signal level of −145 dbm. At 11:37 GMT, after allowing the spacecraft to reacquire the Sun and Earth (to insure proper pointing of the high gain antenna), an antenna switchover command was transmitted to the spacecraft. This raised the signal level to −112 dbm. Shortly after the transmission of this command DSIF-2 conducted a search for the seismometer capsule signal. A signal at the capsule frequency was detected at −150 dbm. DSIF-2 received the capsule transmission until 13:11 GMT when tracking of the transponder signal was resumed.

The DSIF continued its tracking and telemetry recording program. DSIF-4 and then DSIF-5 each successfully acquired and tracked the spacecraft signal until it passed below their horizons.

Soon after DSIF-5 acquired the spacecraft DSIF-1 was also requested to track the spacecraft. DSIF-1 is normally not required to track after its initial view period; however, because a discrepancy was discovered in the post-mid-course doppler data from DSIF-3, it was necessary to reactivate DSIF-1. Aside from DSIF-3, DSIF-1 was the only station which had a transmitter and, therefore, was the only other station capable of providing doppler data of sufficient accuracy to allow an accurate post-maneuver orbit to be determined. The time of transmission of the terminal maneuver command could not be determined until an accurate post-maneuver orbit had been computed.

DSIF-1 first acquired the spacecraft signal at 04:23:49 GMT on January 28. At 04:47:31 GMT the spacecraft transponder acquired the DSIF-1 transmitter and the tracking system was locked in the two-way mode. The received signal strength held fairly steady at approximately −131 dbm. At 08:45 GMT two-way mode tracking was interrupted to allow the spacecraft transponder to acquire the Goldstone transmitter. At 08:49:09 GMT, after the Goldstone tracking system was locked in two-way doppler, the DSIF-1 resumed one-way mode tracking. At 10:40:12 GMT the spacecraft passed below the DSIF-1 horizon, and tracking was terminated.

After successful two-way acquisition by DSIF-3 at 08:47:03 GMT, both DSIF-2 and -3 tracked until lock was lost during the spacecraft terminal maneuver. Preparation for the terminal maneuver began with the transmission of the three required stored commands at approximately 1-min intervals starting at 16:29:41 GMT. The terminal-maneuver initiate command was transmitted from DSIF-3 at 17:21:39 GMT.The spacecraft began the terminal maneuver and received signal strengths held steady at −118 dbm at DSIF-3 and −111 dbm at DSIF-2. However, at 17:28:21 GMT the signal strength began decreasing and by 17:32:04 GMT both stations had lost lock. Reacquisition attempts were not immediately successful, but by 17:39:18 GMT both stations had reacquired. The signal strengths, however, had deteriorated and were fluctuating at both stations (−145 to −149 dbm at DSIF-2 and −149 to −153 dbm at DSIF-3).

This decrease in signal strength meant that receiving television pictures of the lunar surface was impossible. In an attempt to improve the signal from the spacecraft, several commands were sent from DSIF-3 (Table 3) but none had the effect of raising the signal strength. At 18:36:20 GMT, the spacecraft telemetry mode was commanded to the cruise mode, and attempts to retrieve any television pictures were conducted at all stations. DSIF-4 had been tracking the spacecraft since 15:01 GMT. Before the spacecraft passed below the Goldstone horizon at 18:52 GMT, a roll over-ride command was sent to the spacecraft. This command was sent at 18:37:50 GMT and disoriented the spacecraft from its terminal maneuver attitude and increased the signal strength slightly at DSIF-4.

After the unsuccessful terminal maneuver, the DSIF continued tracking the spacecraft. However, problems soon became apparent in the received signal. During the period following the terminal maneuver at 23:01 GMT, while DSIF-4 and DSIF-5 were tracking, the transponder signal disappeared. Momentary signals were heard by DSIF-4 until 23:28 GMT. After disappearance of the signal, the stations alternated periods of capsule tracking

Table 3. Sequence of commands transmitted to improve the received signal strength during terminal maneuver

Time	Action commanded
18:05:17	Switch transponder signal to omni-antenna
18:11:05	Switch transponder signal to high gain antenna
18:13:43	Change hinge angle of high gain antenna
18:17:00	Switch transponder signal to the omni-antenna
18:23:00	Switch transponder signal to the high gain antenna

with periods of searching for the transponder signal. The transponder signal was not acquired again until 05:34:18 GMT on January 29 after the spacecraft had set below the DSIF-4 horizon.

After reacquisition, the transponder signal had developed a periodic dropout condition; every 13 sec the spacecraft signal would disappear. This condition did not exist when the spacecraft was being tracked in the two-way mode.

Several additional attempts were made to command the spacecraft from Goldstone. On January 29, an attempt was made to initiate a maneuver by transmitting, using the mid-course maneuver command addresses, three stored commands and an initiate command. No response was observed. On the following day, January 30, the configuration of the Goldstone Station was modified to allow the transmitted power to be increased from 200 w to 7 kw. This modification required replacing the tracking feed with the transmitting feed and, therefore (without the tracking feed, auto tracking was no longer possible), both antennas were positioned using the coordinate converter computer. Many attempts were made to command the spacecraft; this effort culminated in the transmission of 211 commands (alternate roll over-ride and telemetry mode change commands). These command attempts produced no spacecraft reaction. On the following day, January 31, 20 antenna switchover commands were transmitted. The modulation frequency was varied for these commands but no response was obtained from the spacecraft. At the conclusion of the tracking period on January 31, DSIF-3 ceased participation in the *Ranger III* operation.

In the interim between tracking periods at DSIF-2 and -3, DSIF-4 and -5 continued tracking. Signal strengths were approximately -130 to -140 dbm. During the final tracking period at DSIF-3, the condition of the spacecraft signal was deteriorating. The average level was -140 dbm, but there was a continual variation ± 20 db about this average. By the time DSIF-4 acquired on February 1, only momentary locks of 1-min duration were possible. At this time the stations began alternately searching, for ½-hr periods, for either the seismometer capsule signal or the transponder signal. At this time only momentary locks were being obtained. DSIF-2 and -5 were then instructed to secure. DSIF-4 continued attempting signal acquisition at weekly intervals and, to this date, has had only minimal success.

II. Facilities and Capabilities

A. New Equipment

1. Parametric Amplifier

Phase I of the DSIF 960–2295-mc parametric amplifier (paramp) subsystem was initiated in April 1961, and resulted in fabrication and complete tests of a prototype paramp subsystem. Basic desired paramp characteristics were outlined in *SPS 37-10* and *SPS 37-11*. Phase I was essentially completed in September 1961, after systems tests at Goldstone Pioneer Site and environmental tests at Hughes Aircraft Company (HAC). Prototype test results led to redesign of the system in several areas. The most significant improvements were in the areas of moisture sealing, noise couplers, klystron power supply, RF connectors, temperature control power supply, and vibration tolerance. All significant specifications were met or exceeded.

Phase II of the procurement resulted in the fabrication of four paramp subsystems, three complete spare paramp assemblies and paramp power source assemblies, selected module and component spares, module and component test equipment, and complete manufacturing type documentation. Phase II was initiated in September 1961, and was essentially complete in February 1962.

Installation of the paramp subsystem at all three DSIF stations was completed by the launching of *Ranger III*. The Woomera Station installation was completed on January 2, 1962, the Johannesburg Station installation on January 16, 1962, and the Goldstone Station installation on January 8, 1962.

a. System integration. The paramp subsystem is employed in two separate configurations in the DSIF (Fig 1). The first is the normal mode as a low-noise amplifier in the reference channel of the Goldstone Duplicate Standard (GSDS) 960-mc phase lock receiver. The second is as a follow-in amplifier for the 960-mc cavity maser. The DSIF intends to utilize high gain traveling-wave masers at 2295 mc so that use of the paramp as a follow-on amplifier will not be required.

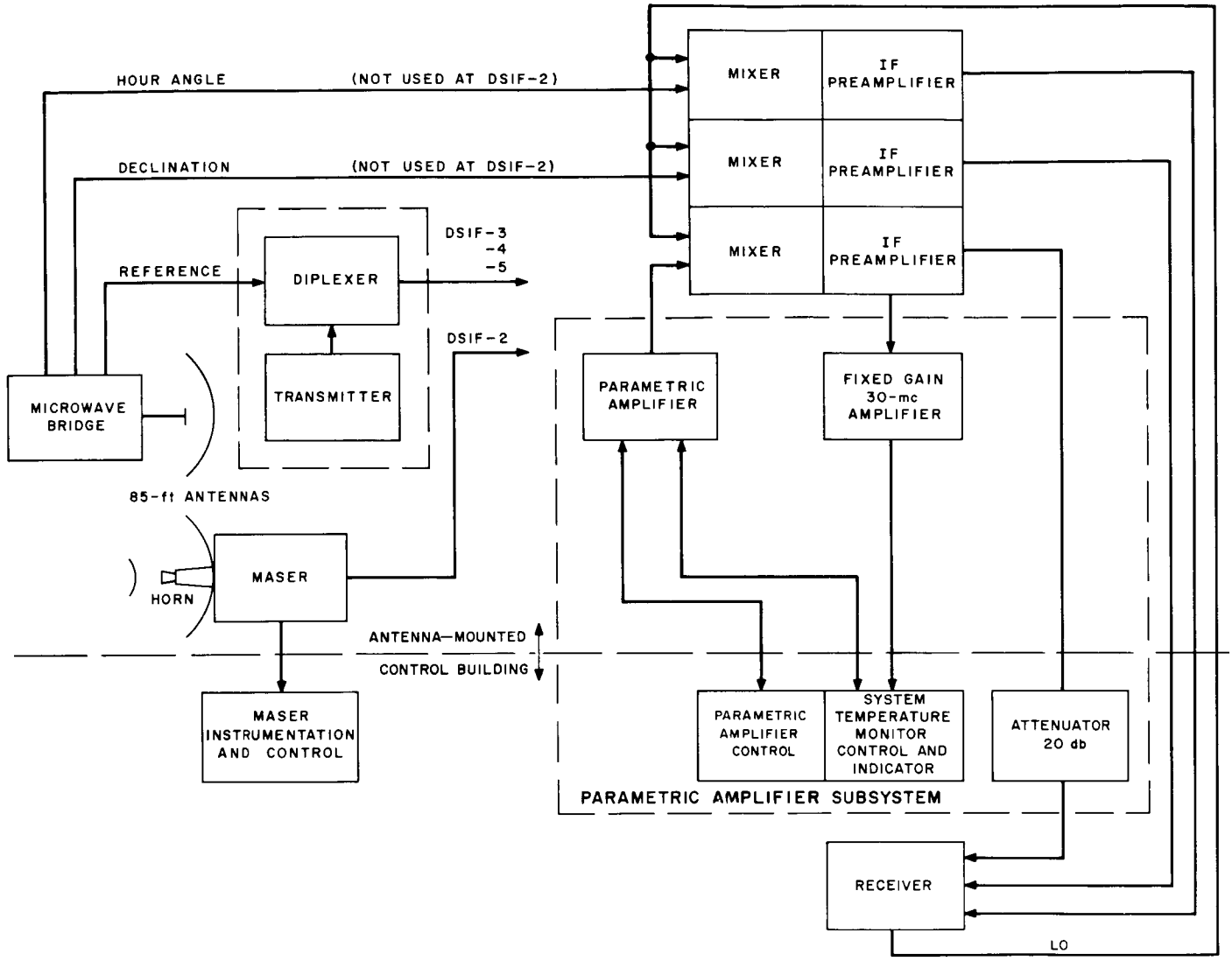

Figure 1. Parametric amplifier installation

The paramp subsystem is designed for installation in the 85-ft HA-Dec antenna system; however, it is adaptable to other configurations (Fig 2). The paramp assembly can be located on the quadripod apex, in the Cassegrain structure, or in the antenna cage. The paramp power source assembly (Fig 3) is located either in the antenna cage or in the Cassegrain structure. The paramp assembly can be located up to 60 ft from the paramp power source assembly. Cables from the paramp power source assembly to the console control assembly (in the control room) are approximately 400 ft long. The paramp can be operated in a diplexed or listening only mode.

Modification or special testing of DSIF equipment was required as follows:

(1) The Collins 30-mc preamplifier was modified to add a noise amplifier that was not AGC controlled. There was no change in the preamplifier gain or bandwidth.

(2) Because of the 20-db gain of the paramp, the reference channel level had to be decreased by 20 db so that receiver AGC gain tracking could be maintained in the angle channels. A 20-db pad that can be switched in or out as desired was inserted in the 455-kc IF amplifier.

(3) The effect of spurious frequencies or high power klystron noise resulting from diplexing with a 10-kw transmitter operating at 890 mc was an unknown

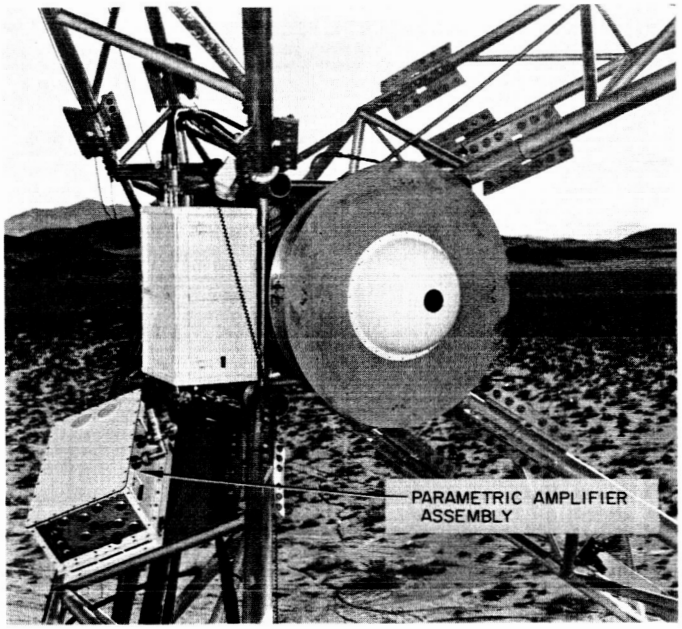

Figure 2. Parametric amplifier mounted at the apex of the Echo Station antenna

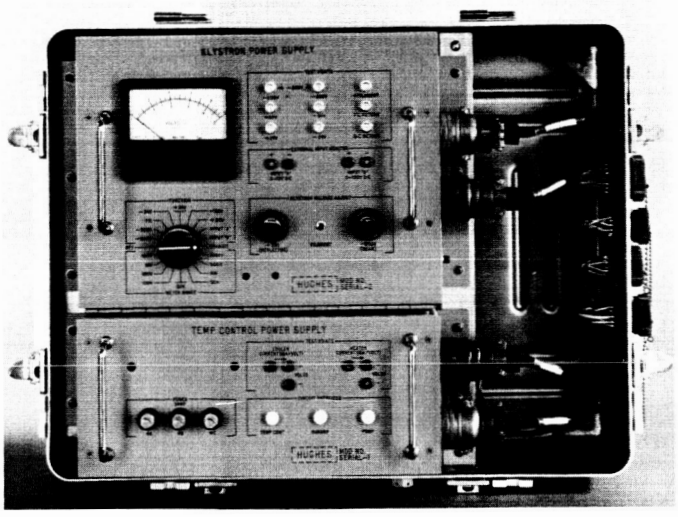

Figure 3. Parametric amplifier power supply assembly

and had to be determined. A further consideration was the contribution of the diplexer, line-loss, antenna feed, etc., to indicated system temperature. No quantitative tests were performed to detect small differences from expected values since the system temperature monitor was used as the detector (accuracy ±20°K). However, there was general agreement with expected values in the following areas: (a) antenna temperature (Collins feed), 30°K; (b) Moon temperature, 30°K (drift test); (c) horizon temperature, 150°K; (d) Sun temperature, 5000°K; (e) 10-kw diplexer insertion temperature, 20°K; and (f) 200-w diplexer insertion temperature, 70°K.

System temperatures as low as 120°K have been achieved at 960 mc using a Collins tracking feed, with 3 ft of ⅞-in. heliax feeding the paramp, and looking into a cold sky.

At the Echo Station, interference tests were conducted on the prototype model by inserting at the input spurious signals consisting of various combinations of the sum and difference frequencies of the transmitter, receiver LO, pump, and receiver frequencies. No interference was noted. However, when operated simultaneously with 200 w of radiated power, interference on the pump power monitor line was observed. This was due to rectification of 890-mc leakage on the pump power monitor diode and was eliminated by inserting a low pass filter in the pump power monitor diode output line. No transmitters were operating at the stations with HA-Dec antennas so comparisons were not possible at these sites. However, the paramp assembly location on the HA-Dec antennas is better isolated from the primary pattern of the feed and no further interference problems are anticipated.

The 2295-mc paramp was tested at HAC only. It is operationally ready to be connected to an S-band receiver and it is necessary only to switch the pump to the S-band paramp by activating the waveguide switch.

There was some concern of the effect of differential phase shift between the reference and angle channels as a function of paramp gain and paramp on–off conditions. In one sense a paramp acts like a voltage-controlled phase shifter and its phase shift is a function of both pump power and bias voltage. It was found that during normal operation, the stability of both of these quantities resulted in no perceptible phase shift, but when the pump was turned off, approximately 40- to 80-deg phase shift resulted, depending on the varactor used and paramp adjustments. Thus, it was found necessary to change the reference phase to the angle channels if angle tracking is required when the paramp pump is turned off.

One of the major installation problems was ground loop noise. In some cases, 3 to 5 v of noise, etc., appeared between different points of the same grounded line. Judicious grounding and shielding, coupled with much patience were required to eliminate this problem.

The paramp system was designed for minimal adjustments under operational conditions. The normal daily checks during a mission consist of checking the gain and logging the system temperature. This requires about

5 min. The paramp system which was sent to Woomera was adjusted prior to shipment and required no further adjustments when it was installed and turned on. Although adjustments were made to familiarize the station personnel, the system temperature has remained within 5 to 10 deg of 130°K over a period of about 45 days without further adjustments. During this same time the gain has remained within 1 db of the original setting of 20 db.

b. Parametric amplifier characteristics. The parametric amplifier type employed is a nondegenerate three-frequency type. The pump is switched, as desired, to operate either the S- or the L-band paramp unit, one located on the lower left side and the other on the upper right side. A block diagram of the paramp is shown in Figure 4.

The SDI-11-5 linearly graded point contact silicon p-m junction varactor diode is utilized. Typical characteristics are as follows:

Cutoff at zero bias, 35 to 50 Gc

C_0 (static capacity), 0.7 to 0.9 pf

R_s (spreading resistance), $\approx$5 ohms (measured at 1000 mc)

The diodes for the JPL paramp are designated with a "d" after the serial number. This "d" specifies that the diodes meet the voltage current specification which result in the lowest noise figures.

It is interesting to note that the best diodes, once the cutoff frequency has been determined as adequate and that C_0 was in the proper range, could be selected with a Simpson 260 volt–ohm meter by measuring diodes forward resistance on the low ohm scale. Values measured below 20 ohms exhibited a direct relationship between forward resistance and noise figure. The diode supplier agreed to furnish diodes to operate in the JPL paramp to the following specifications:

Specification	L-band	S-band
Required noise figure (measured per AIL Mod 70 hot–cold load), db	1.6	1.85
Required pump power (±3 db) at 17.4 Gc, mw	20	40
Required gain stability ratio (at 20-db insertion gain)		
$\frac{\Delta \text{ Parametric amplifier gain}}{\Delta \text{ Pump power}}$	<10	<10

Over 40 diodes were procured but about one-half the diodes originally furnished would not meet the requirements and were rejected.

The lowest noise figure measured for the L-band paramp was 1.1 ±0.2 db and 1.5 ±0.2 db for S-band. These correspond to T_e of 85 and 125°K, respectively. These figures include the coupler, circulator, and paramp only, from the input ⅞-in. EIA flange through the output ⅞-in. flange. Additional mixer contribution is approximately 15°K. The L- and S-band circulator insertion loss is approximately 0.2 db; however, one L-band circulator was measured at 0.06 db. Input–output isolation of better than 40 db was achieved through the use of a two-circulator combination. At 20-db insertion gain of the paramp (cold loss is $\approx$2.5 db), the input VSWR is less than 1.5. The $G^{1/2}$ bandwidth product is 150 mc for the L-band paramp and 250 mc for the S-band paramp (at 20-db gain). Insertion gains above 40 db have been measured, and appear relatively stable (±3 db) over a ½-hr period.

The system gain stability at 20-db insertion gain (22.5-db electronic gain) was measured as ±0.1 db over a 12-hr period at room temperature. With external ambient variation from −23 to 55°C, the gain stability is ±0.3 db. High frequency gain stability is greater than 0.1 db and variations consist mainly of 400-cps noise. If the pump normalizer loop was opened and the pump power manually controlled, the high frequency gain variation was not measurable with the equipment used (0.01 db threshold). The RF assembly removed from the temperature controlled assembly is shown in Figure 5. The complete paramp assembly with cover removed is shown in Figure 6. The paramp assembly with front access panel removed is shown in Figure 7.

c. Pump circuit. A Varian VA240 reflex klystron is utilized as the pump source. Using the main heat diffuser plate as a heat sink, it is maintained at 30 ± 1°C. Table 1 lists the average characteristics of the pump klystron.

A Raytheon SOU 283 two-cavity klystron was also evaluated as a pump source. It has a slightly higher power dissipation than the VA 240, but can be used interchangeably as the paramp pump, with the exception that the SOU 283 does not require a reflector supply.

In view of the critical performance requirements for pump frequency and for pump power stability (at 20-db gain, a 0.1-db change in pump power results in approximately 1 db of paramp gain change), the pump power is normalized in a regulating loop and controlled with a ferrite attenuator. A precisely regulated power supply

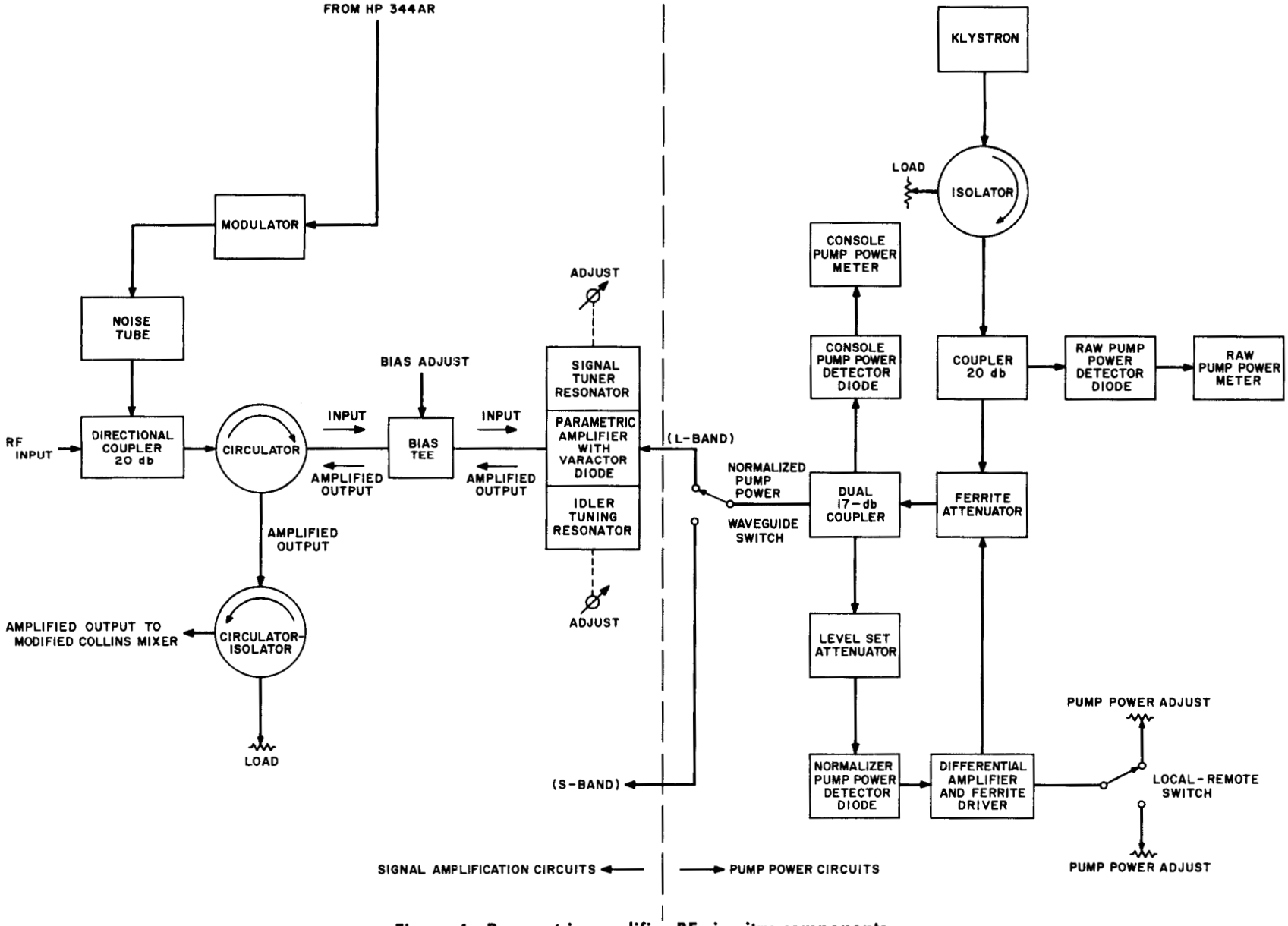

Figure 4. Parametric amplifier RF circuitry components

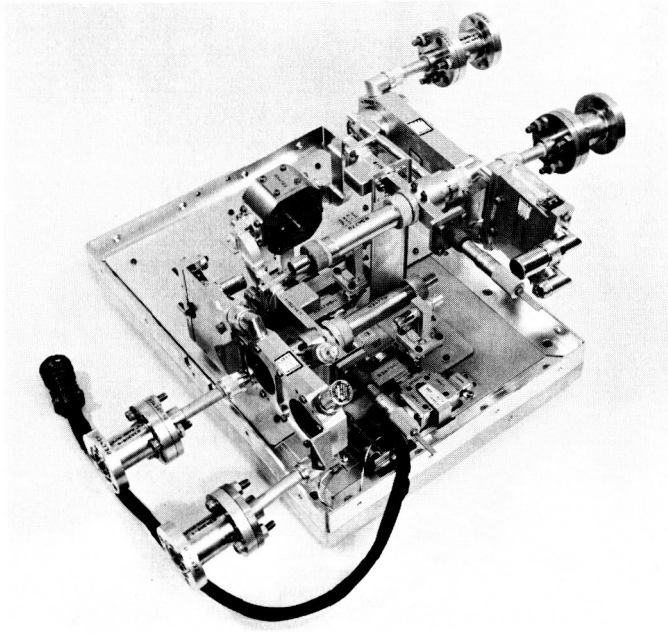

Figure 5. Parametric amplifier assembly with cover removed

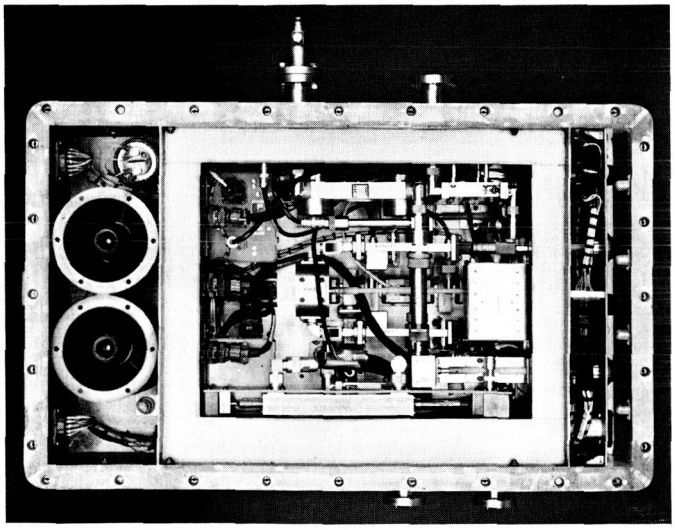

Figure 6. Parametric amplifier

is used to provide system reference voltages and klystron voltages. The power supply is completely solid state, and critical components are temperature-stabilized at 70°C. Beam, reflector, bias, and reference voltages are stable within 0.03% from −23 to 55°C. The long term pump stability (over 24 hr) is better than ±0.03 db.

d. System temperature monitor. To provide a qualitative system performance indication, the parametric amplifier subsystem incorporates a system temperature monitoring capability. A modified Hewlett-Packard HP 344AR automatic noise-figure meter, a HP 78AE noise

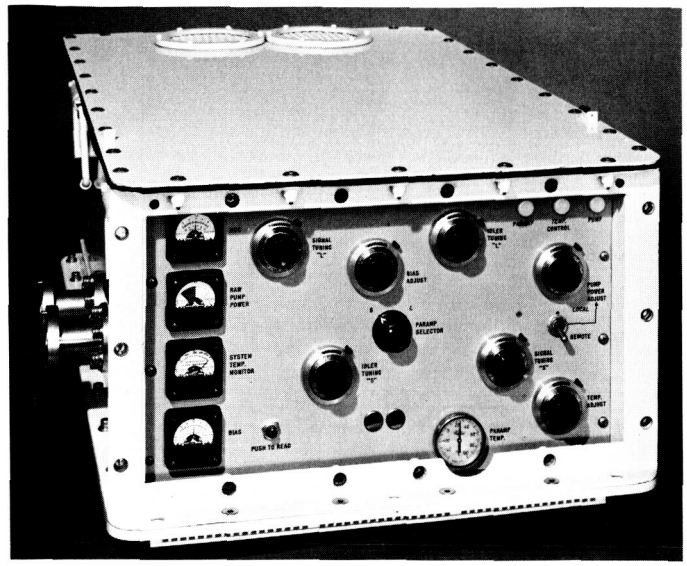

Figure 7. Parametric amplifier assembly with front access panel removed

tube modulator, and a HP 349AR UHF coaxial argon noise source are used in the measurement system. A directional coupler at the input of the paramp injects 96°K noise pulses into the paramp. The noise measurement system compares the noise pulse power plus system noise power with the system noise power and maintains the former at constant output amplitude with an AGC system. The difference between these two values is displayed on a meter calibrated in degrees Kelvin. The indicated accuracy of this system at 200 is ±20°K.

During calibration of the prototype system temperature monitor with a hot-cold load (373 and 77°K), it was found that the excess temperature of the Bendix noise tube Model TD72 in the HP 349AR coaxial source was 0.6 to 0.8 db higher than the published value of 15.2 db. Complete tests were conducted on several similar sources

Table 1. VA 240 klystron characteristics

Parameter	Value
Frequency, Gc	17.4
Power output (50 Ω), mw	150
Temperature coefficient, kc/°C	100
V_{beam}, v	620
V_{refl}, v	230
V_f, v	5.7
I_{beam}, ma	20
Total power dissipated, w	18
Modulation sensitivity, mc/v	1.2
Life, hr	1000

and modulators with the result that the average measured value at 2295 mc was 15.8 db and at 960 mc was 16.0 db. The noise couplers were adjusted to compensate for this apparent excess output.

Measurement of system temperature in the DSIF receiver is possible during phase lock from −120 to −162 dbm (threshold) without disturbing either the system temperature measurement or the system threshold. Signal power exceeding −120 dbm at the paramp input results in system temperatures in excess of those existing.

e. Parametric amplifier temperature control. The parametric amplifier assembly is maintained at a constant temperature of 30 ±1°C. The unit has been tested at external ambients from −23 to 55°C and has performed within specification. Typical pull-down or stabilization time is 1 hr under the most extreme case at 55°C. The temperature control system utilizes a heater blanket mounted on a heat diffuser plate for heating, and bismuth-telluride p-n junction heat pump modules for cooling. Maximum heater power is 270 w. Maximum heat pump capacity at a hot junction temperature of 65°C and a cold junction temperature of 20°C is 75 w with an input power of 350 w. A blower-heat exchange combination is used to reject heat during operation. During 55°C pull-down, the heat exchanger is required to remove about 450 w. At steady-state at 55°C ambient, about 250 w are continuously removed. The peltier cooling modules utilized are built by HAC and can maintain a 90°C ΔT in vacuum at an optimum current of 15 amp with cold junction at 15°C. Heat leakage through the walls of the paramp assembly is less than 1 w/°C. Special thin wall stainless steel heat barrier coaxial lines were fabricated for input–output connections. Total dissipation of the electronics within the temperature-controlled chamber is less than 35 w.

f. Results of tests. One of the prime considerations in development of the paramp subsystem was that it not require daily or even weekly adjustment, and that it be maintainable in the field. Besides the conduct of technical systematic tests, evaluation of the degree to which these two requirements were met received the greatest emphasis during prototype testing.

Environmental testing of the paramp subsystem included the following:

(1) Temperature testing within −23 to 55°C.

(2) Leakage tests in simulated driving rain.

(3) Vibration tests at 1 *g* from 5 to 400 cps.

(4) Humidity tests at 39°C from 5 to 95% relative.

(5) Altitude tests from sea level to 10,000 ft.

(6) Operation in any position.

Results of testing the prototype model uncovered problems in the following areas which have been subsequently corrected:

Gain stability with temperature. Over the temperature range from 55 to −23°C the paramp gain varied from 23.5 to 18.5 db (Fig 8). This gain drift was attributed to klystron reflector voltage drift and consequent frequency shift (pump amplitude remained essentially constant). Drift was reduced to acceptable values by replacing several temperature sensitive resistors in the klystron power supply with compensating types. The total gain change after this fix was from 20.2 to 19.6 db through the same temperature range over a 5-hr period. Klystron power supply voltages now are stable to better than 0.03% from −23 to 55°C.

Vibration testing. The most significant result of vibration testing was that mechanical strengthening of various components was shown to be necessary. Bracketry and lock nuts were added in several cases. No deleterious electrical effects of vibration were encountered.

Leakage testing. One of the more significant problems encountered was water leakage into the paramp assembly and the paramp power source assembly during heavy rain. The majority of the leakage stemmed from enclosure breathing when cycled between off–on conditions (hot–cold) and from insufficient sealing around the heat exchanger blowers. Fixes have been incorporated and units are undergoing operational field environmental testing.

Testing of parametric amplifier characteristics with various diodes. The paramp was tested with diodes of

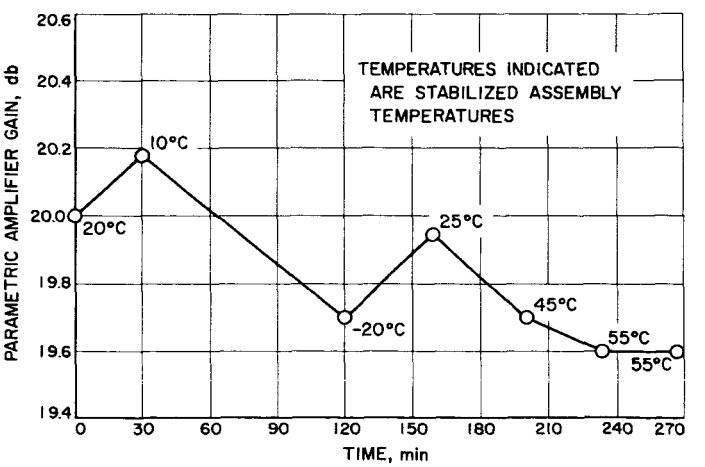

Figure 8. Gain stability vs temperature

various types. Gallium-arsenide, silver-bonded germanium, and silicon diodes were tested. The SDI-11-5 linearly-graded point contact diode appeared to have the best gain stability, noise figure, and ease-of-adjustment characteristics in the paramp, and was selected. Time limitations prevented an exhaustive study of all manufacturers' types. After the SDI-11-5 was selected, an attempt was made to determine standard measureable characteristics so that it could be given a model number. However, selection by proper operation in the paramp was still shown to be required, and at least one-half of the diodes supplied were rejected. See Table 2 for a listing of various parameters of the same type diode and the indicated performance.

Klystron tests. The VA 240 klystron supplied by Varian was subjected to frequency and amplitude stability tests. While stabilized at 20°C (heat sink), and with precision voltages applied, frequency shift was less than 10 kc at 17.4 Gc over a 1-hr period. Output amplitude stability is such that during periods of operation of 12 hr or less, use of the power normalizer circuitry is not required to meet permissible paramp gain variations of ±1 db.

Phase shift and pump power sensitivity tests. Figure 9 indicates the results of phase shift and gain sensitivity tests of the paramp as the pump power is varied.

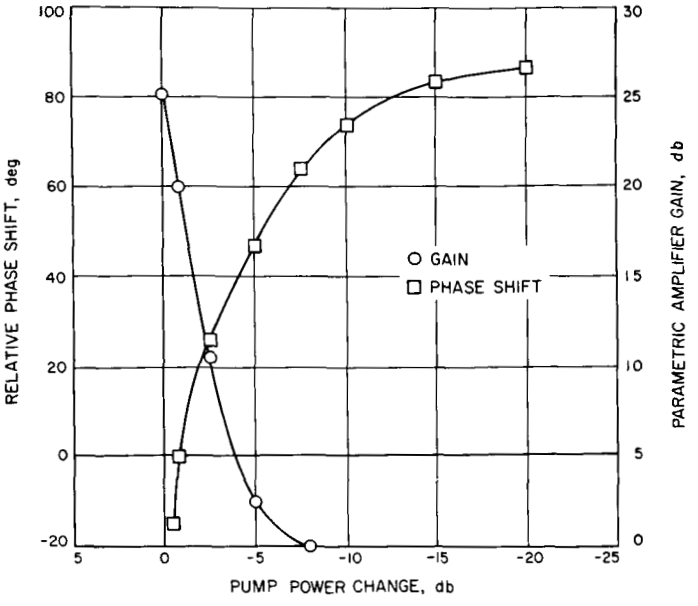

Figure 9. Phase shift and gain sensitivity vs pump power variations

RF threshold tests. Figure 10 illustrates a threshold test made in conjunction with the GSDS 960-mc receiver at 20-cps noise bandwidth. The signal generator used for this test was Motorola Serial 5 test transponder, which

Table 2. Prototype test results of typical SDI-11-5 silicon diodes

Diode	T_e, °k	Forward resistance at 1v, Ω	Pump power at 20 db, mw	Pump power for oscillator, mw	15 min gain stability, db	Time for tuning, min	Bias voltage	C_0, pf
556	180	22	18	21	0.2	15	—	0.82
29	200	19	23	29	0.3	30	—	0.93
110	140[a]	180	27	31		10	—	0.96
440	340	28	13	15	±0.3 (very noisy)	10	—	0.74
554	—	22	—	—	—	—	—	0.75
557	170	21	74	—	±0.1 (very quiet)	15	—	0.84
582	230	29	21	25	±0.5 (noisy)	15	—	0.72
586	—	17.5	<5	<5	—	30	−0.1	0.71
587	260	21	7	9	±0.3 (noisy)	20	−0.5	0.74
590	135[a]	16	22	25	−0.2	15	−0.1	0.89
592	325	38	27	33	±0.15	15	−0.5	0.74
593	350	24	33	34	>1	20	0.1	0.86
594	210	24	20	22	±0.3	15	−0.1	0.75
678	160	20	27	30	±0.15 (quiet)	10	−0.1	0.86
679	170	19	23	27	±0.1 (quiet)	10	−0.05	0.84

[a]Current–voltage characteristics duplicated and formed basis for ordering the production diodes.

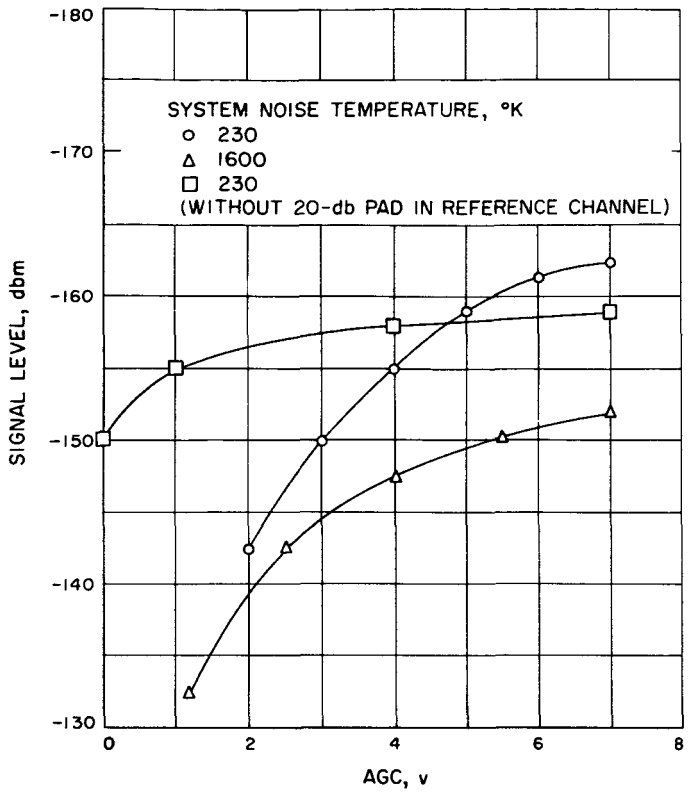

Figure 10. RF threshold test with and without the parametric amplifier

is accurate to ±2 db. Threshold tests were also conducted with the 20-db gain pad omitted from the reference channel and resulted in the rather sharp threshold AGC characteristic curve.

Angle jitter tests. Since the reference channel has about a 10-db improvement in signal to noise ratio, the angle channels noise spectral density degrades by 10 db at the new threshold. Figure 11 illustrates the rms angle jitter degrading by a factor of three at threshold. This is to be expected as the angle variance, $\sigma^2 = 2B_L\Phi$, where $2B_L$ is the noise bandwidth and Φ the noise spectral power density. It is also to be noted that there is a net improvement of 0.01 deg at −150 dbm. This is probably a result of less amplitude and phase noise in the reference channel.

Noise figure accuracy tests. Particular care was taken to ensure proper calibration of the system temperature monitor equipment. An AIL Model 70 hot–cold load was employed as the calibration standard. Its performance was also checked against another Model 70 and a cold load designed by HAC. The Y-factor measurement method using an AIL 132 receiver was employed for all noise figure measurements. Discrepancies noted in commercial noise tubes are described elsewhere in this report.

Pump power stabilization ratio. A nominal amplitude 20-db stabilization ratio was measured through the pump power normalizer circuit. With a 3-db input change, the output change was less than 1%.

Diplexed operation tests. Operational configuration of the paramp involves diplexing with a 10-kw CW transmitter at 890 mc. Results of preliminary tests indicate little or no effect on system noise temperature; however, additional tests will be conducted and reported on in a later *SPS* as the present tests are not conclusive.

g. Maintenance considerations. The design-goal mean time before failure for the paramp subsystem was nominally 1 year not including the klystron. In view of this requirement the equipment was designed almost completely using solid-state electronic techniques. The two exceptions are the klystron and the 30-mc noise amplifier.

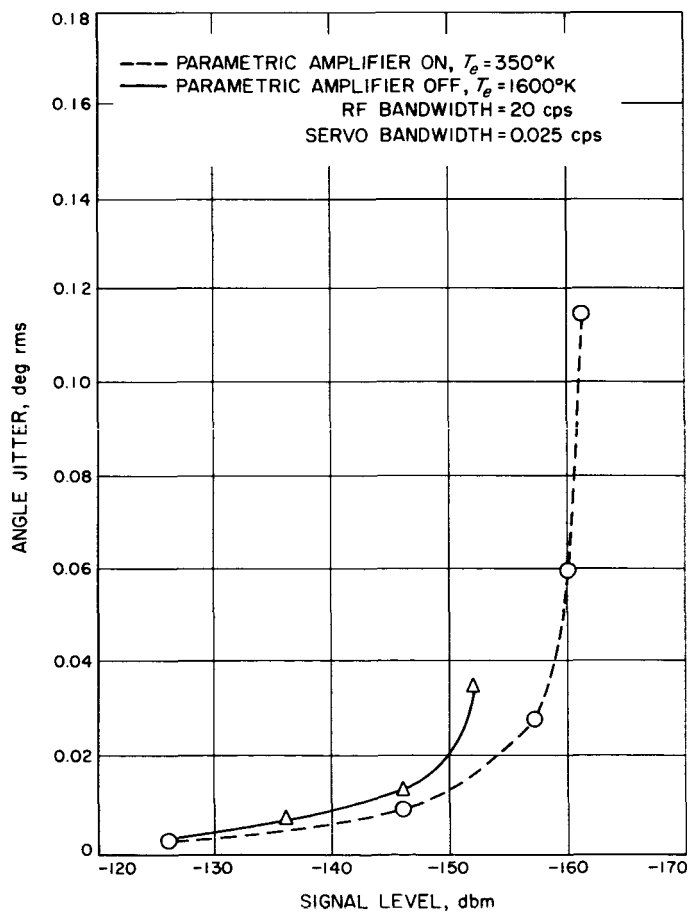

Figure 11. Angle jitter (rms) vs signal level in the declination channel with the parametric amplifier in the reference channel

With an accumulation of some 2000 operational hr among four paramp subsystems only one failure has occurred; that was a VA 240 klystron (which failed at 1100 hr).

Three levels of spares were supplied with the paramp subsystem, complete assembly spares (paramp assembly, paramp power source assembly, and system temperature monitor), module spares (klystron power supply, dc amplifiers, noise tube modulator, etc.) and component spares (varactors, power diodes, paramp cavities, klystrons, etc.). The purpose of providing assembly spares is to allow immediate replacement of a failed unit without trouble shooting to determine the module failure. A module tester is being supplied to assist in determining the failed module and will test input-output for each of the seven major modules. It will be described in future *SPS*. It is hoped that all module replacement can be accomplished in the field and that failed modules and components will be forwarded to the Goldstone maintenance depot or the manufacturer for repair.

Documentation supplied with the paramp subsystem includes complete manufacturing drawings, specifications, and procedures and also includes an operation and maintenance manual for field use.

2. *Very Stable Oscillator*

In order to provide sufficiently accurate doppler data for *Ranger III*, it was necessary to increase the stability of the DSIF-1 and -3 transmitter control oscillators from 10^{-6} to 10^{-8}. The short time from recognition of the problem to the start of the countdown proceedings precluded the complete development of an oscillator with this stability capability. Resdel Engineering Company of Pasadena had as a shelf item an oscillator which would provide the required stability, and also had a basic design similar to units which had been developed at JPL.

Six of these oscillators were ordered and two were received and tested in time for the *Ranger III* operation. One was used at the Mobile Tracking Station and the other at the Goldstone Echo Station. The Resdel oscillators are housed in a thermistor controlled oven which has a minimum stabilization factor of 0.005 deg/deg. The housing of the Resdel oscillator, however, did not provide the radio frequency interference (RFI) shielding required of GSDS equipment. An RFI tight housing was designed for the oscillator assembly, along with a zener regulator circuit, a bias adjustment circuit, and a power line filter (Figs 12 and 13). A switching capability is also being incorporated so that any oscillator can be remotely selected.

These six units will be distributed throughout the DSIF with two units at each transmitter site (DSIF-1, -3, and -5). The first two units received each have a long term stability of better than 10^{-8}, a short term stability of 10^{-8}, and a reasonably low noise component (less than 5 deg peak-to-peak phase jitter after $\times 30$ multiplication). The remaining four units have been received and are being tested for stability at Goldstone; data is not yet available.

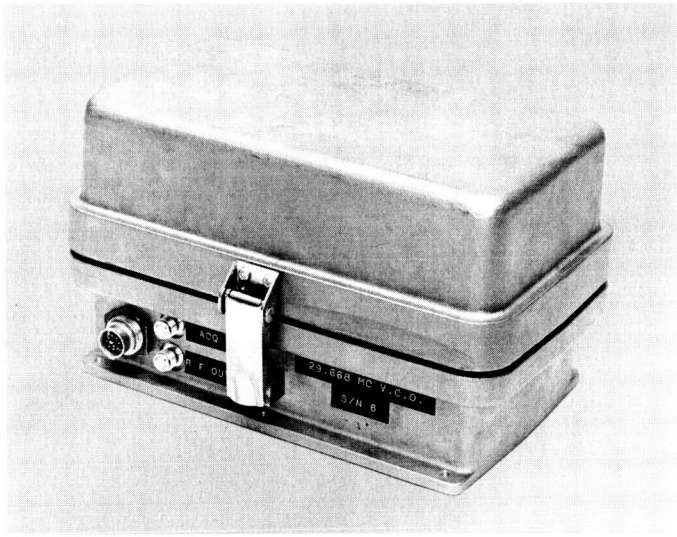

Figure 12. Stable oscillator RFI housing

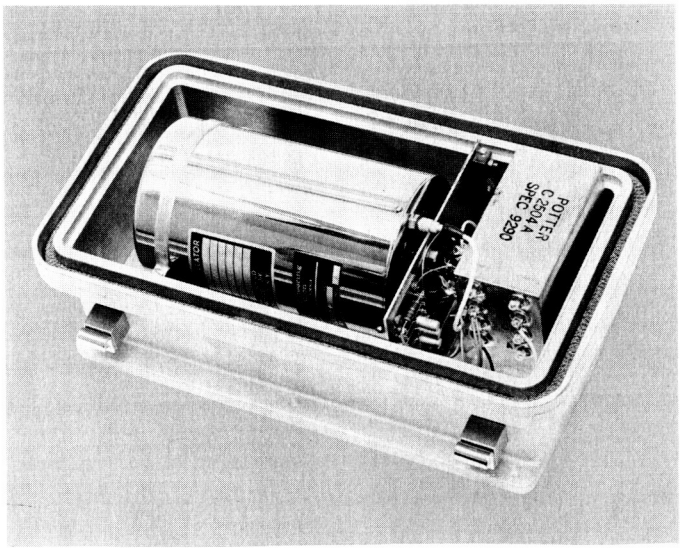

Figure 13. Oscillator and associated circuitry in RFI housing

3. High Power L-Band Feed

The antenna feeds currently used by the DSIF are L-band monopulse tracking (LM) feeds originally designed to operate only at 960 mc. However, with the present system of operating in a diplexed configuration, the LM feed is called upon to transmit 890-mc signals through its sum channel (Ref 1). Because the feed was not designed with this use in mind, it is limited to 200 w of CW power. Furthermore, the feed does not have a very high aperture efficiency even at 960 mc, and its ellipticity is poor at both frequencies.

To provide high power transmitting capability and improved receiving characteristics, the circularly-polarized L-band transmitting (LT) feed shown in Figure 14 has been developed under subcontract to Radiation, Inc., Melbourne, Florida, to meet JPL requirements. This feed is capable of transmitting 10 kw of CW power with an aperture efficiency exceeding 50%. A summary of its performance at both transmitting and receiving frequencies is given in Table 3.

Even in situations where high power commands are not required, it will be advantageous to use the LT feed in place of the LM feed when automatic tracking is not required (for example, in communicating with nearly sidereal targets), since at 960 mc the LT feed has a 2-db higher gain and much lower ellipticity than the LM. Also, the antenna noise temperature with the LT feed should be somewhat lower than with the LM feed, though this has not yet been verified experimentally.

Figure 15 shows the interior of the feed with the radome removed. The iris phase-shifters which convert the circularly-polarized incoming wave to a linearly-polarized TE_{10} mode for the waveguide-to-coax adapter are clearly evident. The polarization may be made either

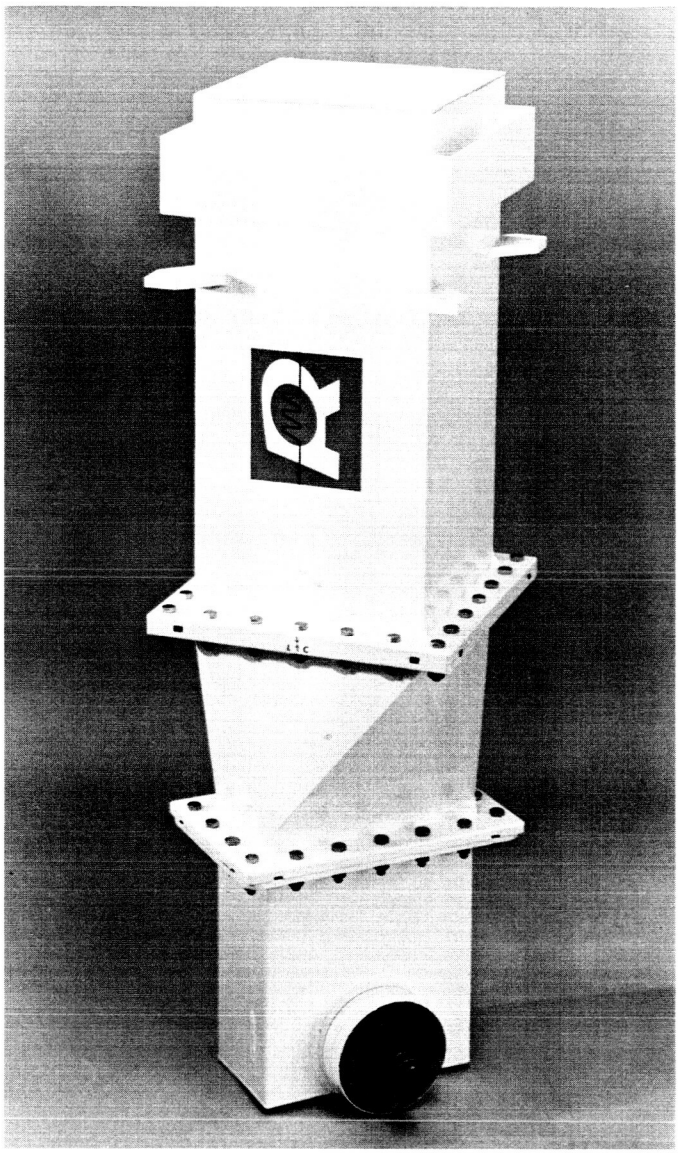

Figure 14. Circularly polarized L-band transmitting feed

Table 3. L-band-feed performance summary

Parameter	Value	
	960 mc	890 mc
Circularly polarized gain G_0, db	45.7 ± 0.8	45.2 ± 0.9
Linear gain $G_{L_{max}}$, db	43.0 ± 0.8	42.8 ± 0.9
Linear gain $G_{L_{min}}$ db	42.5 ± 0.8	41.5 ± 0.9
Ellipticity ε, lb	0.5 ± 0.1	1.3 ± 0.1
3-db beamwidth[a] α_3, deg	0.81 ± .015	0.86 ± .015
Highest sidelobe, db	−22	−24
CW power capacity, kw	—	>10
VSWR	<1.2	<1.2

[a]Tolerance includes measurement inaccuracy plus slight ellipticity in power contours.

right-or left-handed by rotating the square aperture section 90 deg with respect to the adapter and rectangular-to-square twisted taper sections (Fig 14). The ¼ lambda choke surrounding the aperture is not to provide beam-shaping; it reduces surface currents which cause a degradation in the ellipticity.

It is anticipated that by the end of May 1962, all stations of the DSIF will be equipped with this feed.

4. New 85-Ft HA-Dec Antenna

A new 85-ft HA-Dec antenna is being erected at the Golden Echo Station. This new antenna will be similar to the HA-Dec antenna used at the Pioneer Station when

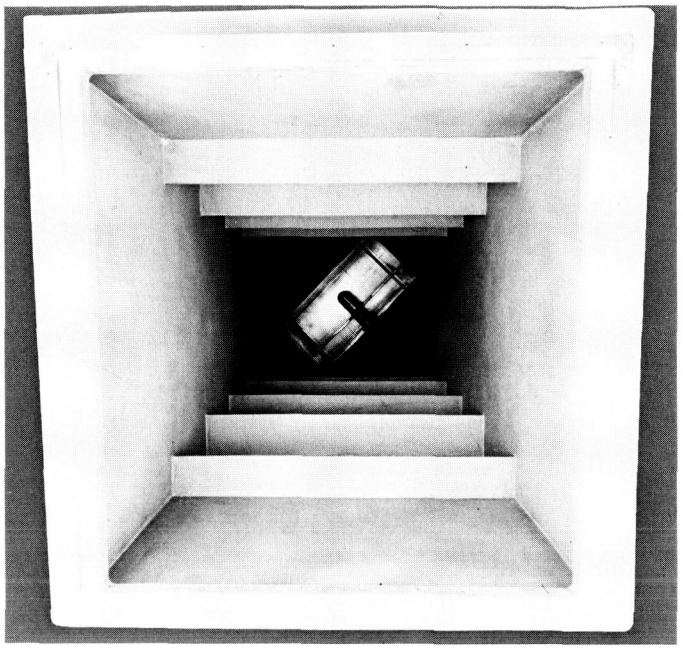

Figure 15. Interior of LT feed

completed, and will be used in tracking operations in place of the present Az-El antenna. The 85-ft diameter Az-El antenna presently located at the Echo Station will be moved to the high power transmitter installation site (*SPS 37-13*).

Erection of the new antenna is underway (Fig 16). The antenna pedestal is complete and the polar drive assemblies are in place. The antenna is scheduled to be operational for the *Mariner* R mission.

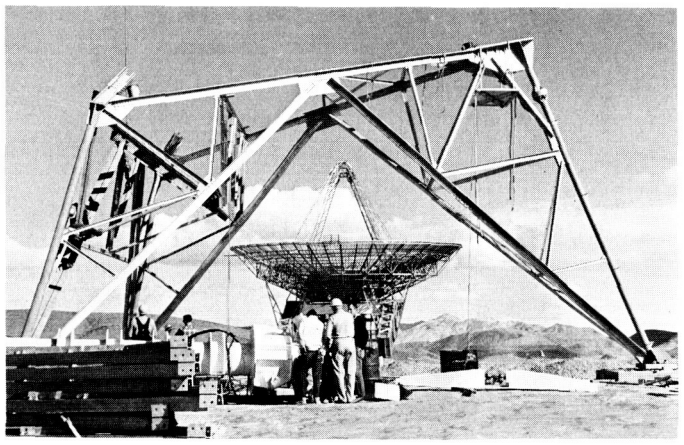

Figure 16. New 85-ft HA-Dec antenna February 15, 1962

B. Engineering Development

1. Acquisition Aid Experiment

During the *Ranger III* mission an acquisition aid experiment (*SPS 37-13*) was conducted at the Johannesburg Station. This experiment was designed to evaluate an auxiliary antenna system which was intended to provide detection and automatic acquisition of a spacecraft within the beamwidth of the acquisition antenna. The acquisition antenna system was mounted on the periphery of the 85-ft reflector and consisted of a quadhelical array antenna with a beamwidth of 22 deg and a gain of approximately 15 db.

a. Installation and checkout. The system was installed during the 3-week period prior to the *Ranger III* launch. Only two significant problems were encountered during the system checkout. The most serious was an anticipated problem: the antenna, because of its broad beamwidth, was affected by multipath reflections of the radiation from the collimation tower. The second problem was that switching from the acquisition aid to the main antenna required a receiver mechanization such that phase shifts occurred when this switching was done.

The multipath problem prevented a quantitative evaluation of the system with the equipment and time available. The collimation tower proved to be unacceptable for obtaining data on the acquisition system since the multipath effects produced a multitude of false nulls in the difference patterns and distorted the sum channel patterns. Therefore, to obtain a greater elevation angle and reduce reflections, the antenna mobile service tower was utilized as a close range collimation tower. This procedure, although not entirely satisfactory, was the only available method. The test transponder was placed in the mobile service tower and used with a 960-mc ¼ λ stub antenna. The patterns obtained are shown in Figures 17 and 18. (These patterns were taken at approximately 30-deg elevation angle.)

The primary problem with this close-range procedure was that the mobile service tower, as well as the dish and quadripod legs, produced reflections which distorted the patterns. As a result, it was impossible to obtain an accurate determination of the S-curve or a plot of the null planes. The latter prevented the fine adjustment of the acquisition antenna elements to obtain orthogonality with the antenna axes, and thereby introduced undesirable cross-coupling of the error channels. The former necessitated a trial and error procedure utilizing aircraft tracks to obtain approximate gains for the servo system.

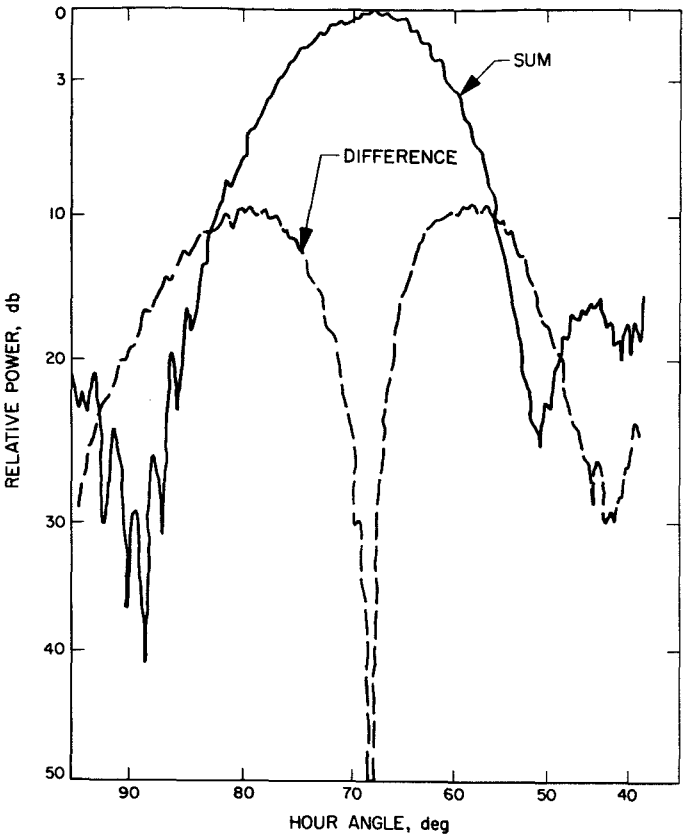

Figure 17. Feed patterns in hour angle for the sum and difference channel

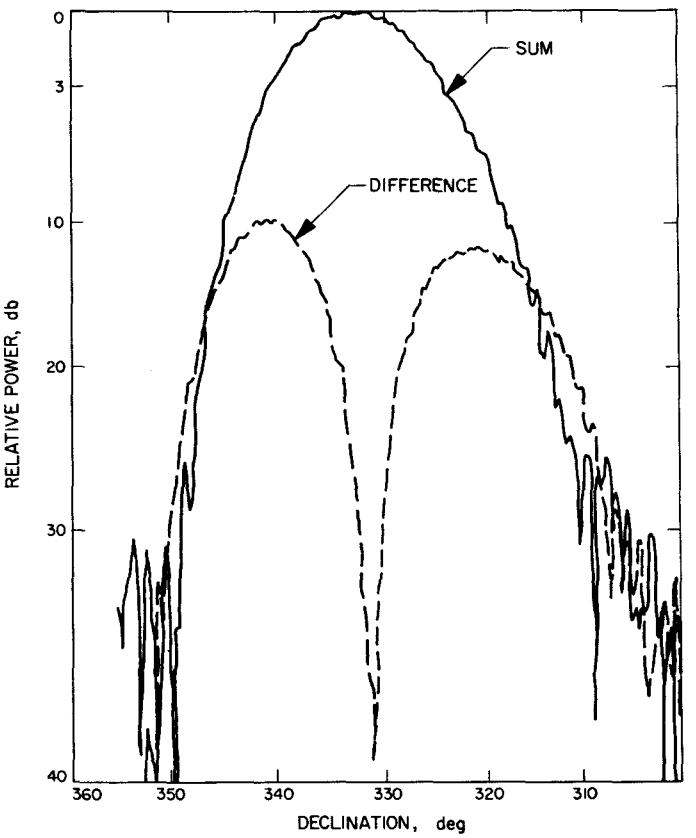

Figure 18. Acquisition antenna feed patterns in declination for the sum and difference channels

The phase shifts in the sum channel of the receiver occurred since, with the parametric amplifier in the system, a 20-db pad must be switched into the sum channel to allow the difference channels to gain track correctly. When in the acquisition mode, the pad is switched out. This circuitry produces a phase shift in the difference channels. The parametric amplifier produces an additional phase shift whose magnitude depends upon whether or not it is operating. As there were operational problems with the parametric amplifier following its installation (concurrent with the acquisition system), difficulties were encountered in trying to phase the difference channels of the receiver for both the main feed and the acquisition system.

Based upon these problems, it is recommended that on any future installation, the acquisition antenna be modified to permit its mounting on the quadripod tip rather than on the periphery of the dish. This mounting would eliminate reflection from the quadripod legs and any phasing problems, as the acquisition antenna could be switched ahead of the parametric amplifier. Possibly more important, it would reduce the cable loss and increase system threshold of the acquisition system by approximately 8 db, due to the parametric amplifier.

b. Final checkout and operator training. The system final checkout and operator training were accomplished with aircraft tracks. An attempt to collimate the two antennas was made on the initial flights. Due to the narrow field of view of the television camera (approximately 0.5 deg) and the rather high angular jitter at elevation angles less than 30 deg, it was rather difficult to collimate the acquisition antenna with the electrical biasing network. The period of time that the aircraft was above 30 deg was rather short and the angular rates were correspondingly high.

In attempting to switch from the acquisition antenna to the main feed, it was found that reliable switchover could not be accomplished below 30-deg elevation due to multipath effects. Based upon this and the high gain required in the servo system isolation amplifier for the S-curve of the acquisition antenna, a variable bandwidth reduction was incorporated into the servo system in the acquisition mode. This reduced the angular jitter and the gain required in the isolation amplifier.

Tracking tests following this modification proved highly successful. Switchover to the main feed could usually be accomplished within 2 or 3 deg of the horizon. Phase transients in the receiver due to switching were approximately 2 msec in duration and never resulted in a loss of lock. The transients in the servo system were due to the two antennas not being exactly collimated and the difference between the servo gains of the two systems, but these were negligible. Switchover was attempted several times with the antenna at near maximum rates and was successful on every occasion.

Instantaneous indication that the antenna was within the beamwidth of the main feed was obtained from the spectrum analyzer which eliminated any confusion as to whether the switchover was successful. The system can be switched at will without fear of losing the target.

The anticipated problems of antenna switchover at low elevation angles were greatly reduced by this capability of frequent switching. Due to the increased angular jitter in this region, the antenna would pass back and forth through the main beam of the antenna. By switching rapidly until the correct indication was obtained on the spectrum analyzer, the switchover could be accomplished at low elevation angles. Although this is somewhat of a random process, it has proved to be quite reliable.

The acquisition procedure utilized for the dynamic tracking tests consisted of a 10-deg search paralleling the horizon, and 5 deg above the horizon. This procedure proved completely successful and was tested with acquisition rates from 0.01 to 0.06 deg/sec.

c. **Ranger III** ***mission.*** The acquisition system, although not optimized, proved quite successful on the *Ranger III* mission. A last-minute malfunction in the parametric amplifier necessitated a modification to the system. The aforementioned phase shift problems resulted in a phase reversal in the difference channels of the receiver between the two antennas. This required the insertion of manually operated phase shifters in the difference channels which operationally complicated the switching procedure.

The acquisition system, by virtue of its beamwidth, reduced, if not eliminated, the dependency of the station upon prediction data. To cover as many contingencies as possible in vehicle performance, a search pattern, as described above, was used on *Ranger III*. It was intended to continue this search until signal detection and not attempt to follow the predicted trajectory. This procedure eliminated any problems that may have occurred due to the time discrepancy in the prediction data received prior to acquisition. The acquisition of *Ranger III* would have been identical without any prediction information at all other than the prelaunch trajectory plots.

The signal was initially detected at 20:56:25 GMT, at which time the spacecraft was approximately 2 deg above the local horizon. The system was automatically tracking with the acquisition antenna at 20:56:39 GMT. Immediately following this, DSIF 1 acquired the transponder two-way, which pulled the receiver at DSIF 5 out of lock. The transponder was reacquired and the system automatically tracking again at 20:57:40 GMT. The antenna was switched to the main feed for the first time at 20:59:30 GMT and was successful. The full significance of this type of simple, but reliable, acquisition procedure would have been evident if the spacecraft had been 3 min later than the predictions rather than 3 min early.

2. S-Band Ranging Experiment

At this time all DSIF stations are equipped to locate and track satellites and space probes by obtaining and recording angles (either azimuth and elevation or hour angle and declination) and two-way coherent doppler. This method is acceptable and sufficiently accurate for limited distances, where angular changes are appreciable and signal levels high enough for reliable doppler. For planetary and interplanetary range determinations, it was concluded some time ago that a more powerful method would have to be devised, preferably one whose accuracy is not a function of the distance involved. During the past 3 years, work in research and development led to the design, construction, and testing of several versions of precision ranging by essentially digital means. This report concerns the application of these methods to provide precision ranging for the *Ranger* RA-6, -7, -8 and -9 lunar probes.

a. Purpose. The purpose of this experiment is to demonstrate a precision ranging system capable of operation to any of the inner planets, to obtain useful data which will aid in the determination of the lunar spacecraft trajectory and the distance to the Moon, and to provide means for translating research ideas and developments into DSIF capabilities. Previous efforts in research and development have, over the past 3 years, yielded useful range data with passive satellites and the planet Venus. Most of the methods and techniques that were developed are directly applicable to spacecraft ranging.

b. Objectives. The objectives of this experiment are to:

(1) Demonstrate the feasibility and accuracy of a precision ranging system with a view to its subsequent use for space flights to the inner planets, at which distances range determinations from angles and doppler become inaccurate.

(2) Initiate establishment of a precision ranging capability in the DSIF.

(3) Make precise range determinations for the lunar probes, which should be of particular value at the times of mid-course maneuver and lunar impact.

(4) Accomplish these things without the possibility of adversely affecting the mission objectives of the *Ranger* RA-6, -7, -8, and -9 program, which are to obtain data on the physical conditions of the lunar surface by means of high resolution TV experiments.

c. Transponder ranging system. The general form of a transponder ranging system is shown in Figure 19. The carrier from the ground transmitter is modulated by a ranging code. The transponder regenerates both the carrier and the code, modulates the regenerated carrier with the regenerated code, and transmits the modulated carrier back to the ground receiver. The ground receiver contains a receiver coder which produces a local model of the received code for cross-correlation detection. When the local model has been synchronized with the received code, the phase difference between the transmitted code and the local model is a measure of the round-trip propagation time to the spacecraft, and thus a measure of the range. Since the phase difference is counted continuously by the range tally, a real-time continuous range measurement is obtained.

In its simplest form, precision ranging is performed by radar reflection from the object ranged on. This can be done where there is enough power returned from the object, that is, at short distances or with very large reflecting bodies. This form of ranging was used for the earlier experiments mentioned above.

The *Ranger* ranging experiment represents the next logical step toward a full-fledged, coded-transponder ranging system with automatic acquisition, which can be used to planetary distances. In this experiment the spacecraft turn-around transponder regenerates the carrier but not the range code. It detects the range code from the Earth-to-spacecraft carrier and directly modulates it on the returned carrier.

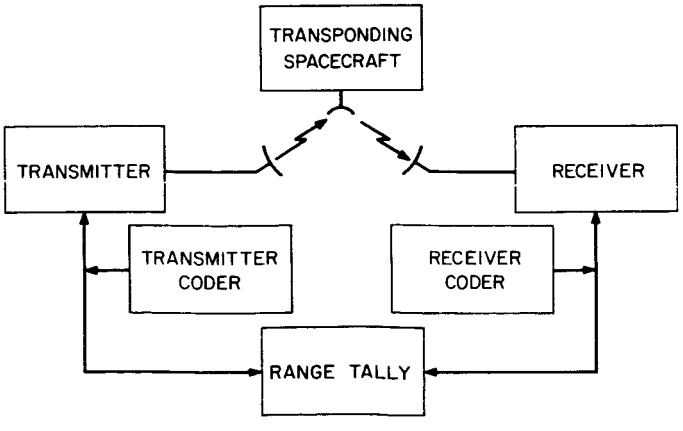

Figure 19. General form of a transponder ranging system

The system being planned is patterned after that in *SPS 37-11*, *-12*, and *-13*. The digital ranging equipment proper is expected to be similar to that referred to in these earlier publications as the Mod II equipment, which features a stored-program controller. The RF portion of the system will, however, be at S-band having a nominal transmitting frequency of 2113 mc and a receiving frequency of 2295 mc.

d. General concepts. The requirements of *Surveyor* (1963) and *Mariner* (1964) space probes are such that it is mandatory to prove out S-band flight equipment by actual use prior to that time. For this reason an S-band transponder was included in the *Ranger* spacecraft design plan at an early date. Its operation is entirely independent of, and can be simultaneous with, that of the L-band system which carries the full mission responsibility. The requirement of noninterference with the *Ranger* mission is met by the choice of S-band for the ranging experiment. Fuller utilization of the S-band transponder is also effected, at the cost of only very minor modifications to permit transponding the ranging modulation.

The transponder used is of the turn-around type, and requires no coders in the spacecraft. Transponders with coders and automatic acquisition capability will be needed at distances in excess of 10^6 mi from the Earth. Even so, they would likely be operable as turn-around transponders at the time for a mid-course maneuver for a planetary probe, which might occur 4 or 5 hr from launch. It is desirable, therefore, to prove out such a transponder at this time, for lunar distances.

The Mod II ranging equipment planned for use with this experiment is capable of generating code wavelengths of from 10^3 to 2×10^8 mi. The code wavelength represents the maximum round-trip distance which can be ranged without ambiguity. Thus, it is evident that this equipment, when proved out to lunar distances, can readily be employed for operational ranging to planetary distances.

e. System concepts. Figure 20 shows a functional block diagram of the various system components of the experiment, and the manner in which they are inter-related. Design of many of these components has been completed. Some are already built. The Mod II ranging equipment

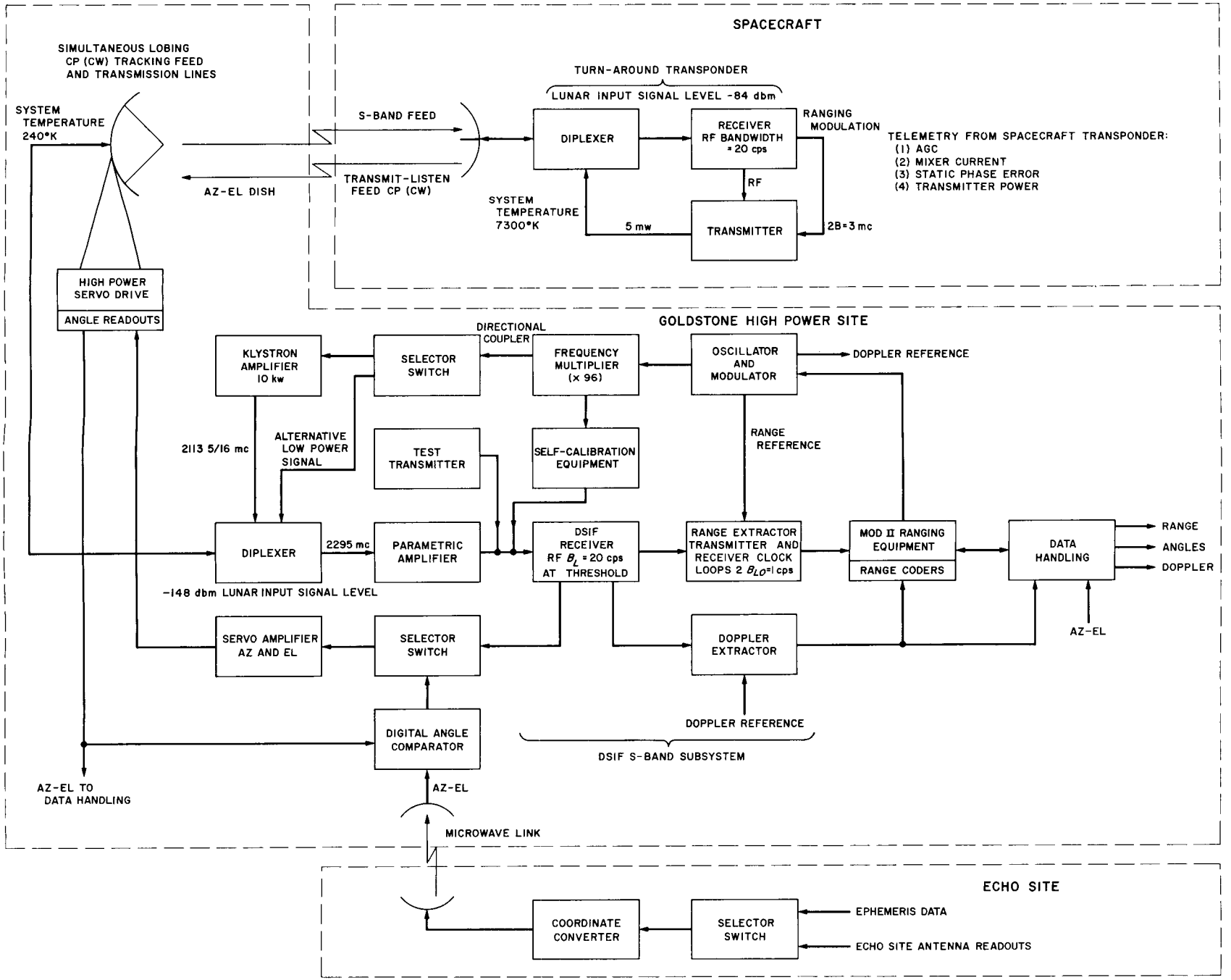

Figure 20. Functional diagram for *Ranger* RA-6, -7, -8, and -9 ranging experiment

is at this time being temporarily integrated into a system with an L-band receiver and transmitter. The S-band equipment, ranging equipment, data handling equipment, etc., will all be located at the high power transmitter site.

The spacecraft transponder and the ground support equipment (GSE) required to check it out have been modified where necessary to permit their use with the ranging feature. The design of the coders which must accompany the GSE is inherently available from the appropriate portion of the ranging equipment. The former Advanced Research Projects Agency data handling system, is being modified for subsequent installation. The S-band receiver and transmitter are the DSIF prototypes. Their early evaluation and acceptance should expedite and facilitate the changeover from L-band to S-band of the overseas stations in particular.

3. Mariner R Telemetry to Teletype Data Encoder

The purpose of the *Mariner* R telemetry to teletype data encoder is to convert the telemetry data format as received from the spacecraft at each DSIF station, to a format suitable for transmission over teletype or telephone lines. Each encoder has the capability of producing teletype tape and modulating tone keyers, used on voice circuits, simultaneously.

a. Data formats. The telemetry data format, as received from the spacecraft telemetry demodulator, is shown in Figure 21. The data output is a nonreturn to zero (NRZ) type of signal where 0 v represents binary "0" and −12 v represents binary "1." The bit sync and word sync outputs are pulses which are used to synchronize the data extraction process.

Figure 22 shows the paper tape format to be used for teletype transmission and the format to be used for voice line transmission. The time data, which includes station identification, day of year, hours, minutes and seconds, is punched on the tape in binary coded decimal form with each of the ten digits occupying four of the five holes available in each teletype tape character as shown. The data and word sync information is punched in binary form and occupies eight of the ten holes available in two teletype characters. The fifth hole in each character is used for parity information and is punched when the number of punched data holes in the other four levels is odd, thus producing an even number of punched holes for each character of data.

When teletype commands are injected in the format, a parity code is not generated. The carriage return and

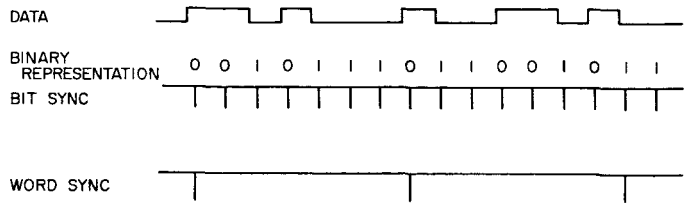

Figure 21. *Mariner* R telemetry format

line feed teletype functions are included so that a teletype page printer will print the data in a uniform format, and communications personnel will be able to determine major teletype system malfunctions. Because the data transmission is not a plain language type transmission, the data printout on a page printer will not be suitable for visual monitoring, except to determine that the basic format is correct.

Two other teletype characters are used which violate the parity check. Two space characters indicate that time data follows, and two figure "5" characters indicate out of lock. A double transmission of these characters is used to minimize the probability of data characters, with a parity error, indicating either of these functions.

b. Encoder operation. A block diagram of the data encoder is shown in Figure 23. The encoder operation is started when a word sync pulse is received from the demodulator (in-lock indication) and the start time in hours, minutes, and seconds, GMT, is stored and punched on the tape. The incoming data on the data line is converted from NRZ to *return-to-zero*-type data and stored in the storage register. When a complete word of seven bits is received and stored, it is transferred to a readout register along with the stored word sync data and from this register is punched on the tape.

In the operation of the telemetry demodulator, word sync pulses can be missing. To ensure proper operation of the encoder, an internally generated word sync pulse is derived by counting seven of the bit sync pulses, which are always available. The internally generated word sync pulse is used to perform the data transfer and readout, and is resynchronized every time a word sync pulse is received from the demodulator. If a series of nine word sync pulses from the demodulator are missing, the demodulator is considered to be out of lock. The encoder determines when this condition occurs by counting the number of consecutive missing pulses and generates an out of lock printout on the tape as well as stopping the data readout. When a word sync pulse is again received, the encoder restarts with a new cycle of operation.

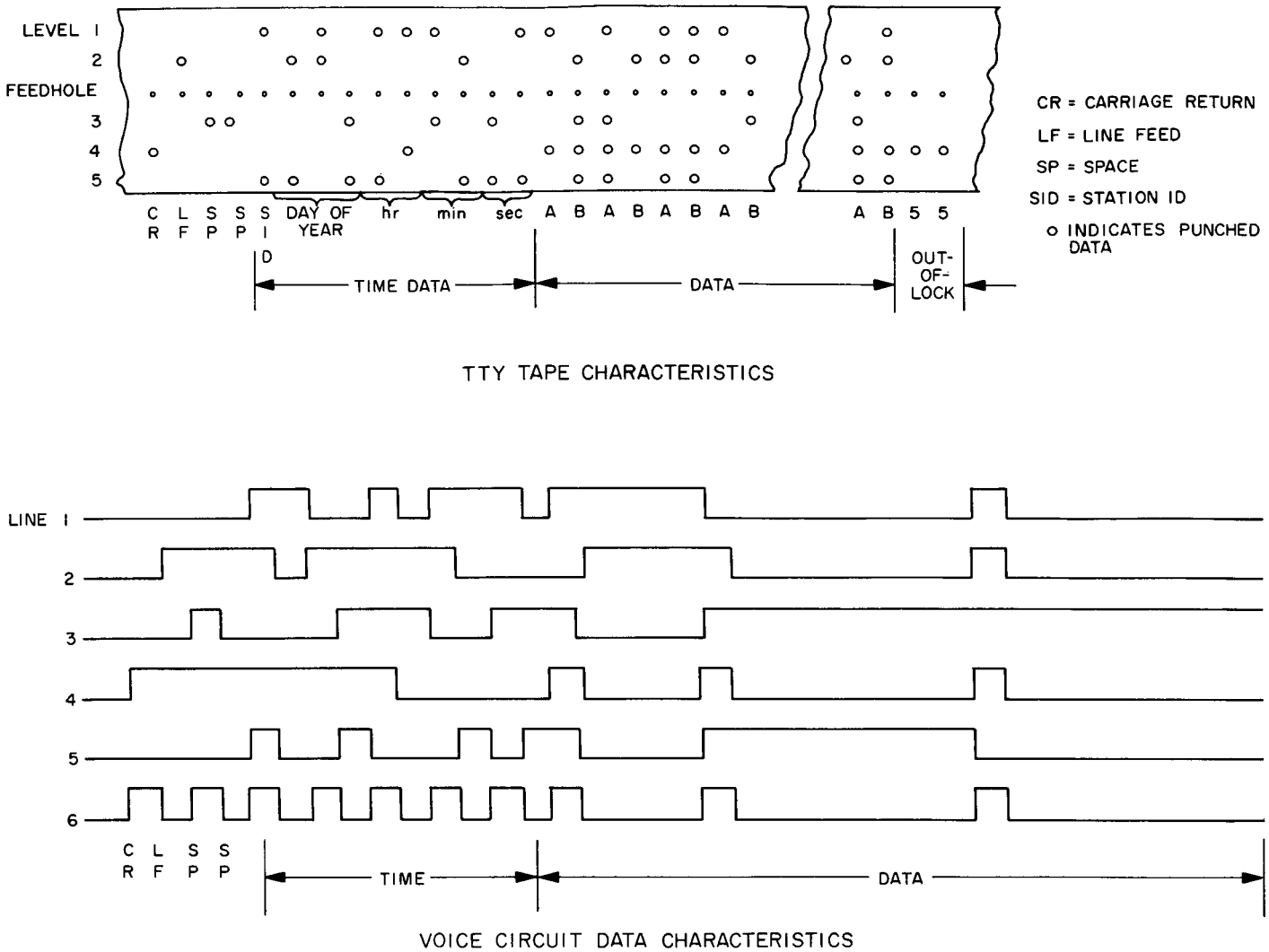

Figure 22. Paper tape formats

To provide time readout at frequent intervals, a time label is injected in the data format every 5 min. This time readout corresponds to the time when the first bit of the data word following the time printout was received by the encoder.

To provide signals for operation over voice lines, the data input to the punch is connected to a converter which converts the signals to a NRZ-type data which then modulates five tone keyers. A sixth tone keyer provides data timing information for retiming the data at the receiving station.

4. Diplexer Development

In general, a diplexed antenna system provides, with a single exception, all the capabilities of completely independent transmitting and receiving antennas with a great reduction in cost and complexity, and a corresponding increase in reliability. The single exception, of course, is that transmission and reception are restricted to the same radius vector in the diplexed case.

In practice there may be some degradation in system performance since the diplexer unavoidably introduces some extra insertion loss into both the transmitter and receiver transmission lines. In the case of the transmitter line, this loss can be kept low and is not serious. However, because of the high rejections required, the extra insertion loss in the receiver line may reach 0.3 db, which is equivalent to 20°K in a low noise system. This may amount to a 50% increase in system noise temperature.

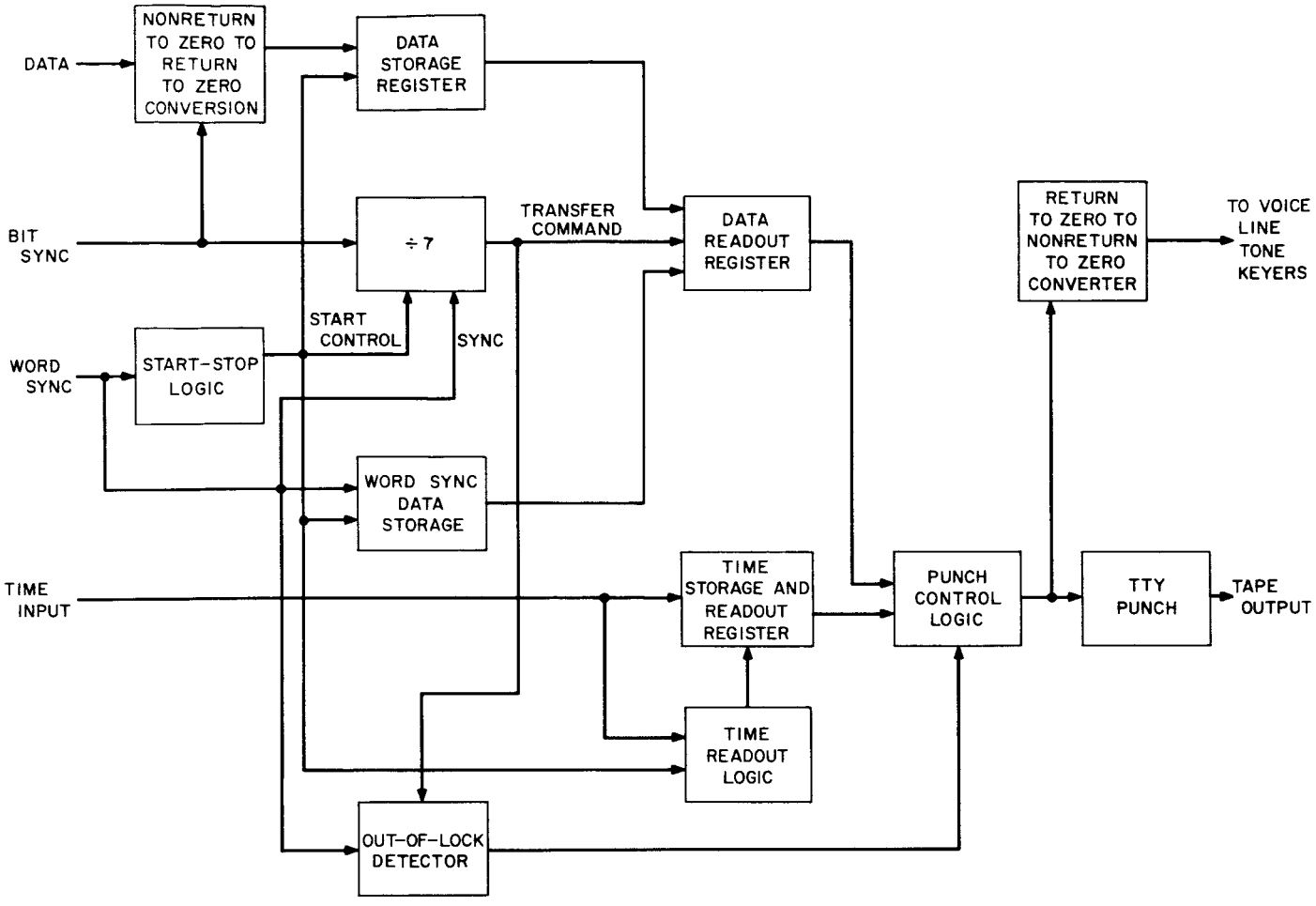

Figure 23. *Mariner* R telemetry to teletype encoder

Nonetheless, diplexed operation will become important to the DSIF as mission densities increase, because it will permit the use of existing facilities with much greater efficiency.

a. High power L-band diplexer. To provide immediate L-band capability for diplexed operation at the Goldstone Stations, two additional units of the 200-w diplexer that had been developed for the Mobile Tracking Station were temporarily mounted on the antennas during 1961. Meanwhile, a prototype high power L-band diplexer (LD) has been developed under subcontract to Rantec Corporation of Calabasas, California.

Figure 24 shows the sum-channel diplexer and Figure 25 shows one of the two difference-channel filters which together comprise the monopulse diplexer.

The prototype LD was determined to have the insertion losses and rejections listed in Table 4.

Table 4. Insertion loss and rejections for prototype diplexer

Terminals	Frequency, mc	Loss or rejection, db
Antenna–transmitter	890	<0.05
Antenna–receiver	960	0.23 ± 0.03
Transmitter–receiver	890	143
Antenna–transmitter	960	35
Difference filter	960	<0.3
Difference filter	890	~ 140

Note: The passband VSWR are less than 1.2 for all terminals.

On December 21, 1961 the sum-channel diplexer was mounted at the apex of the Echo Site antenna together with the prototype LT feed (Fig 26) in order to verify the power handling capability of each. No difficulty was experienced at a CW power level of 10 kw, nor was there a detectable degradation in receiver threshold with full transmitter power on. Tests will be performed in the future to determine if the transmitter power will raise

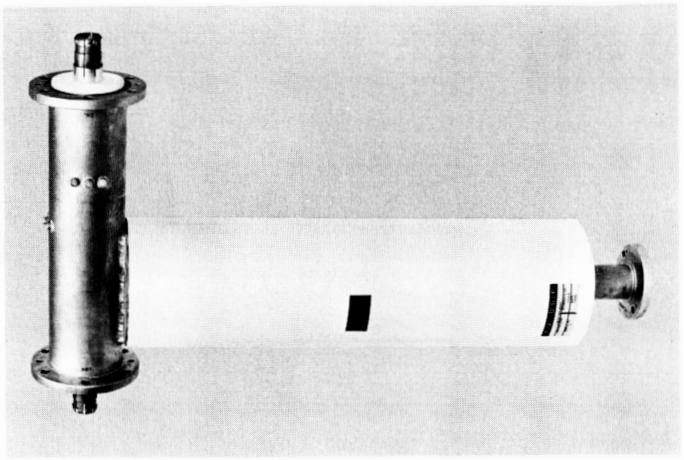

Figure 24. L-band diplexer for the sum channel

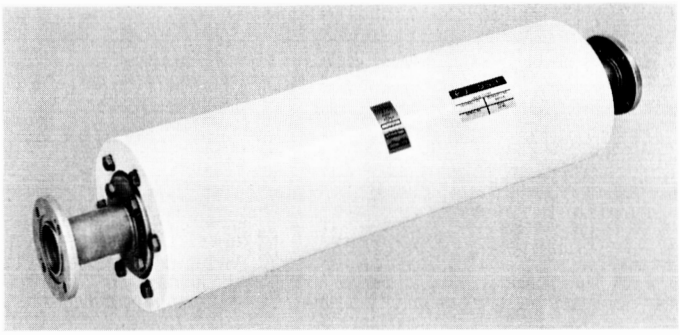

Figure 25. L-band filter for a difference channel

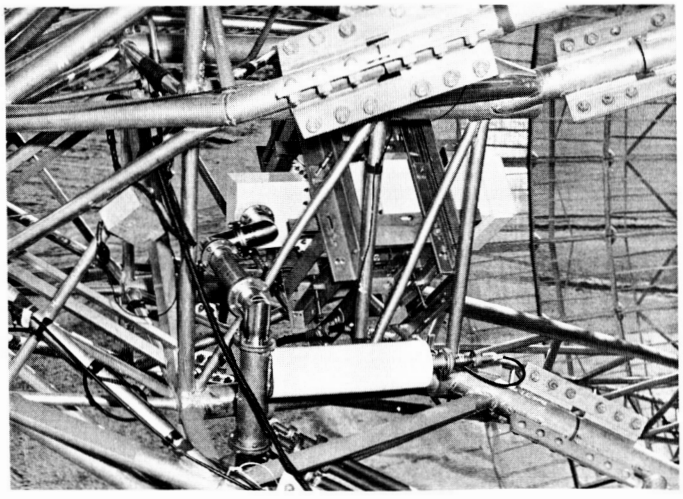

Figure 26. L-band transmitting feed and diplexer installed on the Echo Station antenna

the system noise temperature when a parametric amplifier is installed at the apex.

Although the prototype LD satisfied the requirements of the specification, the rejection bandwidth at 890 mc was somewhat narrower than desirable for reliable field operation. As a result, the second LD will incorporate a modification to broaden the rejection bandwidth.

b. S-band diplexer. To provide for diplexed operation at 2113 to 2295 mc, an S-band diplexer (SD) is being developed under subcontract to Rantec Corporation to meet the requirements. The first prototype SD, fabricated in WR-430 waveguide, has been delivered to JPL for evaluation. The transmitter arm of the sum-channel diplexer is expected to be able to carry well in excess of 10 kw of CW power without breakdown. The insertion loss of the receiver arm is anticipated to be about 0.25 db.

5. S-Band RF Subsystems Prototype Program

DSIF S-band RF subsystems prototype functional hardware is in the final stages of fabrication and module check-out. Except for a minimum of changes which will result from system testing, the over-all prototype configuration is firm.

Physical assembly of the system, as well as the design and fabrication of control, test, and monitoring instrumentation, is now underway at JPL. Over-all S-band RF subsystem testing will commence in late spring. It is expected that a complete RF subsystem complex (receiver, exciter, doppler extractor, ranging interface) will be through functional testing at JPL and ready for preliminary operational evaluation by mid-summer. Present scheduling projects installation of the prototype at Goldstone in time for complete S-band system testing before the end of the year.

C. Engineering Studies

1. Investigation of Angular Encoder Errors at the Echo Station

During the Echo Site pretrack calibrations for *Ranger II*, a large cyclic error was evident in the star track data. This error had a frequency of approximately one cycle per 13 deg of antenna rotation (i.e., approximately 27 cycles for one antenna revolution). Because of the 27:1 electrical step up in the servo follow-up chain,

the frequency of the errors indicated trouble in the angle encoding system rather than a mechanical structural deformation. Both the azimuth and elevation systems were removed from the antenna and checked on a Leitz optical dividing head (Fig 27). These tests showed a large difference from data taken at the time when correction cams were cut.

In an effort to ensure that all conditions were known, a new correction cam was cut and data taken without disturbing the mechanical position of the resolvers. This data showed approximately 10-sec rms error which is about half of the normal system design error. As an additional check, the 27:1 resolver was removed from the dividing head and then reinstalled on the head, using, as before, the standard installation procedure. Another test was run and errors were found to be approximately 1-min rms. The standard installation procedure was checked to be certain there were no mistakes; and the resolvers were removed and reinstalled several times with tests being conducted each time. These tests showed that data did not repeat.

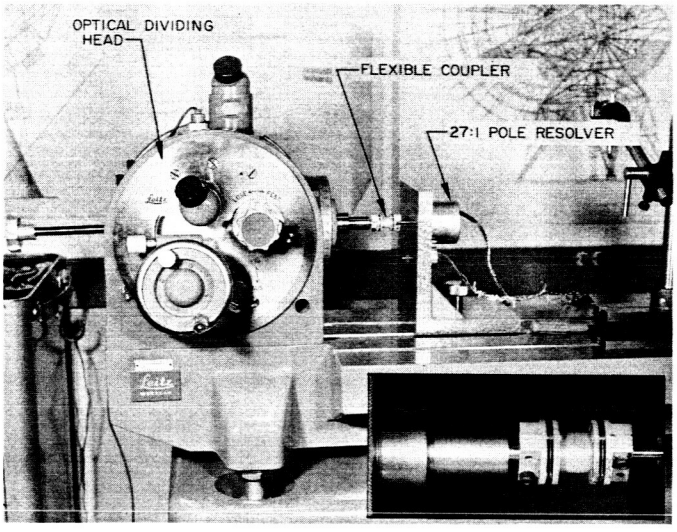

Figure 27. Resolver test setup on the Lietz optical dividing head

Numerous tests showed that the error was a function of the relative position of the two flexible couplers (Fig 27) used in the system. Measurements of the couplers showed a small mechanical deformation of one. As a result of these tests, other couplers were substituted and more tests conducted. These tests revealed that the cyclic errors observed were a function of the couplers used and could be minimized by careful selection of the couplers. Further tests showed that these couplers, when physically displaced, would take a set which would work out gradually as the shafts rotated many times.

Since the tracking schedule required the use of the systems, and only a small number of these couplers were available (and all of these had been used), the best known couplers were used and new correction cams were cut (Fig 28). The system was checked and reinstalled on the antenna and a series of star track runs showed a large decrease in the cyclic errors. Investigations were also made of the antenna system, and mechanical interference was found in the azimuth torque tube. This problem was corrected but did not explain the errors in the elevation system. Further star tracks were run and the results of these tests were similar to the results obtained before the antenna work was done.

At this time, because of the nature of the errors, the only conclusion to be made is that any deformation of the flexible couplers causes a distortion of the resolver electrical signals, possibly due to axial or radial stresses on the shaft of the resolvers. In an effort to further identify the system errors, other couplers have been purchased which will be checked before installation on the

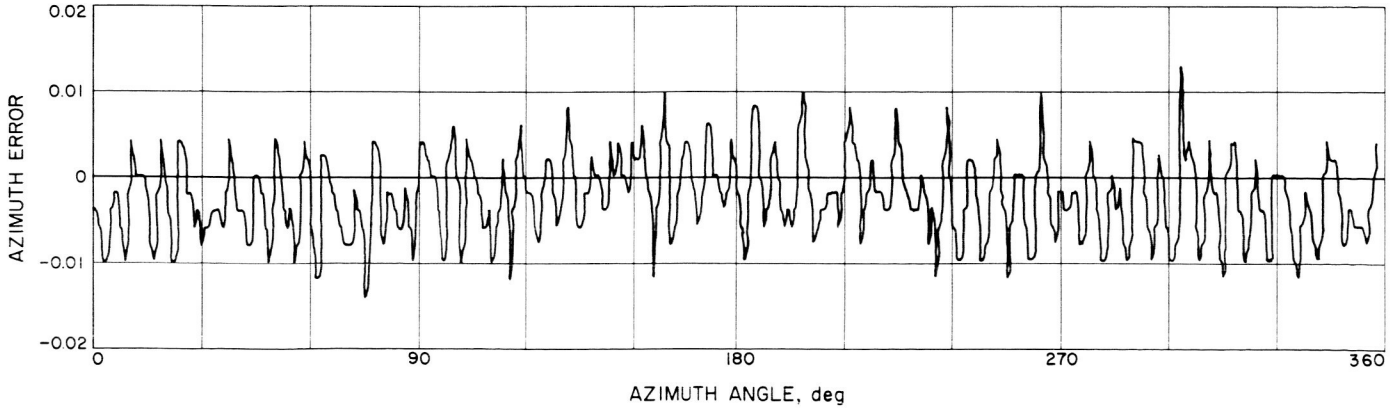

Figure 28. Azimuth error vs azimuth angle prior to installation of resolver on antenna

antenna to determine whether the couplers are being permanently damaged by some mechanical stresses of the antenna shaft, or if the couplers are inherently unsatisfactory. One problem which is still questionable is the magnitude of the errors shown in the test setup never reached that demonstrated in the star track data taken prior to the tests.

2. Modifications to GTS Antennas

Structural modifications to improve the communication and tracking capability of the HA-Dec and Az-El 85-ft antennas are now under design study by a commercial engineering concern.

The deflections from dead weight and wind loading were first checked using a graphical analysis method. Also, a digital computer program developed at JPL for spacecraft structures analysis has been used. Deflections of the dish structure supported on the declination axis bearings with the idealized Cassegrain feed supporting cone, the quadripod, and the declination gear supporting structure were calculated on the JPL IBM 7090 computer. Dead weight deflections were calculated with the dish looking at zenith and at the horizon with the declination axis in the vertical and horizontal position, respectively. Some idealizing of the dish structure was necessary to keep within the limitations of the computer program.

An investigation is being made of reinforcing existing members to decrease the deflection of the dish structure. The computer study on the HA-Dec has pointed out the reinforcing effect of the quadripod in decreasing the dish deflection along the ribs located at 90 deg to the declination axis line. It has also revealed two other basic considerations for designing an accurate dish structure.

First, because in the horizontal look of the dish structure, all the joints in the horizontal plane through the center of the dish are restrained in the horizontal plane. These joints only deflect up or down; above and below the horizontal plane all deflections are equal but opposite in signs. It follows that with the dish in this position, turning gravity on from off in the computer calculations will not deflect the paraboloidal surface out of the original shape. There will be, however, a rotation of the paraboloid axis.

The other consideration is, that in the zenith position, the deflection must be made as even as possible around the periphery of the dish. When this is done, very little astigmatic deflection of the paraboloid surface should result when the dish is rotated to the horizontal look position. A focal length change will occur, which can be allowed for by refocusing either the primary feed or the Cassegrain subreflector.

Reference

1. Renzetti, N., and D. Stelma, *Deep Space Instrumentation Facility Specification*, TM 33-26 (Vol II.B.3.3.) Jet Propulsion Laboratory, Pasadena, July 15, 1960.

III. Research and Development

A. Transponder Ranging System

1. Introduction and General System Description

The objective of this advanced development effort is to demonstrate the feasibility of a transponder ranging system which can make continuous real time precision range measurements at interplanetary distances. Previous effort which has resulted in the ranging of passive satellites has been preliminary to the work on the spacecraft ranging problem and has been done in such a way that most of the results are directly applicable. This report describes the general form of the system that is being developed and the work that has been completed thus far.

The first phase of the advanced development program is to demonstrate that a ranging code which has a gate width of 1 μsec and a gate repetition time of 10^9 μsec can be synchronized rapidly and reliably. Rapid synchronizations and reliability are to be achieved even though the link includes a transponder, transmission on two different frequencies and in two directions simultaneously, and uses ranges of 108 mi or more. The first evaluation of the transponder ranging system will be accomplished using a helicopter to simulate the spacecraft. The helicopter with the transponder will take off from an airport at El Monte, California, and fly to a surveyed landing site at JPL. The range-code acquisition time will be measured as a function of signal level, and the range accuracy will be determined by comparing the final value in the range tally after landing with the surveyed range.

A *Ranger*-type transponder will be used in the helicopter. Therefore, the ground-to-helicopter link will be on 890 mc, and the helicopter-to-ground link on 960 mc. Since the transponder was initially designed to be compatible with the wide bandwidth ranging code, very little modification to the transponder is required other than the addition of the coding equipment, demodulator, and clock loop.

The form of the transponder ranging system is shown in Figure 1 of DSIF article Section II-B-2 *S-Band Ranging Experiment*. The carrier from the ground transmitter is modulated by a ranging code. The transponder regenerates both the carrier and the code, modulates the regenerated carrier with the regenerated code, and transmits the modulated carrier back to the ground receiver. The ground receiver contains a receiver coder which produces a local model of the received code for cross-correlation detection. When the local model has been synchronized with the received code, the phase difference between the transmitted code and the local model is a measure of the round trip propagation time to the spacecraft, and thus a measure of the range. Since the phase difference is counted continuously by the range tally, a real time continuous range measurement is obtained. It is no accident that the form of the transponder ranging system is similar to the form of the radar ranging system previously developed (*RS 36-2*, Vol I). The differences between the two systems are primarily con-

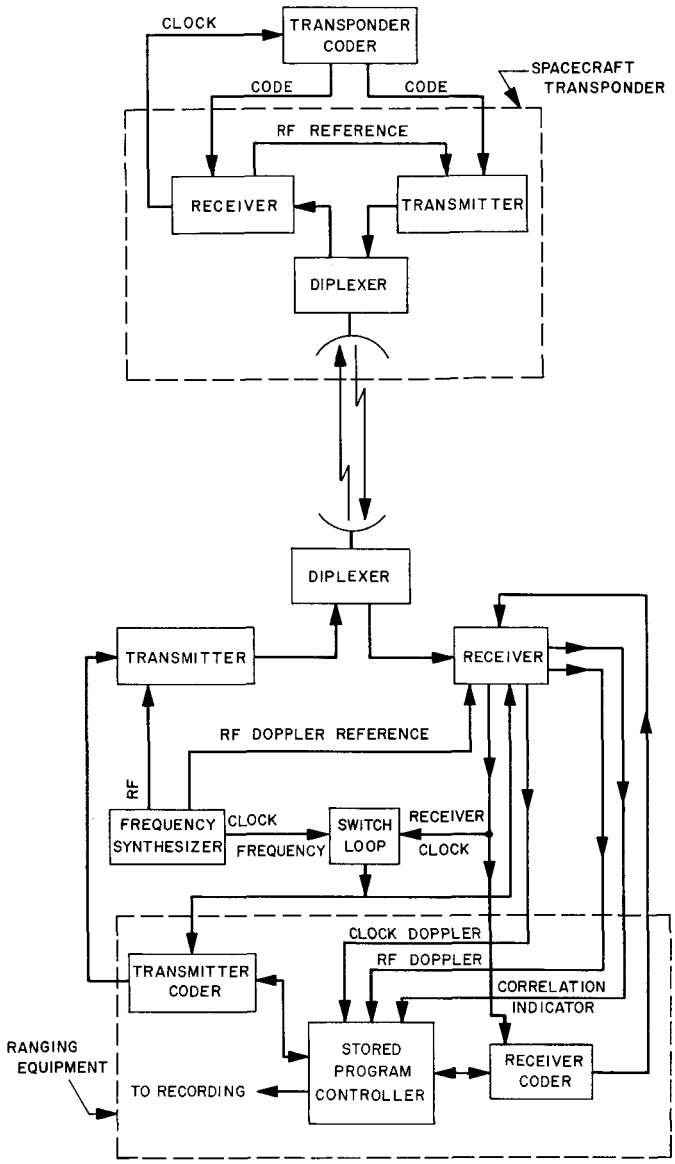

Figure 1. Experimental transponder ranging system

sequences of the vastly increased range to be measured and the necessity for using a transponder. The new system will incorporate improvements in technique resulting from the work on the previous system.

For various practical reasons, the 890–960-mc prototype makes use of a common antenna for the ground transmitter and ground receiver. Similarly, the transponder receiver and transmitter share the same antenna. It should be emphasized that this choice does not affect the principles of the ranging system in any significant way. The specific form of the system is shown in Figure 1, which is a block diagram showing the several functional parts of this system.

The frequency standard and synthesizer is the source of coherent signals derived from a signal oscillator which provides the carrier for the transmitter, timing for the transmitter coder, references for synchronous detection of signals in the receiver, and references for obtaining two-way doppler frequencies. The transmitter produces the microwave signal, modulated by the ranging code, which is radiated to the spacecraft. The receiver portion of the transponder contains a closed loop for tracking the range code and its clock. Regenerated versions of the received carrier and the received code are provided to the transmitter portion of the transponder which produces the modulated microwave signal, offset in frequency, for retransmission to the ground station. The ground receiver tracks the received carrier and code and provides doppler signals to the tally. While the transmitter coder normally is timed by the frequency standard, it is necessary to time it from the receiver clock during initial synchronization; the switching loop is provided for this purpose.

The several parts of the system have been designed and built, and the system is being assembled and tested in preparation for the helicopter flights.

2. Code Structure and Acquisition Procedure

The code structure and acquisition procedure have been designed with an effort to keep the spacecraft equipment as simple as possible while maintaining unambiguous range measurements to 100 million miles and making use of any a priori knowledge of range. The range code for the spacecraft-to-ground link is a six-component, fully acquirable code (*RS 36-10*, Vol I) while the code for the ground-to-spacecraft link is a six-component code which is acquirable only in its entirety. The several codes are listed in Table 1; the need for the several modes is explained in the following acquisition procedure:

(1) Prior to any acquisition the transponder is transmitting. The transmitted frequency is controlled by an internal crystal oscillator. This mode of operation is selected by a switching circuit operated by the receiver AGC voltage. The switching circuit is also connected to the transmitter code combiner and in this mode of operation causes the transmitted signal to be modulated by a clock, Mode 1, of the transponder transmitter code.

(2) Transponder-to-ground RF signal is acquired.

(3) Clock modulation on the transponder-to-ground RF signal is acquired by the ranging equipment using Mode 1 of the ground receiver code.

Table 1. Ranging codes

Component lengths (all codes)	
X-component	7
A-component	11
B-component	23
C-component	31
D-component	47
E-component	103
Ground transmitter code	
$X + A + B + C + D + E + C1$	
Transponder receiver code	
$X + A + B + C + D + E$	
Transponder transmitter code	
Mode 1. C1	
Mode 2. $XC1 + X[(ABC + ABD + ABE + ACD + ACE + ADE + BCD + BCE + BDE + CDE) + C1]$	
Mode 3. $XC1 + X[A + B + C + D + E + C1]$	
Ground receiver code	
Mode 1. 0	
Mode 2a. 0	
Mode 2b. $X[A + B + C + D + E]$	
Mode 2c. XA	
Mode 2d. XB	
Mode 2e. XC	
Mode 2f. XD	
Mode 2g. XE	
Mode 2h. $X[ABC + ABD + ABE + ACD + ACE + ADE + BCD + BCE + BDE + CDE]$	
Mode 3. $X[A + B + C + D + E]$	

(4) Ground-to-transponder RF signal is acquired by sweeping the transmitted RF frequency.

(5) When the transponder receiver achieves RF lock the switching circuit associated with the AGC circuit switches control of the transmitted frequency from the crystal oscillator to the receiver VCO. At the same time the switching circuit controls the transmitter code combiner to cause the transmitted signal to be modulated by the acquirable ranging code, Mode 2 of the transponder transmitter code.

(6) The change in the source of frequency for the transponder-to-ground RF signal may cause the ground receiver to lose lock. If so, the clock loop would also lose lock. In this case the RF must be reacquired and then the procedure can continue. If the change in the source of frequency for the transponder-to-ground RF signal does not cause the ground receiver to lose lock, the RF acquisition

Table 2. Correlation indications for ground receiver

Transmitter code	Receiver code	Situation	Correlation, %
Mode 1	Mode 1	Clock not acquired	0
Mode 1	Mode 1	Clock acquired	100
Mode 2	Mode 1 or Mode 2a	Clock acquired	50
Mode 2	Mode 2b	X not acquired	25
Mode 2	Mode 2b	X acquired	50
Mode 2	Mode 2c	A not acquired	50
Mode 2	Mode 2c	A acquired	75
Mode 2	Mode 2d	B not acquired	50
Mode 2	Mode 2d	B acquired	75
Mode 2	Mode 2e	C not acquired	50
Mode 2	Mode 2e	C acquired	75
Mode 2	Mode 2f	D not acquired	50
Mode 2	Mode 2f	D acquired	75
Mode 2	Mode 2g	E not acquired	50
Mode 2	Mode 2g	E acquired	75
Mode 2	Mode 2h	All components acquired	100
Mode 3	Mode 2h	All components acquired	50
Mode 3	Mode 3	All components acquired	100

in the transponder is signaled by the change in modulation from a clock to a code. The change from Mode 1 to Mode 2 does not cause the clock loop to lose lock, unless the RF loses lock, but the clock correlation indicator shows a decrease in correlation which is detectable. The correlation for the several steps in this acquisition procedure are shown in Table 2.

(7) Sweeping of the ground-to-transponder RF signal is stopped and the frequency set at the desired frequency.

(8) Transponder-to-ground code is acquired component by component using the several forms of Mode 2 of the ground received code as indicated in Tables 1 and 2.

(9) Ground transmitter code is synchronized to the receiver code and the range tally set to zero.

(10) Transmitter code is offset by an amount equal to the round trip time (with the tally operating). The round trip time is estimated from any information that may be available.

(11) Ground-to-transponder code is acquired by sweeping the transmitter clock. Note that the ground-to-transponder ranging code is not an acquirable code; i.e., it has only one peak in its autocorrelation function, even though it is made up of the same components as are used in the transponder-to-ground code.

(12) When the ground-to-transponder code is acquired, the transponder clock lock indicator activates an associated switching circuit. This switching circuit controls the transmitter code combiner to cause the transmitted code to change its form, Mode 3 of the transponder transmitter code. This signals the acquisition of the code in the transponder. (The form of the code is such that there is a clock component and clock lock on the ground is not lost.)

(13) Transponder-to-ground ranging code is reacquired by changing the form of the receiver code to correspond to the new form of the received code.

At the completion of the above acquisition procedure the RF and clock loops are locked in both the transponder and the ground receiver and the range tally is tallying true range. Since the full two-way lock assures that the ranging code is coherent with the RF on both links the vernier part of the tally may be placed in operation (*RS 36-4*, Vol I) and precision range recorded.

3. Ground Transmit–Receive System, 890–960 mc

This report covers the progress of the ground transmit–receive system development. Thus far, construction and preliminary alinement of the system have been completed on schedule, and the equipment has been delivered for integration with the ranging equipment and the transponder.

The ground system is shown schematically in Figure 2, and the system design parameters shown in Table 3 are a first approximation to the optimum characteristics for a transmit–receive system designed primarily for tracking and ranging a flight transponder. The ground transmitter–receiver subsystem will be evaluated as part of the over-all transponder ranging system, and complete analysis will be prepared for use in the design of future systems employing these techniques for interplanetary ranging.

a. Transmitter. The system transmit section contains a variable power 890-mc transmitter which will be used to simulate a wide range of phase-modulated signal levels to the flight transponder. The transmitted frequency is derived from a master oscillator with a short term frequency stability of 1 part in 10^7. Before modulation, the oscillator frequency is multiplied by five and then modulated with the ranging code. The phase deviation at the modulator output is adjustable from 0 to 15 deg which, after a further $\times 6$ multiplication, becomes 0 to 90 deg at the antenna.

Table 3. Transmitter–receiver system design specifications

Component/parameter	Value
Antenna	
Polarization	Vertical
Gain	18.2 db at 960 mc 18.3 db at 890 mc
3-db beamwidth	15 deg at 960 mc 16 deg at 890 mc
VSWR	1.29 at 960 mc 1.07 at 890 mc
Transmitter	
Frequency	890.04 mc
Power output range	−79 to +44 dbm
Master oscillator stability	1 part in 10^7
VSWR	<1.3
Phase modulation range (at antenna)	0 to 90 deg
Receiver	
Receiver frequency	960.04 mc
Input impedance	50 ohms
VSWR	<1.3
Noise temperature including diplexer	1540 deg
Predetection noise bandwidth	1.850 kc
Receiver threshold bandwidths $2B_{Lo}$ (defined as 0 db P_N/P_s in $2B_{Lo}$)	16 cps 32 cps 64 cps
Receiver strong signal bandwidths $2B_L$ (−76-dbm signal level)	145.9 cps 216.3 cps 326.4 cps
Receiver threshold sensitivity	−154.67 dbm −151.67 dbm −148.66 dbm
RF gain range	114 db
Limiter suppression factor	0.08214 0.1158 0.1627
Phase detector gain constant K_M	0.667 v/deg
31-mc VCO gain constant K_V	500 cps/v
Frequency multiplication factor	30
Open loop gain G_0	2.959×10^5 4.171×10^5 5.861×10^5
AGC loop characteristics	
Receiver gain constant K_A	
threshold	3 db/v
strong signal	14.5 db/v
Synchronous amplitude detector constant K_D	
threshold	0.44 v/db
strong signal	0.37 v/db
AGC amplifier gain constant K	10
AGC open loop gain	
threshold	13
strong signal	54
AGC filter time constants	
narrow	300 sec
wide	10 sec
AGC loop noise threshold bandwidth ($2B_{Lo}$)	
narrow	0.022 cps
wide	0.65 cps
AGC loop strong signal bandwidth ($2B_L$)	
narrow	0.09 cps
wide	2.7 cps

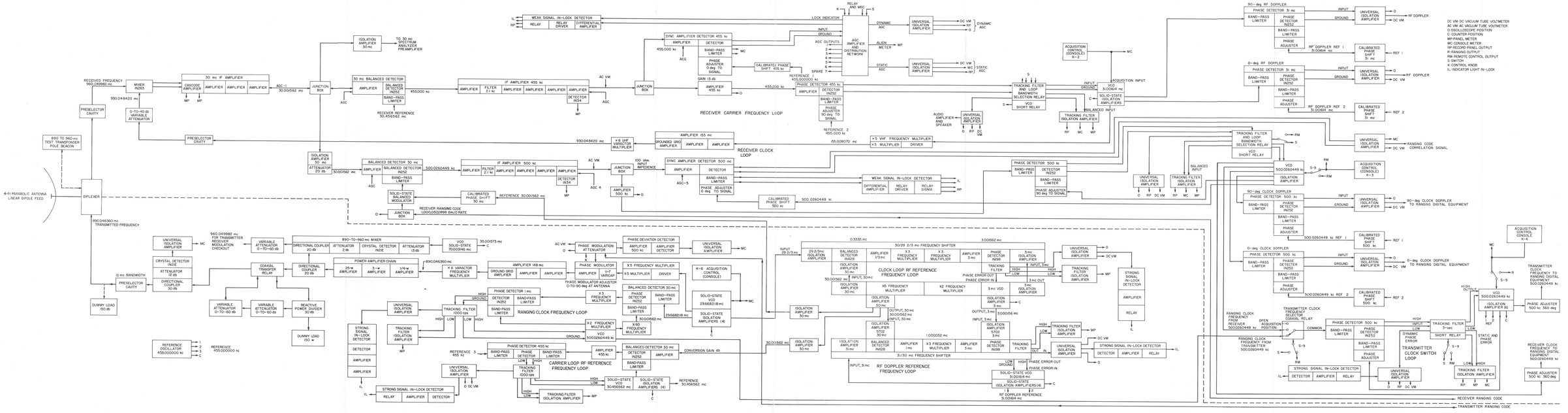

Figure 2. Transmit–receive transponder ranging system

Page intentionally left blank

b. Antenna. The antenna for the experiments is shown in the photograph in Figure 3 and its radiation pattern is shown in Figure 4. The antenna will be located on the roof of a building overlooking the helicopter landing pad. Approximately 215 ft of nitrogen-filled heliax cable will be used for connection to the receiver. While this constitutes a degradation in system threshold of 3.4 db, for this series of experiments the absolute value of threshold is unimportant, since the tracking distance is less than 20 mi and the transponder output power will require attenuation to permit reaching even this degraded system threshold.

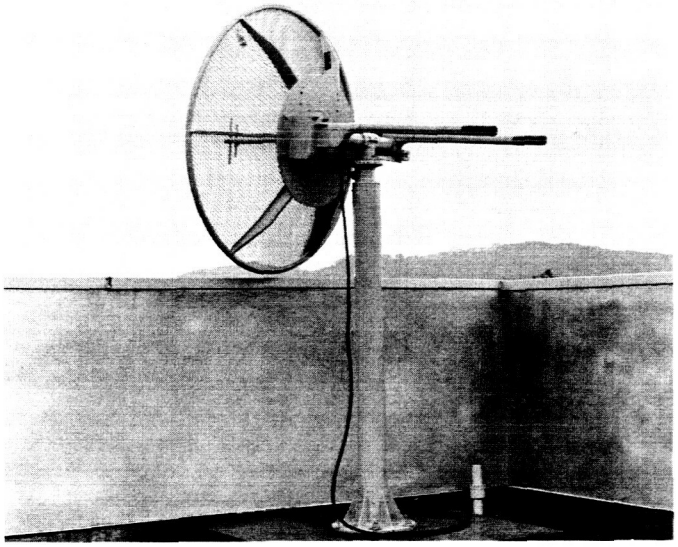

Figure 3. Antenna used for transponder ranging system

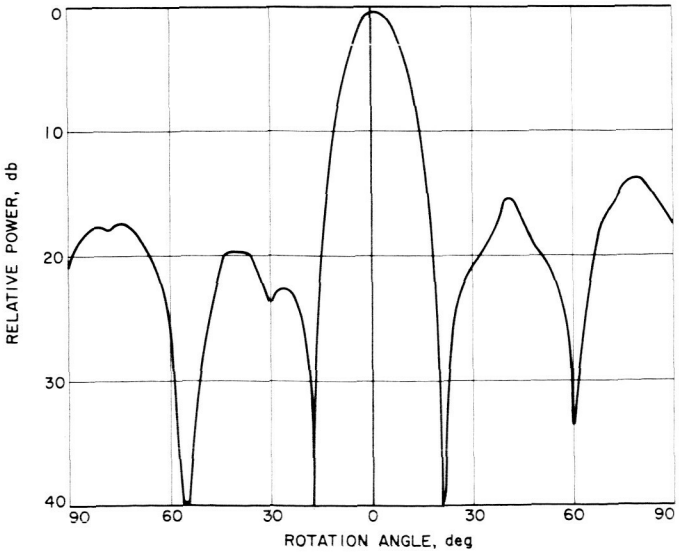

Figure 4. Radiation pattern for transponder ranging system antenna

Tracking of the helicopter with the manually steered antenna will require movement of the antenna only when the helicopter is close to the landing pad and will not be a problem in flight due to the 15-deg antenna beamwidth and the straight line flight path.

c. Receiver. The receiver is a highly stable, narrow band double conversion superheterodyne type with coherent phase-locked oscillators designed specifically to yield experimental data. The receiver is capable of tracking the RF carrier and the ranging codes from a moving transponder and providing doppler and correlation information for processing in the ranging equipment.

The system design parameters are shown in Table 3 and preliminary measurements indicate very close agreement will be possible when the system is finally adjusted.

General mechanical construction follows the DSIF type of component mounting using vertical, sliding aluminum heat sink plates as shown in Figure 5. Because of the experimental nature of the system, a great number of control and measurement points are provided to

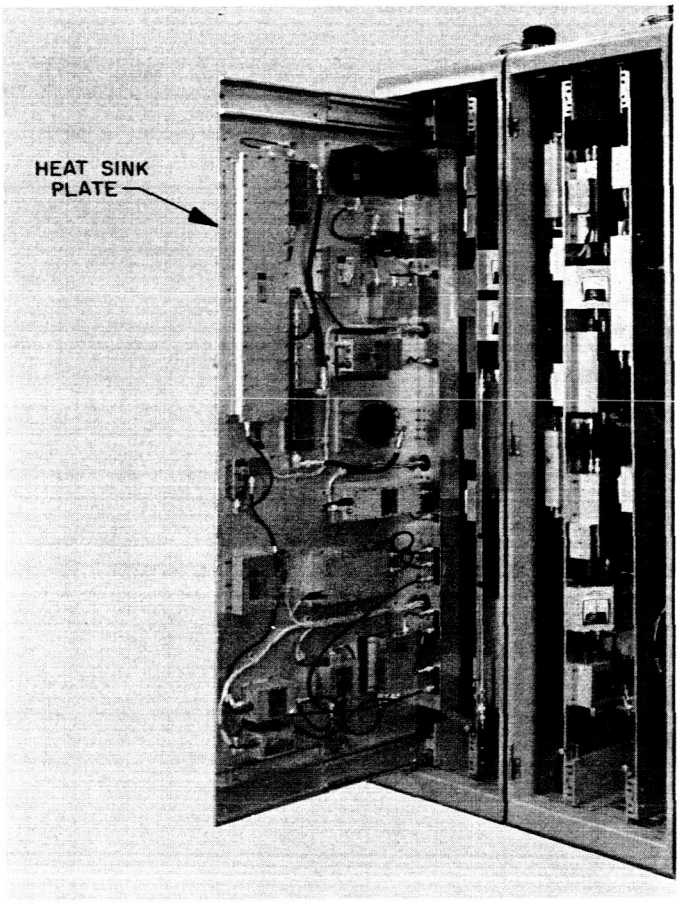

Figure 5. Component mounting techniques for transponder ranging system

enhance the versatility of the system. Every signal in the system which might be of experimental interest is made available, through highly stable isolation amplifiers and low crosstalk coaxial relays, to the front panel instruments and to panels in the rear of the racks for connection to recording instruments. Figure 6 shows the measurement and control centers of the system. A test transponder is provided for closed-loop system tests within the laboratory.

Extreme precautions were taken in the design and construction of the system to avoid coherent leakage problems which are time consuming and costly to correct after construction is completed. Each module is designed to have as few cover plates as possible (extensive use of castings and solid block milled boxes), and the cover plates are alined with close tolerance guide pins and evenly torqued down with special screw drivers to ensure the same repositioning each time the cover plates are removed. After assembly, probe measurements were made of coherent RF leakage around joints and connector fittings, and conducted leakage measurements were made on all power lines entering the modules. Corrections were made where necessary to ensure less than 10 μv (relative measurement based upon past experience and using a special probe or line stabilization network) radiated and conducted leakage. The module layout on the sliding plates was arranged for minimum sensitive cable lengths; where long cable runs were necessary from bay to bay within the racks, separate steel conduits were provided for individual isolation of cables conveying coherent signals. In addition, all power supply wiring is of the shielded dual conductor type, and all shielded grounds are returned to a single large silver plated brass block. TNC fittings and double shielded coaxial cables are used exclusively throughout the system because of their lower leakage characteristics.

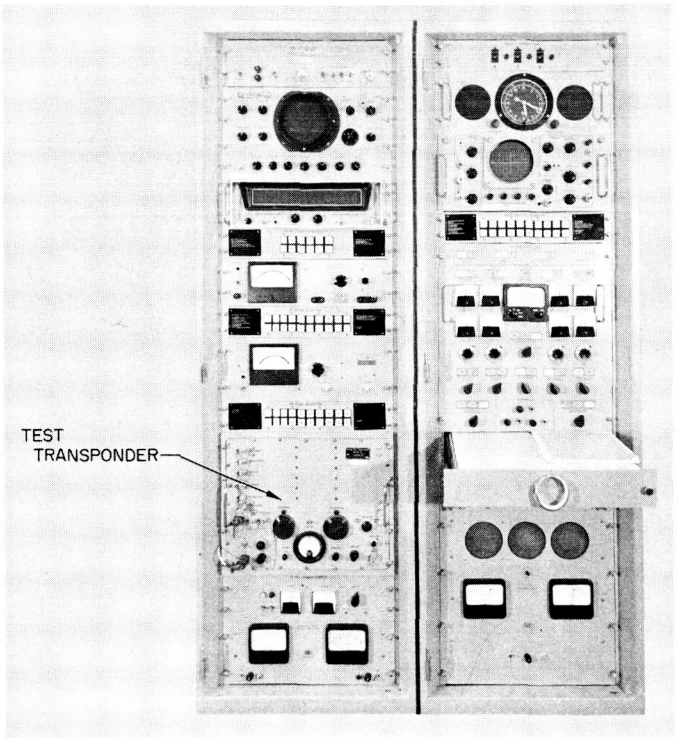

Figure 6. Measurement and control center

d. Test equipment. The system includes the following test equipment (Fig 6) combined with push button actuated selector relays for parameter measurements:

(1) Spectrum amplifier (30 mc) with a 1 μv/cm sensitivity.

(2) Direct reading frequency counter (1 cps to 40 mc) with a 1 part in 10^8 frequency standard.

(3) Vacuum tube voltmeter (dc 1.0%).

(4) Vacuum tube voltmeter (ac 1.0%, 10 cps to 4.0 mc).

(5) Test transponder with a -30 to -130-dbm calibrated output level at 960 mc capable of being phase or amplitude modulated.

(6) Oscilloscope (dc to 15 mc).

e. Control panel. Figure 6 represents the control center of the system which, together with the measurement devices discussed previously, enables a complete experiment to be performed from one position by one operator.

All coherent loops including the carrier tracking loop, the clock loop, and all reference loops are monitored by in-lock indicators which operate control panel lights to indicate in-lock or out-of-lock condition of the loops. The static phase errors of all but the reference loops are monitored on panel meters, and their respective voltage-controlled oscillators can be frequency adjusted from the front panel. One of three loop bandwidths can be manually selected for the carrier tracking loop and the clock loop either before or during an experiment, permitting a wide range of doppler rates or simulated doppler rates to be tracked by the system.

A highly stable manual gain control voltage can be switched in at any time and adjusted over the normal AGC range. An additional provision is made available for completely remoting all of the control features for automatic acquisition and control when these functions become possible.

f. Project status. At present, final adjustments are being made to the transmitter–receiver concurrent with its integration into the ranging system complex. The period before the helicopter tests will be spent solving interface problems and performing system calibrations necessary for the tests. During the following months, system development will continue and a complete behavioral analysis will be performed to provide information required for the construction of new systems.

4. Stored Program Controller, Mod II

The following section is the fourth in a series of reports describing the details of the development of the Mod II ranging equipment (*SPS 37-11*, *-12*, and *-13*). These four reports describe the work that has been done to date. The resulting machine is operable and capable of being used to conduct the helicopter experiments; although a number of additional features are planned which will make the machine more versatile.

a. Tape reader. The primary means for entering programs and data into the memory of the stored program controller (SPC) is the paper tape reader. The format used on the paper tape is adapted from that used on the Datatron Flexowriters and is shown in Figure 7. Numerical characters are identified by a punch in Channel 6. All input data is in the form of octal (Base-8) numbers, so the punches in Channels 1, 2, and 3 have weights 1, 2, and 4, respectively. (Channel 4 would have a weight of 8 if it were used.) A negative sign is indicated by a "1" and a plus by a "0."

A punch in Channel 5 marks the end of a word and has no numerical value.

The Datatron tape-preparation units normally punch a hole in Channel 5 at the end of a word and follow immediately with a Channel 1 to 3 combination, which the Flexowriter recognizes as a carriage return code. The logic of the SPC tape reader is arranged so that any character following a Channel 5 punch causes the tape reader word to be made available to the control unit

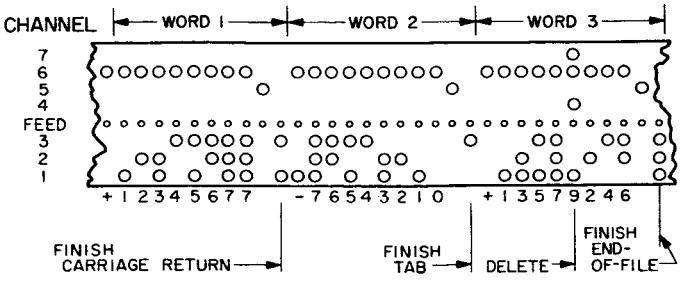

Figure 7. Sample of tape showing format used in SPC

(CU). Thus, it is possible to replace the Channel 1 to 3 code with a Channel 3 punch, which will cause a tab operation on the Flexowriter. Similarly, a Channel 1, 2, 3 code will cause the Flexowriter to stop.

In Figure 7, Word 1 is an example of a normal SPC word which would be read as +12345677. Word 2 would read in as −76543210 (which would have the numerical value of −01234570 due to the use of 2's complement notation for negative numbers).

A carriage return signal would be sent to the SPC with Word 1, but not with Word 2. This feature will be used in the future to identify the various words of a set of data, such as time and range on an ephemeris tape.

Word 3 shows the use of the Channel 7 punch which over-rides all other action, causing the character to be skipped completely. In this example, it is assumed that the punch operator inadvertently struck the 9 key, then backed the tape one space and pressed the delete key, punching a hole in Channel 7. The word would read in as +01357246, the 9 being deleted, and the leading zero left over from the previous word. At the end of Word 3, the SPC can interpret the end-of-file signal as the end of a program and stop the read-in process.

Operation of the tape reader is shown in Figure 8. A tape read command comes into the system as a 25-μsec pulse on the signal line which has the Address 23000. This pulse sets the clutch control flip-flop and resets all other flip-flops. The clutch control flip-flop actuates the clutch driver in the tape reader, setting the tape in motion. The holes are sensed by photodiodes which drive switch transistors whose outputs are compatible with the logical elements used in the SPC. The feed-hole signal has a slicing-level adjustment in the reader, and its output is used to strobe all the other output signals.

The feedhole signal enters the shaping logic which detects the leading and trailing edges of the feedhole waveform and produces pulses at *T*25 in the SPC timing system approximately 50 μsec after the respective edges, thus eliminating any uncertainties arising from the asynchronous nature of the tape reader.

Each leading-edge pulse initiates the action indicated by the signals on Channels 1 through 6. If there is a punch in Channel 7, the shaping logic is inhibited and no action takes place.

A Channel 6 pulse sets the write-in control for 25 μsec. This disables Gate a, the normal circulation path in the tape reader register, and enables Gate e, lengthening the circulation path by 3 bit times. This has the effect of shifting the contents of the register three binary places.

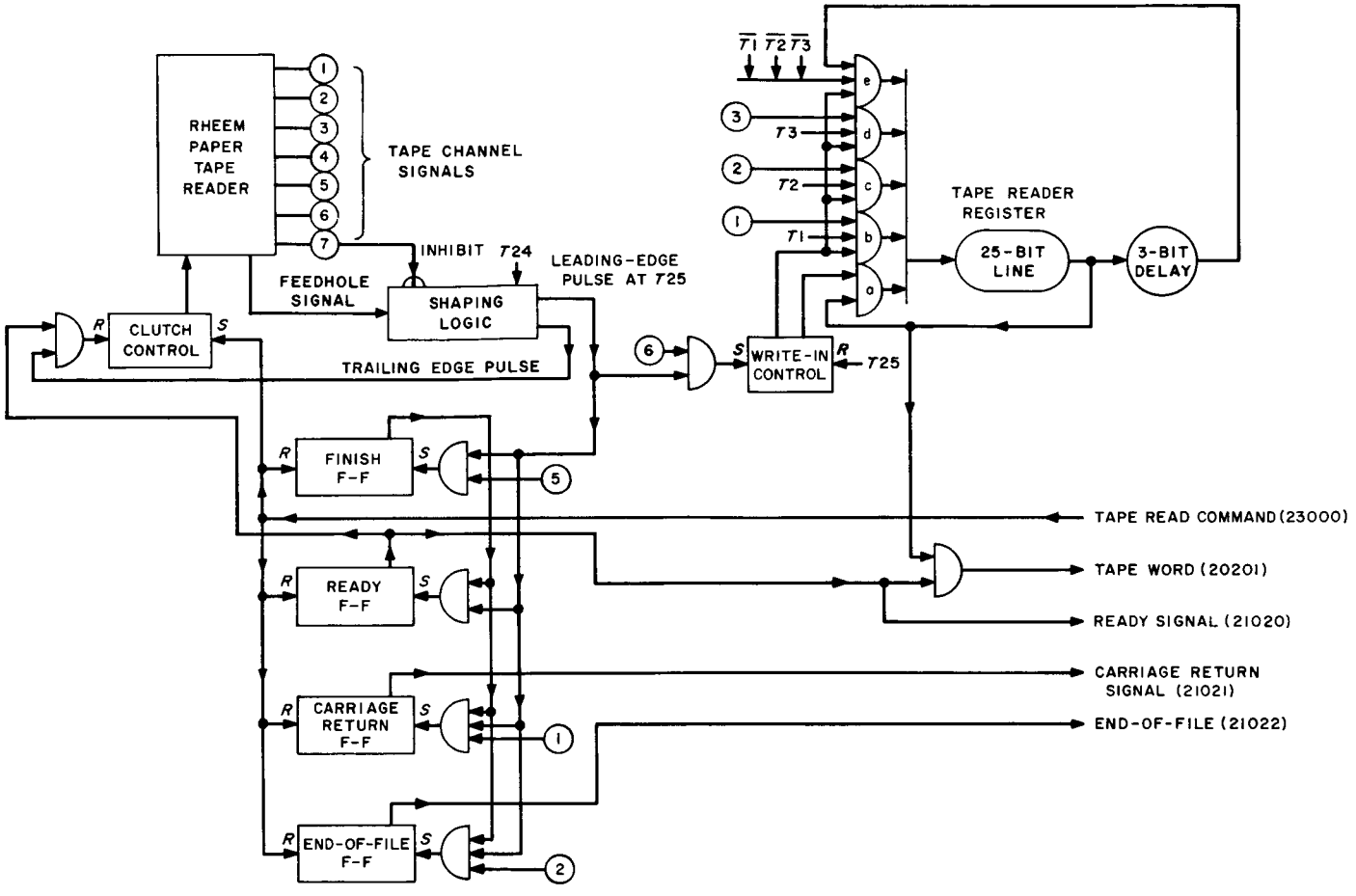

Figure 8. Tape reader

Gate e is disabled by $\overline{T1}$, $\overline{T2}$, and $\overline{T3}$, erasing one octal digit of previous contents to make room for a new digit. At the same time, Gates b, c, and d permit $T1$, $T2$, and $T3$ to sample tape Channels 1, 2, and 3 to write in the new octal digit. After nine characters, a sign and eight octal digits, the old number is completely replaced by a new one.

A punch in Channel 5 allows the leading-edge pulse to set the *finish* flip-flop. This enables the next leading-edge pulse to set the *ready* flip-flop and the *carriage return* or *end-of-file* flip-flops if Channels 1 or 2 are punched, respectively.

The *ready* flip-flop enables the trailing-edge pulse to reset the clutch control and stop the tape between characters if no further reading is called for.

The *ready* flip-flop enables the word in the tape reader register to be made available to Address 20201 and causes Input Signal 21020 to become true.

A portion of a typical tape reading program is shown in Figure 9. Commands 200 and 201 assure that the tape reader is not still in motion from some previous operation, by testing Signal 21020, the *tape reader ready* signal. If ready, the program skips to 202, which sends a 25-μsec pulse to the tape reader, Address 23000. Commands 203 and 204 again test the *ready* signal, awaiting completion of the *read* operation. The Rheem tape reader reads 100 characters per second, so an 11-character word requires about 0.11 sec. When the word is ready, the program skips to 205, which clears the accumulator and adds the contents of the tape reader register, Address 20201. Command 206 tests for end-of-file, proceeding to 207 if Signal 21022 is true or skipping to 210 if signal is zero or false. Command 207 permits a transfer to a special exit routine to handle the last word of a series. Command 210 senses a *tab* code by testing the carriage return signal, 21021, which will be zero if the word ended with a *tab* code. 211 transfers to routine which handles *tab* words. If 21021 is 1, the word ended with a carriage return and is processed by the program in 212 and successive orders. One example of the utility of this type of program would be in the handling of ephemeris data. The tape could be organized in pairs of words, time and frequency, with

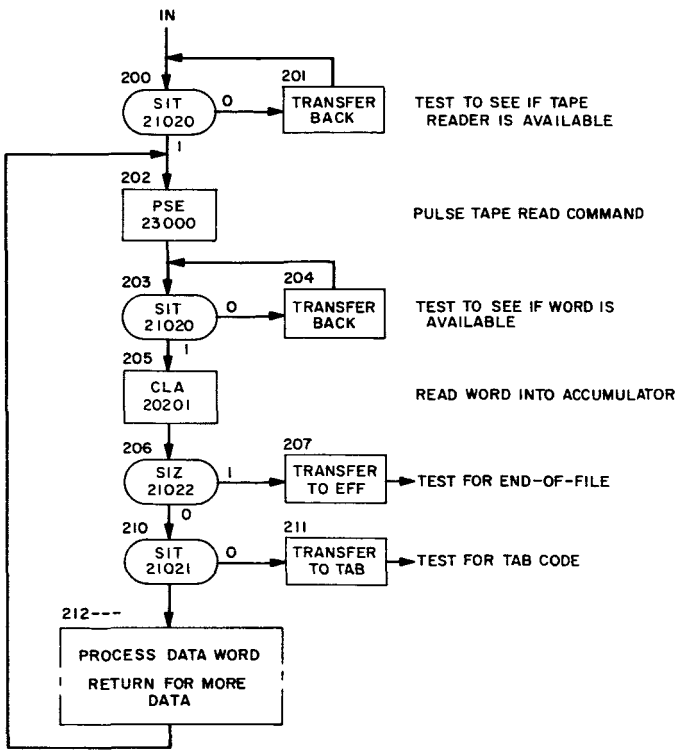

Figure 9. Tape reader program starting in Location 200

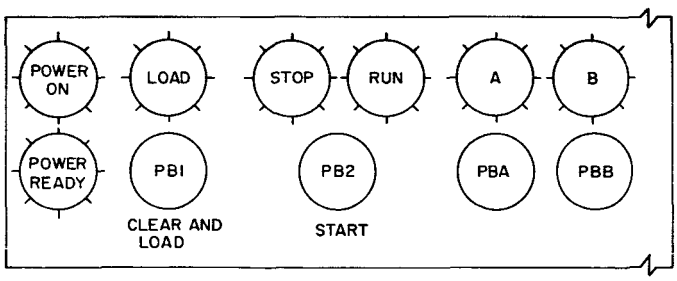

Figure 10. Ranging control panel

time followed by *tab* and frequency followed by *carriage return*, with an end-of-file code at the end of the data to signify cessation of operations.

Another example would be the loading of changes into a program in memory, with a location word followed by *tab* and a data word followed by *carriage return*. The *tab* routine would set up the address into which the *process* routine stored the data word. The end-of-file could then indicate a transfer order to enter the modified program at a specified location.

b. Manual controls for ranging. The manual control panel for the Mod II ranging equipment consists of four push buttons and seven indicators mounted on one 1¾-in. panel (Fig 10). When main power is turned on, the *power on* indicator lights. Pushing the *clear and load* push button turns on the relay supply, lighting a *ready* indicator. The *clear and load* button also initiates action in the manual control section of the CU which first clears memory and resets all output flip-flops and then loads memory from a paper tape. The flip-flops and memory are all cleared within 1.6 msec after pushing the buttons, while the relay supply voltages are not available until 20 to 50 msec have passed, due to the operating time of Relays A and B (Fig 11). This assures that no unpredictable external relay operations will occur while the SPC is being turned on. While the loading operation is in progress, a *load* indicator is lighted.

The second push button is the *start* button which causes the SPC to proceed to the next order in sequence. At the end of the loading operation both the command line and program counter are cleared so the first command will be taken from Address 00000. When the SPC is running, a *run* indicator is lighted, and when it is stopped, a *stop* indicator is lighted.

The two remaining indicators and push buttons are labeled simply *A* and *B*. These are provided to cover situations where the mission requires that some decisions be reserved for a human operator. When the decisions are required, the program will turn on flip-flops to light Indicator *A* and/or *B* to show what type of guidance it needs, and then stop. The operator will push the *start* button and Button *A* or *B*, according to his wishes. Both buttons will be connected as input signals to be interrogated by program, and the operation will then proceed along the selected path. An example of this sort of operation would be in a test program. Following a ranging acquisition procedure, one has the choice of going back to the start and performing the exercise again or continuing to track as the helicopter returns to its base. Here the program might turn on both lights and continue operating, periodically testing Buttons *A* and *B*. Whenever one is pushed, the program would acknowledge by extinguishing the lights and then following the indicated program option.

c. SPC manual controls. While the controls described in the preceding section are sufficient for ranging operations, additional controls are provided for operation of the SPC itself. These are required for checking new programs, where it is desirable to single-step the SPC, and for insertion of small test programs for exercising the machine or peripheral equipment and for making modifications to programs.

The SPC control panel is mounted on Frame VI which carries the clock, manual control logic, control unit, and

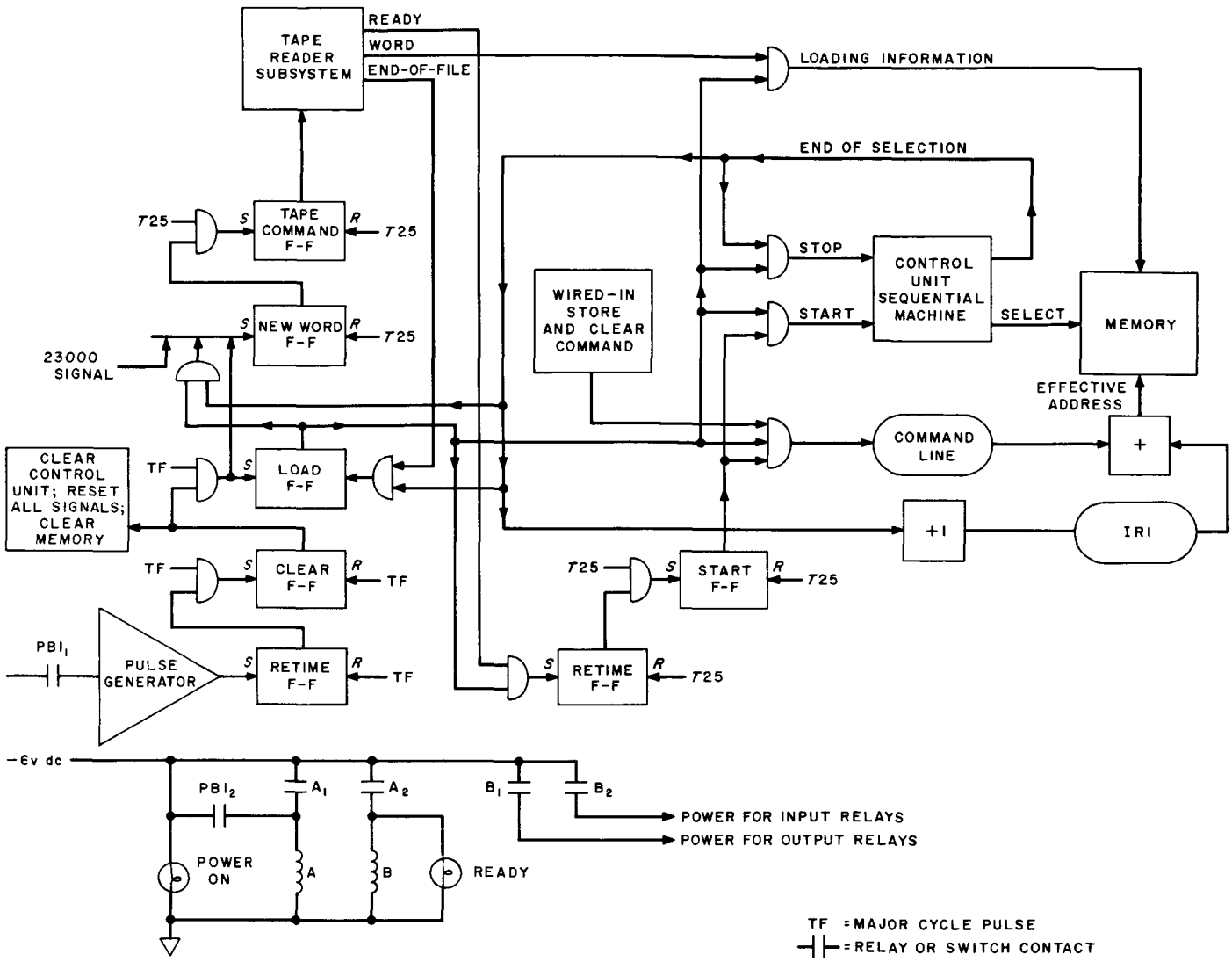

Figure 11. Manual control logic

memory. Two keyboards are provided, a five octal digit address generator and a word generator consisting of sign and eight octal digits. Included on the panel are switches and push buttons to permit loading words into any specified cell in memory, entering a program at any command, running program at full speed, single step modes or stopping on break-point commands which have a "1" in bit 15 of the word. The single-step mode may be modified to run faster by injecting external pulses from an oscilloscope or other test equipment.

These controls are not available in normal operation, and an alarm circuit will be provided which will show the operator if conflicting controls are active.

d. Test programs. As each of the various portions of the machine has been completed, small test programs have been inserted to test for successful operation. For example, a memory test was used which loaded all cells with orders and then processed the orders. If the orders were altered in the memory, the machine would stop.

Another program tested the tape reader by reading the program over and over, comparing each word with that read the previous cycle, the tape having been spliced into an endless loop. This test ran for about 16 hr (overnight) with no errors after reading in excess of 250,000 words.

When the ranging coder assembly was installed in the equipment, a program was written which permitted direct control of all the elementary capabilities of the assembly, such as shifting, synchronizing, and changing combinations. The various options in the program are selected

by a set of 16 toggle switches on an auxiliary manual control panel. (These switches will also be used with the experimental ranging programs used with the early helicopter tests until procedures are well enough established to permit fully automatic operation.) The switches are numbered 0 through 17 (octal) and have Addresses 21000 through 21017. In flow diagrams they will be identified as BP0, BP1, · · · , BP17. Figure 12 is the flow diagram of the coder test program. The entire program required less than 70 words of storage.

e. Ranging acquisition program. The program to be used in the initial L-band ranging transponder helicopter tests will be a modification of the final operational program. The various phases of the operation will be completely controlled by the operator to permit personnel

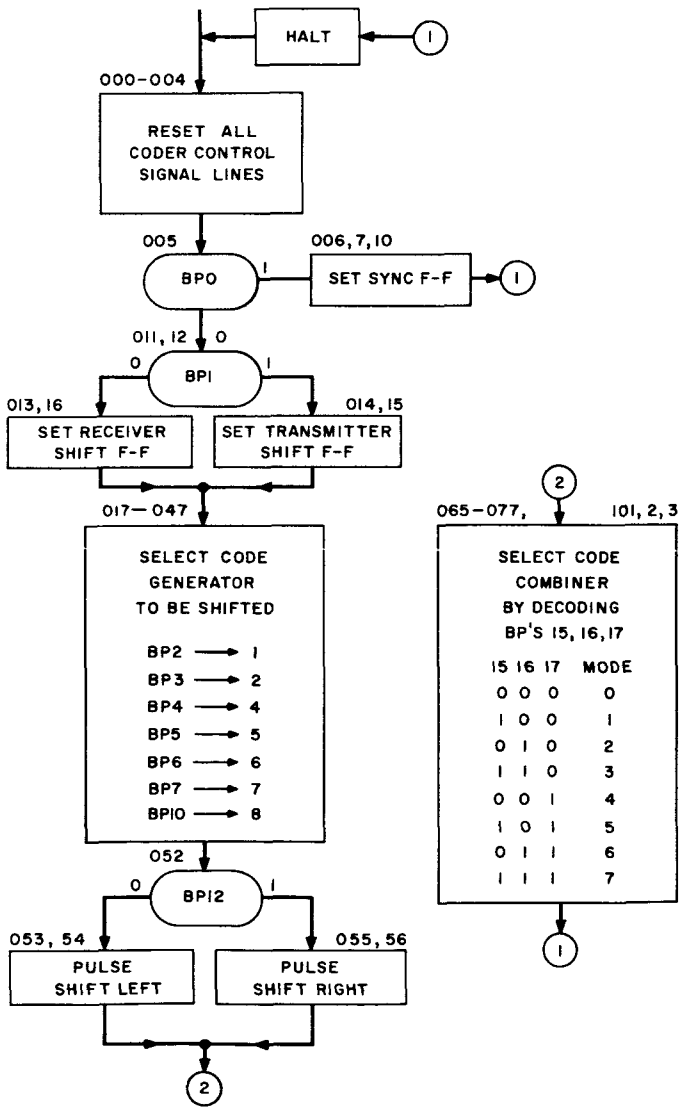

Figure 12. Coder test program

to become familiar with the details of the procedure. The various decisions will be implemented with break-point switches. Later, the correlation meter will be replaced by an analog-to-digital converter; manual tuning of transmitter and receiver will be replaced by control voltages generated by one or more digital-to-analog converters, and the system should be capable of one-button operation.

Figure 13 gives the flow diagram of ranging acquisition program 1. The entire program occupies less than 150 memory cells. The procedure starts by turning everything off, permitting the ground receiver to acquire the transponder RF and clock signals, and then permitting the transponder to acquire the ground transmitter RF. This latter action is recognized by a drop in correlation from 100 to 50%, due to the transponder code changing from pure 500-kc clock to a composite code when the transponder receiver acquires the ground RF.

BP0 keeps the program in this semi-dormant condition until the operator raises BP1 and lowers BP0. At this point the receiver code is turned on, the code combiner is set for Mode 7, Receiver Coder 1 is selected for shifting, and the shift subroutine is entered. This routine interrogates two push buttons to cause a shift left or right each time the appropriate button is pushed. The program contains the necessary logic to assure that one and only one shift is produced for each switch operation, regardless of contact bounce. The operator watches the correlation meter until he notes a jump which indicates that the first code component has been acquired.

Similarly, BP2 through BP6 enable manipulating the other codes to acquire them. BP7 changes the receiver code combiner to insert the full composite code, Mode 6, and the program stops to permit the operator to decide whether or not full correlation has been achieved. BP10 now enables the program to return to earlier acquisition phases if correlation was not satisfactory or to proceed. BP11 will also send the program back or ahead.

At this point, for long range operations, an estimated range would be read in from the tape ephemeris and a computation made to determine how far each code component must be offset to cause the ground transmitter code to be positioned near the transponder's receiver code. The computation consists of dividing the range in microseconds by each code component length in turn, and shifting each code generator by a number equal to the remainder. Following the shifting, the doppler counter is reset, the transmitter clock switch loop is set to sweep position, the transmitter code is turned on and the acquisition voltage manipulated to cause the ground-

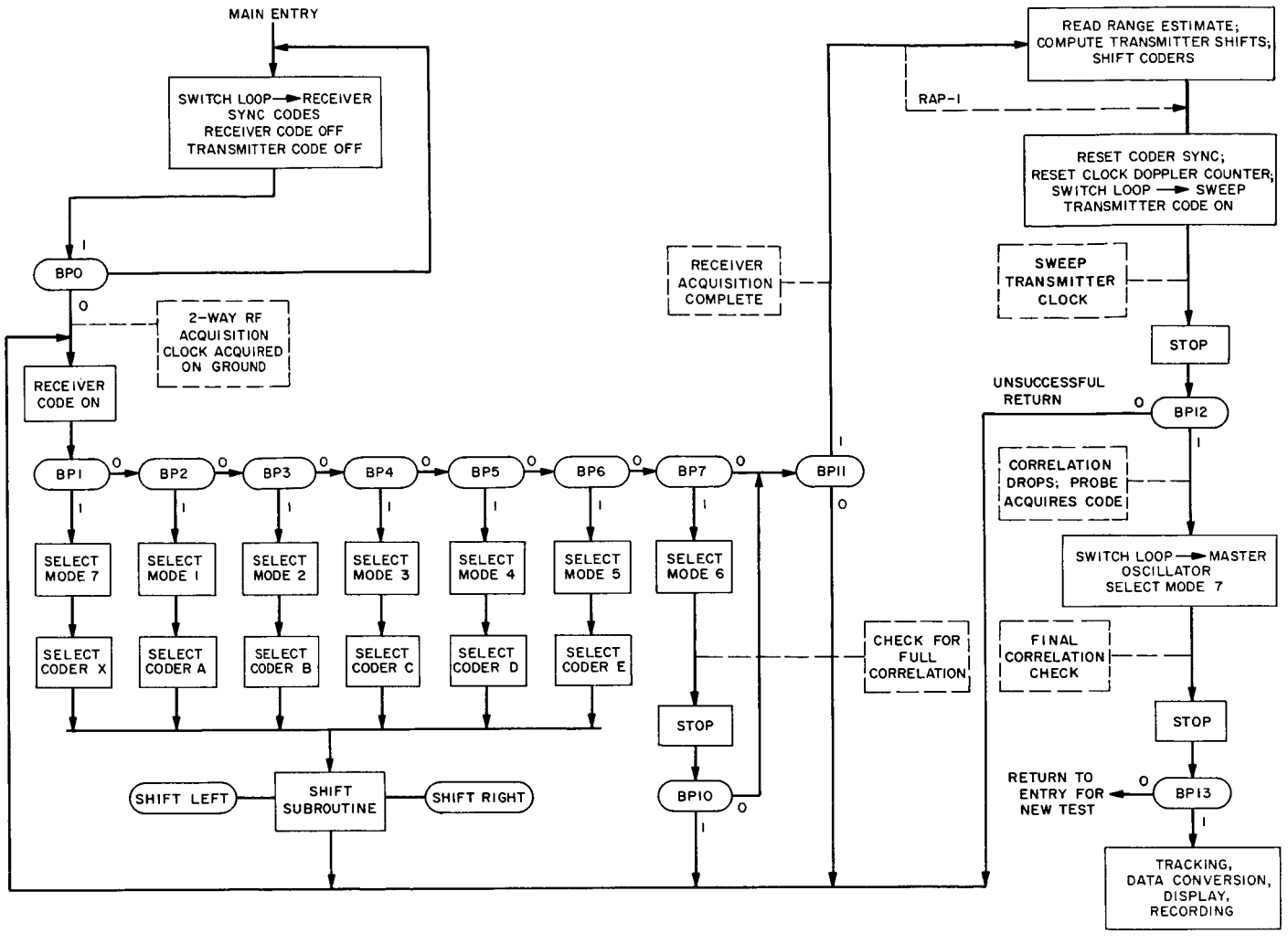

Figure 13. Ranging acquisition program

to-transponder code to sweep back and forth around the transponder's correlation window. The transponder's clock loop will lock up and indicate this fact by changing the transponder-to-ground code to a different function which will be recognized as a 50% drop in correlation on the ground.

During these last operations the machine has been stopped. When started, BP12 can send the program back if the operator suspects that something is wrong or ahead if all is well. The next step is to remove the manual acquisition voltage, turn transmitter clock switch loop to *master oscillator* position, set receiver code combiner to Mode 7, and stop again to permit another check. At this point, if all is well, the acquisition is complete. Range can be computed by adding the estimated range which was used to determine transmitter coder shifts to twice the clock doppler count to give the range in microseconds. This number will be displayed on an oscilloscope during initial tests but later will be converted to the desired units (miles, kilometers, etc.) converted to decimal and printed, punched on tape, displayed and/or sent to other data recording equipment.

In the laboratory, the initial range will be so short that no transmitter code shifting will be required, all the offset being handled by sweeping the transmitter clock. Even helicopter ranges may be handled this way, but the shifting technique will be used to check this mode of operation.

f. Project status. The digital equipment and the 890–960 transmitter–receiver have been interconnected and the acquisition procedure checked, using the coder test program. The transponder and laboratory flight coders have been interconnected and checked out, so the next step will be to assemble the entire system in the laboratory.

Following this, the transponder equipment will be installed in a helicopter and tests made of acquisition time versus signal strength and repeatability measurements made by tracking the helicopter to a known, measurable landing spot.

Figure 14 shows the Mod II ranging equipment with doors removed. The left-hand bay contains test equipment and control panels. Starting at the top of the bay, these units are:

(1) Kin-Tel dc voltmeter (used to indicate correlation).

(2) Tektronix RM 35 oscilloscope.

(3) Acquisition control panel with adjustable voltages that can be used to sweep the receiver VCO for ground RF acquisition and to sweep the transmitter clock switch loop VCO for ground-to-probe code acquisition.

(4) Ranging manual controls.

(5) Panel with break-point switches for manual supervision of program.

(6) Sliding shelf for writing.

(7) Systron counter-timer.

The short unit at the right (Fig 14) is the dolly containing the peripheral equipment used for input and output. On top is the Commercial Controls paper tape punch which will punch 20 characters/sec. Below that is the Rheem Paper Tape Reader which reads 100 characters/sec. At the bottom is a Hewlett-Packard digital printer which prints five 11-digit lines/sec.

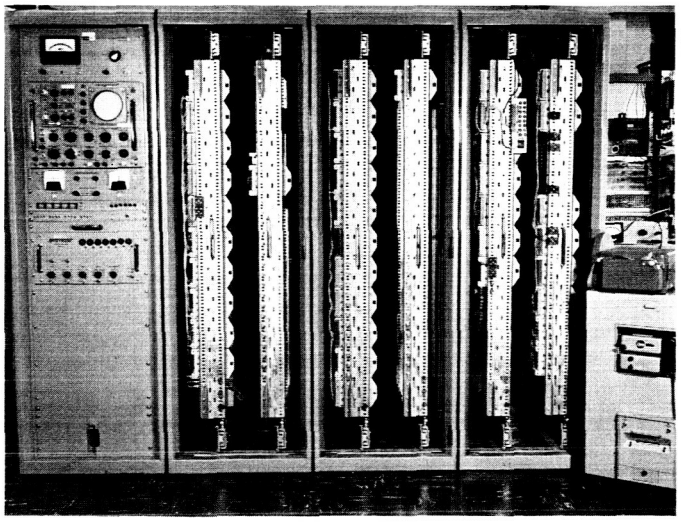

Figure 14. Mod II ranging equipment

The three right-hand bays (Fig 14) contain frames which hold 3C BLOC's and other equipment which can be pulled out on ball-bearing sliders. The six frames are numbered from left to right: I, II, III, IV, V, and VI. Frame I contains the transmitter and receiver coders. Frame II contains the clock doppler counter, doppler couplers and manual controls, and will eventually house the vernier system. Frame III is the input–output interface unit, carrying all the relays, drivers, and other input–output controls. Frame IV currently contains the tape reader logic and will eventually house the punch, printer, and display units. Frame V houses the arithmetic unit and the time clock, and Frame VI contains the machine clock, manual control logic, supervisory manual control panel, control unit, selection system, and memory.

Figure 15 shows Frames IV and VI partially drawn out. Frame IV is the nearer one. The top unit is the in–out address register and some of the YZ-decoders. The second block is the W- and X-decoders for input and the signal and word collection buffers. Block III contains the gating for 1-mc input word lines. The fourth

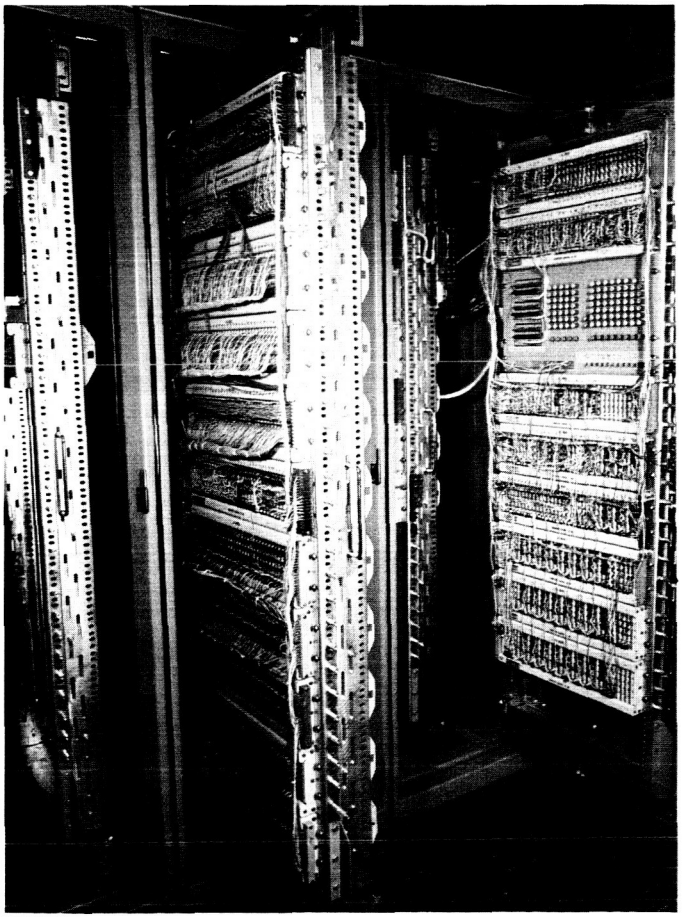

Figure 15. Frames IV and VI pulled out

block selects internal input signals, and the fifth selects external input signals by means of relays. The sixth block contains W- and X-decoders for output and YZ-decoders for setting and resetting output flip-flops. The seventh block is for output 1-mc word gating. The eighth block holds the flip-flops for internal binary signals while the bottom three blocks provide the flip-flops and relays for external binary signals.

Frame VI at right contains the clock, control unit, and memory. The top unit is the machine clock. The second block contains word generators controlled by the address keyboard and the word keyboard on the panel below, as well as the manual control logic for clearing, loading, and starting and stopping the machine. Below the two keyboards are the supervisory manual controls used in code-checking and for manual insertion of programs. The block below the control panel is the control unit sequential machine, program counter, and command line. The next block down provides for selection of index registers, indexing of addresses, and address comparison for selection. Immediately below is the selection block which decodes memory addresses. At the right of these latter two blocks are the three index registers, the three limit lines, and their associated controls. The last three blocks are the memory, the upper two containing eight 32-word lines each for a total of 512 words, and the bottom block containing eight 1-word or "scratch-pad" lines. There is room for another block of 1-word lines at the bottom of Frame VI, and Frame V has room for another four blocks which could expand the total to 1024 words in long lines and 32 1-word lines.

Figure 16 shows a closeup of the doppler unit, consisting of three major units. The top unit is for manual or semi-automatic testing of the equipment. The next unit consists of the operational amplifiers which are used as snap-action limiters to condition the doppler signals for entry into the doppler counter. The third unit is the clock doppler counter, consisting of axis-crossing logic which marks the 0-, 90-, 180-, and 270-deg points on a doppler cycle, a serial adder–subtractor to tally the doppler counts, and a "grabber" line to sample the counter at the beginning of each second under the control of time clock.

Figure 17 shows the interface patch bay mounted between Bays 2 and 3. All signal leads to and from Frame III run to taper-pin terminal blocks, by way of slack cables, so that interface connections can be made at one central point. Cables are braided, laced, or wrapped with Spi-Wrap according to size and stiffness of bundle.

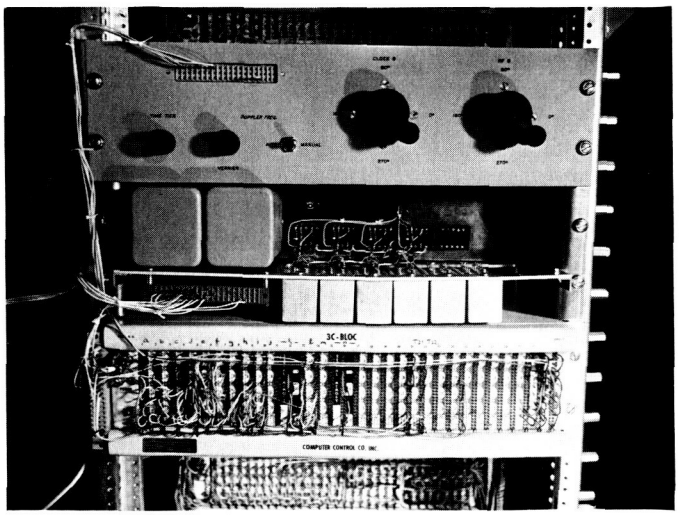

Figure 16. Clock doppler system

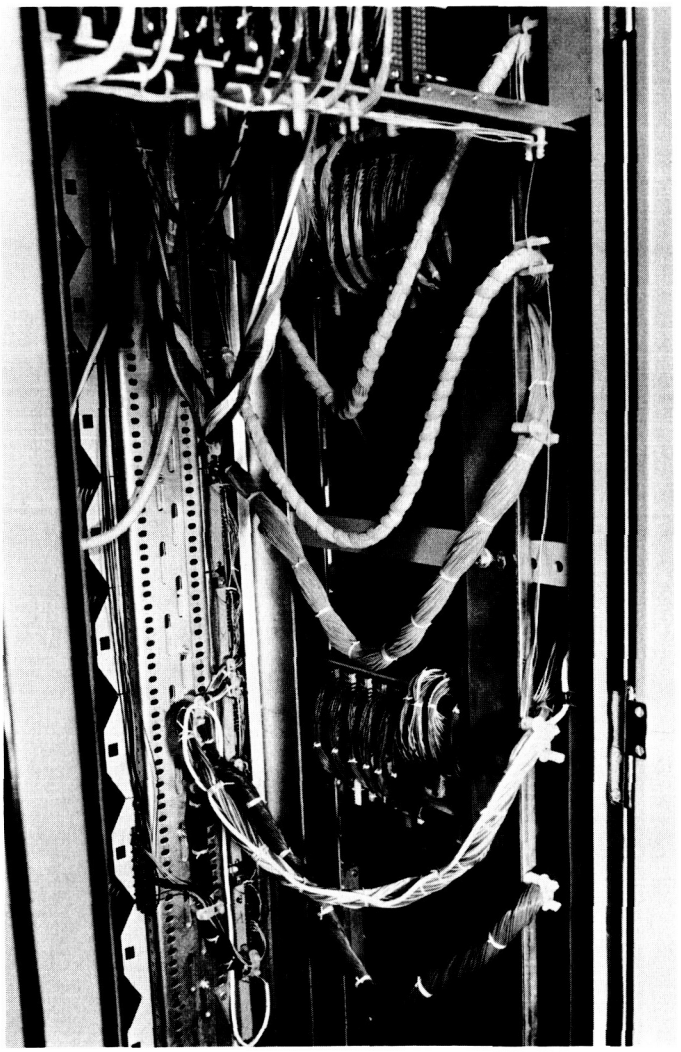

Figure 17. Interface connections

5. Mod II Coders

The Mod II coders are the range code generators associated with the Mod II ranging equipment. In general, they generate the ground transmitter code and the ground receiver code in any ranging system of which the Mod II equipment is a part. Specifically, they generate the ground codes to be used in the transponder ranging system experiment. They also produce the codes necessary for the turnaround transponder ranging system experiment.

The coders are contained in one frame of the Mod II ranging equipment and consist of ten blocks of Computer Controls Company T-Pacs. The subsystem includes the transmitter coder (XC) and the receiver coder (RC), each of which comprises five blocks. The respective code generators in XC and RC are, to all intents and purposes, identical. They are contained, respectively, in Blocks XC I, II, III, IV and RC I, II, III, IV.

Seven component code lengths have been included in the design of the coders. Provision is made for later addition of two more, should this become desirable (Code 3 of length 19, and Code 9 of length 127). The component codes are binary PN sequences which have two-level auto-correlation and whose periods are prime.

Code	Generating coders	Bits
1	XC I and RC I	7
2	XC I and RC I	11
4	XC II and RC II	23
5	XC II and RC II	31
6	XC III and RC III	47
7	XC III and RC III	79
8	XC IV and RC IV	103

The codes of lengths 7 and 31 are maximum-length shift register sequences, generated in standard fashion. The codes of lengths 47, 79, and 103 are shortened maximum length codes of respective lengths 63, 127 and 127, converted to Legendre sequences of equal respective lengths by means of logical conversion matrices. The codes of lengths 11 and 23 are directly-generated Legendre sequences. The Legendre sequences of length N are derived from the formula $X^2 = A$ (modulo N), where $X = 1, 2, 3, \cdots, N/2$, A = position of a "1" in the sequence (all remaining positions being "0").

The master clock for the XC is located in XC V; the master clock for the RC is located in RC V. These master clocks are driven by the transmitter clock and the receiver clock, respectively. The clock frequencies are doubled to generate pulses at the required 1-mc rate. XC I, II, III, IV are driven by slave clocks fed by the master clock in XC V. RC I, II, III, IV are driven by slave clocks fed by the master clock in RC V.

Prior to a ranging acquisition it is necessary to synchronize the transmitter and receiver coders. Specifically, the XC's must be synchronized to the RC's. The command to do so (23041) enters the subsystem as Input 14; its negation is Input 15. This command enters the subsystem asynchronously to the internal timing structure. Two static flip-flops, *sa* and *sb*, and a logical element *s* serve to synchronize the command to the timing structure, utilizing a word detector pulse from Code 1 (1*w*). This is shown in Figure 18.

To synchronize the coders, the output of each receiver code generator is fed into the generator package of the corresponding transmitter code, gated by the *s* pulses. Since this synchronizing command lasts over 125 ms, the respective receiver code has time to take over, and it is not necessary to disable the normal generator logic of the respective transmitter coder. The 1-μsec discrepancy, engendered by making the transmitter code generator follow the receiver code generator, is compensated by a specially introduced equal delay in the receiver code combiner.

Each code component in either XC or RC may be independently shifted left or right by one bit on appropriate pulsed command. This is done, as required, by the explicit introduction of a "1" bit into the generator when normally a "0" would be fed back into it, or by inhibiting the generation of a "1" which was dictated by the feedback logic. The time in the normal sequence when this must occur is determined by a word detector logic circuit. The result is that, in the case of a left shift,

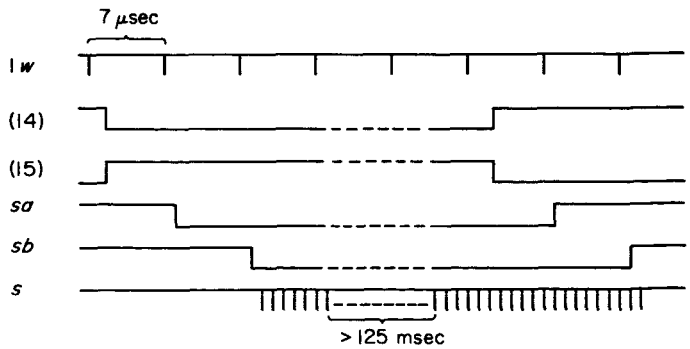

Figure 18. Generation of commands to synchronize transmitter coder to receiver coder

the code is shortened (once) by one bit; in the case of a right shift, the code is lengthened (once) by one bit.

As in the case of synchronizing the coders, discussed above, the programmed commands to shift left (23057) or right (23060) are introduced into XC V and RC V as Inputs 16 and 18, respectively, along with their negations, 17 and 19, respectively. Generation of the shift left commands l (in XC V) and L (in RC V) and the shift right commands r (in XC V) and R (in RC V) is accomplished by logic and timing exactly analogous to that used for generating the internal synchronizing command s. The discussion which follows is restricted to the shifting of Code 1 (length 7) of the XC only, realizing that the arguments apply equally well to all other transmitter and receiver codes with appropriate changes in symbols.

The signals l and r feed into each individual transmitter coder; the signals L and R feed into each receiver coder. A code select signal (level) feeds into each respective coder. Thus, Program Command 23046 activates subsystem Input 1, which gates the shifting functions of both Coders 1. Transmitter and receiver coders are, further, distinguished by the simultaneous activation of subsystem Input 10 (XC select, Command 23044), or 11 (RC select, Command 23045), which go to XC V and RC V, respectively.

Referring to Figure 19, it is shown how Code 1 in the transmitter coder is generated under normal conditions (length 7) as well as under abnormal conditions, when a left shift is introduced (length 6), and when a right shift is introduced (length 8). The left shift (l) and right shift (r) commands obtain from XC V, as previously mentioned, at the indicated times relative to the word detector pulse $1w$. Signals $1l$ are derived from l in that they start 1 μsec after l and end in time with the next $1w$ pulse. Similarly, $1r$ pulses start 1 μsec after r and end 2 μsec after the next $1w$ pulse. The $1p$ pulse is generated 1 μsec after coincidence of $1l$ and $1w$. This pulse inhibits the 1 which would normally be generated by g, 1 μsec later. Coincidence of $1r$ with $1w$ delayed by 2 μsec causes g to generate an extra "1," 1 μsec later. Note that in the logical equations in Figure 19, the output functions are obtained 1 μsec after their input conditions are fulfilled, by the nature of the digital modules employed.

Code combiners are provided to produce all of the transmitter and receiver combinations described in the section above on code structures; they also produce test combinations so that the ground receiver can be alined and so that the ground transmitter can be used, via the offset mixer and oscillator, to simulate the transponder experiment mentioned above.

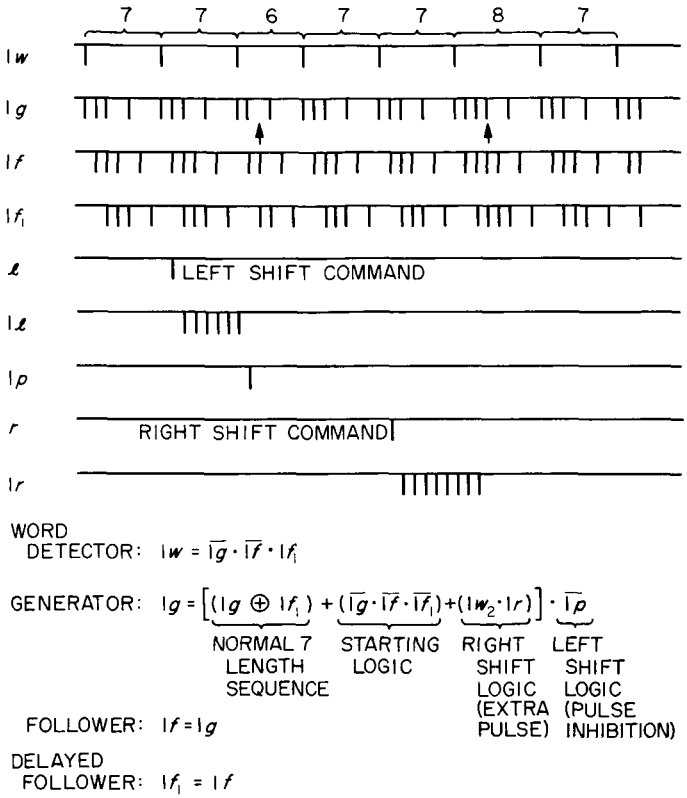

Figure 19. Length 7 code generation showing left and right shifts

6. Ranging Transponder

a. L-band Mod II transponder. The performance characteristics of the Mod I transponder has been reported in *SPS 5* and *RS 36-5*, Volume I. Additional transponder development has resulted in the Mod II design which was required to make the transponder capability compatible with planetary mission requirements. This development has been a joint effort between JPL and the Military Electronics Division of Motorola, Inc.

There were three objectives in the design of the Mod II L-band transponder:

(1) Reduction of the loop noise bandwidth ($2B_L$) from 100 to 20 cps to improve the sensitivity of the receiver for planetary missions.

(2) To incorporate any design changes that will ultimately be required for the S-band ranging transponder.

(3) To improve the design of any circuitry that has been found to be critical.

The Mod I L-band transponder was designed primarily as a lunar communications system. With a loop noise bandwidth of 100 cps and a system noise temperature

of 9170°K, including the preselector, the system threshold signal level is −139 dbm. The 100-cps loop noise bandwidth was selected to maintain less than 0.1-rad transient error during the maximum accelerated period that occurs just prior to booster cutoff. With the noise bandwidth reduced to 20 cps, the Mod II system threshold is 7 db below that of the Mod I. To accommodate the loop noise bandwidth change, it was necessary to extend the linearity of the final IF stage and AGC detector to handle the increased predetection noise power due to a greater noise-to-signal ratio in the AGC loop. The 6-kc bandpass filter in the 10-mc IF amplifier was reduced to 3 kc to partially alleviate this problem. The larger predetection noise-to-signal ratio increases the amount of signal suppression, thereby reducing the detector gain to approximately 1/14 of its strong signal value. Under these conditions, a detector unbalance of 70 mv degrades the system threshold by 1 db. Improvement in the detector design was necessary to maintain the unbalance below 50 mv over the temperature and signal level ranges. In addition, the 20-mc voltage controlled oscillator sensitivity was reduced from a nominal value of 600 to 120 cps/v to obtain the improvement in stability required in a narrow band system.

Simultaneous with the design of the L-band system for a narrower loop noise bandwidth, additional design changes were made to facilitate the use of applicable modules to the S-band ranging system. The block diagram of Figure 20 designates the nine modules that are common to both the L- and S-band systems. The features ultimately desired in these modules are those required

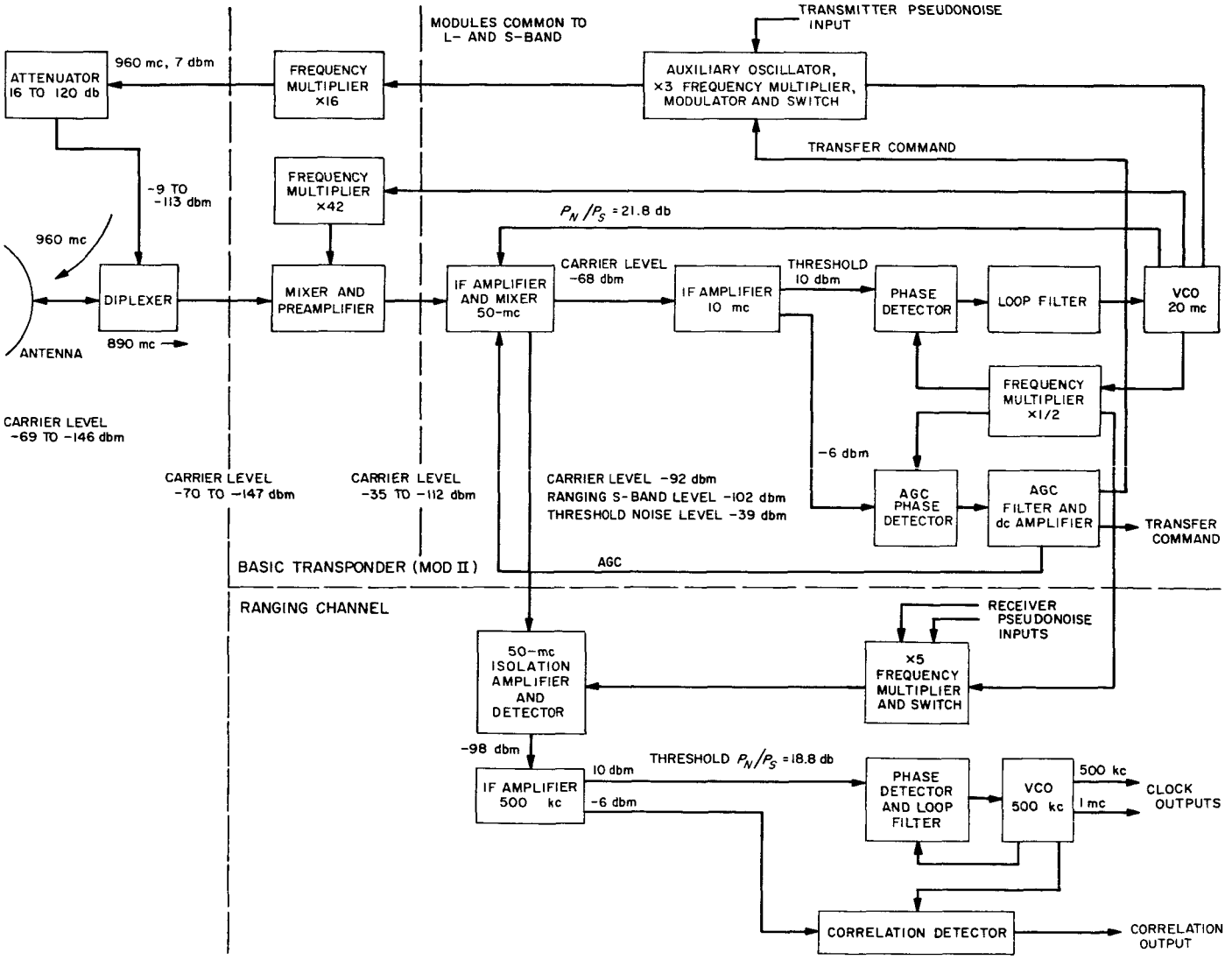

Figure 20. Ranging transponder functional circuit

for the S-band ranging system. To simplify the design of the ranging loop it was decided to operate the receiver at fixed gain beyond the point where the modulated ranging signal is extracted. This eliminates the requirement for gain tracking of the 10-mc IF amplifier in the receiver reference loop and the 500-kc IF amplifier in the ranging loop. In addition, the bandwidth of the IF amplifier at 50 mc has been increased to provide a ranging channel bandwidth of 3.3 mc.

Limiting the automatic gain control to the first three stages of the 50-mc IF amplifier means that several stages of IF amplification operate at fixed gain directly preceding the detector. As a result of this, under strong signal conditions, thermal noise exists at the output of the IF amplifiers. The amount of fixed gain in the receiver immediately preceding the detector has been selected to maintain the noise level 40 db below the signal level. Figure 20 shows the gain distribution as well as signal-to-noise ratios in the IF amplifiers at the L-band system. Additional design parameters of the Mod II transponder are shown in Table 4.

Table 4. Mark II transponder design parameters

Component/parameter	Value	
Receiver		
Noise temperature, including preselector, °K	9170	
Threshold signal level, unity P_N/P_S in $2B_{Lo}$, dbm	−146	
Dynamic range, to threshold, dbm	−70	
Maximum receiver RF gain, db	16.3	
Ranging channel bandwidth, mc	3.3	
APC loop, threshold design values		
Loop noise bandwidth $2B_{Lo}$, cps	20	
Suppression factor α_0	0.0723	
Detector gain K_M, v/deg	0.175	
VCO gain at 20 mc K_V, cps/v	120	
Frequency multiplication factor	44.5	
Predetection bandwidth, kc	3.0	
Ranging loop, threshold design values		
Loop noise bandwidth $2B_{Lo}$, cps	1	
Suppression factor α_0	0.0723	
Detector gain K_M, v/deg	0.245	
VCO gain K_V, cps/v	4.0	
Predetection bandwidth, cps	150	
AGC loop	Threshold	Strong signal
Receiver gain K_A, db/v	5.0	5.0
Detector gain K_D, v/db	0.10	0.10
Amplifier gain K, v/v	7.15	7.15
Noise bandwidth $2B_L$, cps	0.1	1.0

Concurrent with the design of the Mod II system, the supply voltages were reduced from plus and minus 20 v to plus and minus 15 v. Maintaining the same current drains, the power consumption has been reduced from 10.0 to 7.5 w.

The modules of the Mod II transponder are packaged in a chassis of the same basic design as the standard *Ranger* units (Fig 21). The new packaging has reduced the weight of the transponder from 17.5 to 10.5 lb. Since *Ranger*-type packaging, designed to be an integral part of the spacecraft structure, will permit the use of a lighter hexagon section chassis for the communications subsystem, an additional weight reduction will be realized.

b. Ranging channel redesign. The general design characteristics of the ranging channel are identical to those of the experimental ranging transponder described in *RS 36-9*. The important difference is that the circuits have all been transistorized to make them suitable for flight use. The module packaging is identical to that of the basic Mod II transponder. Essential characteristics of the modules appear in Table 4. Changes from the ranging channel of the experimental ranging transponder are summarized in the following paragraphs.

The 50-mc isolation amplifier serves three separate functions. It provides forward gain to the 50-mc modulated signal. In addition to this, it must provide isolation in the reverse direction, to prevent the 50-mc phase detector reference signal from re-entering the receiver. Finally, it must provide sufficient bandwidth for the forward signal, but still have good rejection to spurious signals at 40 and 60 mc. For this purpose the amplifier is built with a wide bandpass characteristic centered at 50 mc, and traps are added to give attenuation at 40 and 60 mc.

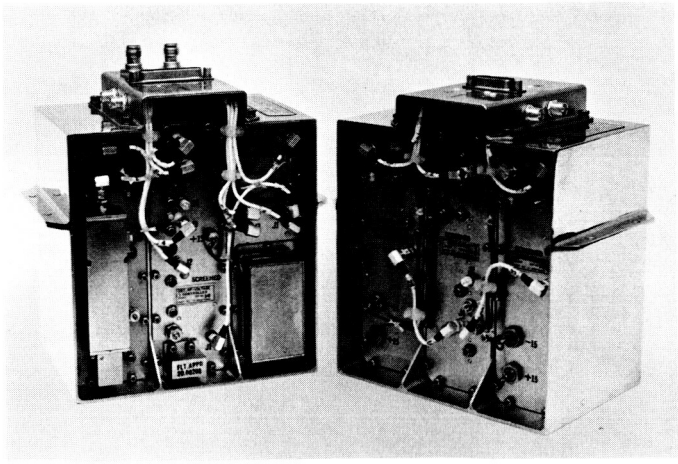

Figure 21. Mark II L-band transponder

The 50-mc phase detector is a standard push–pull design, using two high speed, high conductance diodes. The poor coupling attainable in the transformers at 50 mc and the fact that the diode impedance varies rapidly with drive, makes careful impedance matching a necessity, in order to minimize the conversion loss. The present design achieves a conversion loss of 11 db from modulated 50-mc input to 500-kc output.

The bandwidth of the 500-kc IF amplifier is limited to 150 cps by a crystal filter. This value is chosen to give the same signal suppression factor as exists in the RF carrier tracking loop.

The 500-kc phase and correlation detectors are identical except that the phase detector has a hard limiter at the signal input. The circuit is essentially that of a standard push–pull phase detector and is similar to the 50-mc phase detector mentioned above, except that the output is dc. The phase detector module also includes the tracking filter for the ranging phase locked loop. The correlation detector module includes a low pass filter for the correlation signal. This filter has a time constant of 3 sec.

The 500-kc voltage controlled oscillator is a crystal oscillator which may be tuned over a narrow frequency range by the use of a variable capacitance diode. It has four independent outputs. Two are the references for the phase and correlation detectors, one is the 500-kc clock signal to the digital code generators, and one is doubled in frequency to provide a 1-mc timing signal for the code generators.

The phase switch and $\times 5$ frequency multiplier which were described in *RS 36-9* have been considerably improved. The filter in the $\times 5$ circuit has been redesigned to reduce the amplitude of the unwanted harmonics, especially 40 and 60 mc. Changes to optimize the performance of the phase switch have resulted in the waveforms shown in Figure 22. Figure 22 is triggered on each half cycle of the 500-kc square-wave driving signal, thus demonstrating the 180-deg phase shift of the 50-mc carrier. The spectrum of the waveform shown has a carrier suppression of 55 db.

It is expected that the absolute phase shift vs temperature will be critically important for nearly all the modules of the receiver and ranging channel. At the present time only the $\times 5$ and phase switch circuits have been studied in this regard. The other modules are currently undergoing measurements and will be compensated where necessary.

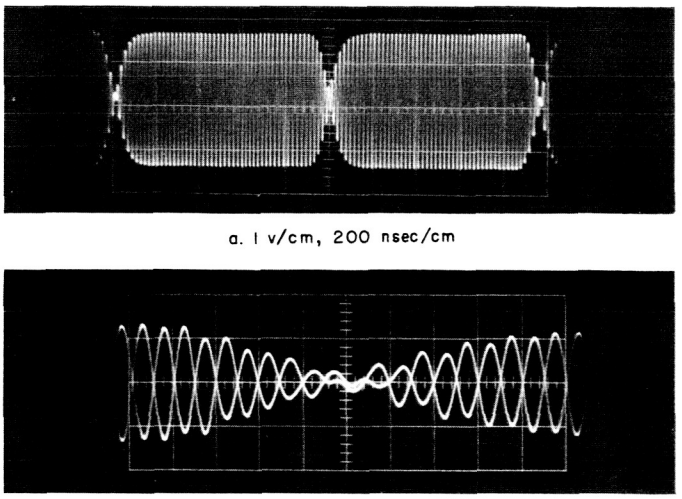

a. 1 v/cm, 200 nsec/cm

b. 1 v/cm, 20 nsec/cm (DOUBLE TRACE)

Figure 22. Phase switch output with square wave drive

Figure 23. Helicopter ranging transponder

c. Ranging experiment transponder. The Mod II L-band transponder being used in the ranging experiment has been modified to increase the bandwidth of the preamplifier. The transponder, together with the prototype ranging channel and a commercial power supply, have been assembled into a cabinet (Fig 23) for this experi-

ment. This system represents the initial design. Development is continuing to finalize the design for the S-band *Mariner* system.

7. Transponder Coders

The transponder coders generate the ranging codes for the transponder as described in the section on code structure. Because of size and weight requirements, no attempt is made to make the transponder coders general purpose; equipment is limited to that required for a particular mission.

A functional block diagram of the spacecraft transponder coding equipment is shown in Figure 24. The peripheral input–output boxes perform the necessary electrical transformation of timing, control, and code signals to and from the digital equipment in the sequence generator. Design of the input–output circuitry was based on compatibility with space-borne receiver and transmitter circuitry and is capable of operation in a space environment. The digital logic in the sequence generator is presently implemented with commercially available ground type equipment (Computer Control Co., S-Pac Series). Logic circuitry that will consume minimum power and will operate over a wide temperature range is presently in the design phase. The speed and fan-out capability of the logic is tailored to synchronous sequential switching applications such as the sequence generator, but will have general purpose applications also. A prototype spacecraft sequence generator should be developed by May 1962.

Sequence generator. The sequence generator is built around a base of six component generators. Method and

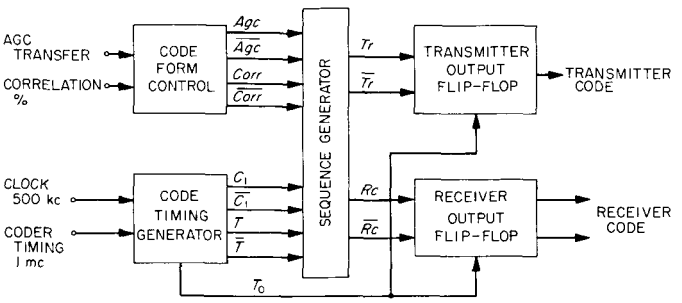

Figure 24. Transponder coding equipment

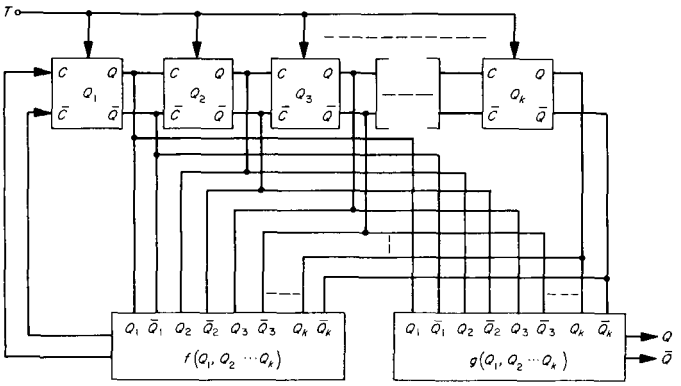

Figure 25. Code component generator

logic used to generate the code components is shown in Figure 25 and Table 5. The combined code sequence used in the receiver loop is a linear combination of the code components:

$$R(X, A, B, C, D, E) = X + A + B + C + D + E \quad (1)$$

Table 5. Code component generation

Component	Length	Type	Generation method	k	f ( )	g ( )
X	7	Maximal length	Direct	3	$X_1X_3 + X_1X_3 + X_2X_3$	X_1
A	11	Legendre	Direct	5	$A_1A_4 + A_2A_5 + A_3A_4A_5$	A_1
B	23	Legendre	Direct	7	$B_3B_5B_6 + B_3B_4B_5 + B_1B_4B_6 + B_1B_5B_7 + B_5B_6B_7$	B_1
C	31	Maximal length	Direct	5	$C_2C_5 + C_2C_5 + C_1C_2C_3C_4$	C_1
D	47	Legendre	Indirect	6	$D_5D_6 + D_5D_6 + D_1D_2D_3D_4D_6 + D_1D_2D_3D_4D_5$	$D_1D_3D_4D_6 + D_1D_2D_3 + D_1D_2D_5D_6 + D_2D_3D_4D_5D_6 + D_1D_4D_5 + D_1D_2D_4D_5 + D_1D_3D_5D_6 + D_1D_2D_5D_6$
E	103	Legendre	Indirect	7	$E_6E_7 + E_6E_7 + E_1E_2E_3E_6E_7$	$E_2E_3E_4E_5E_6E_7 + E_2E_3E_6E_7 + E_1E_2E_3E_4E_7 + E_1E_3E_4E_5E_6 + E_3E_4E_5E_6E_7 + E_1E_2E_3E_4E_6 + E_1E_2E_3E_4E_5E_7 + E_1E_2E_4E_5 + E_1E_2E_3E_4E_5E_6 + E_3E_4E_5E_6 + E_1E_2E_3E_4E_6 + E_1E_2E_6E_7 + E_1E_2E_3E_4E_6 + E_3E_4E_5E_6E_7 + E_1E_2E_3E_6E_7 + E_1E_2E_3E_4E_7 + E_2E_4E_5E_6E_7 + E_1E_5E_6E_7$

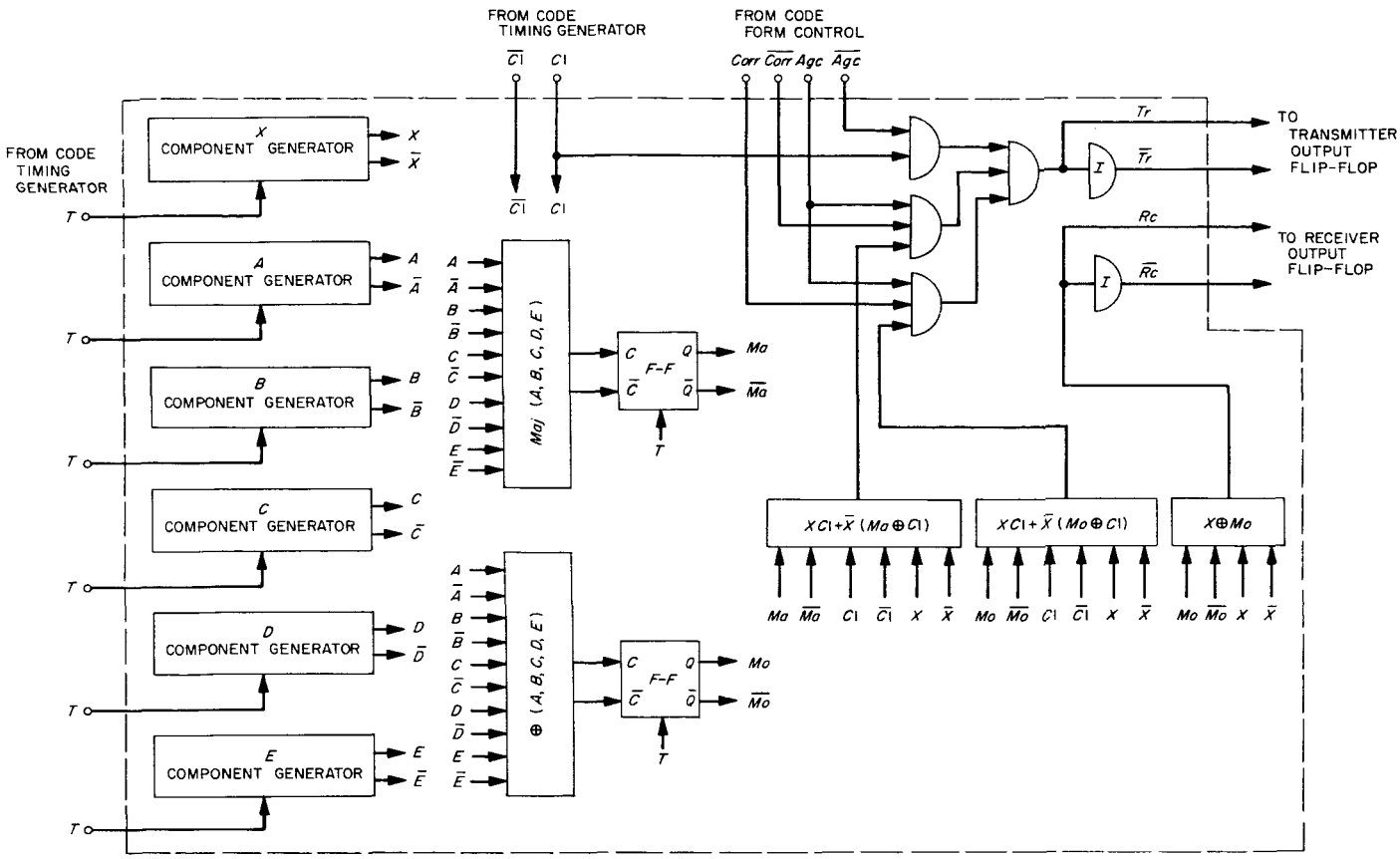

Figure 26. Sequence generator

The transmitter code is of the form:

$$T(X, G, C1) = X \cdot C1 + \dot{\bar{X}}(G + C1) \qquad (2)$$

as described previously in the section on code structure.

Sequence G is altered in accordance with the detection situation in the transponder receiver. The present control parameters are RF lock indicated by transponder AGC transfer and clock lock indicated by present correlation in the clock loop. A detailed block diagram of the sequence generator appears in Figure 26.

Code timing generator. The timing reference for the code timing generator is the local oscillator in the clock detection loop. A functional block diagram of the timing system is shown in Figure 27. The 500-kc clock frequency and the doubled clock frequency are fed to threshold detectors which sense the zero crossovers of the input sine waves. The 500-kc reference is then translated to give the required electrical representation of "1" and "0" to mate with the sequence generator. Here it is retimed by the sequence generator timing and handled as another code component.

The 1-mc signal is the critical timing reference. Since it controls the symbol transitions of the output code sequences, any error introduced reveals itself in the range measurement. For this reason, the 1-mc reference is split at the input to the timing generator. The machine timing to the sequence generator requires high fan-out along with the generation of a particular pulse waveshape. The distortion introduced in this translation may be bypassed by retiming the output with the input timing signal. This minimizes the contribution to range error introduced in the coding process and, furthermore, allows for less critical timing requirements in the sequence generator.

Output flip-flops. The transmitter code and receiver code output flip-flops provide: (1) a single bit buffer storage for retiming of the coded sequence, and (2) electrical translation of the "1" and "0" levels to satisfy the input requirements of the modulator and demodulator in the transponder.

Present design configuration is a transistor gated, DCTL, delay flip-flop. Minimum response times are achieved by using high speed switching transistors and

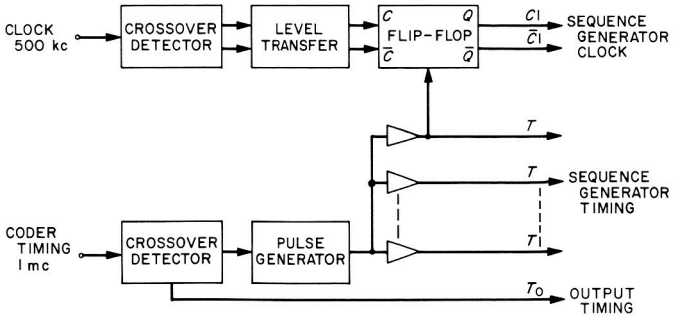

Figure 27. Code timing generator

Figure 28. Helicopter antenna installation

by limiting collector and base saturation circuits. Through a bias adjustment in the crossover detector, the start of an output symbol transition can be selected to occur anywhere within a ± 20 nsec range with reference to the input 1-mc sine wave. The difference in the start of "$1 \rightarrow 0$" transition and "$0 \rightarrow 1$" transition is less than 5 nsec at 25°C. Timing tolerances as a function of temperature/supply-voltage variations are to be determined.

Code form control. The code form control circuitry receives input information from the AGC transfer flip-flop in the receiver and a percent correlation indication from the in-phase detector in the clock loop. The AGC input is already a two-state variable, and must only be conditioned to comply with the input requirements of the sequence generator. The clock correlation level enters a decision circuit that provides a two-state output indicating whether or not the received code is acquired. The detection level is set so that false indication of acquisition

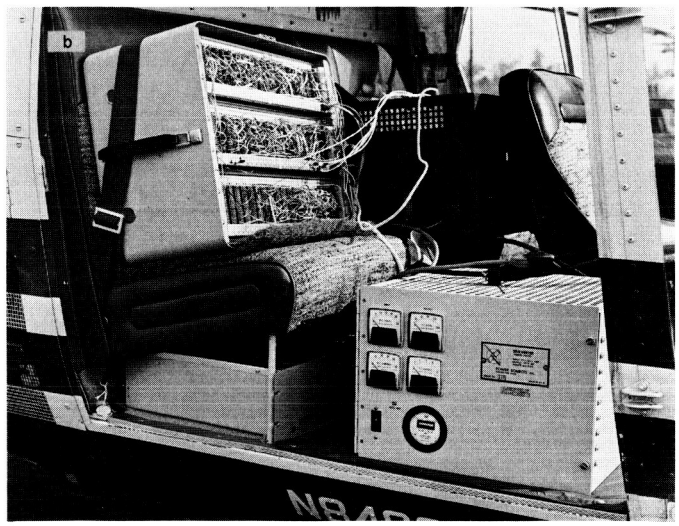

Figure 29. Interior view of helicopter installation

or false indication of its loss occurs with near-zero probability. Precise determination of this decision level is incomplete and must await the forthcoming integrated system tests.

8. Helicopter Installation

The helicopter installation consists of arranging the transponder and transponder coder (together with the necessary power supplies) in the helicopter, mounting an antenna for the transponder, and providing communications from the operator to the ground equipment operator.

a. Antenna installation. A vertically polarized, omnidirectional, ground plane antenna is installed on the under side of the helicopter as shown in Figure 28. The gain of the antenna is approximately unity.

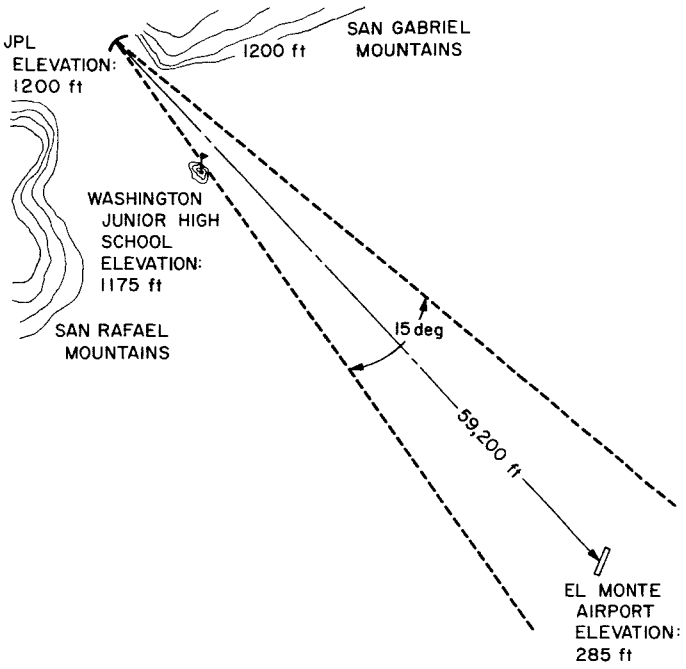

Figure 30. Proposed helicopter flight path

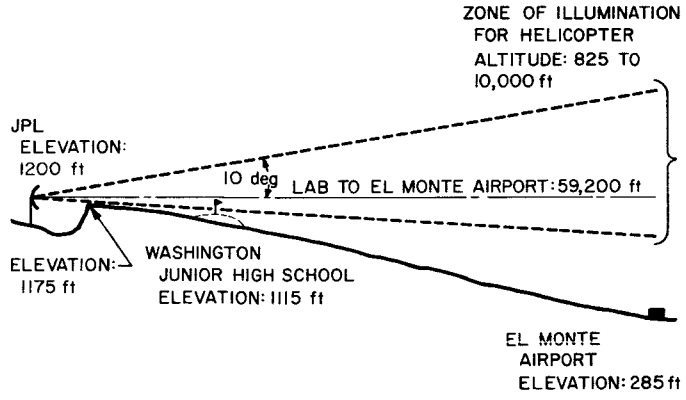

Figure 31. Profile of maximum allowable helicopter altitude for detection

b. Transponder and coder installation. Figure 29a is an internal view of the helicopter showing the transponder, coder, and their respective power supplies. In order to facilitate removal of the equipment during periods when the helicopter is used for passenger service, the transponder and coder are in separate cabinets. Since the helicopter will operate only in relatively calm weather with no violent maneuvers required, it is not necessary to bolt the equipment to the helicopter. A microphone is also provided to enable the operator to talk to the ground equipment operator in the laboratory.

c. Power supplies. Both the transponder and coder cabinets contain regulated power supplies requiring a 60-cps, 115-v source with a total 500 v-amp capability. The available power in the helicopter is 28 v dc at approximately 30 amp. Therefore, it was necessary to purchase and install the 500 v-amp sine-wave inverter shown in Figure 29b.

d. Helicopter flight path. Figure 30 is a map showing the proposed flight path of the helicopter. Due to the surrounding mountains, El Monte, California, is the only open area available. The helicopter will fly a straight line course from the pad at JPL to El Monte and return. It is on the return leg that the ground station will acquire and range the helicopter. Due to the wide (15 deg) beamwidth of the ground antenna, it is anticipated that tracking of the helicopter by manual positioning of the antenna will not be required.

Figure 31 is an elevation map along the flight path of the helicopter. Again, the wide beam of the ground antenna enables the helicopter to remain inside the beam without repositioning the antenna.

B. Low Noise Systems

1. Cassegrain System, 960 mc

a. Antenna temperature and calibration studies. A series of radiometric measurements with the 960-mc Cassegrain antenna at Goldstone have been completed. *SPS 37-13*, Volume I listed five objectives and the initial results of Objectives (1) and (5); those objectives were:

(1) The measurement of minimum absolute antenna temperature for a "quiet" sky. (The 85-ft antenna is pointed approximately vertical and at a region away from the plane of the galaxy and away from the Sun and the Moon.)

(2) Absolute antenna temperature versus elevation angle to evaluate the effect of the sidelobe and backlobe ground temperature contribution. (There is an atmospheric contribution which is strongly dependent on elevation angle (*SPS 37-13*, Vol I, p 70). The ground temperature contribution is dependent on the elevation angle, the type of terrain, the height of the terrain, and the antenna polarization.)

(3) The measurement of antenna temperature for several strong radio sources. (Radiometry methods appear to provide the most promising technique

for future gain calibrations of large antennas. Precise temperature measurements of a source at different hour angles can provide a test of gain variation with orientation of the antenna due to deflections of the antenna surface and feed support structure.)

(4) Measurements of radio source position versus antenna orientation. (Using reliable calibrations of radio source positions (*RS 36-13*) and removing the effects of atmospheric refraction (Ref 1), some knowledge of the over-all antenna pointing accuracy may be obtained.)

(5) Measurements of the extra atmospheric background level by means of absolute antenna temperature measurements. (An upper limit of $T_{bgd} \leq 4.0°K$ for quiet zenith conditions at 960 mc is quoted in *SPS 37-13*. This value is expected to decrease rapidly with increasing frequency.)

The minimum antenna temperature for Objective (1) was measured on a number of occasions. The antenna was pointed at the zenith, or at a declination of 27 deg (the declination of the galactic pole), on the local meridian. The antenna temperature was then calibrated for periods of many hours. As the result of averaging data over a period of 1 hr for several days' observations, the minimum antenna temperature T_A (min) near the galactic pole was initially (*SPS 37-13*)

$$T_A \text{ (min)} = 10.5°K \pm 2.0°K$$

A test to determine the effect of the dish surface cracks on minimum temperature and gain was performed and the cracks between the panels were covered with aluminum tapes (*RS 36-13*). After the cracks were covered, a lower value was obtained:

$$T_A \text{ (min)} = 9.5°K \pm 2.0°K$$

Impedance tests of the antenna and all of the reference loads were performed before and after each measurement period. The impedance tests were performed using either a slotted line or a reflectometer. A reflectometer is most valuable because bandwidth may be tested and any possible mismatch off center frequency will be discovered. The impedance match of the helium cooled load (Ref 1) and the antenna have the most critical effect on the temperature measurement accuracy.

Measurements of antenna temperature as a function of hour angle were carried out on November 11, 1961. A rotatable linear feed was used to scan in hour angle while the declination was kept constant at 332.2 deg.

Orthogonal linear modes were obtained by switching between ports of a turnstile junction. The junction was first alined to have the E-vector either in the north–south or east–west direction. In the second scan the junction was alined with the vertical and horizontal axis, when looking at the horizon. Figure 32 presents the results.

At zenith with this configuration the T_A was 11°K. A curve of the form

$$T_A = \frac{a}{\cos(90° - \theta)} - a + T \text{ (zenith)}$$

was fitted to the data from zenith to 10 deg above the horizon and the average temperature was computed

$$T_A = \frac{4.2}{\cos(90° - \theta)} - 4.2 + 11°K$$

take

$$\overline{T}_A = \frac{\int_{\Omega_1} T_A \, d\Omega}{\int_{\Omega_1} d\Omega}$$

where Ω_1 is the solid angle above 10-deg elevation

$$\overline{T}_A = 15.7°K$$

The decrease in antenna temperature due to covering the surface cracks with aluminum tape reduced the minimum zenith temperature to 9.5°K (from 11 deg for this measurement). Then

$$\overline{T}_A = 14.2°K$$

and

$$\Delta\overline{T}_A = \overline{T}_A - T_A \text{ (min)} = 4.7°K$$

Tests of radio source temperatures were limited to a few of the stronger sources. Table 6 lists the sources tested prior to January 6, 1962 with the measured antenna temperatures. The measured temperatures are corrected, also, for atmospheric attenuation (Ref 2) and transmission line loss. Figure 33 is a typical plot of antenna elevation angle and attenuation for the Crab Nebula. The measured and corrected antenna temperatures for the Crab Nebula are shown in Figure 34. It may be noted from Figure 33 that the differential attenuation between the meridian crossing and a local hour angle of ±75 deg is less than 1.0%. Using all measurements (37) in this region, the rms temperature is 96.4°K and the standard deviation is 2.0°K. If data is used only for hour angles less than 60 deg, the differential attenuation is less than 0.5%, and the rms temperature becomes 96.6°K. The change is insignificant and was not used. Correcting for atmospheric and transmission line losses, the antenna temperature of the Crab Nebula becomes 97.9 deg. There is not sufficient data to speculate about the source antenna

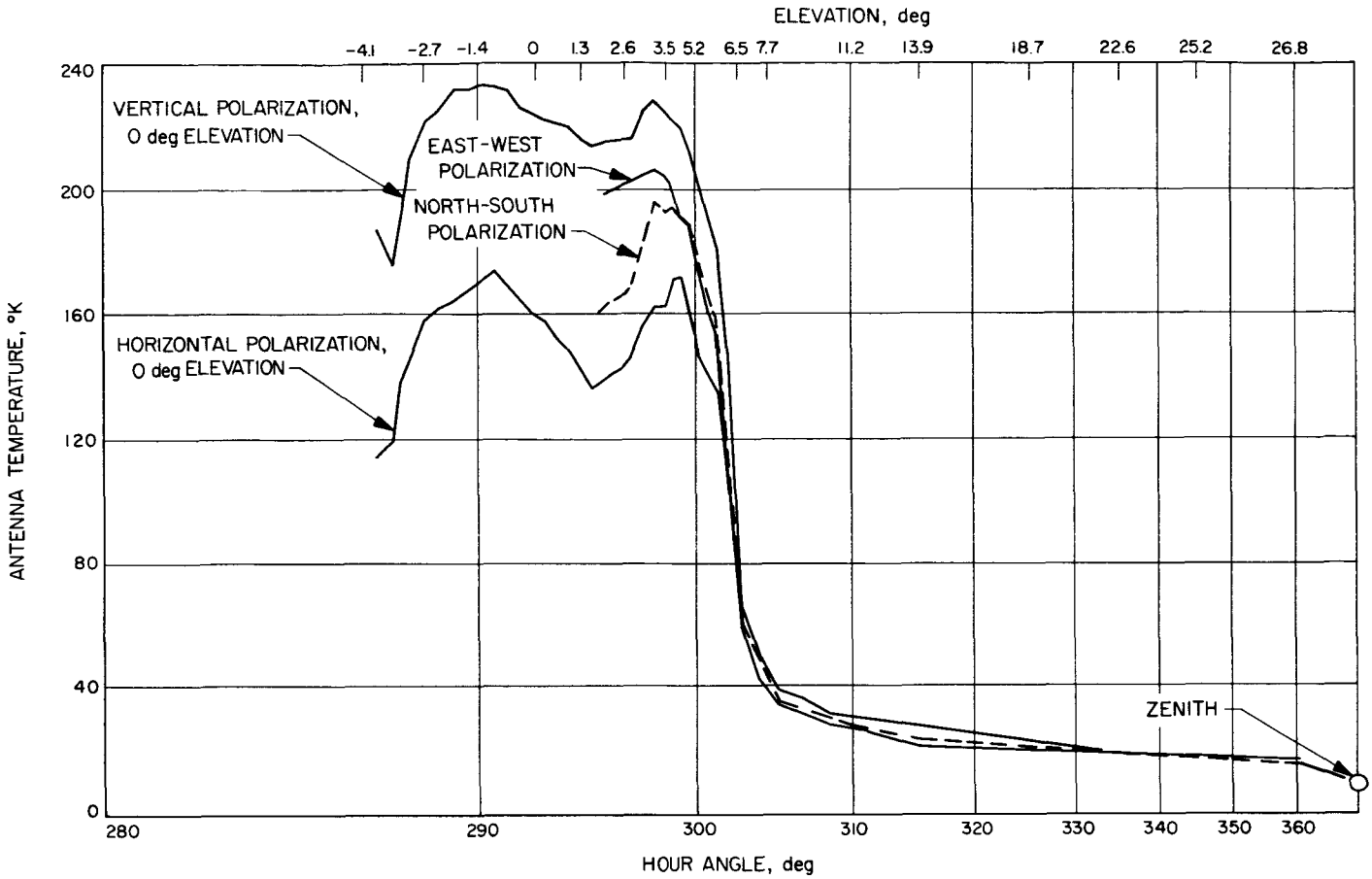

Figure 32. Antenna temperature vs local hour angle, 960 m

Table 6. Antenna temperatures due to sources

Source	Antenna polarization	Number of tests	Test dates	Antenna temperature above background, °K	Temperature corrected for atmospheric and line losses, °K	Measured temperature ratio to M87 (Dec 1961)	Temperature ratio to M87 CIT-radio observatory
Cassiopeia A	Linear	6	12/29/61	321 ±12	326	11.6 ±0.8	10.4 ±0.5
Cygnus A	Linear	10	12/29/61 1/3/62 1/5/62	218 ±8	221	7.9 ±0.6	7.2 ±0.4
Crab Nebula	Linear	34	12/29/61 12/30/61 1/3/62 1/4/62	96.4 ±2 peak	97.9	3.27 to 3.49 ±0.2 (for one ratio)	3.43 ±0.15
Orion	Linear	4	1/5/62	33.4 ±1.5	33.9	1.21 ±0.10	1.20 ±0.03
M87	Linear	10	1/3/62 1/4/62	27.6 ±1	28.0	1.00	1.00
Hercules A	Linear	6	11/13/61	5.9 ±0.5	6.0	0.21 ±0.03	0.245 ±0.020
Moon	Linear	3	11/14/61	32.9 ±2	33.4	1.19 ±0.12	—

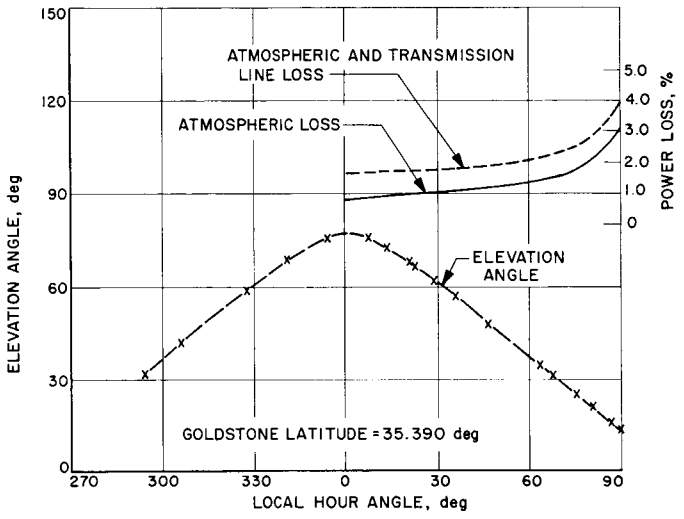

Figure 33. Elevation angle and attenuation vs local hour angle for the Crab Nebula

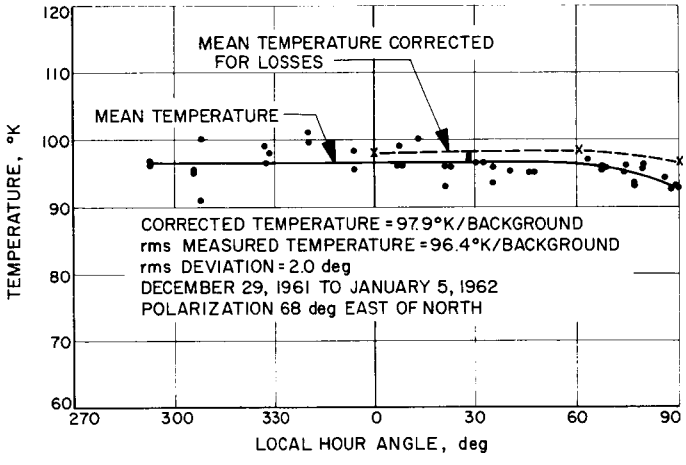

Figure 34. Antenna temperature of the Crab Nebula vs local hour angle

temperature and antenna gain variations over small hour angles. However, the standard deviation of the Crab Nebula temperature is equivalent to an antenna gain variation of approximately 0.1 db. The deviation of the corrected temperatures at the minimum elevation angle of 13 deg is also approximately 0.1 db.

Table 6 lists the temperature for each source as a ratio to the source M87. Also listed are the ratios measured by the CIT Radio Observatory in 1960 at 960 mc (Ref 3). The discrepancies for the two strongest sources are rather large, but the tolerances overlap. The source sizes, on the order of 3 to 4 min of arc, cannot have any significant effect in this case. The measurements were performed at the same frequency with CIT using a 90-ft diameter antenna and JPL using one of 85 ft.

Another observed temperature ratio of general interest is that of Cassiopeia A to Cygnus A due to the possible decreasing intensity of Cassiopeia A (Ref 4).

$$\frac{\text{Observed temperature of Cassiopeia A}}{\text{Observed temperature of Cygnus A}} = 1.47 \pm 0.10 \quad \text{(December 1961)}$$

On January 6, 1962 the cracks between the dish surface panels were covered with aluminum tape as an experiment. As mentioned previously, the minimum antenna temperature decreased from 10.5 to 9.5°K. Afterward the temperatures of three of the strong sources were remeasured and two other strong sources were measured. The peak temperature of the Crab Nebula increased from 96.4 to 101.3°K, yielding an antenna gain increase of 5.1% or 0.22 db.

The measured temperatures and temperature ratios obtained after taping the panel cracks for the five sources mentioned are listed in Table 7. Values have been calculated for the other sources on the basis of the data of Table 6 and the gain increase resulting from covering the cracks. The approximate flux densities were calculated by

$$G = \frac{2kT_A}{\eta A\left(\frac{1+(AR)^2}{2}\right)}\left(1+\frac{d^2}{B^2}\right)$$

where

k = Boltzmann's constant

T_A = antenna temperature corrected for atmospheric and transmission line attenuation (total = 1.5% minimum)

A = antenna aperture area

η = antenna efficiency corrected for any effective antenna polarization at the time of the source temperature measurement

$d \simeq$ source half intensity width (assuming a gaussian brightness distribution)

B = antenna half-power beamwidth

$(AR)^2$ = apparent axial ratio (in temperature) of the source polarization

The expression for the source polarization has been added to correct for the apparent polarization of Cassiopeia A and the Crab Nebula. The assumption of a gaussian source distribution is poor in many cases (Ref 5). Here, the corrections are small and the assumption is satisfactory for all of the sources except the Sun and

Table 7. Antenna temperatures due to source (after panel cracks taped)

Source	Antenna polarization	Number of tests	Test dates	Measured peak antenna temperature above background, °K	Temperature corrected for atmospheric and line losses, °k	Measured temperature ratio to M87 (Jan 1962)	Flux density, 10^{-26} WM^{-2} cps^{-1}
Crab Nebula	Linear	8	1/6/62	101.3 ±3 peak	103.0	3.24 to 3.47 ±.3 (for one ratio)	1090 Average
	Circular	4	1/10/62	93.9 ±3	95.4	3.47 ±.30 (expected 3.41)	1090
M87	Linear	—	Calculated from B	29.2	29.6	1.00	318
	Circular	4	1/10/62	27.1 ±1.5	27.5	1.00	—
Moon	Linear	4	1/9/62	35.9 ±2	36.5	1.23 ±.14	—
NGC 5128	Linear	3	1/9/62	40.3 ±2.5	40.9	1.38 ±.16	439
3C392	Linear	4	1/10/62	36.6 ±2 (above wide angle background)	37.2	1.25 ±.14	399
Cassiopeia A	Linear	—	—	338 (calculated from Table 1)	343	11.6	3670
Cygnus A	Linear	—	—	229 (calculated from Table 1)	233	7.85	2500
Orion	Linear	—	—	35.1 (calculated from Table 1)	35.6	1.20	384
Hercules A	Linear	—	—	6.3 (calculated)	6.4	0.22	69

Moon. A brightness temperature (T_b) has been calculated for the Moon on the basis of a curve of antenna efficiency e_θ vs angle from the beam axis. The curve is obtained (*SPS 37-10*, Vol I) by using the measured gain G_0, the measured power pattern of the main beam $P(\theta, \phi)$ and integrating by graphical means

$$e(\theta) = G_0 \frac{\int_0^{2\pi}\int_0^{\theta_b} P(\theta,\phi)\sin\theta\, d\phi}{\int\int_{4\pi} \sin\theta\, d\theta\, d\phi} = \frac{G_0}{2}\int_{\theta_b} P(\theta)\sin\theta\, d\theta$$

The assumption of circular symmetry in ϕ is good in this case. We have

$$T_b = \frac{T_A}{e(\theta_b)}$$

where

T_A = the corrected antenna temperature

θ_b = the half angle to the source edge

Then

T_b (Moon) = 208 (±30°K); (January 9, 1962)

Polarization tests. Tests of antenna polarization were performed on the three most intense sources using the rotatable, orthogonal linear-mode turnstile junction that has been previously described. The antenna drive was adjusted to track the approximate center of a source with the receiver connected to one linearly polarized mode of the turnstile junction. The polarization was rotated until maximum intensity was achieved. Then several drift curves were taken while switching the receiver between the orthogonal linear ports at intervals of about 45 sec. A temperature calibration was performed before and after each drift curve. The apparent major axis of the polarization ellipse was at the same angle, inclined about 68 deg east of north, for Cassiopeia A, Cygnus A, and the Crab Nebula. Table 3 lists the measured polarization percentages. Prior to these tests, a measurement was made of antenna gain vs polarization angle using the collimation tower antenna as an illuminator. The measurement indicated an antenna gain variation of about 4.8%. However, this test was subject to multipath effects and other errors due to the low elevation angle to the tower. The indicated polarization major axis was inclined about 45 deg east of north. At the position of the collimation tower, the major axis (E-vector) was horizontal.

As a result of the measurements in Table 8, we might assume that for high elevation angles the probable value of antenna gain variation vs polarization angle is about that measured for Cygnus A. It is expected that Cassiopeia A and the Crab Nebula will exhibit some polarization. A measurement of 7% has been reported for the

latter at X-band (Ref 6). However, it is not worthwhile at the moment to say anything about true polarizations of the three sources due to the uncertainty in the antenna gain variation and possible ambiguities in the source major axis orientations.

Radio astronomical techniques were used to determine the RF pointing accuracy of the antenna (Objective 4). The radio sources observed and the best estimates of their positions are listed in Table 9. The positions used in data reduction were from Reference 7.

Declination positions were obtained by driving the antenna at a sidereal rate in hour angle and scanning in declination. The mid-point of equal amplitude levels on either side of the signal maximum was obtained. After obtaining the declination bearing, the declination axis was locked and the sidereal hour angle (SHA) was obtained by determining the time and local hour angle of the signal maximum. Most SHA determinations were made by allowing the source to drift through the beam while the antenna was held stationary. The time of maximum signal was determined by averaging the mid-points of many different amplitude levels. In addition, several driven scans were used. The values of declination, time, hour angle, and meterological data were used in a digital computer program to correct for refractive effects. The error is defined as corrected observed data minus the position computed from the ephemeris.

Figure 35 shows the average hour angle error for five sources at a local hour angle of 0, 30, and 60 deg vs declination. Figure 36 is a similar presentation of the average declination angle.

The most striking feature in Figure 36 is the large error produced when observing the Crab Nebula. The reason for this is unknown at present. However, it is probably due to structural deflections somewhere in the microwave optics system.

Table 8. Source polarization data

Source	Measured source and antenna polarization, %
Cygnus A	3.3
Cassiopeia A	4.4
Crab Nebula	6.7

Table 9. Source positions

Source	Reference 7						Reference 8				
	α 1962			δ 1962			α 1950			δ 1950	
	hr	min	sec	deg	min	sec	hr	min	sec	deg	min
Cassiopeia A	23	21	43.9	58	36	47	23	21	7.9	58	29.8
Cygnus A	19	58	09.4	40	37	41	19	57	44.1	40	33.7
Virgo A	12	28	54.1	12	36	00	12	28	17.0	12	37.6
Orion Nebula	5	33	26.2	−5	24	47	5	32	47.0	−5	27.7
Taurus A	5	32	8.7	21	59	31	5	31	35.5	21	56.5
	Reference 7						Reference 3				
	α 1950			δ 1950			α 1950			δ 1950	
	hr	min	sec	deg	min	sec	hr	min	sec	deg	min
Cassiopeia A	23	21	11.4	58	32	48	23	21	11.4	58	31.9
Cygnus A	19	57	44	40	35	46	19	57	44.5	40	35.8
Virgo A	12	28	17.6	12	39	59	12	28	18	12	40.1
Orion Nebula	5	32	50.9	−5	25	16	5	32	49	−5	25.3
Taurus A	5	31	30.8	21	59	02	5	31	30	21	59.3
	Reference 9										
	α 1950			δ 1950							
	hr	min		deg	min						
Cassiopeia A	23	21.2		58	32						
Cygnus A	19	57.75		40	35						
Virgo A	12	28.3		12	40						
Orion Nebula	5	32.8		−5	25						
Taurus A	5	31.5		22	00						

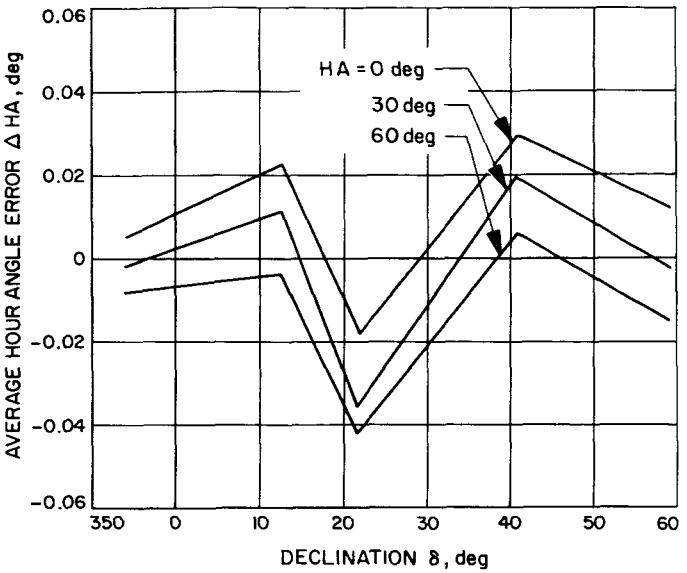

Figure 35. Average hour angle error vs declination (Ref 6)

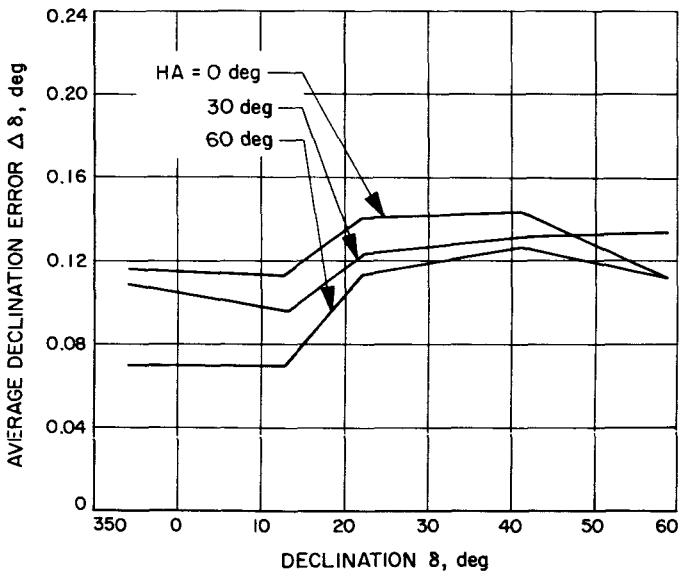

Figure 36. Average declination error vs declination (Ref 6)

b. Polarization experiment. Some form of polarization diversity or selection has been considered for spacecraft tracking and communication. Also, the use of a spacecraft signal for one-way Faraday polarization rotation measurement appears practical.

On the night of January 31, 1962, *Ranger III* was observed with a polarization tracking feed at the Goldstone Pioneer Site. The system employed is illustrated in Figure 37. A signal from the Cassegrain antenna system comes from the feedhorn, through a waveguide rotary joint to a turnstile junction. The junction is adjusted to divide the signal into two orthogonal linear modes. One linear mode is used as the reference channel (normal spacecraft listening channel), and the other as a polarization error channel. The reference channel goes through 3⅛-in. rigid coax to a single channel rotary joint and then to the circulator and maser. From the maser the signal goes via heliax to the reference mixer of the TRAC(E) receiver. The error channel signal comes from the turnstile via a 6-ft length of RG-9 coaxial cable, which is wrapped around the coaxial rotary joint, and leads to a section of heliax which goes to a parametric amplifier. From the parametric amplifier the signal is sent via heliax to the TRAC(E) declination error channel mixer. From the mixer the dc output signal is treated exactly as the normal simultaneous lobing error channel signal.

The transmission line components from the circular waveguide rotary joint to the coaxial rotary joint are rotated by a remotely controlled dc motor. Angular position is indicated by a synchro readout. This system is designed to keep the polarization oriented for maximum gain in the maser reference channel as well as for obtaining information about the orientation of the plane of polarization.

The system was controlled by having an operator rotate the turnstile until an error channel null was obtained. The sync reading and time were then recorded. The error voltage was also recorded by a chart recorder.

A calibration was made by using the collimation tower beacon. Figure 38 shows sync readout as a function of collimation tower antenna polarization. It should be pointed out that the polarization rotator at the collimation tower has poor resolution. The sync readout indicated 100 units for 360-deg rotation. Each point on Figure 38 was obtained by positioning the collimation tower polarization and then nulling the error channel. Figure 39 shows the angular offset vs error voltage. This curve remained essentially constant over a signal level variation from −100 to −140 dbm. There was no integration (other than the meter movement) on the error channel; below −140 dbm, a good S-curve was not obtained due to noise. Null position angular repeatability was within the $\frac{3}{10}$-deg resolution of the sync to −140 dbm, and to within 3 deg at −150 dbm.

Figure 40 shows the orientation of *E*-vector of the signal received from *Ranger III* as a function of time. Polarization orientation is attributable to the projection of the spacecraft high gain antenna feed dipole on the line

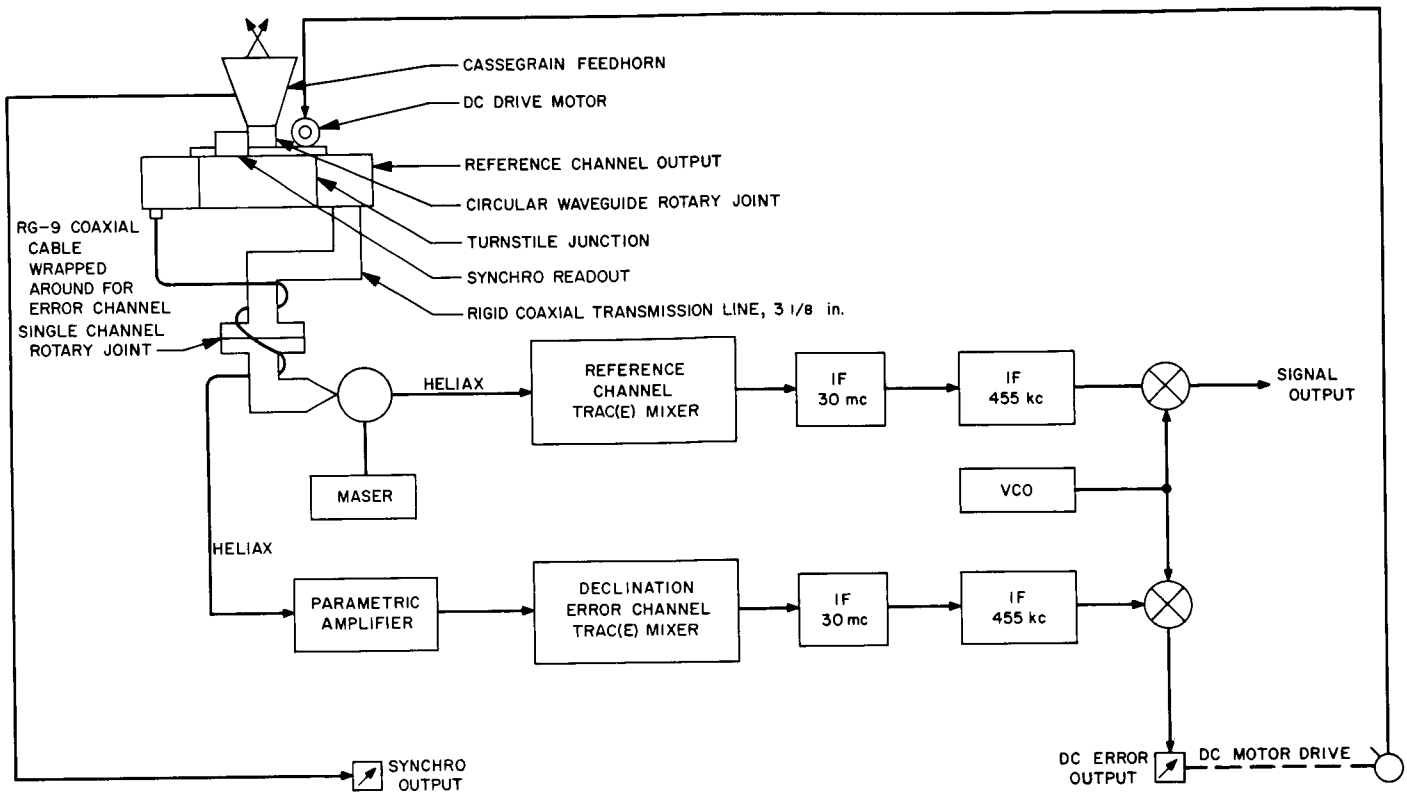

Figure 37. Polarization tracking system

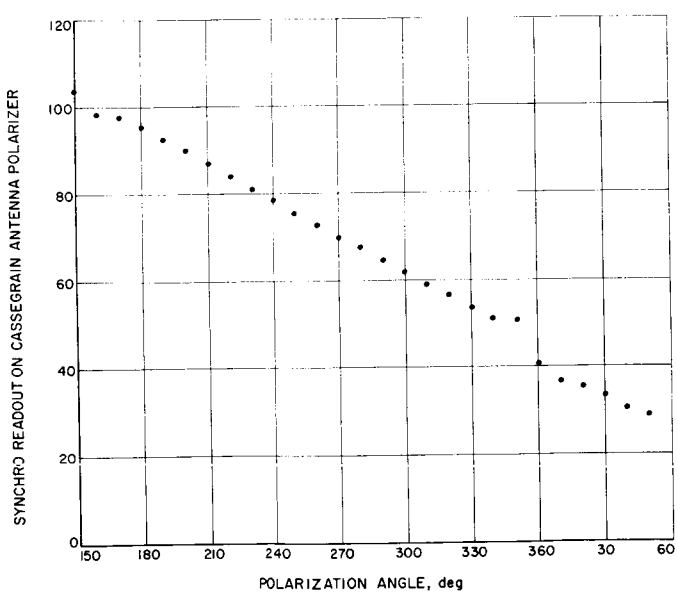

Figure 38. Synchro readout vs collimation antenna polarization

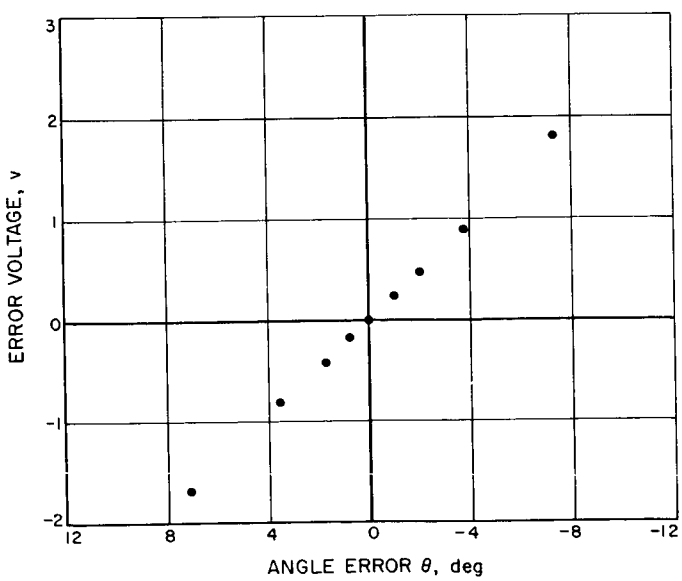

Figure 39. Error voltage vs angle error

of sight. This orientation is further modulated by a Faraday rotation effect. Ingalls, James, and Stone (Ref 10) have reported apparent Faraday rotation short period fluctuation of the order of ± 10 deg when performing lunar echo experiments at 440 mc. They attributed these fluctuations to surface phenomena rather than true Faraday effects. If, however, the most pessimistic case is taken and it is assumed that the fluctuations were ionospherically induced and the 960-mc one-way path is

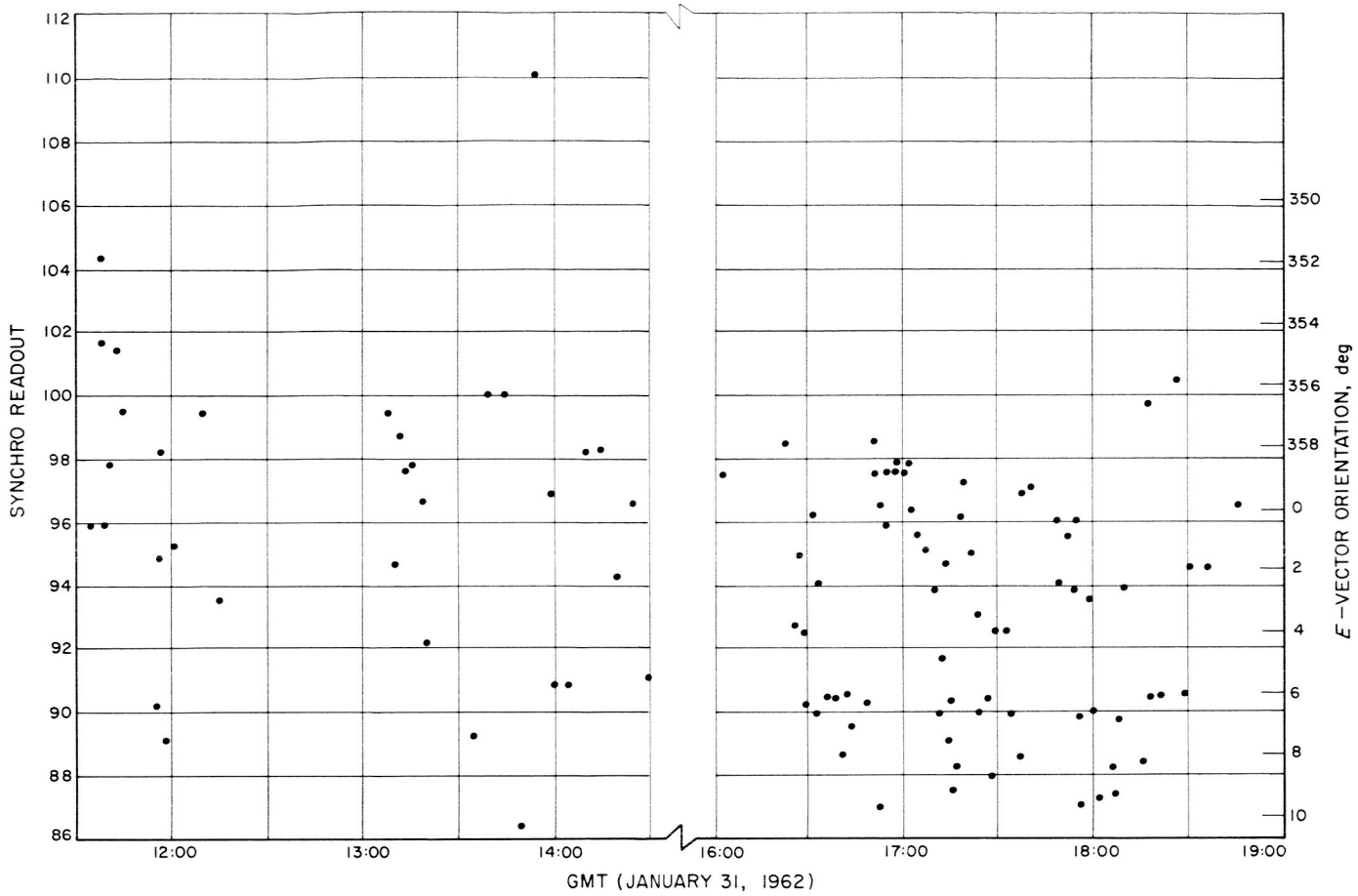

Figure 40. *E*-vector orientation vs time

scaled from two-way 440 mc, then these fluctuations should only be approximately ±1 deg.

At the time of observation, the attitude control system was still operating, but the gas pressure and power supply voltage were both low. Therefore, it is probable that the position noise observed was primarily due to vehicular motion rather than ionospheric modulation.

2. Closed Cycle He System

A closed cycle liquid helium refrigerator (CCR) has been delivered to JPL by Arthur D. Little, Inc. This system has been tested at JPL and is currently being installed at the Pioneer Site for further testing with the 960-mc maser on the HA-Dec antenna.

The system consists of a compressor unit (Fig 41) and a refrigerator unit (Fig 42). The compressor unit is located on the ground and is connected to the refrigerator unit by means of three lines carrying gaseous helium at ambient temperature. The refrigerator unit is seen to be

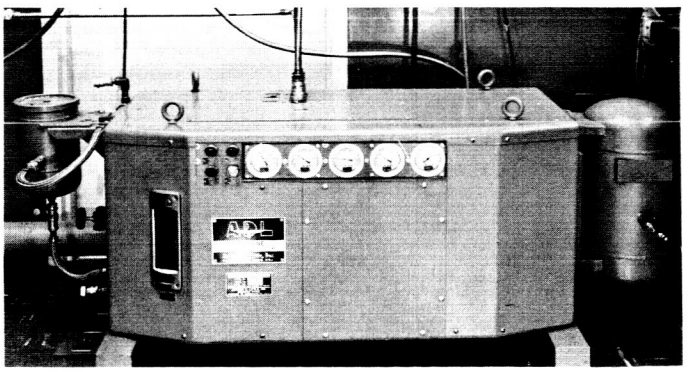

Figure 41. Compressor unit

in the same configuration as the JPL dewar system and will be mounted in the Cassegrain cone.

One characteristic of the CCR which differentiates it from an open cycle cryogenic system is the breakdown characteristic as shown in Figure 43. The solid line in this figure indicates the no-load characteristic of the CCR as the Joule-Thompson (JT) valve is adjusted for optimum refrigeration. The dashed lines indicate the breakdown

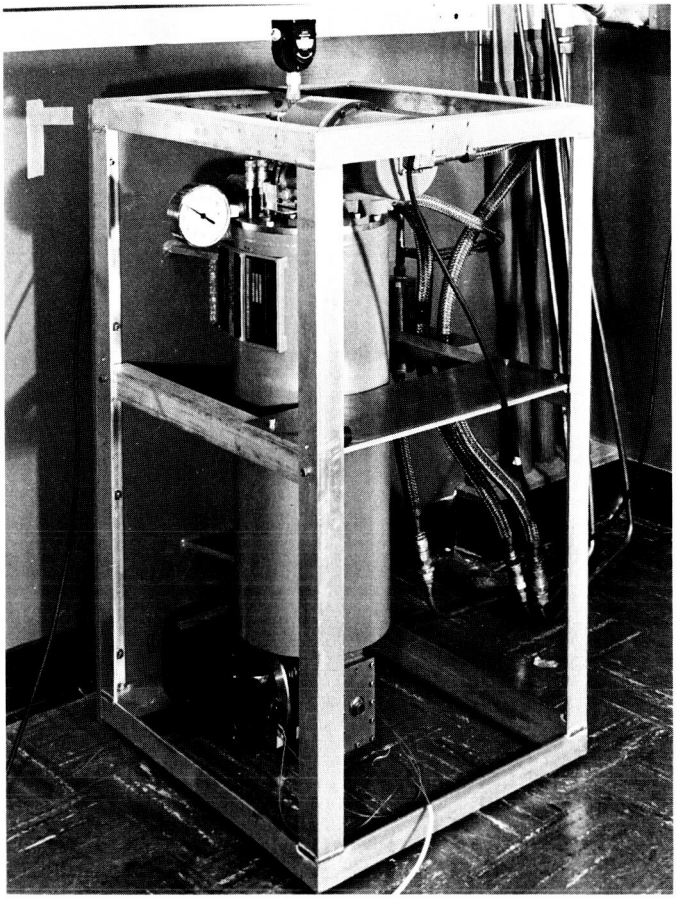

Figure 42. Refrigerator unit

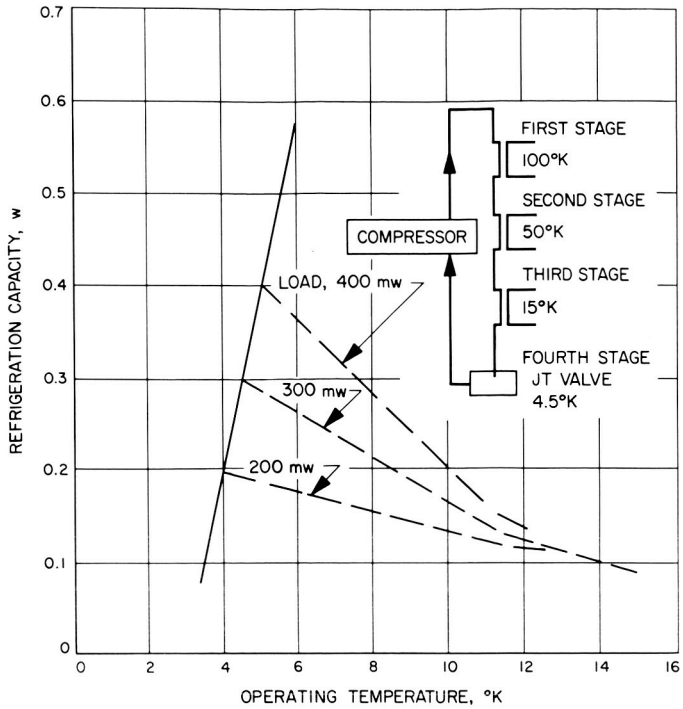

Figure 43. Typical breakdown characteristic for CCR

behavior for various loads. These lines indicate what happens to the fourth stage temperature as one tries to adjust the JT valve to achieve a lower temperature. The breakdown occurs in a matter of seconds and the temperature rises to some value between the second and third stage temperatures; subsequent recovery of the fourth stage temperature requires about an hour. Thus, it is important to operate at a temperature well above the breakdown value.

The explanation for the behavior may be stated as follows: The refrigeration load on the fourth stage includes a small contribution from the He gas itself which has been precooled to around 15°K. The amount of refrigeration produced depends on the rate of flow of He, but so does the heat load. Thus, the lowest temperature is achieved at that flow rate which is just adequate for the given load. Increasing the flow above this value also increases the heat input and the temperature will rise. However, for stable operation the flow should be slightly higher than the optimum for minimum temperature.

3. *Traveling Wave Maser*

The application of the traveling wave maser (TWM) to the DSIF is being investigated. As stated previously the only technical point in doubt is that of meeting the gain and bandwidth requirements at temperatures provided by present day closed-cycle helium refrigerators (4.2 to 4.5°K).

Tests were conducted to establish experimentally the temperature characteristics of ruby masers. The dramatic dependence of maser gain (for fixed bandwidth) on bath temperature is indicated in Figure 44. A good order-of-magnitude figure that can be used (for the 1.5 to 4.5°K region) is: 10-db gain change per degree change in bath temperature. Figure 44 illustrates why maser engineers are inclined to operate their equipment in the region of 1.5 to 2.0°K.

Actually, the prognosis for a high temperature (4.5°K) maser is not hopeless as might first appear from Figure 44, which applies for pink ruby (0.04 to 0.05% Cr concentration). It is known from the physics of ruby that by increasing the concentration of chromium (darker ruby) that a peak in the gain vs temperature characteristic can be obtained at a high temperature. Hence, the first design goal would be to find the optimum concentration of Cr in the ruby for 4.5°K.

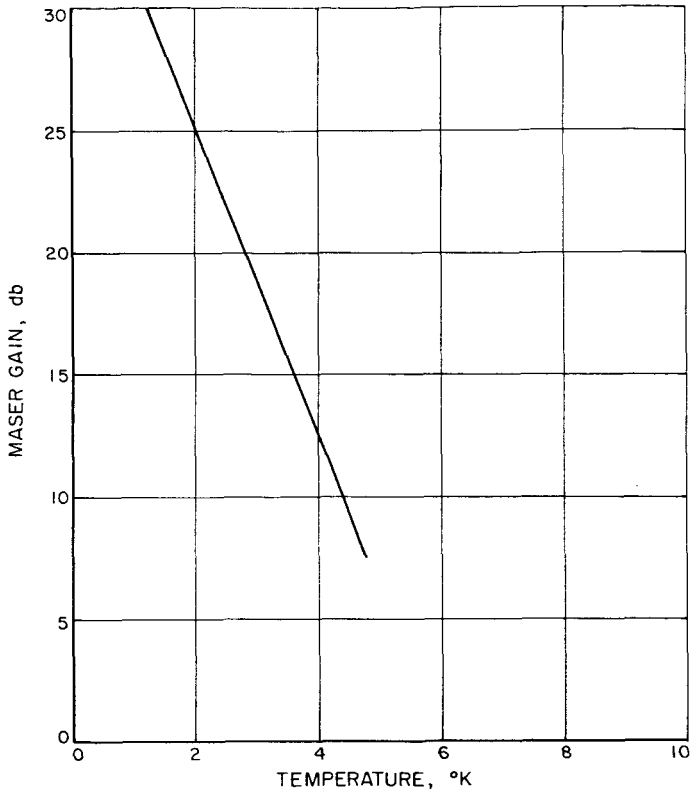

Figure 44. Typical gain vs temperature for ruby maser

4. Maser for Use in Ranger III and RA-4, 960 mc

The 960-mc maser system installed at the Pioneer Site was placed into operation for the *Ranger III* mission on January 10, 1962. Continuous operation was maintained throughout the system checkout and the actual flight of *Ranger III*, a period of 3 weeks. No maser subsystem failures were encountered.

The average system temperature (antenna, maser, and paramp) varied from 47 to 50°K depending on the local hour angle of the antenna. The measured sensitivity (threshold) of the Pioneer Site receiver system varied from −167 to −168 dbm. The extreme sensitivity of the Pioneer Site receiver system enabled this station to maintain RF lock during most of the critical spacecraft maneuver phases.

C. X-Band Communications Components

1. X-Band Feed

To provide high performance feed systems for the X-band planetary radar experiment, and also to gain further experience with feed systems of the general type that will be used in the Advanced Antenna System, low noise Cassegrain systems will be designed and installed for the X-band planetary radar experiment. Work with the Goldstone 960-mc Cassegrain system has demonstrated the feasibility of ultra-low noise temperature and good aperture efficiency performance for large Cassegrain systems.

The X-band feeds are presently visualized as utilizing the same Cassegrain geometry for both the transmitting and receiving systems. The major difference between the two feed systems will involve the feed horn output and transmission line circuitry. The expected gain of the transmitter and receiver antenna systems (as referenced to the feed horn output) is given in Table 10.

The receiving feed system will have a single channel listening connection and an alternate bridge system to provide angle error outputs, even though the receiving system is not designed for closed loop use of these signals. It is anticipated that the error signals will provide valuable data on the antenna pointing performance, as well as contribute to design techniques for AAS feed system design. It is presently hoped that a scaled monopulse bridge similar to the DSIF S-band bridge described in *SPS 37-12*, may be utilized together with a suitable horn aperture to provide the necessary performance. An estimate of the expected zenith noise temperature is given in Table 11. The optimized single channel interchangeable listening system will be utilized during critical signal strength portions of the experiment. All of the feeds will have left and right circular polarization capability.

2. Maser System

An X-band maser system intended for use at Goldstone Space Communications Stations in communications R&D experiments is being fabricated for JPL by the Hughes

Table 10. Expected antenna gains

Parameter	Transmitter, db	Receiver[a], db
Theoretical maximum	+67.2	+67.2
Aperture illumination	− 2.2	− 2.2
Quadripod scattering	− 0.3	− 0.2
Surface deviations	− 2.5[b]	− 1.2[c]
Losses in transmission line system	− 0.3	− 0.2
Total	61.9	63.4

[a]Single channel listening.
[b]Assumed rms surface error = λ/16.
[c]Assumed rms surface error = λ/24.

Table 11. Expected single channel listening and monopulse receiving antennas noise temperature

Parameter	Noise contribution, °K
Atmospheric loss (dry atmosphere)	4
Spillover	3
Quadripod scattering	3
Loss in bridge	5
Loss in polarizer	5
Loss in transmission line and instrumentation coupler	10
Total	
Listening	25
Angle tracking	30

Research Laboratories. The principal features of the maser are:

f_o, 8450 mc

Gain, 23 db with a target of 26 db

Bandwidth, $\geq$7 mc

Noise temperatures, $\leq$20°K

Duty per fill of liquid helium, at least 24 hr

The maser will be similar to several that Hughes has built for other users. The unique feature of this device is that it consists of several cavity-type masers cascaded by means of ferrite isolators. Hence, it is actually a traveling wave maser. The magnetic field is provided by a small magnet which is mounted internally and cooled to 4.2°K. Trimmer coils provide the necessary vernier control of the field.

The dewar is also novel in that the helium vapor is used to cool the radiation shield surrounding the helium tank. Thus, no liquid nitrogen is necessary.

3. System Temperature Instrumentation

The operational performance and capability of an ultra-low noise receiving system is greatly dependent on the associated instrumentation. The experience gained in the

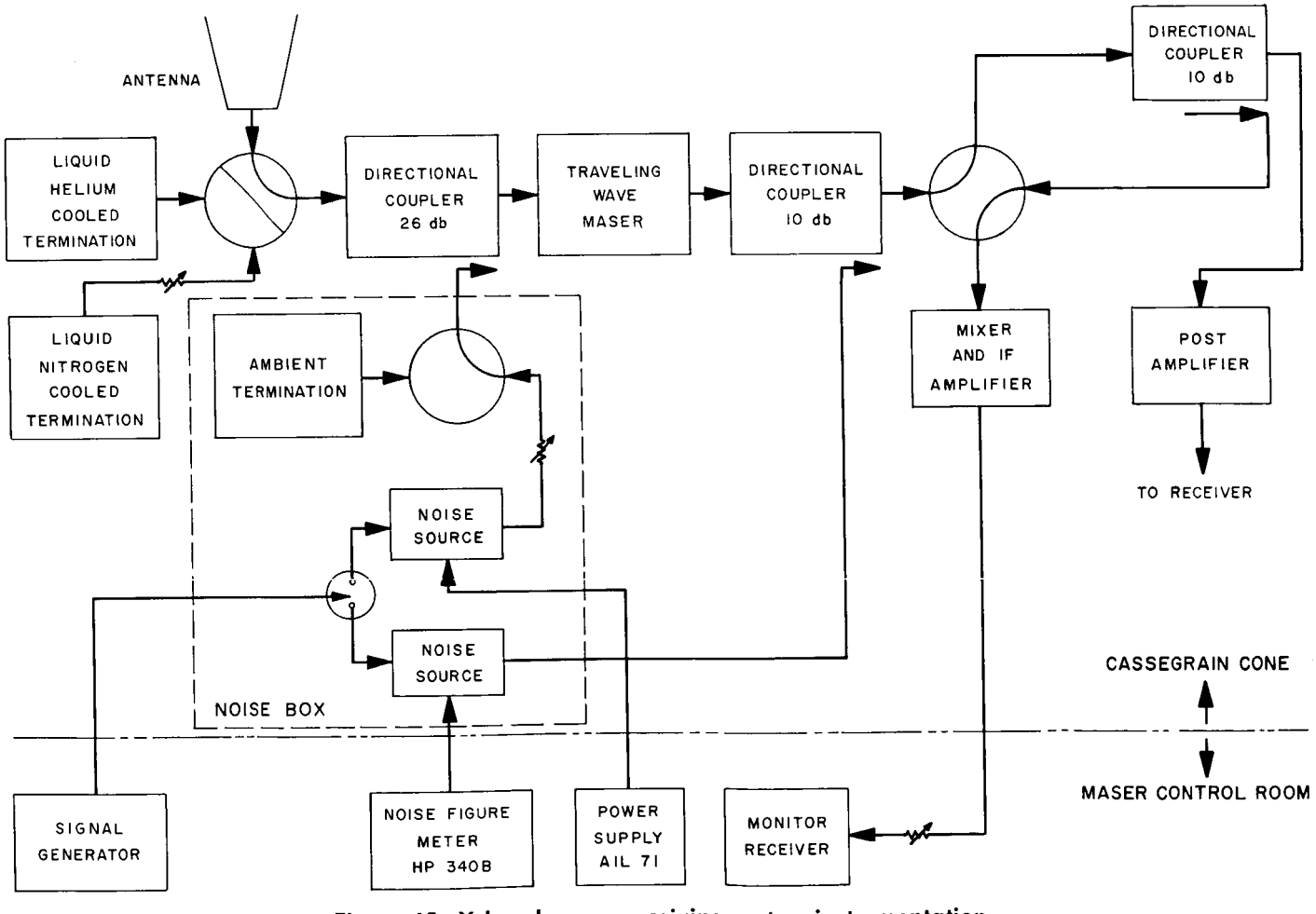

Figure 45. X-band maser receiving system instrumentation

2388-mc Venus radar experiment is of great benefit in planning the present system.

A block diagram of the proposed instrumentation is shown in Figure 45. Waveguide will be used throughout the system. The cooled reference terminations can be used in conjunction with the monitor receiver to make accurate temperature calibrations (from 5 to 300°K) for absolute antenna temperature measurements and to evaluate the receiver temperature irrespective of the antenna temperature. The system temperature can be accurately measured by the Y-factor method by setting the total system noise level to the same value with the AIL precision attenuator when the noise source is on as it was when off. The temperature of the followup amplifier is measured with the HP 340B noise figure meter. The traveling wave maser insertion gain is measured by injecting a signal into the system both before and after the maser and observing on the monitor receiver.

The noise injected into the maser can be turned on and off (at any rate desired up to 1 kc) by switching between the noise source and an ambient termination. This allows the received pulse to be simulated, and actual receiver sensitivity measured and calibrated by adjusting the signal level with the variable attenuator.

D. Advanced Receiving Techniques

1. High Speed and High Capacity Autocorrelator

a. Introduction. The central problem of estimating, or measuring, the power spectrum of a random signal is the stability of the measurement; that is, separate measurements made on the same process will generally yield different results. The reason for this variability is the fact that different samples of the random signal are being observed. In order to produce a useful spectral estimate, it is necessary to know the stability of the measurement and to take whatever steps are needed to reduce it to an acceptable level.

An effective way to produce stable spectral estimates is to measure the autocorrelation (Ref 11) function of the signal, and then take the Fourier transform of that function. This yields the desired power spectrum. The variability can be reduced to any level by analyzing a sufficiently long sample of the signal.

The most convenient way of mechanizing this method is to sample the signal, quantize and record the samples, and use a general purpose digital computer to find the autocorrelation function. Unfortunately, the analysis of several hours of a signal of reasonable bandwidth requires many thousands of hours of machine time.

This discussion describes, in some detail, a special purpose computer which can measure the autocorrelation function of the signal as fast as samples arrive; so that the answer is ready at the end of the observation.

The plan (Ref 12) is based on the configuration shown in Figure 46. The signal is fed through a band-pass filter, a snap-action limiter, is sampled at the Nyquist rate, and goes to the special purpose computer to be described subsequently. The task of the computer is to calculate the autocorrelation function $R_y(kT)$ by the sums:

$$R_y(kT) = \frac{1}{N}\sum_{n=1}^{N} y_n y_{n+k} \qquad k = 1, 2, \cdots, K \qquad (1)$$

where T is the period between samples, y_n is nth sample of y, N is the total number of samples used, and K is the number of points on the autocorrelation function that are computed.

Of course, the signal is distorted by the limiter; but, fortunately, a simple formula (Ref 13) relates the autocorrelation function at x, $R_x(kT)$, to that at y:

$$R_x(kT) = R_x(0)\sin\left[\pi/2R_y(kT)\right] \qquad (2)$$

This formula is valid for gaussian signals.

R_y is the quantity which is measured by the correlator. It is corrected by Equation (2) and Fourier transformed to yield the desired spectrum. That part of the analysis is done on a general purpose machine and takes less than a minute.

An example of a spectrum taken by this method is given in Figure 47. The signal was from a laboratory generator producing white noise. The filter bandwidth

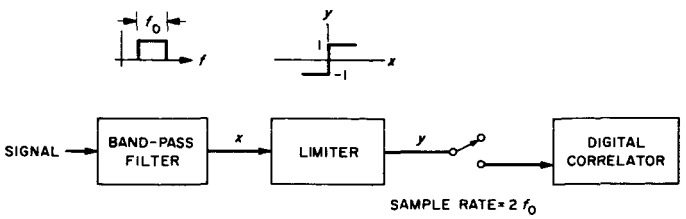

Figure 46. Digital spectrometer

was 400 cps, and fifteen seconds of signal were analyzed. Three separate runs were made and their spectra superposed. The extent of the instability of the measurement shows up quite clearly in Figure 47. Figure 48 shows three runs made with an integration time of 5 min. The improvement in stability is marked, and agrees with the analysis of Reference 12.

A weak signal, that would be lost in the measurement of Figure 47 because of the variability, may show up clearly in the measurement of Figure 48. For very weak signals an integration time of hours may be needed; and it is in this area that this scheme has advantages over the more customary approach.

b. The correlator. The logical circuitry used to construct the correlator consists of the so-called *and-or* dynamic logic. The basic module is shown in Figure 49. In this type of circuitry, the state *one* is represented by a pulse on the line in question, and the state *zero* by the absence of pulse. An *and* gate is activated if pulses arrive at all four of its inputs simultaneously. The *or* gate is activated if any *and* gate is turned on. The clock pulse is used to fix precisely the timing of pulses from the *or* gate, and the amplifier regenerates the pulse to a standard shape. An output appears 1 μsec after the set of inputs that caused it. A complementary output is also available from each module. That is, if the main output is *zero*, the complement is *one*, and vice-versa.

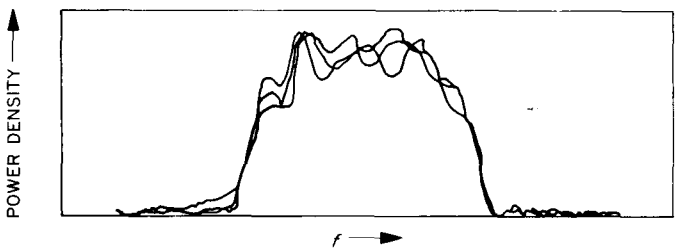

Figure 47. Noise spectrum, 15-sec integration

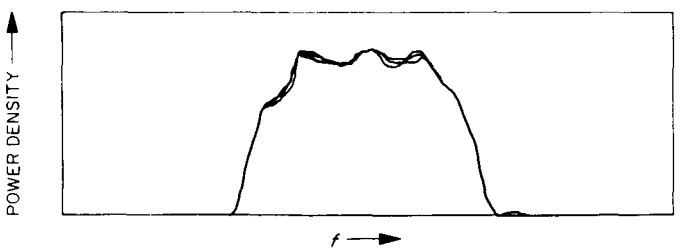

Figure 48. Noise spectrum, 5-min integration

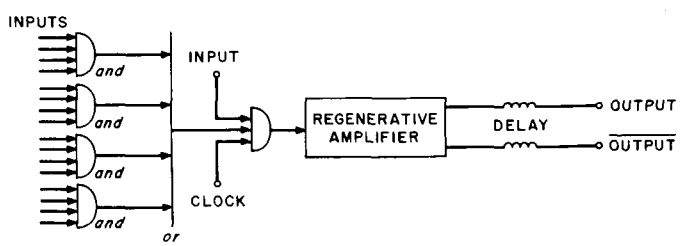

Figure 49. Digital module

A second basic module is composed of delay lines with a multiple of 1-μsec duration. An example, shown in Figure 50, will demonstrate some of the properties of these devices. Here we have an active module driving three delay lines (plus three more for complementation). From the diagram, one can see that there will be an output from the active module W if 1 μsec previously W and Z were both *one*, or if W and Z were both *zero*. This can be expressed symbolically by the Boolean equation

$$W = WZ + \overline{W}\overline{Z} \tag{3}$$

Equation (3) is a standard symbolism for a difference equation relating the output of module W to its inputs one clock period earlier. The product notation signifies logical *and* and the plus indicates inclusive *or*.

When the circuit of Figure 50 is energized, the delay lines will be empty. That is, W, X, Y, and Z will be in the *zero* state, and their complements, $\overline{W}$, $\overline{X}$, $\overline{Y}$, and $\overline{Z}$, will be *one*'s. The next microsecond W will be *one* (the lower *and* gate will have fired). As the signals propagate down the line the following pattern is generated:

W	X	Y	Z	*Bit time*
0	0	0	0	1st
1	0	0	0	2nd
0	1	0	0	3rd
1	0	1	0	4th
0	1	0	1	5th
0	0	1	0	6th
1	0	0	1	7th
1	1	0	0	8th
0	1	1	0	9th
1	0	1	1	10th
1	1	0	1	11th
1	1	1	0	12th
0	1	1	1	13th
0	0	1	1	14th
0	0	0	1	15th
0	0	0	0	16th
Repeat				

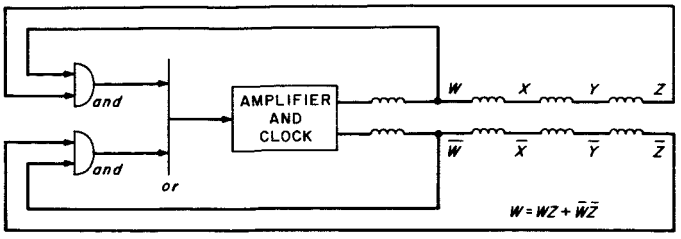

Figure 50. Sequence generator

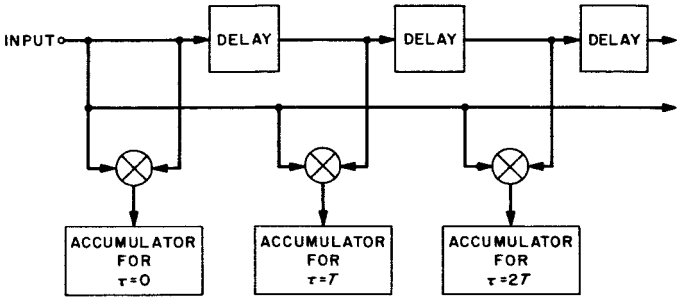

Figure 51. Correlator

This pattern, of 15-μsec duration, will keep repeating itself continuously. If a single pulse once every 15 μsec is desired, it may be obtained merely by connecting W, X, and Y to an *and* gate ($F = WXY$). The tabulation shows this gate would fire exactly once every cycle (at the 12th bit time).

Figure 51 shows a tentative design for a correlator which can be constructed with these modules. Each multiplier gives an output if both of its inputs are *one* or if both are *zero*: e.g., $F = y_n y_{n+k} + \bar{y}_n \bar{y}_{n+k}$. Each accumulator is a chain of flip-flops that adds one to the count every time the corresponding multiplier produces an output. Thus the accumulator for $\tau = kT$ counts the total number of "agreements" between y_n and y_{n+k}. Since $\Sigma\, y_n y_{n+k}$ equals the number of agreements minus the number of disagreements, and the total number of both is stored in the accumulator for $\tau = 0$, then $\Sigma\, y_n y_{n+k} = 2$ (count in accumulator k − count in accumulator 0). This relation obviates the need for accumulators that can count both up and down, and simplifies the circuitry considerably.

The plan described in Figure 51 is impractical because of the large amount of hardware it demands. Each delay line must be 15 units long (the sampling period = 15 μsec) and, since 45 points on the autocorrelation function are to be calculated, there must be 45 such delays. This adds up to an extravagant amount of delay. The accumulators represent an impractical amount of hardware also. Since the correlator is to run all day without an overflow, each accumulator must have a capacity of 32 bits. If each bit were realized with a flip-flop, 32×45, or 1440 flip-flops would be necessary.

The amount of delay can be reduced by a factor of 15 by the simple strategy of storing the last 45 samples of the input in a recirculating delay line. Then, whenever the input is to be sampled, the oldest data element is removed from the delay line and lost, while the new sample is inserted into its proper place in the line.

A similar idea can be used to reduce the number of flop-flops in the accumulators. Each accumulator can be realized by a circulating delay line of 32 bits. The disadvantage of this method lies in the timing; i.e., input data can only be assimilated when the circulating line is in the correct alinement, once every 32 bit times. The input rate is higher than that, although the rate drops one octave for every bit position from the front of the accumulator.

Figure 52 illustrates a scheme which allows an accumulator to "fan out" into recirculating delay lines. Assume input pulses arrive no faster than every bit time. Then the minimum period between overflows of the second bit flip-flop is $2^2 = 4$ bit times, the same time that is required between successive alinements of the 4 bit recirculating line. Although the maximum overflow rate is slow enough, an overflow may occur at any time. Hence, a buffer state is necessary to hold the overflow until it can be used by the next state; at which time the buffer must be reset to zero. This process is repeated in the 4 bit line, where the 4$^{\text{th}}$ position is reserved to act as a buffer. The first 3 bits of this line cannot have overflows closer together than $4\,(2)^3 = 32$ bit times, just right for the 32 bit recirculating line that follows. In this way a 32 bit accumulator (now grown to 37 bits) is realized with 3 flip-flops and 2 recirculating lines.

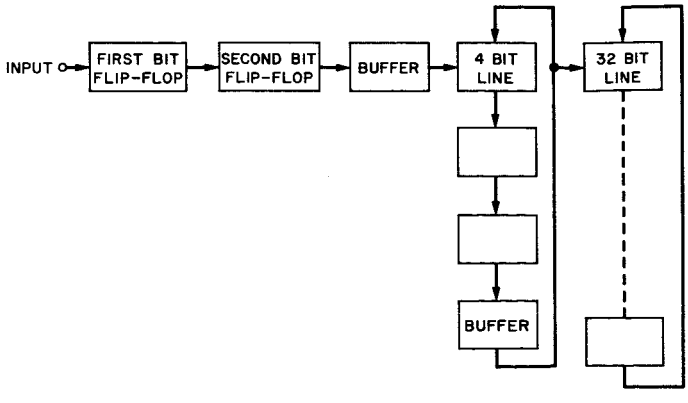

Figure 52. One 37 bit accumulator

Next consider what happens if input pulses do not arrive every bit time, but only once every 15 times. Then the mechanization of Figure 52 may be replaced by that of Figure 8. The timing is still correct since all times have been divided by 15. However, 14/15 of the accumulators capacity is unused. Now it is possible to make the set of lines of Figure 53 perform as 15 independent accumulators, and a great saving of hardware has been achieved. The first bit position in the first line holds the least significant digit for $R(0)$, the second position holds that for $R(T)$, the third for $R(2T)$, and so on. The second line holds the next significant digit for $R(0)$, $R(T)$, $R(2T)$, etc. This interlacing continues through to the last line, where the first 32 positions hold the 32 most significant digits of $R(0)$, the next 32 for $R(T)$, and the next for $R(2T)$, etc.

Figure 54 illustrates how the input storage mentioned above may be combined with the 15 accumulators of Figure 53 to produce the first 15 points on the autocorrelation function. The last 15 samples of the input wave are stored in the recirculating line. In addition, the last sample is stored separately in a flip-flop. The comparator is shown comparing the n^{th} sample with itself. One bit time later, it compares the n^{th} sample with the $(n-14)^{th}$, and the next bit time with $(n-13)$ and then $(n-12)$ and so on. In this way, the successive outputs of the comparator are $R(0)$, $R(14T)$, $R(13T)$, $\cdots$, $R(T)$. The line continues to recirculate after that until the input wave is sampled again. At the next alinement of the delay line after the sampling instant, the oldest data element $(n-14)$ is removed, each sample is advanced one place in the line, and the new sample is inserted. The comparator output repeats $R(0)$, $R(14T)$, $\cdots$, $R(T)$; but this time the products are based on the latest piece of input data. These comparator outputs arrive just in time to be accepted by all 15 channels of the composite accumulator.

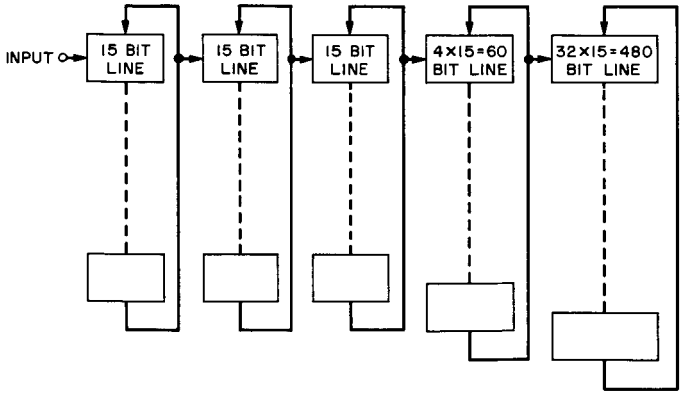

Figure 53. Fifteen 37 bit accumulators

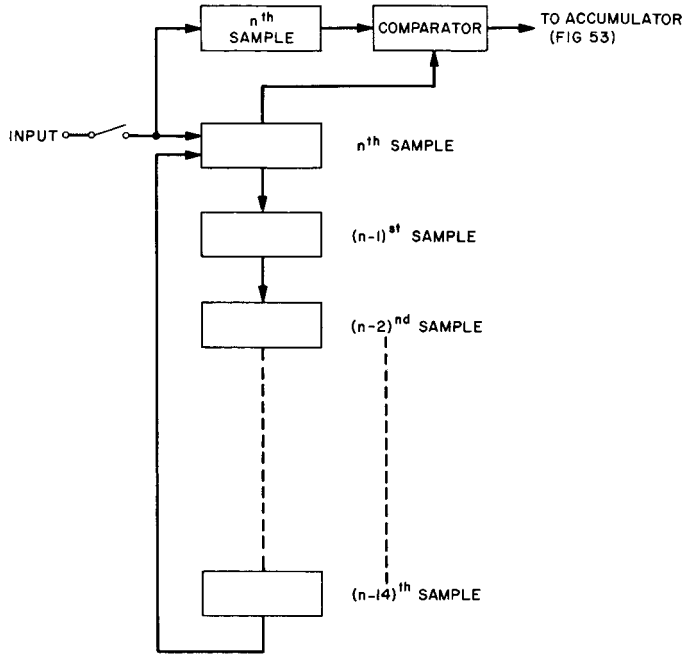

Figure 54. Input storage device

The correlator used in the 1961 Venus radar experiment (Ref 14) paralleled three sets of devices identical to those illustrated in Figures 53 and 54 in order to compute $3 \times 15 = 45$ points on the autocorrelation function.

c. Complete logical equations. Figure 55 shows a block diagram of the completed correlator. In addition to the digital circuitry described, several timing generators are needed. One is a pulse every 15 sec to mark the alinement of the input storage line. The realization for this, of course, is the circuit of Figure 50. The logical equation for it is:

$$A = A_2A_3 + \overline{A}_2\overline{A}_3 \tag{4}$$

where the subscript notation indicates the number of delays. B (Fig 55) is an *and* gate set to recognize only one combination, and thus produce an output pulse once every 15 μsec.

$$B = AA_1A_2 \tag{5}$$

In order to sample the 60 bit line every 32 μsec, a pulse must be available at that rate. This generator consists of flip-flop C driving four unit delays, with feedback logic that produces a sequence of period 32.

$$C = \overline{D}C_4\overline{C}_2 + \overline{C}_4C_2 + \overline{C}\overline{C}_1\overline{C}_2\overline{C}_3\overline{C}_4 \tag{6}$$

$$D = \overline{C}\overline{C}_1\overline{C}_2C_3\overline{C}_4 \tag{7}$$

The one pulse needed for each period of C is produced by *and* gate D.

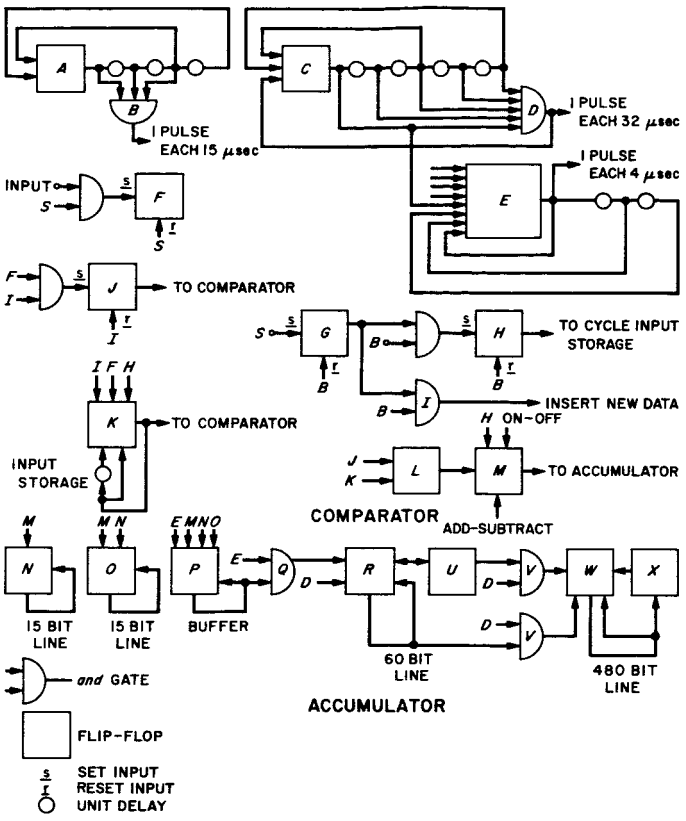

Figure 55. Autocorrelator

A pulse is needed every 4 μsec in order to test the first buffer line. It is produced by flip-flop E:

$$E = \bar{E}\bar{E}_1\bar{E}_2 + \bar{C}\bar{C}_1\bar{C}_2C_3\bar{C}_4 \tag{8}$$

The purpose of the last term of Equation (8) is to make sure that the pulse from D coincides with one of the pulses from E.

One other timing pulse S is necessary to sample the input waveform. It is convenient to make the rate of S-pulses variable so that different bandwidths may be analyzed. (The sample rate must be twice the input bandwidth [Fig 46]). Therefore S may be obtained either digitally, or from a tunable external oscillator.

The sample pulse S stores the value of the input waveform in flip-flop F.

$$F = (\text{input})\,S + \bar{S}F \tag{9}$$

S also sets flip-flop G so that the correlator is aware that a sample occurred.

$$G = S + G\bar{B} \tag{10}$$

G holds that information until the next alinement of the input storage line as marked by the pulse from B, which resets G. At that instant flip-flop H is set. The purpose of H is to lengthen the input storage line by one bit for one complete circulation. This processes each data element by one position, and removes the oldest one.

$$H = GB + H\bar{B} \tag{11}$$

H is reset after exactly 15 μsec by the next pulse from B. As H is reset, *and* Gate I inserts the latest data point into input storage (the data being held by F all the while).

$$I = GB \tag{12}$$

The data point is also transferred to flip-flop J which is one input to the comparator. This frees F to receive another input, if one comes along.

$$J = FI + J\bar{I} \tag{13}$$

The input storage consists of a driver, flip-flop K, connected as a 15-bit recirculating line.

$$K = K_{14}\bar{H} + K_{15}H\bar{I} + IF \tag{14}$$

The comparator consists of two flip-flops, L and M. L acknowledges agreements between the latest data point (stored in J) and the earlier ones which arrive successively from K.

$$L = JK + \overline{JK} \tag{15}$$

M allows outputs from L to be utilized only once for each data point; hence when the input storage is recirculating and no new inputs arrive, then no outputs go to the accumulator. M is also a convenient place to put an on–off switch so that inputs to the accumulator may be halted if desired. In addition, it may be desirable for the comparator to acknowledge disagreements instead of agreements. This has the effect of producing the negative of the autocorrelation function and thus makes it possible for the correlator to measure the difference between the autocorrelation functions of two signals. This is accomplished by the logical connections:

$$M = [L\,(add) + \bar{L}\,(subtract)]\,H\,(on) + I_2\,(on) \tag{16}$$

The last term of Equation (16) provides for an output from the comparator whenever the correlation for zero delay, $R(0)$, is being considered, regardless of whether the correlator is in the *add* or *subtract* mode. Thus $R(0)$ always equals the total number of samples taken.

Next we consider the accumulator described in Figure 53. The first line, driven by flip-flop N, holds the least significant bit of the autocorrelation function.

$$N = M\bar{N}_{14} + \bar{M}N_{14} \tag{17}$$

The next line, driven by flip-flop 0, holds the second significant bit.

$$O = MN_{14}\overline{O}_{14} + \overline{M}O_{14} + \overline{N}_{14}O_{14} \tag{18}$$

The next line holds the buffer bits.

$$P = MN_{14}O_{14} + P_{14}\overline{E} \tag{19}$$

Whenever E resets one of these bits, *and* gate Q sends a pulse to the next line. This line is 60 bits long and holds the next three bits of each $R(kT)$ and one buffer bit. Flip-flop R, connected as a serial adder, drives this line and flip-flop U serves to supply the carry for the addition.

$$Q = P_{14}E \tag{20}$$

$$R = D\,(U\overline{R}_{59} + \overline{R}_{59}Q + R_{59}\overline{QU}) \tag{21}$$

$$U = R_{59}\,(Q + U) \tag{22}$$

Gate D tests and resets the buffer bit every 32 μsec. Gate V records this action by sending a pulse to the final accumulator line which contains 480 bits. This line is driven by flip-flop W, connected as a serial adder. Flip-flop X is used to provide the carry.

$$V = R_{59}D + UD \tag{23}$$

$$W = \overline{W}_{479}V + \overline{W}_{479}X\overline{W} + W_{479}W\overline{V} + \overline{X}W_{479}\overline{V} \tag{24}$$

$$X = W_{479} \tag{25}$$

d. Remarks. The numbers A_i circulating in the final storage line are not the correlation coefficients of Equation (1), but they are closely related. As explained earlier, the normalized correlation coefficients may be found by the expression

$$R_y\,(kT) = \frac{2A_k - A_o}{A_o} \tag{26}$$

Because of the "fanning-out" of numbers into delay lines of increasing length, the A_i stored in the last line are not in numerical order. Since the first buffer is tested every fourth μsec, the A_i in the 60-bit line are ordered as $4i$, taken modulo 15. These are then tested every 32 μsec, with the result that the A_i stored in the 480 bit line are ordered as $2i$, taken Modulo 15.

In order to compute the next fifteen values of $R_y\,(kT)$, the equipment from flip-flop K on must be duplicated. There is a minor change in the logic for M, as the last term must be omitted (Eq [16]). Also, the input to K must be changed so that its input is the oldest data which is removed from the input storage line for the first 15 values.

E. Mesa Antenna Range

A new illuminator platform (Fig 56) has been installed for the Antlab spacecraft antenna range. The platform was designed to reduce ground reflections from the sides and bottom of the adjacent canyon. The floor has been covered with a 200-mc, 20-db absorber.

A study contract has been established with Emerson & Cuming, Inc., Canton, Massachusetts to aid in the design of an anechoic chamber. The study contract covers two technical problems important in the design and use of a chamber: (1) the way the chamber RF performance is measured; and (2) characteristics of an existing anechoic chamber operated below its design frequency.

A second independent study contract has been established with Lockheed Missiles and Space Division, Sunnyvale, California. It provides for an evaluation, using several different measurement techniques, of an anechoic chamber designed by their antenna group.

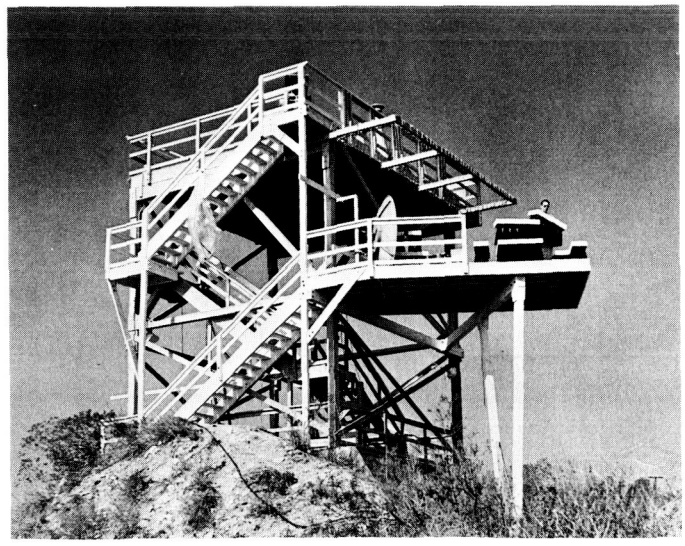

Figure 56. New platform for Antlab spacecraft antenna range

References

1. Stelzreid, C. T., "A Liquid Helium Cooled Coaxial Termination," Proceedings IRE, Letter to the Editor, July 1951.

2. Hogg, D. C., "Effective Antenna Temperatures Due to Oxygen and Water Vapor in the Atmosphere," *JAP*, Vol 30, No. 9, September 1959.

3. Harris, D. E., and J. A. Roberts, "Radio Source Measurements at 960 Mc/s," *Astronomical Society of the Pacific*, Vol 72, No. 427, August 1960.

4. Hogbom, J. A., and J. R. Shakeshaft," Secular Variation of the Flux Density of the Radio Source Cassiopeia A," *Nature*, February 18, 1961.

5. Maltby, P., and A. T. Moffet, "Brightness Distribution in Discrete Radio Sources III. The Structure of the Sources," Observations of the California Institute of Technology Radio Observatory, 1962.

6. Mayer, C. H., and R. M. Sloanaker, "Polarization of the 10-cm Radiation From the Crab Nebula and Other Sources," *Astronomical Journal*, Vol 64, No. 8, p 339, October 1959.

7. Matthews, T. A. (Private Communication), California Institute of Technology Radio Observatory, January 1962.

8. Sloanaker, R. M., and J. H. Nichols, "Positions, Intensities and Sizes of Bright Celestial Sources at a Wave Length of 10.2 cm," *Astronomical Journal*, Vol 65, No. 3, p 109, April 1960.

9. Kuz'min, A. D., M. T. Levchenko, R. I. Noskova, and A. E. Salomonovich, "Observations of Discrete Radio Sources on 9.6 cm," *Soviet Astronomy—AJ*, Vol 4, No. 6, p 909, May–June 1961.

10. Ingalls, R. P., J. C. James, and M. L. Stone, "A Study of UHF Space Communications Through an Aurora Using the Moon as a Reflector," 4th Symposium on Ballistic Missile and Space Technology, University of California, August 24–27, 1959.

11. Blackman and Tukey, *The Measurement of Power Spectra*, p 7, Dover Publications, Inc., New York, 1958.

12. Goldstein, R. M., *A Technique for the Measurement of the Power Spectra of Very Weak Signals*, IRE, PGSET, to be published.

13. Davenport and Root, *Random Signals and Noise*, p 276, McGraw-Hill Book Co., Inc., New York, 1958.

14. Golomb, S. W., R. Stevens, and W. K. Victor, "Radar Exploration of Venus; Goldstone Observatory Report for March–May 1961," *Technical Report 32-132*, Jet Propulsion Laboratory, Pasadena, August 30, 1961.

Page intentionally left blank

IV. Advanced Antenna System

A. Synopsis

A new large aperture, low noise advanced antenna system (AAS) is planned for installation in the DSIF. This antenna will give an approximate 10-db performance increase over the 85-ft antennas now used, thus providing an order of magnitude increase in the data rate from future spacecraft.

Preliminary feasibility studies for the AAS were completed by four companies in April 1961. Further investigations into the engineering design of the AAS are presently being conducted by the Equipment Division of the Blaw-Knox Company, Pittsburgh, Pennsylvania, under a task-order-type contract. The objective of this work is to produce a sound engineering design for the AAS by mid-1962. If that objective is satisfactorily accomplished, the task of detailing, fabricating, erecting, and testing will be contracted during fiscal year 1963.

The Blaw-Knox Company has conducted a comparative analysis of several variations of a basic pedestal-alidade-kingpost-bearing-gear and axis readout configuration. The spring constants, weights, and mass moments of inertia for the variations were calculated. Analysis of reflector deflection dependency on support point and backup structure rigidity was accomplished. Reflector deflections, due to racking load imposed by elevation drive unbalance, were calculated. The important deflections, stiffnesses, weights, and equivalent optical blockages were calculated for a Cassegrain system hyperboloid support configuration in each of the variations. Alternate locations of elevation and azimuth gears were evaluated. Drive stiffness was carefully studied. Calculations were made to establish the best method of mounting gears for optimum stiffness; i.e., would maximum stiffness be achieved from revolving a stationary azimuth gear?

As a result of these detailed analyses, a specific configuration for the AAS has been chosen and some of its critical parameters are now definite:

Diameter, 210 ft

Focal length-to-diameter ratio, 0.42

Axis readout, Master equatorial in sidereal coordinates using optical techniques

RF configuration, Cassegrain feed

B. Supporting Studies

1. Seismic Studies

The AAS requires a high resonant frequency structure to meet servo drive requirements under wind environment. The use of such a structure in a locale subject to high seismic activity is a significant problem area in the advanced antenna. Building code requirements generally specify as a seismic loading design criteria that 20% of the gravity load be considered as acting laterally through the center of gravity of the structure. However, high resonant frequency structures with low damping characteristics can require as great as 100% gravity loads.

2. Steel Brittle Fracture

Brittle fracture of steel in cold weather is a serious consideration in structures the size of the AAS. This problem was encountered by JPL during the development stages of some of the *Sergeant* ground equipment, which had to operate at −40°F. In this instance it was solved by the use of U.S. Steel Corporation's T-1. Indications at this time are that the problem can be solved by the use of a manganese steel such as A-299 or by a high nickel content steel as used by Blaw-Knox in the NASA *X-Y* mount antenna now operational in Alaska.

3. Servo and Dynamic Tests

Early in the course of the AAS project, areas of uncertainty were brought to light in the practical design requirements of precisely controlled large structures and their high horsepower servo drives. The development of more information in these areas was needed to enable design criteria to be established.

A major area selected for exploration, having an extreme effect on the total cost of the AAS, involves the dynamic behavior criteria and the enabling design requirements to achieve a specific precision in performance.

A reasonably representative 85-ft model of the proposed large antenna is available at the Goldstone Tracking Station and has been used for experimental work. Model test information would be applicable to the analytical treatment of the proposed large antenna in supplying or verifying assumptions in regard to characteristics of the system, and of system components as installed in a working apparatus.

A test plan for the GTS 85-ft Az-El antenna was developed jointly by JPL and the AAS design study contractor. The plan included all requirements of the contractor, who is responsible for system analysis as an aspect of the design study. Some additional test items were included which JPL considered necessary to understand and to improve the performance of existing facilities.

The full servo and dynamic test program for the GTS 85-ft Az-El antenna follows:

a. Azimuth axis, high and low speed.
Loading sharing and pressure survey. Measure load sharing of the four parallel drive units and make pressure survey of the hydraulic system.

Transfer functions, pressure and rate loops. Determine the experimental transfer functions for the pressure and rate loops over a sine wave frequency spectrum of 0.05 to 20.0 cps, and revise electrical circuitry for optimum performance.

b. Elevation, high and low speed. Same as Test *a* except load sharing not applicable.

c. System vibration modes, servo excited:

(1) Excite the antenna system at various frequencies by means of the azimuth servo system, covering the above frequency spectrum. Record the output of three-axis accelerometer packages located to monitor system structural component acceleration and phase relationship.

(2) Repeat, using the elevation instead of the azimuth servo system.

d. Wind tests:

(1) Experimentally determine the effect of wind load on pointing error by driving the antenna simultaneously in azimuth and elevation, at various rates, in various attitudes relative to the wind direction, in a high wind condition. Record simultaneously, and continuously, the error signal, position information, wind characteristics, and other pertinent data.

(2) Repeat all runs and record data in a still-air condition to determine the tare error.

e. Drive motor inertia effect. Increase, in effect, the inertia of each of the azimuth high speed hydraulic motors by attaching external weights. Determine the effect on system vibration modes by rerunning the transfer function and additionally recording the output of at least one accelerometer package located on the edge of the antenna dish.

f. System vibration modes, external excitation. By means of mechanical excitation applied directly to structural components, excite, identify, measure, and record the vibration modes of the structural–mechanical portion of the antenna system lying within the frequency spectrum of 0.7 to 10.0 cps.

Tests *a*, *b*, and *c* were performed during a previous scheduled period at GTS. Near the end of the period a sizable internal hydraulic leak around the azimuth high speed servo valve was discovered which invalidated the data of Tests *a* and *b*. The hydraulic circuit was corrected and Tests *a* and *b* have been rerun.

The AAS Design Study Contractor has participated in Tests *a* through *c* and is in possession of all test data.

4. Servo Simulator Studies

A servo simulator has been installed in the servo laboratory at JPL which is a simplified mechanical simulation of the azimuth high speed drive system of the Az-El antenna with some deviations.

The use of the simulator as an adjunct to the testing on the 85-ft Az-El antenna has certain advantages: it is continuously available and can be modified at a relatively low cost.

In view of these advantages, a study program was begun with a test of the simulator identical to Test *a* (previous discussion *3. Servo and Dynamic Tests*); an additional test was made using only two drive units. This test was completed, with personnel from the AAS contractor participating.

5. Wind Measurements at AAS Site

The basic objective of the wind study program is to observe the local wind system at Goldstone Site 8 long enough, and in enough detail, to allow some reasonable conclusions to be made concerning the effects of winds on the 210-ft antenna proposed for construction at the site.

The three towers described in *SPS 37-13* were completed in mid-December, at which time the Beckman–Whitley interim instrumentation was installed. Figure 2 shows the top section of the main tower.

There are two basic problems of interest: (1) steady-state or large scale winds, their character, duration, vertical profile, etc.; and (2) small scale or turbulent winds. The problem of turbulent winds is the most pressing at this time; analysis has been made on some data taken with the interim instrumentation on January 9, 1962 at an altitude of 10 m. The data covers a 4-hr period from 11:00 am to 3:00 pm.

Figures 2 and 3 are plots of gust factor at various velocities. Gust factor is defined to be the ratio of the peak wind speed of a given duration in a time interval to the mean wind speed for a given averaging period. In both figures, the peak speeds are instantaneous readings; i.e., the duration of the speed is dependent only on the response of the anemometer. The manufacturers' response data for the anemometer is given in terms of feet of wind which must pass the device before it will respond. The distance constant for the anemometer used is 5 ft. Knowing the distance constant and the average speed, the actual duration of averaging time for the peak winds can be calculated for each point on the curves.

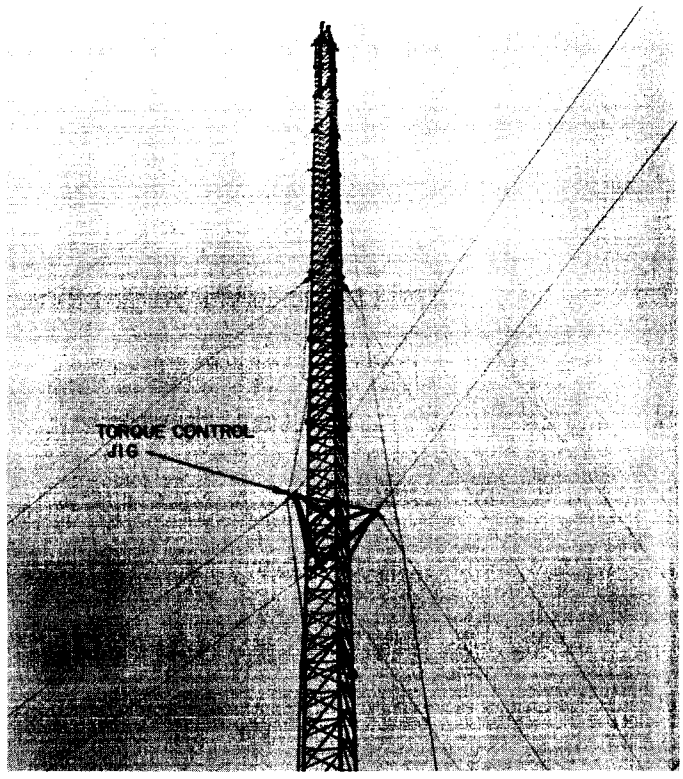

Figure 1. Top section of main tower

The averaging time for the mean wind of Figure 2 was 100 sec; for Figure 3 it was 300 sec.

Reference 1 states that the gust factor will be larger the shorter the duration of the peak wind and the longer the time interval of the mean wind averaging period; 5 min is given as the standard averaging period. The data of Figure 3 is compared with data of Reference 1, which is given in Table 1.

Figure 3 agrees reasonably well with the data of Table 1, although there is probably no particular reason that it should; Figure 2 bears out the statement that the gust factor should be lower for a shorter mean wind averaging time. Reference 1 further states that there is some doubt that there exists any real variation of gust factor with the mean wind speed, a doubt which is strengthened by Figures 2 and 3.

The problem of fluid turbulence was first investigated in 1883 by D. Reynolds. A statistical theory of isotropic turbulence was published by G. I. Taylor in 1935, and forms the basis for the modern theory. The work of Kolmogorov, Von Karman–Howarth, Dryden and others has led to a set of equations which describe the expected power spectrum of isotropic turbulent flow for various regions of turbulent Reynolds number. Thus, a great

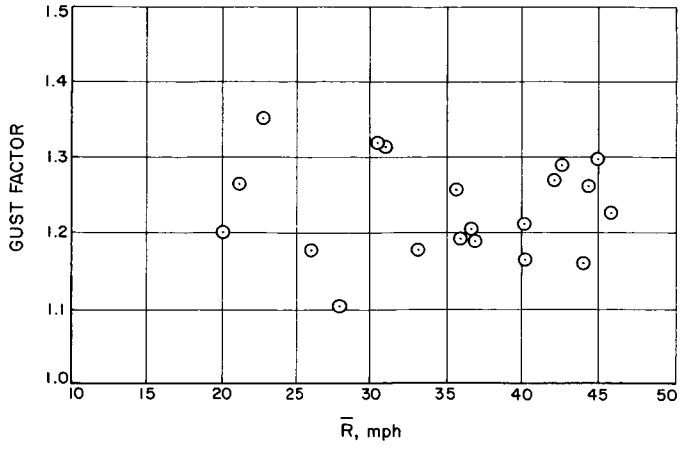

Figure 2. Gust factor, 100-sec averaging time

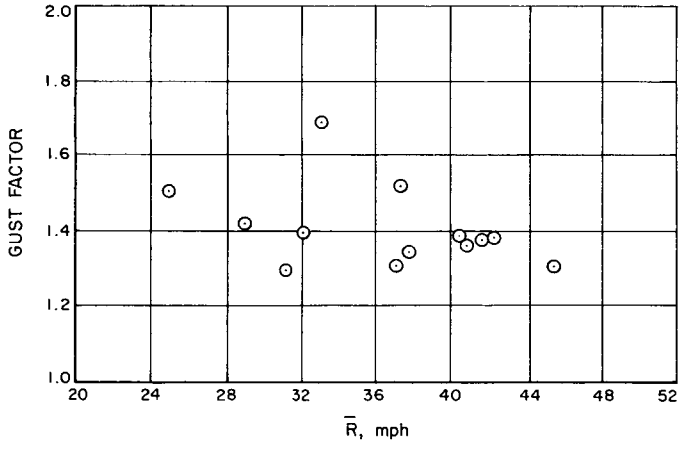

Figure 3. Gust factor, 300-sec averaging time

part of the investigation of turbulent spectra consists in determining what portion of the turbulent Reynolds number range the observed data falls into, and whether or not the data fits the spectral law proposed for the region. The law predicted for the region in which isotropic turbulent winds normally fall is given by

$$\phi(f) = kf^{-5/3} \qquad (1)$$

where $\phi(f)$ is energy and f is frequency.

Figures 4 and 5 are plots of the power spectrum of turbulent winds for two intervals of about 150 sec each. The data was reduced as follows: An Esterline–Angus recording made at 6 in./min was read by a Gerber oscillograph reader at a rate of five samples/sec. That is, one sample per 0.02 in., or about one sample per two pen widths. Thus, the high frequency end of the resultant spectra would tend to be of somewhat dubious value. The data was then processed by the JPL spectrum analysis program (JHB 18).

Table 1. Gust Factors for peak wind speed of 2-sec duration for height intervals approximately 40 to 125 ft

5-min mean wind speed, kt	Gust factor	
	Most probable	Maximum
20	1.5	1.9
30	1.4	1.8
40	1.4	1.7
50	1.4[a]	1.8[a]

[a]Extrapolated values.

The spectrum of Figure 5 fails to resemble the inverse five-thirds law of Equation (1). At first, it was thought that the instrumentation itself might have distorted the spectrum. Further investigation showed that the anemometer basically acts like a linear system and could not attenuate a five-thirds law spectrum in the manner shown. The conclusion is that the data at the particular time violates the important assumption of isotropy over most of the frequency range, and therefore cannot be compared with any of the laws for isotropic turbulence.

The spectrum of Figure 6 is more well behaved. Figure 6 is a plot of the spectrum on log-log scale. The power law coefficient for this data appears to be -2.3, rather than $-5/3$. This effect could be due to attenuation by the instrument and/or the reading process.

The analysis of the interim wind data has been valuable in that it has indicated various areas where the data reduction process must be improved.

6. Wind Tunnel Studies

One of several inter-related problems in the design of paraboloidal reflector directional antennas is wind loads. These wind loads can not only distort the necessarily highly accurate shape of the antenna reflecting surface, but can create large torques which must be overcome by any angular positioning gear, and have been known to cause structural damage. Large antennas of this nature, designed for tracking orbital and interplanetary flights, are particularly sensitive to wind loads in that they should be capable of use during critical phases of the trajectories, in spite of adverse wind conditions.

Although a number of paraboloidal reflector antennas of various sizes, descriptions, and design purposes are in use, a surprisingly small amount of wind load data is available. What information is available, either from small model tests, or field tests of existing installations, contains features which make it nearly impossible to form

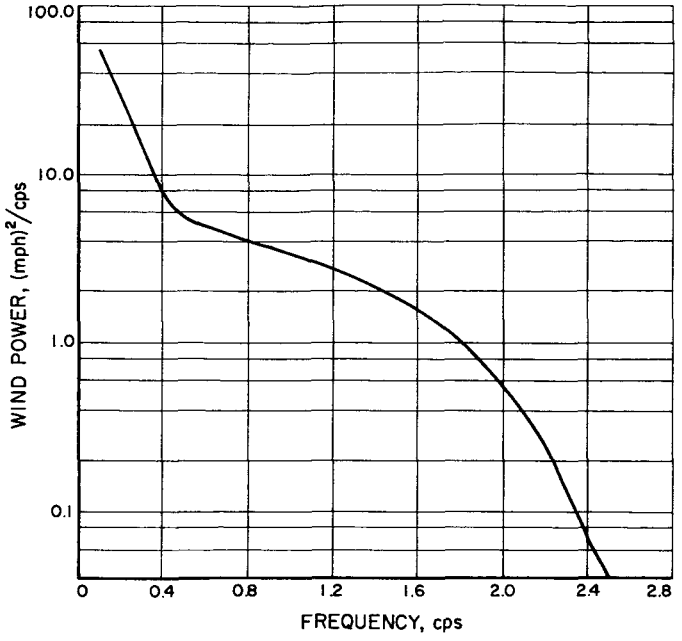

Figure 4. Wind power spectrum, average wind speed = 40.301 mph

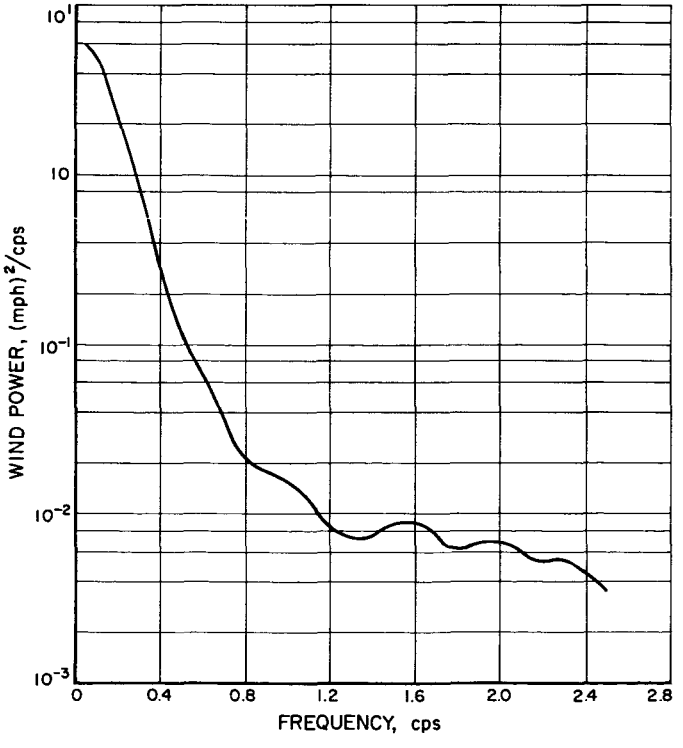

Figure 5. Wind power spectrum, average wind speed = 38.576 mph

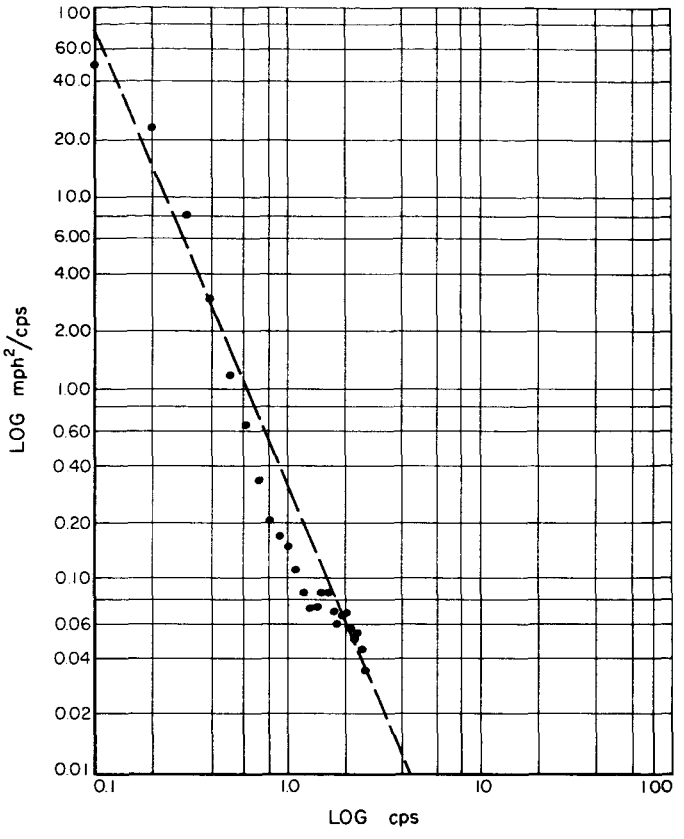

Figure 6. Wind power spectrum, Goldstone Site 8 January 9, 1962

the comparisons necessary for optimization or design use. In order to obtain a consistent set of data showing the effect of parameters, such as focal-length-to-diameter ratio, distribution and amount of reflector surface porosity, devices to reduce loads, etc., a wind tunnel test program was embarked upon. Configurations were chosen for investigation which appeared to be reasonable compromises between aerodynamic loads, structural feasibility, and radio frequency performance.

Throughout this discussion, conventional United States aerodynamic terminology and conventions are used. For the convenience of those in other fields of endeavor, several equivalent terms are presented: (1) yaw angle or moment refers to azimuth angle or moment, (2) pitch angle or moment refers to elevation angle or moment, and (3) force or moment coefficients refer to forces or moments, nondimensionalized by the area, diameter (as appropriate), air density, and wind velocity squared. As an example of the meaning of these nondimensional coefficients, for a 200-ft diameter paraboloidal reflector antenna in a 70-mph wind, a moment coefficient of 0.15

is equivalent to 11.5 × 10^6 ft-lb torque, and a force coefficient of 1.4 is equivalent to 0.54 × 10^6 lb load.

Except as noted, all data presented in this report is in the stability axes system, a mutually orthogonal cartesian coordinate system oriented parallel to the ground surface and the azimuth pointing direction of the reflector (but not to the elevation pointing direction of the reflector).

a. Test description. These tests were performed in the Northrop Subsonic Wind Tunnel, which has a test section 7 ft high by 10 ft wide. All configurations tested used 18-in. diameter paraboloidal reflectors. Larger size models would have caused sufficient distortion to the tunnel air flow so as to seriously affect the reduced data applicability to field installations. These paraboloidal reflectors were spin-formed from commercial copper sheet, ⅛ in. thick. Several were perforated with ¾-in. diameter holes in reasonably uniform patterns to obtain the desired porosities. They were mounted near the tunnel floor, at the center of the 20-ft long test section. A 1¾-in. diameter staff, which was shielded from wind loads by a 2-in. diameter tube, connected the model to the large, accurate balance located below the floor. A knuckle at the top of this staff permitted pitch angle settings from 0 to 180 deg, in 5-deg increments. The models (and balance) were rotated by remote control to any desired yaw angle over a range in excess of 0 to 180 deg.

Major emphasis was placed on force and moment data. In addition, limited amounts of other types of data were obtained, such as:

(1) Pressure distributions on three of the configurations.

(2) Dynamic data, indicative of the severity of aerodynamically forced oscillations as a function of reflector attitude.

(3) Photographs of tufts attached to several models, indicative of the air flow patterns responsible for the previously mentioned data.

The tunnel variables for this test were:

(1) Wind velocity, 85 to 260 mph, at atmospheric pressure, giving Reynolds numbers in the range 1.2 to 3.6 × 10^6.

(2) Tunnel floor boundary layer thickness, 3 and 18 in., the latter approximating the terrestrial wind boundary layer relative to the model.

(3) Clearance between the floor of the tunnel section and the bottom of the reflector surface.

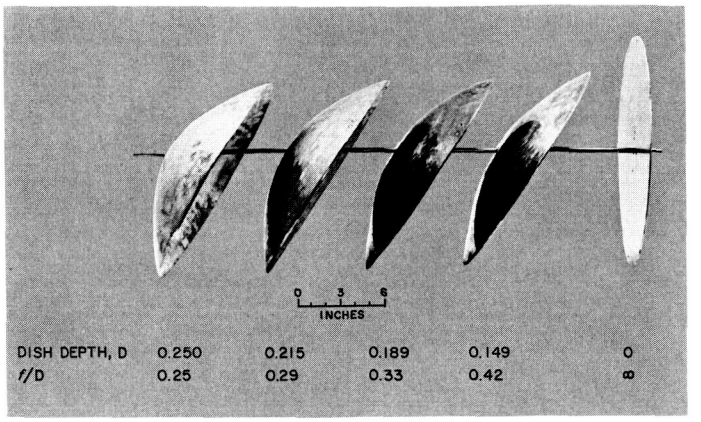

Figure 7. Antenna dishes of various depths

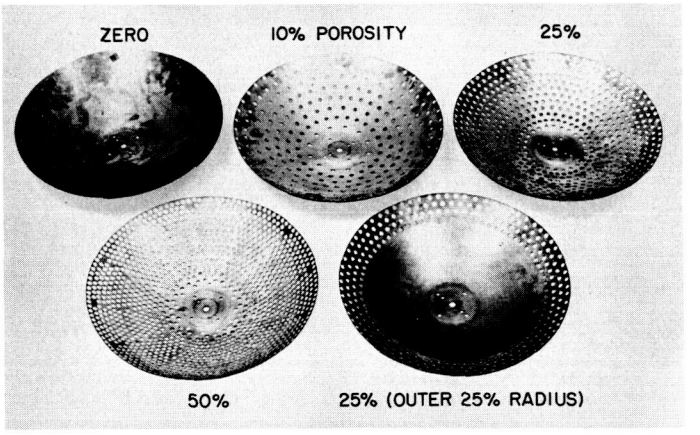

Figure 8. Perforated antenna dishes

The various model configurations tested included the following variables:

(1) Paraboloidal reflector focal-length-to-diameter (f/D) ratios of 0.25, 0.33, 0.42, and infinite (flat plate) corresponding to depth to diameter ratios of 0.250, 0.189, 0.149, and 0 (Fig 7).

(2) Paraboloidal reflector surface uniformly distributed porosities of 0, 10, 25, and 50% (Fig 8).

(3) Paraboloidal reflector surface outer edge porosities of 25 and 50% over the outer 10 and 25% of the reflector radius (Fig 9).

(4) Four protuberance-type spoilers (Fig 10).

(5) Simulated reflector support structure with three sizes of counterweight side surface areas (aerodynamic balances, Fig 9).

(6) A pylon (conical buildup on the 2-in. diameter windshield, Fig 9).

Figure 9. Model of complete antenna configuration

(7) Surface roughness on the back of the reflecting surface, 1½% of the reflector diameter in height (Fig 11).

In all cases, the reflecting surface was thin compared to its diameter; i.e., the case of an enclosed support structure was not examined. (The center 4-in. diameter of all configurations was distorted for mounting purposes, and could not be perforated, Fig 10.)

Only a representative number of the above combinations were tested, and the pitch angle range examined for a number of these combinations was very sparse. The test program included sufficient pertinent combinations to make it possible to estimate the performance of untested combinations by applying mutual differences, interpolation, and extrapolation.

b. Reynolds number effects. One of the problems in applying the results from small scale wind tunnel tests to full scale installations is that of Reynolds number (scaling effects). As shown by Figure 12, in certain regions of Reynolds number, the nondimensional forces (and probably moments) can vary by a factor as great as five. Because such Reynolds number sensitivity data was virtually nonexistent for paraboloidal geometries, it was

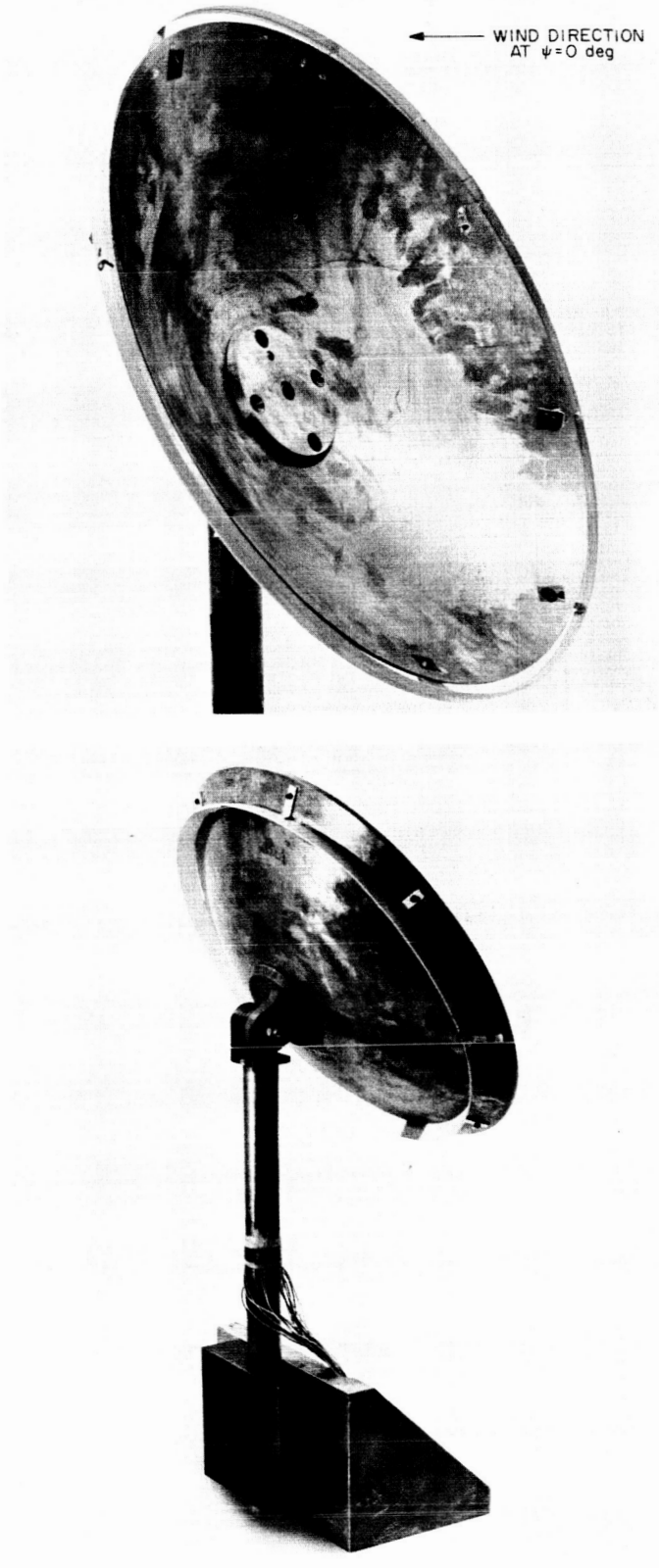

Figure 10. Model with protuberance-type spoilers

Figure 11. Model for back surface roughness tests

necessary to assume that the data represented by Figure 12, based on spheres, cylinders, and flat plates, would be approximately applicable. Based on the evidence that the model test Reynolds number would be in excess of the critical region, the test program was initiated.

During the course of the test, the Reynolds number was varied by a factor of 3 on one solid reflector configuration, and a factor of 1.35 on one porous reflector configuration. For the solid configuration, the yaw moment about the parabola vertex comparison is shown in Figure 13, to demonstrate the lack of this scale effect. Except for these Reynolds number checks, the entire test was carried out at a Reynolds number (based on paraboloidal reflector diameter) of 2.7×10^6. This resulted from a wind velocity of 192 mph at sea level ambient pressure (a dynamic pressure of 95 lb/ft^2).

c. Tunnel floor and support interference effects. If there were no ground plane (tunnel floor) air flow restraint, velocity nonuniformity (tunnel floor boundary layer), or support (windshield) interference, the model would have axial symmetry. Such a symmetrical model would show identical results for pitch and yaw variations. One such comparison is presented in Figure 14, which shows side force and lift force coefficients vs yaw and pitch angles, respectively (in wind axes orientation). The discrepancies between these two curves must, then, be due to one or more of the above itemized factors.

The comparisons outlined in the above paragraph facilitate interpolation and extrapolation of the data resulting from this test. This feature is important in several specific cases:

(1) Data were obtained at a very limited number of pitch angles on all except one configuration.

(2) Due to the design of the balance used for resolving the forces and moments, the pitch and roll moment data are substantially inferior to the other four components.

Another support interference phenomena may be seen in the resulting data. The presence of the pylon shown in Figure 9, which represents a profile area of approximately 10% of the reflector frontal area, increases the moments approximately 10%, and the forces approximately 5%.

d. Reflector focal length (paraboloidal depth). Figure 15 shows the changes in the yaw moment coefficient about the paraboloid vertex as a function of the yaw angle, for the various reflector f/D ratios. This figure shows that the deepest reflector exhibits approximately 20% higher yaw moment positive peak (about the paraboloid vertex) than the shallowest reflector; however, the negative peak yaw moment, while smaller in absolute magnitude than the positive moment, is greater for the shallower reflectors. There is relatively little change in the maximum rate of change of yaw moment with yaw angle.

It is interesting to note the yaw moment vs yaw angle for the flat circular plate, also shown on Figure 15. If it were not for the support effect, this curve would be inversely symmetrical about the 90-deg angle. While the general shape exhibits such symmetry, the lack of comparison in magnitude allows an evaluation of the support interference.

While not illustrated, the axial force (parallel to the ground and in the reflector azimuth direction) exhibits relatively little change for the different reflector focal lengths. As might be expected, the peak forces perpen-

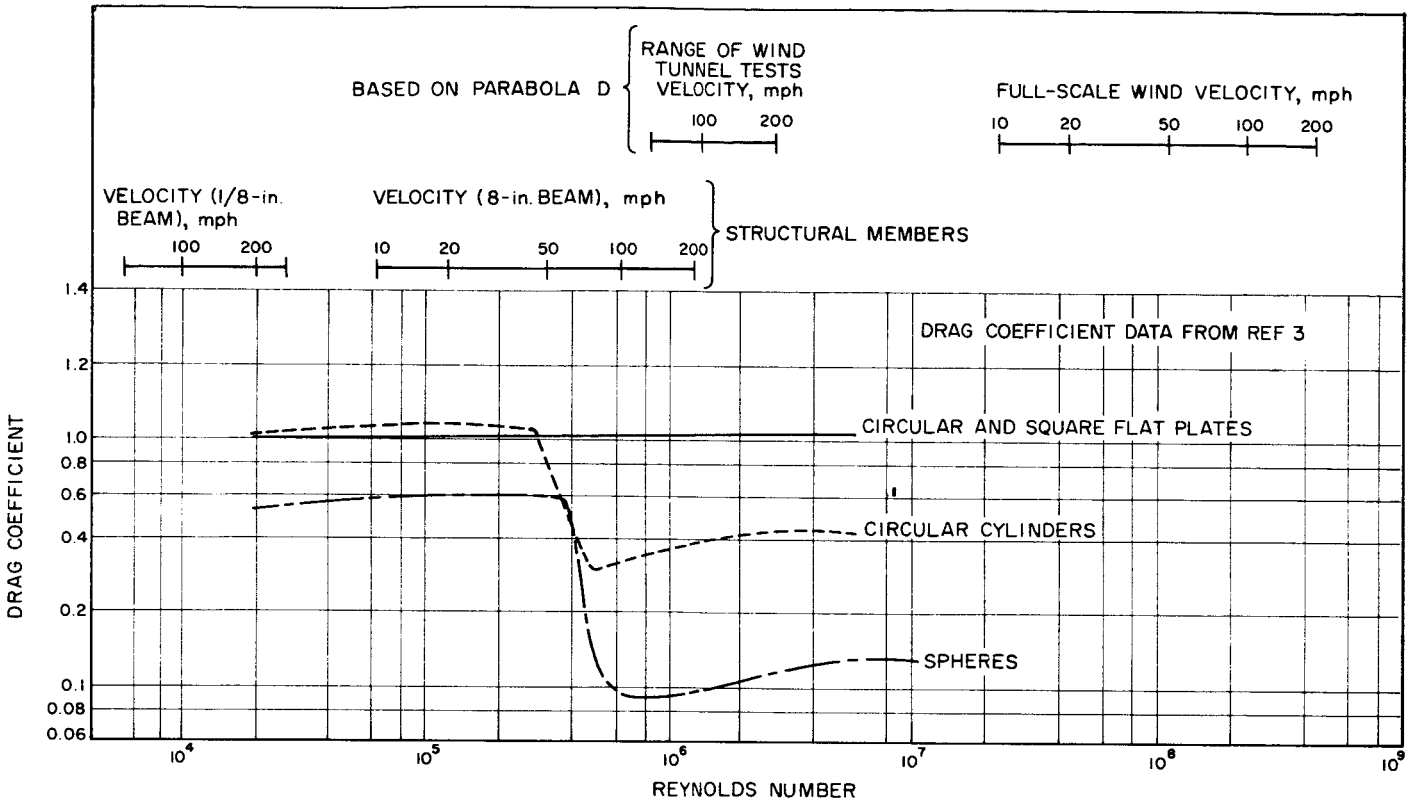

Figure 12. Reynolds number comparison

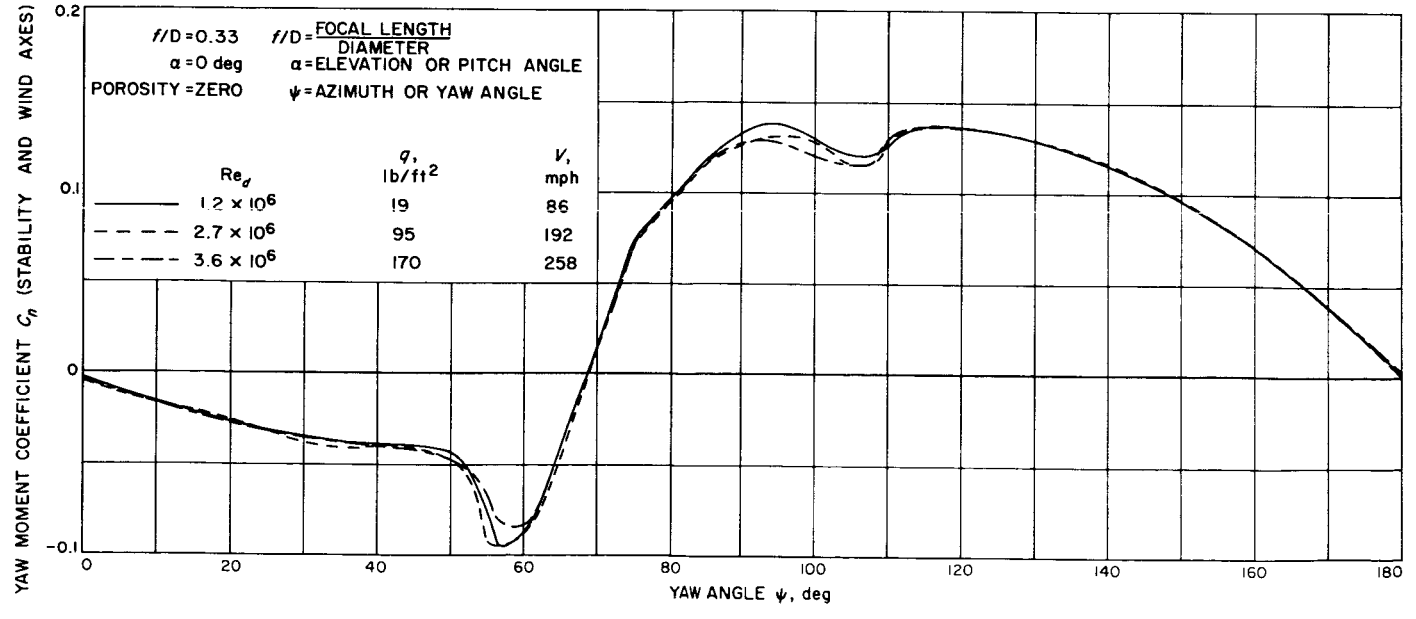

Figure 13. Effect of Reynolds number on yaw moment

dicular to the paraboloid centerline are approximately 55% greater for the deepest reflector than for the shallowest reflector.

e. Angular rotation center location. The reflector angular positioning mechanism must be capable of overcoming the torques due to wind loads. As Figure 16 shows, the

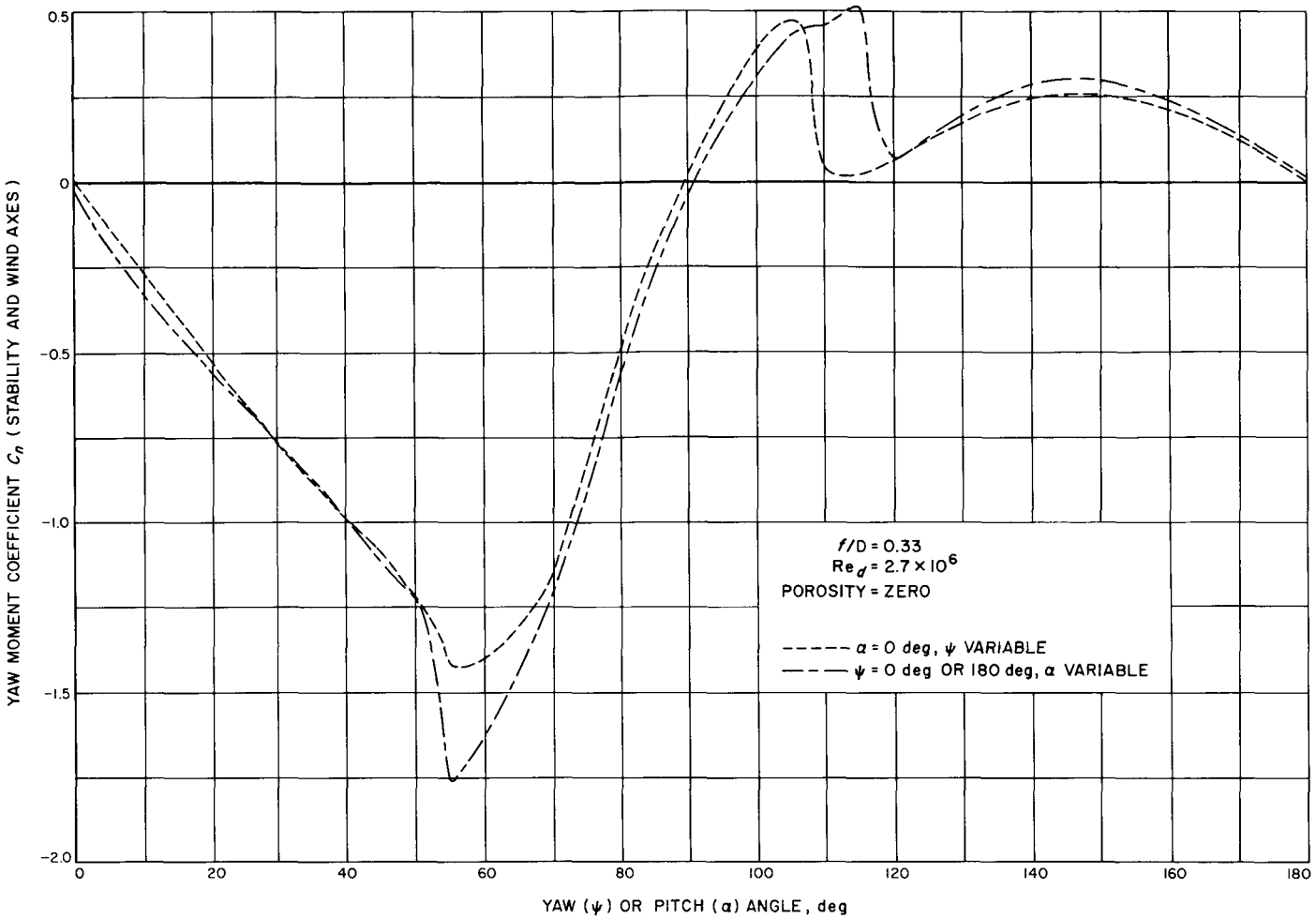

Figure 14. Comparison of side force (wind axes)

magnitude of these torques is affected by the relative position of the moment center. For this solid surface reflector, the peak position yaw moment is reduced 29% for a moment center travel equalling 30% of the diameter. The minimum yaw moment would be obtained with the moment center toward the focal point from the reflector aperture. With the exception of this figure, *all moment curves presented in this discussion are taken about the paraboloid vertex*; i.e., the intersection of the paraboloid centerline with its reflecting surface.

f. Effects of pitch angle on moments and forces. Figure 17 shows an example of the variation of yaw moment vs yaw angle, as a function of pitch angle, for a typical solid surface reflector. With the exception of lift and pitch moment, the forces and moments show peak values near zero pitch angle; the lift and pitch moment show peak values at approximately 60-deg pitch angle.

g. Uniformly distributed porosity. Figures 18 and 19 show the effect of uniformly distributed porosity on axial force and yaw moment. This effect of uniform porosity is the strongest influence noted throughout the test: 50% porosity reduces the peak yaw moment (about the vertex) 25%, eliminates any negative yaw moment, reduces the rate-of-change of moment with angle 84%, the peak axial force by 50%, and the peak lift (at 60-deg pitch angle) 80%. Some of these reductions would be even more significant, in percent, as the moment center moved away from the paraboloid focal point. It is interesting to note that these reductions are on the order of linear with porosity up to 25% porosity; additional reductions due to 50% porosity are on the order of half of those due to 25%.

h. Rim porosity. Figure 20 illustrates the effect of reflector surface porosity on the rim only, the central portion being solid. While the reduction in forces and

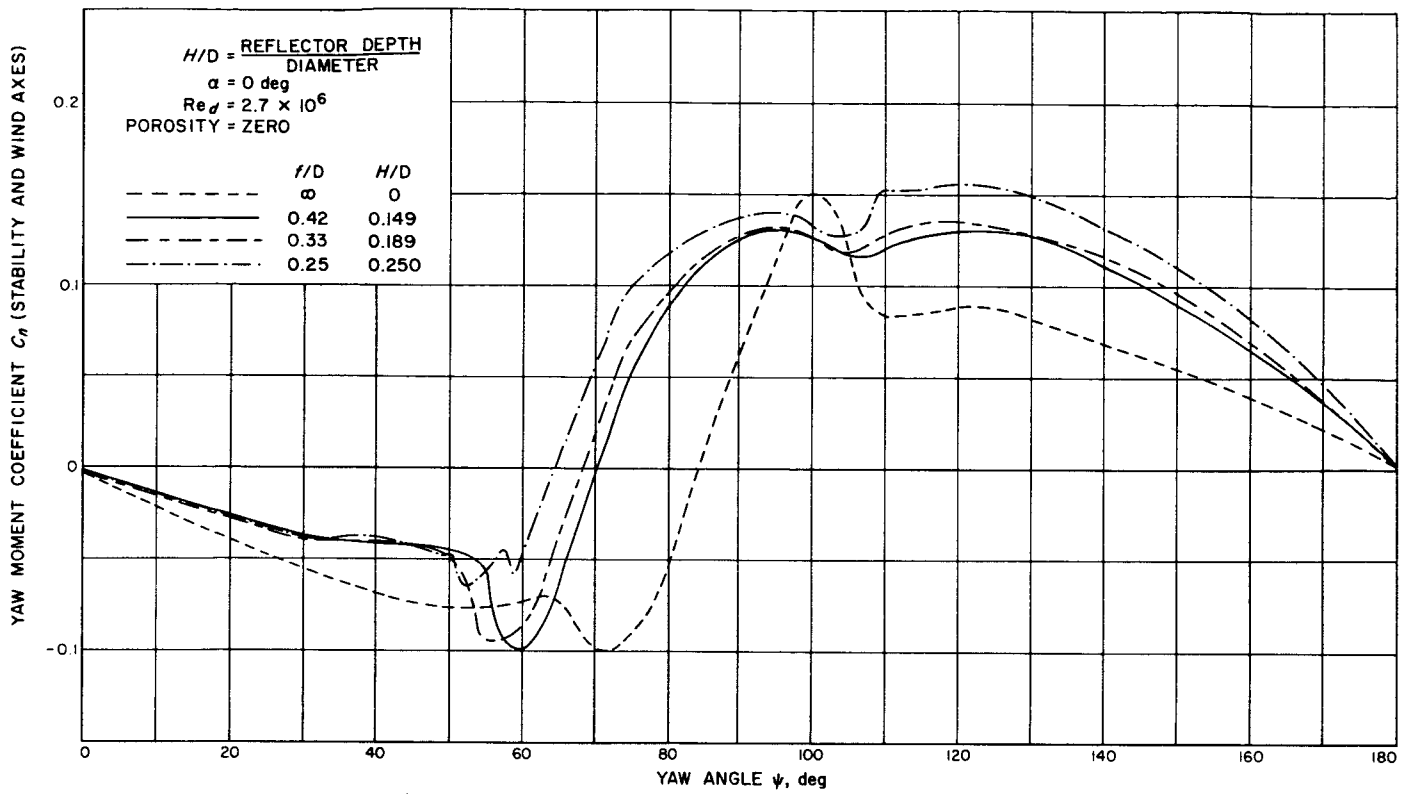

Figure 15. Effect of antenna reflector depth on yaw moment

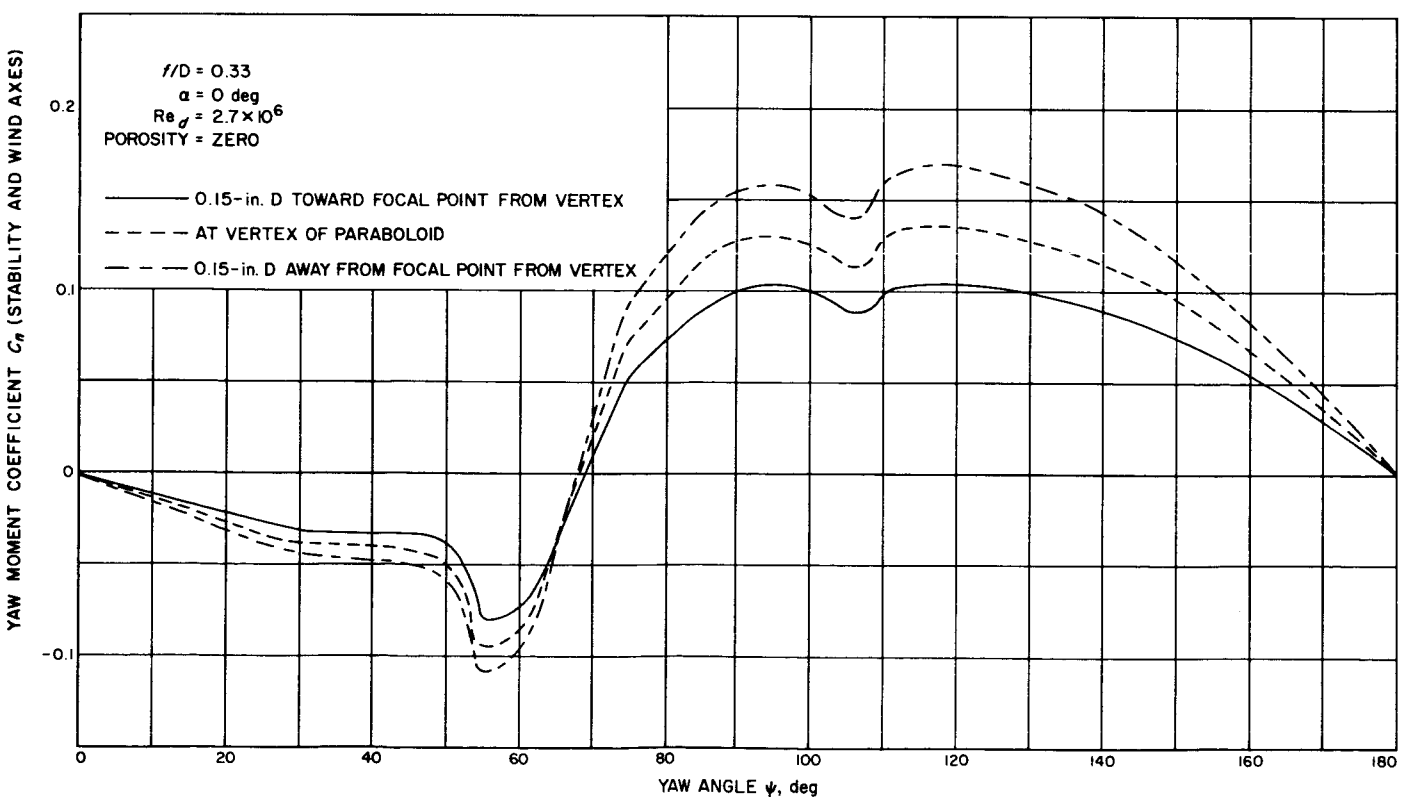

Figure 16. Effect of yaw axis location on yaw moment

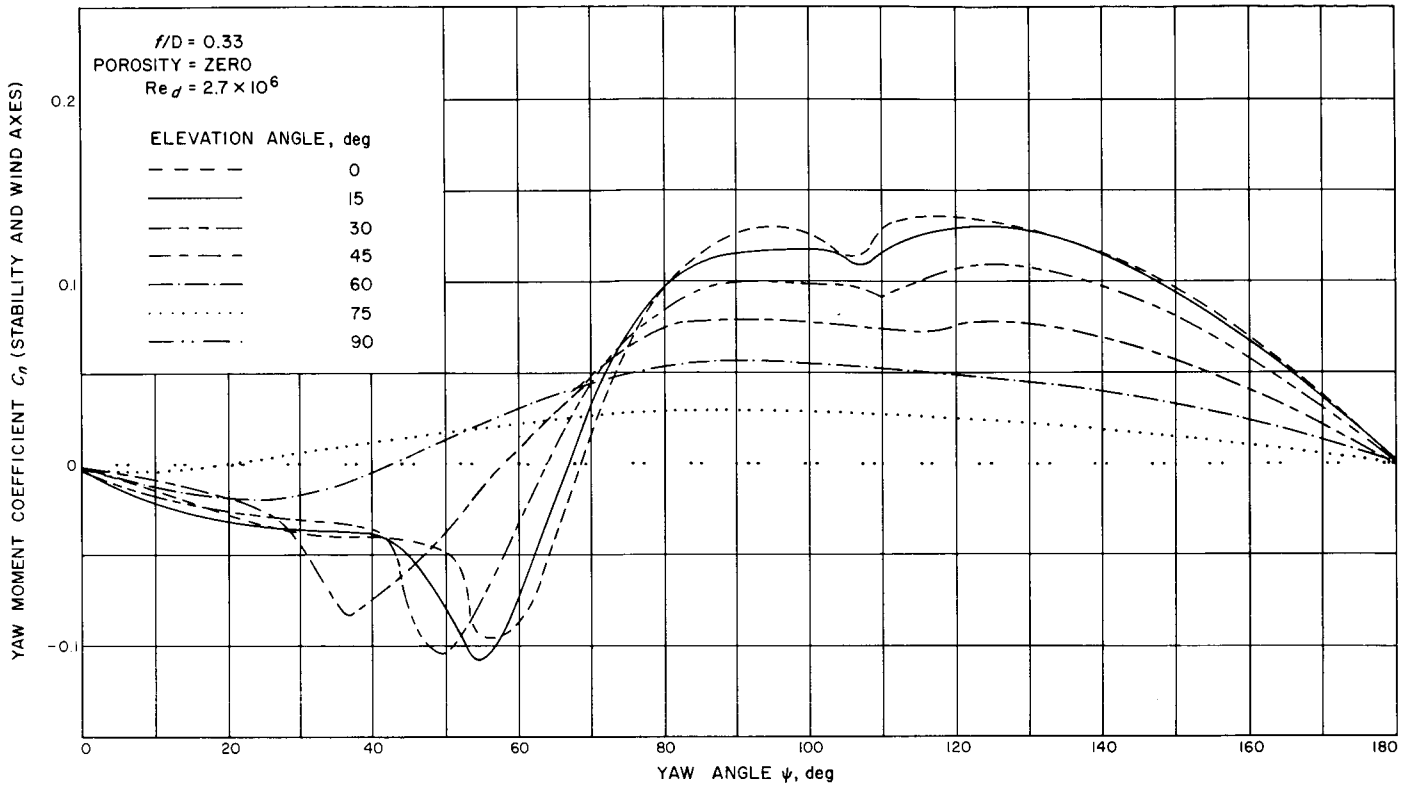

Figure 17. Effect of elevation (pitch) angle on yaw moment

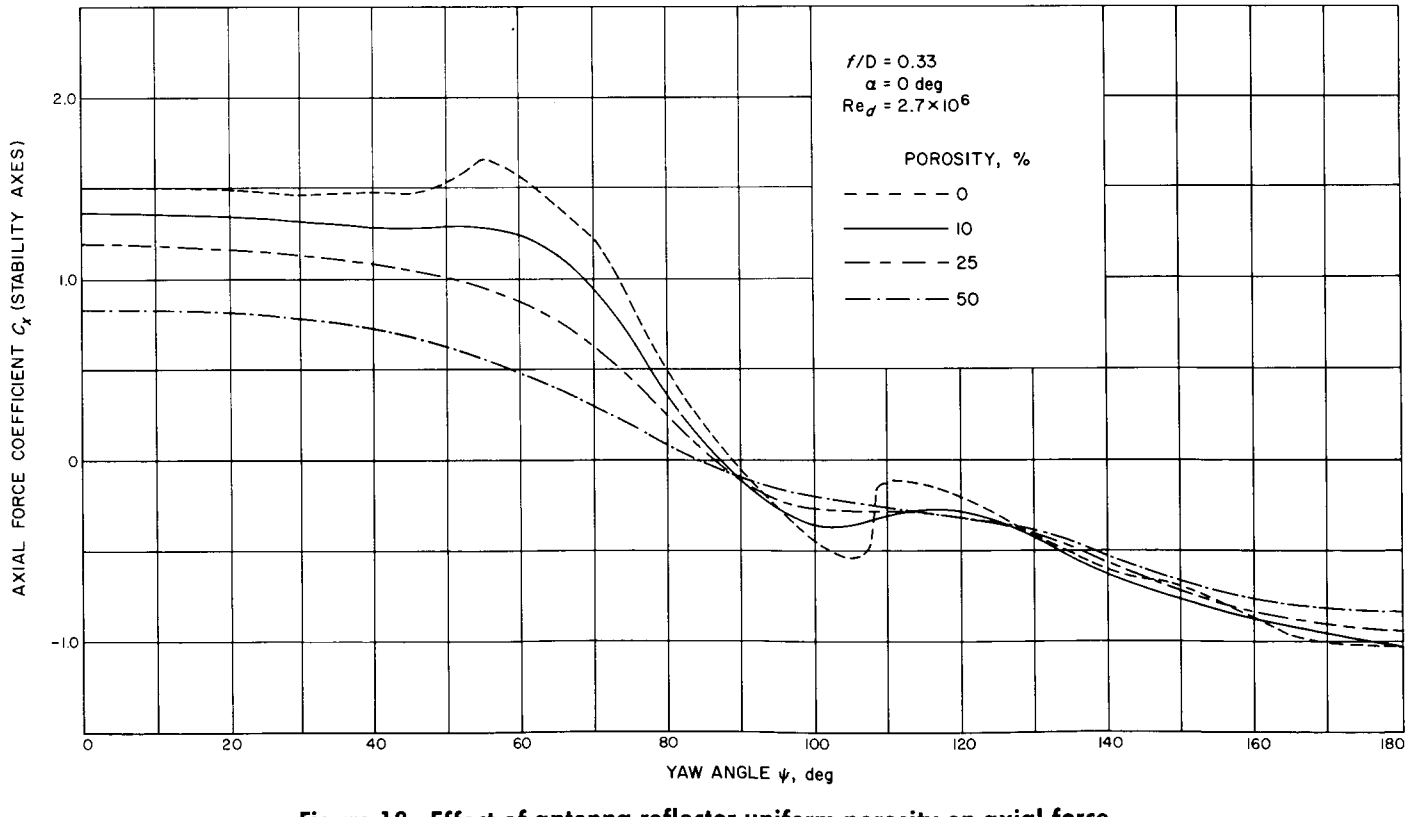

Figure 18. Effect of antenna reflector uniform porosity on axial force

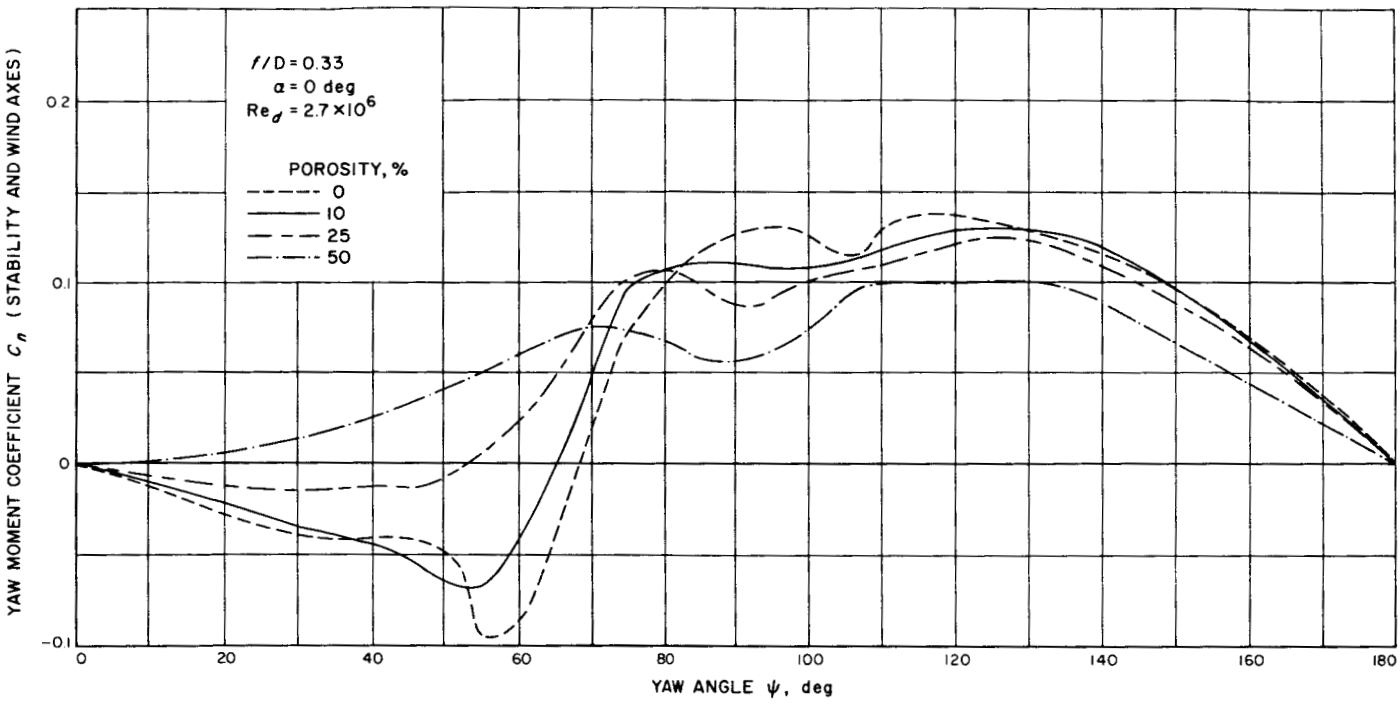

Figure 19. Effect of antenna reflector uniform porosity on yaw moment

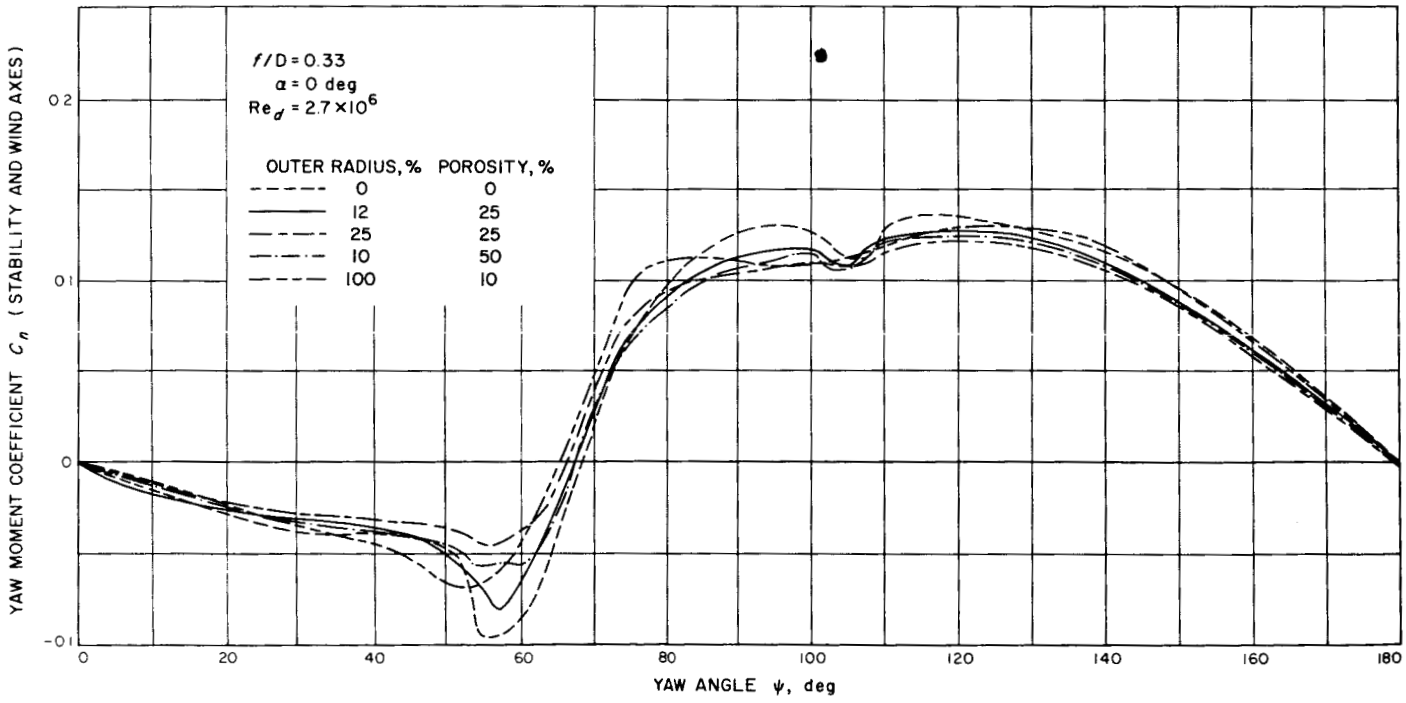

Figure 20. Effect of antenna dish rim porosity on yaw moment

moments is smaller than that for the uniformly distributed porosity, for the same total amount of porosity, the effect is slightly larger when it is distributed at the edges only. There appear to be other advantages, outside of wind loads, which may result from distributing the porosity at the edges only.

i. Spoilers. Two types of protuberance spoilers were investigated. One consisted of a cowl-ring around the

reflector periphery; relative to the no spoiler configuration, it did not significantly reduce the moments, and it increased the forces slightly. As shown by Figure 21, trip-fence spoilers had a beneficial effect. The larger of the two tested, having a height of 4% of the reflector diameter, reduced the peak yaw moment approximately 9%, the peak axial force 9%, and the maximum rate of change of moment with angle 17%. This particular configuration was the only one tested which showed hysteresis in force or moment vs angle, the hysteresis loop occurring in yaw moment at about a 95-deg angle to the wind.

It is interesting to note that test data exists and full size antennas are in use, incorporating trip-fence spoilers having a height on the order of 10% of the reflector diameter.

j. Reflector support structure. Figures 22 and 23 show the effect of a simulated structural support (Fig 9) behind the otherwise relatively thin paraboloidal reflecting surface, both with and without aerodynamic counterbalancing surfaces (extended counterweight side surface areas). Even with the minimum size counterweights, the structure reduces the peak yaw moment about the vertex approximately 18%, apparently by yielding some aerodynamic counterbalancing. This reduction in yaw moment is, however, at the expense of increasing the side force by a factor of 1.5. Note that the position of the moment center will have a strong influence on the gain due to such counterbalancing. The axial force is not significantly changed.

The simulated reflector support structure was fabricated mainly from ⅛-in. square members, in order to minimize the Reynolds number effects (as indicated by Fig 12 for sharp edged shapes). No check was made on the Reynolds number sensitivity of these configurations. It is realized that this model structure has fewer members, of a larger relative size, than most full scale installations. Fabrication costs prohibited a more detailed model for this phase of the investigation; the results should be at least indicative.

Some care must be taken in designing the support for large antennas where structural members of circular cross-section are utilized. Wind-excited periodic vibrations in such members have produced structural failures on several existing installations. This phenomenon is relatively well understood, however, and is predictable (Ref 2).

k. Complete configuration. Figures 22, 23, and 24 serve to illustrate the forces and moments on one of the several possible complete configurations tested. A simulated complete configuration represented by these figures is illustrated in Figure 9, and incorporates the rim porosity,

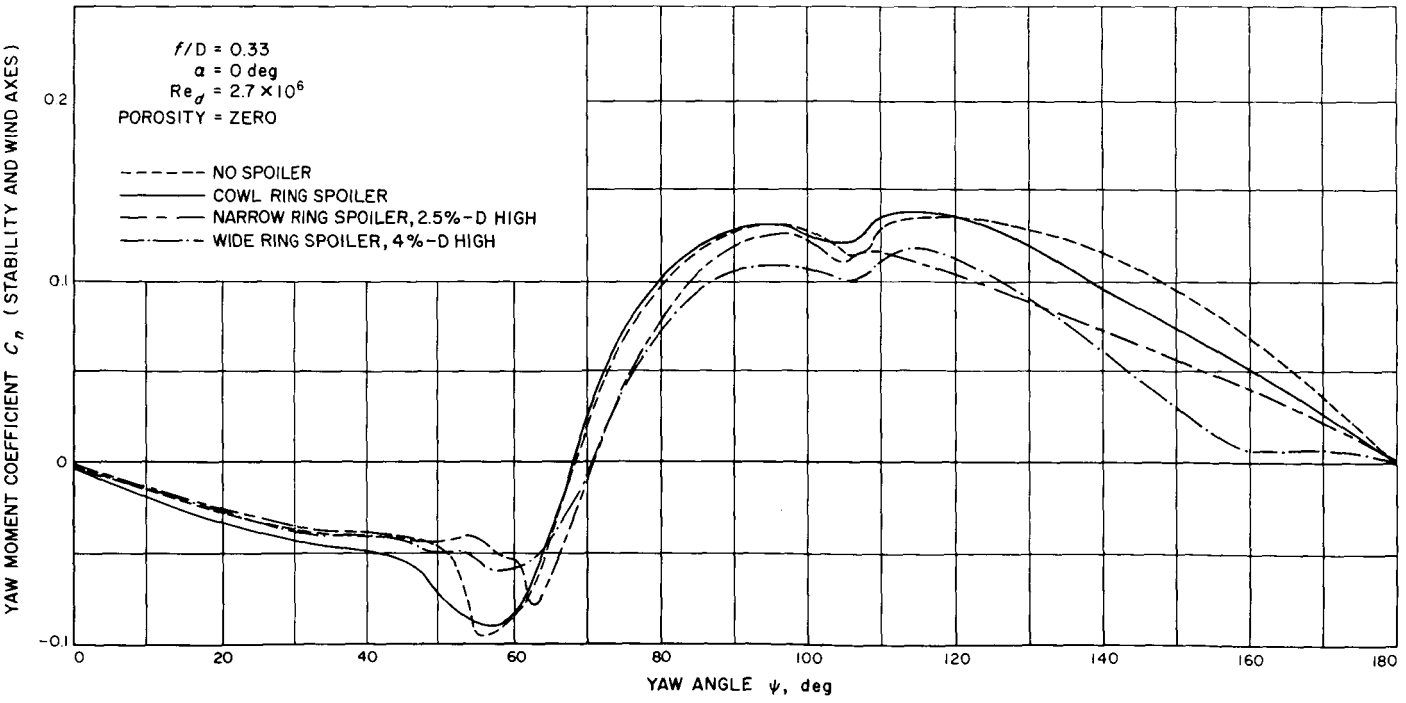

Figure 21. Effect of antenna reflector spoilers on yaw moment

pylon, paraboloidal reflecting surface supporting structure, and extended counterweight side surfaces. Although the yaw moment for this combination is on the order of half of that for the simple solid reflector, the side force is nearly doubled. It remains to be investigated whether or not this is a desirable compromise when compared to structural problems, angular positioning problems, etc.

l. Pressure distribution. Figure 25 shows one of the models on which pressure distribution was measured, and

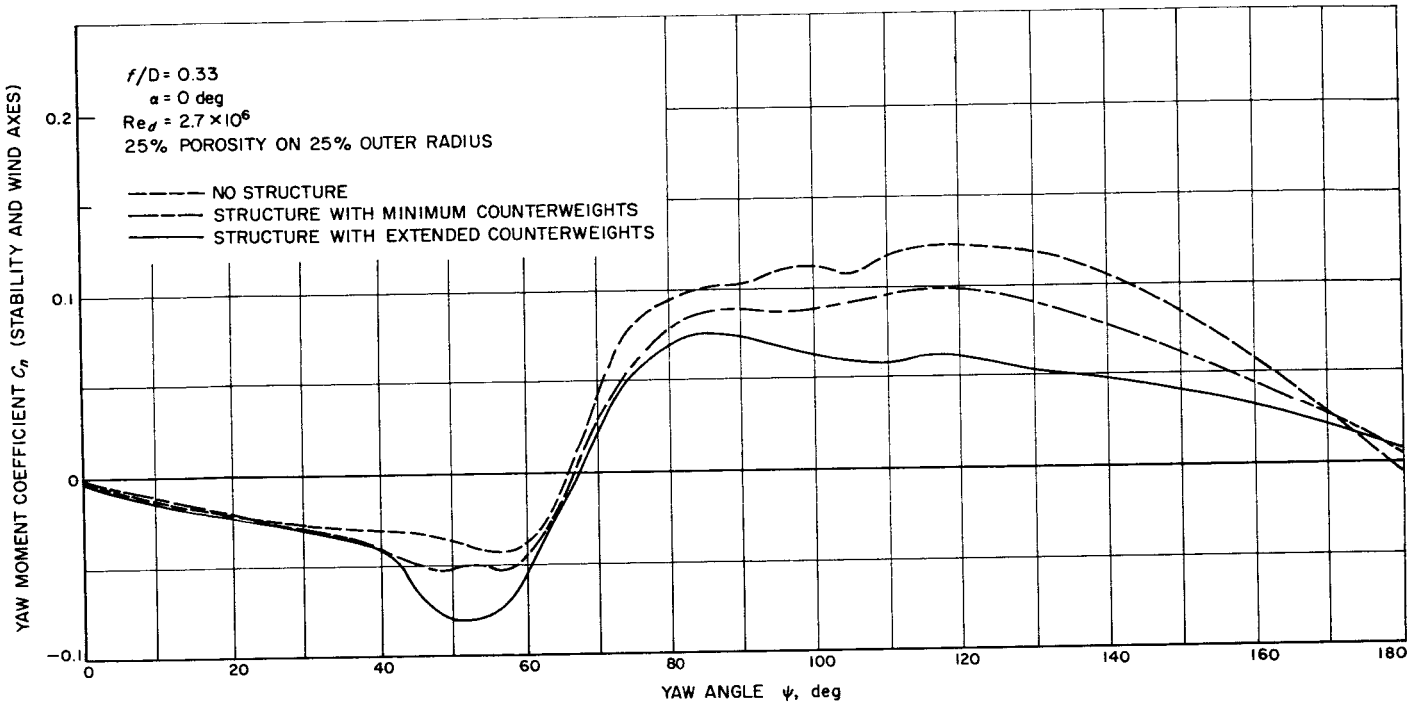

Figure 22. Effect of simulated structural support on yaw moment

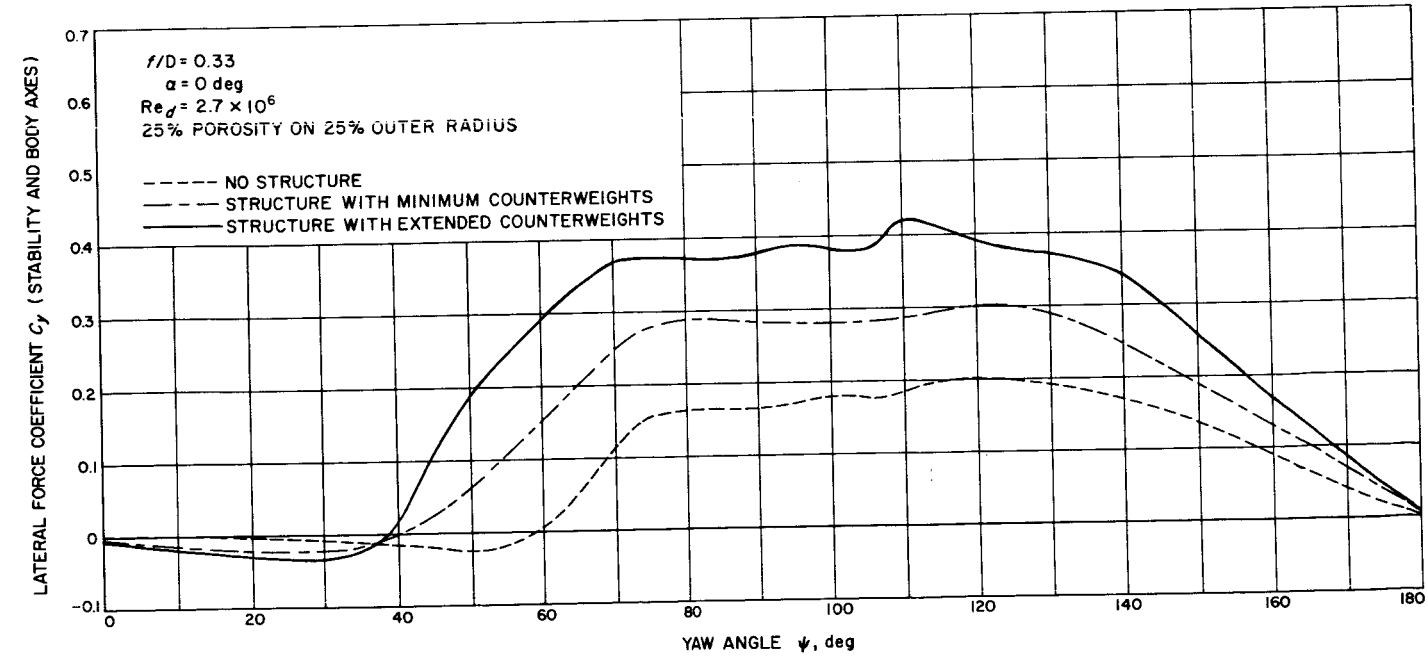

Figure 23. Effect of simulated structural support on lateral force

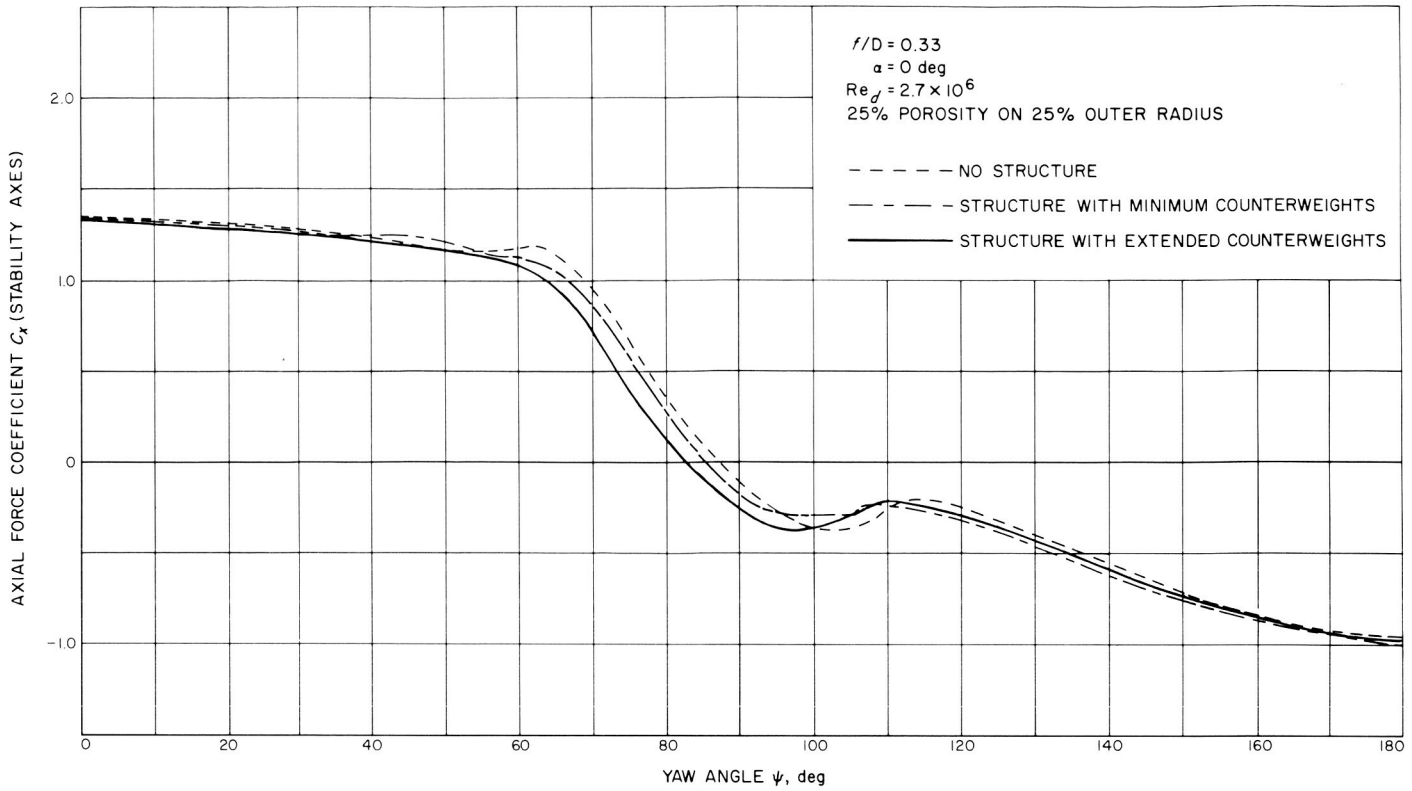

Figure 24. Effect of simulated structural support on axial force

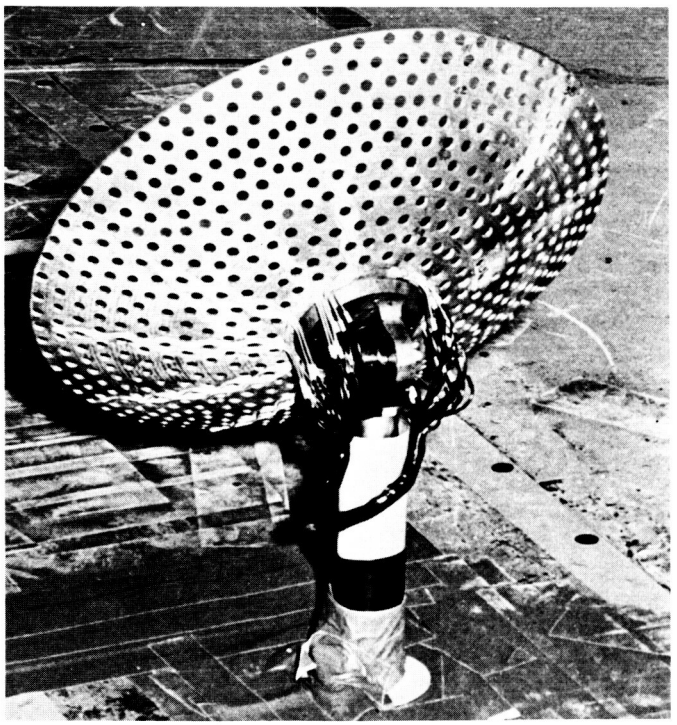

Figure 25. 25% porosity pressure model

Figures 26 and 27 present samples of pressure difference contours across a solid reflecting surface paraboloidal antenna. It is interesting to note that the pressure drops off somewhat near the edge of the reflector, a feature beneficial to reflecting surface elastic deformations caused by wind loads.

m. Dynamic oscillation data. The strain gages attached to the model support staff, from which the dynamic data were obtained, are shown in Figure 5. This data, recorded as oscillograph traces, has not been completely reduced, and is not presented.

n. Summary. The most significant results of the preliminary AAS wind tunnel test program have been presented in this report. These results indicate the significance of the proper design consideration of wind loads on structures of this type.

A complete report on the results of this investigation, including comparisons with data from other sources, is in preparation. Complete tabular data and a large number of working plots, in several different axes orientation systems, are available.

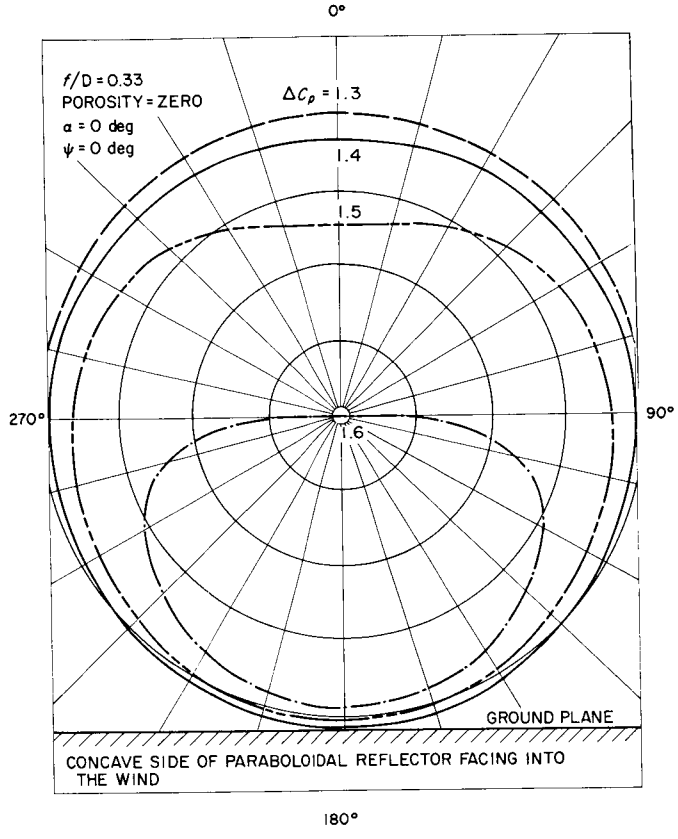

Figure 26. Wind pressure load across paraboloid surface

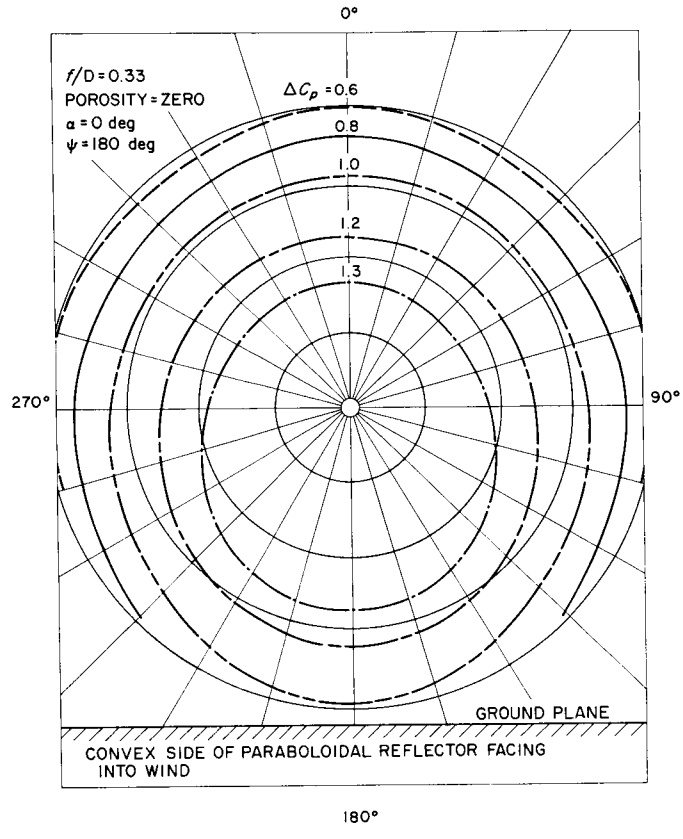

Figure 27. Wind pressure load across paraboloid surface

References

1. Handbook of Geophysics, ed. by U.S. Airforce, The Macmillan Co., New York (revised), 1960.

2. Weaver, W., Jr., "Wind-Induced Variations in Antenna Members," Journal of Engineering Mechanics, p. 41, Proceedings American Society of Civil Engineers, February 1961.

3. Hoerner, Sighard F., *Fluid Dynamic Drag* (Chapter 3), published by author, Midland Park, N. J., 1958.